

# Error Mitigation in Computational Design of Sustainable Energy Materials

**Christensen, Rune**

*Publication date:*
2017

*Document Version*
Publisher's PDF, also known as Version of record

Rune Christensen

---

# Error Mitigation in Computational Design of Sustainable Energy Materials

---

PhD Thesis

November 2016


Department of Energy Conversion and Storage
Technical University of Denmark

**Error Mitigation in Computational Design of Sustainable Energy Materials**

## Author

Rune Christensen
E-mail: runch@dtu.dk

## Supervisors:

Tejs Vegge
Professor, Head of Section
Section for Atomic Scale Modelling and Materials
Department of Energy Conversion and Storage
Technical University of Denmark
E-mail: teve@dtu.dk

Heine Anton Hansen
Researcher
Section for Atomic Scale Modelling and Materials
Department of Energy Conversion and Storage
Technical University of Denmark
E-mail: heih@dtu.dk

## Department of Energy Conversion and Storage

Atomic Scale Modelling and Materials
Technical University of Denmark
Fysikvej, Building 309
2800 Kgs. Lyngby
Denmark

www.energy.dtu.dk/
Tel: +45 46 77 58 00
E-mail: info@energy.dtu.dk

---

Release date: November 23. 2016
ISBN: 978-87-92986-58-0

*A man of genius makes no mistakes.*
*His errors are volitional and are the portals of discovery.*

- James Joyce, Ulysses

# Preface

This thesis is submitted in candidacy for a Ph.D. degree from the Technical University of Denmark (DTU). The work has been conducted between September 2013 and November 2016 at the Section of Atomic Scale Modelling and Materials at the Department of Energy Conversion and Storage supervised by Tejs Vegge and Heine Anton Hansen. Minor parts of the research has been conducted during research stays at the SUNCAT Center for Interface Science and Catalysis at SLAC National Accelerator Laboratory and Stanford University, and at the Catalyst Design Lab at Brown University.

Parts of Chapter 3 resemble parts of my Master's Thesis *"Investigation of systematic errors in density functional theory calculations for lithium-air battery reactions"*. The here presented work including all analysis and non-reference data is original to this work and its included publications and based on a study separate from that previously performed albeit with similarities in methodology.

Rune Christensen
November 2016

# Acknowledgements

I am thankful to a number of people who have helped me in various ways in the making of this thesis.

First and foremost, I thank my supervisors. I am very grateful to Tejs Vegge for the many years of guidance, his trust in my abilities, and his continued excitement for my work. I appreciate Heine Anton Hansen's calm nature and always thoughtful advice.

I am very thankful for being part of both the academic and social environment provided by the entire Atomic Scale Modelling and Materials section and in particular by my past and current office mates Morten Gjerding, Arghya Bhowmik and Mateusz Reda. I have also enjoyed collaborating with Niels Bendtsen Halck, Simon Loftager, Steen Lysgaard, Marko Melander, Juan Maria García-Lastra, Vladimir Tripkovic, Nicolai Rask Mathiesen, Jin Hyun Chang, Jakob Howalt, Jon Steinar Myrdal, Peter Hindsgaul Bjerre Jensen, Paul Jennings, Yedilfana Setarge Mekonnen, and others.

It was a pleasure to meet and work with the people at the SUNCAT Center at Stanford and SLAC including Jens Strabo Hummelshøj, Alan Luntz, Felix Studt, Thomas Bligaard, Keld Lundgaard, Chuan Shi, Jong Suk Yoo, Colin Dickens, and Jens Nørskov.

I have felt very welcome during my stays at Catalyst Design Lab at Brown University and enjoyed working with Alireza Khorshidi and Andrew Peterson.

I appreciate the always friendly and helpful administrative staff including the staff at the Niflheim supercomputer cluster. In particular I thank Lene Danielsen, Annette Bruckloher, and Karina Frederiksen.

Last, but not least, I thank my family and friends. Especially my lovely and very patient girlfriend Amanda and my not so patient but most wonderful son Tue.

This work has been supported by:

- **The Danish Agency for Science, Technology and Innovation**
  Catalysis for Sustainable Energy (CASE)

- **Danish Council for Strategic Research**
  **Programme Commission on Sustainable Energy and Environment**
  **The Danish Innovation Foundation**
  ReLiable project (project no. 11-116792/0603-00462B)

- **The European Union's Seventh Framework Programme (FP7/2007-2013)**
  Grant agreement no. 608575

- **VILLUM FONDEN**
  Research grant 9455; V-SUSTAIN

# Abstract

Transportation based on sustainable energy requires an energy carrier, which is able to store the predominately electrical energy generated from sustainable sources in a high energy density form. Metal-air batteries, hydrogen and synthetic fuels are possible future energy carriers. Density functional theory calculations contribute in research and development of these technologies.

Systematic errors are present in calculations with general gradient approximation functionals for all three technologies. Such functionals will in many cases be the best compromise of computational cost and accuracy if not for the systematic errors. In this thesis it is shown how the systematic errors can be mitigated.

For different alkali and alkaline earth metal oxides, systematic errors have previously been observed. These errors are primarily caused by differences in metal element oxidation state. The systematic errors can be significantly reduced by using metal chlorides rather than pure bulk metals as point of reference for metal oxide energies.

Systematic errors in gas phase $CO_2$ reduction reactions have previously been attributed a molecular O-C-O backbone structure. They are through error correlations found to be caused by individual C=O bonds. Energy corrections applied to C=O bonds significantly reduce systematic errors and can be extended to adsorbates.

A similar study is performed for intermediates in the oxygen evolution and oxygen reduction reactions. An identified systematic error on peroxide bonds is found to also be present in the OOH* adsorbate. However, the systematic error will almost be canceled by inclusion of van der Waals energy. The energy difference between key adsorbates is thus similar to that previously found.

Finally, a method is developed for error estimation in computationally inexpensive neural networks. The method can validate the use of a neural network for emulation of density functional theory calculations for given atomic configuration.

# Resume

Transport baseret på vedvarende energi kræver en energibærer, som kan lagre den primært elektriske energi, der genereres af vedvarende kilder, med høj energitæthed. Metal-luft batterier, hydrogen og syntetiske brændsler er mulige fremtidige energibærere. Beregninger baseret på tæthedsfunktionaleteori bidrager i forskning og udvikling af disse teknologier.

Systematiske fejl er til stede i beregninger med general–gradient–approksimation funktionaler for alle tre teknologier. Sådanne funktionaler vil i mange tilfælde være det bedste kompromis af beregningsmæssig omkostning og nøjagtighed, såfremt der ikke var systematiske fejl. I denne afhandling vises, hvordan de systematiske fejl kan identificeres og korrigeres.

For forskellige alkali- og jordalkalioxider er der tidligere blevet observeret systematiske fejl. Disse fejl er primært forårsaget af forskelle i oxidationstrin af metal elementerne. De systematiske fejl kan reduceres betydeligt ved at anvende metalchlorider i stedet for rene metaller som energireference for metaloxider.

Systematiske fejl i gasfase $CO_2$ redoxreaktioner er tidligere blevet tilskrevet en O-C-O rygrad i molekylære strukturer. De er gennem korrelationer i fejl fundet til at være forårsaget af individuelle C=O bindinger. Energikorrektioner anvendt på C=O bindinger reducerer systematiske fejl signifikant og kan overføres til adsorbater.

En lignende undersøgelse er foretaget for produkter af delreaktioner i oxygenudviklings– og reduktionsreaktioner. En identificeret systematisk fejl på peroxidbindinger er også til stede i adsorberet OOH*. Den systematiske fejl vil næsten blive udlignet af inklusion af van der Waals energi. Energiforskellen mellem de vigtigste adsorbater er derfor sammenlignelig med den tidligere fundne forskel.

Endelig er en metode til fejlestimering af beregningsmæssigt billige neurale netværk blevet udviklet. Metoden kan anvendes til at validere brug af neurale netværk til emulering af tæthedsfunktionaleteoriberegninger for en given atomar konfiguration.

# List of Papers

**Paper I**

Reducing Systematic Errors in Oxide Species with Density Functional Theory Calculations
Rune Christensen, Jens S. Hummelshøj, Heine A. Hansen, and Tejs Vegge
*J. Phys. Chem. C*, **2015**, 119 (31), pp 17596–17601

**Paper II**

Thermodynamic and Kinetic Limitations for Peroxide and Superoxide Formation in Na–$O_2$ Batteries
Yedilfana S. Mekonnen, Rune Christensen, Juan M. Garcia-Lastra, and Tejs Vegge
*In preparation*

**Paper III**

Identifying systematic DFT errors in catalytic reactions
Rune Christensen, Heine A. Hansen, and Tejs Vegge
*Catal. Sci. Technol.*, **2015**, 5, pp 4946–4949

**Paper IV**

Theoretical Insight into the Trends that Guide the Electrochemical Reduction of Carbon Dioxide to Formic Acid
Jong Suk Yoo, Rune Christensen, Tejs Vegge, Jens K. Nørskov, and Felix Studt
*ChemSusChem*, **2016**, 9 (4), pp 358–363

**Paper V**

Functional Independent Scaling Relation for ORR/OER Catalysts
Rune Christensen, Heine A. Hansen, Colin F. Dickens, Jens K. Nørskov, and Tejs Vegge
*J. Phys. Chem. C*, **2016**, 120 (43), pp 24910–24916

**Extract of Paper VI**

The Atomic Simulation Environment — A Python library for working with atoms
Ask Hjorth Larsen, Jens Jørgen Mortensen, Jakob Blomqvist, Ivano E. Castelli, Rune Christensen, Marcin Dułak, Jesper Friis, Michael N. Groves, Bjørk Hammer, Cory Hargus, Eric D. Hermes, Paul C. Jennings, Peter Bjerre Jensen, James Kermode, John R. Kitchin, Esben Leonhard Kolsbjerg, Joseph Kubal, Steen Lysgaard, Jón Bergmann Maronsson, Tristan Maxson, Thomas Olsen, Lars Pastewka, Andrew Peterson, Carsten Rostgaard, Jakob Schiøtz, Ole Schütt, Mikkel Strange, Kristian Thygesen, Tejs Vegge, Lasse Vilhelmsen, Michael Walter, Zhenhua Zeng, and Karsten Wedel Jacobsen
*Submitted*

# Contents

# List of Figures

# List of Tables

CHAPTER 1

# Introduction

## 1.1 Energy Supply from Fossil Fuels

Prior to the industrialization in the mid-19th century the demand for energy was met by burning biofuels.[1] Since the industrialization the demand for energy has continued to increase. The increase in demand has mainly been met by consumption of fossil fuels, i.e. coal, oil and natural gas. Considering only the 41 year time span from 1973 to 2014 the world's primary energy supply has more than doubled from an annual average supply of 8.1 TW to 18.2 TW.[2,3] Since early use of coal in Britain in the 13th century as replacement for firewood, fossil fuels have been used to fulfill the energy demand of continuous economic and technological development.[4] Even though the supply from non-fossil energy sources has increased considerably between 1973 and 2014, fossil fuels have nearly retained their share of the total energy supply changing from 87 % to 81 %.[2] Fossil fuels have become and are expected to remain for at least several decades completely dominant in the world energy supply, as fossil fuels are currently the only cost effective energy sources able to scale with increasing demand across all energy consuming sectors.[4]

### 1.1.1 Global Warming

Despite of their advantages, the drawbacks of fossil fuels will force humanity to find replacements. If use continues, fossil fuel reserves will at some point be depleted. In 2007, Shafiee and Topal[5] calculated depletion times to be 35, 37 and 107 years for oil, gas and coal, respectively, assuming a "business as usual" scenario. However, some of the fossil fuel resources, which are currently considered economically unfeasible, could become part of the accessible reserve

through technological development or increasing fuel prices. An example of this is shale gas extraction in USA.[6] In addition, there are still undiscovered fossil fuel resources, e.g. potential resources in the Arctic. The complexity and uncertainty in fossil fuel depletion predictions is exemplified by the relatively large discrepancy in predictions of oil reserves and production.[7]

Another drawback is related to security of supply. Fossil fuel reserves are geographically concentrated. Nations without fossil fuel reserves have to rely on imports. The political and economical implications of such reliance has the potential to cause significant disruption to societies relying heavily on either importing or exporting fossil fuels.[8]

The most urgent negative consequence of fossil fuel consumption is the emission of anthropogenic $CO_2$ into the atmosphere. Upon extraction and combustion of fossil fuels, carbon stored in geological deposits are reintroduced into the global carbon cycle as $CO_2$ at a highly accelerated rate compared to prehistoric times. This has caused the $CO_2$ concentration in the atmosphere to increase. It was 278 ppm in 1750, 317 ppm in 1960, and 401 ppm in 2015.[9] The current concentration is significantly higher than any concentration obtained from ice core data for the previous 800.000 years, and the average rate of increase over the last century is "with very high confidence, unprecedented in the last 22,000 years".[9] $CO_2$ is a green house gas able to absorb infrared radiation emitted from earth and reemit the energy back towards earth. Changes in green house gas concentrations will impact the radiative balance between incoming solar radiation and outgoing infrared radiation from earth. As an increasing share of infrared radiation will not escape earth the global temperature will increase until the infrared radiation is again able to balance the incoming solar energy.

The average global temperature in 2015 was 0.87 °C above the average for the period 1951-1980.[10,11] This is a very significant increase for such a short time period. In 2013, where the temperature was 0.65 °C above the average for 1951-1980,[10,11] Marcott et al.[12] found that although the temperature had yet to exceed prehistoric temperatures in the current interglacial period dating back 11.300 years, a general long term trend of cooling has been abruptly reversed. All plausible green house gas emission scenarios predict significantly higher global temperatures in 2100 than previously in the current interglacial period.[12] It is difficult to predict how the global average temperature increase will influence the climate regionally, but it is highly likely to cause general climate changes and increase the frequency of extreme weather conditions such as heat waves, drought, heavy precipitation and flooding.[9,13]

## 1.2 Limiting Emissions

It is not an easy task to reduce global $CO_2$ emissions to mitigate global warming. To better comprehend the magnitude of the challenge, global $CO_2$ emissions can be written as a product of different factors as done in the Kaya identity.[14,15]

$$F_{CO_2} = P \times \frac{G}{P} \times \frac{E}{G} \times \frac{F_{CO_2}}{E}. \tag{1.1}$$

$F_{CO_2}$ is the global $CO_2$ emission from combustion of fossil fuels, $P$ is the world population, $G$ is the global gross domestic product (GDP), and $E$ is the global energy consumption.

The world population, $P$, is expected to increase from the current 7.5 billion to nearly 10 billion by 2050.[16] Further, the average GDP per capita, $G/P$, is expected to continue increasing.[15] Many societies in developed countries are build on an ambition of consistent economic growth. At the same time, a large majority of the world's population is currently living in countries with below average GDP per capita. They will strive to improve their economic situation. The GDP and energy consumption of a country are positively correlated as can be seen in Figure 1.1. The fraction $E/G$ is known as the energy intensity. It does depend on the type of economy as some industries are more energy intensive than others, and it can be lowered. However, the overall trend is that economic growth in developing countries will require and/or produce an increase in energy consumption.

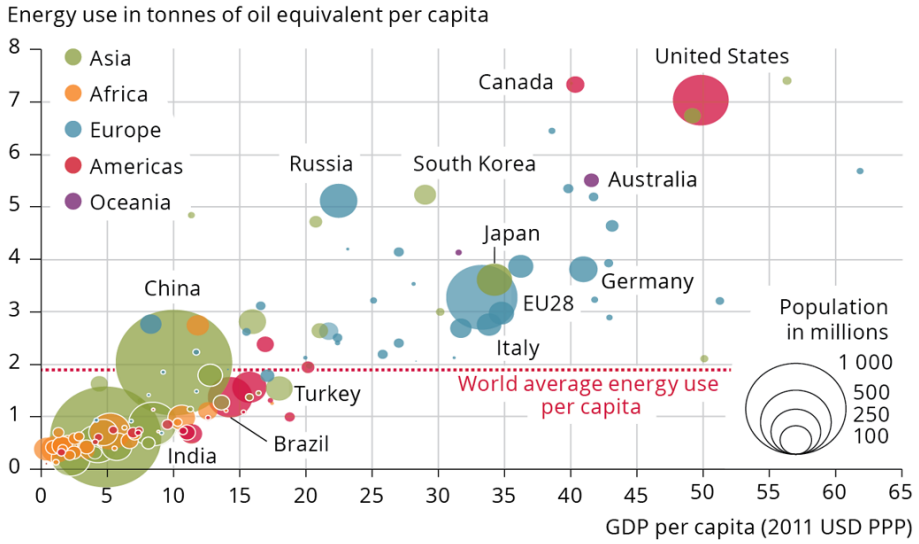


Figure 1.1: GDP, energy use and population of nations. All values are for 2011.[17]

The last factor in the Kaya identity, $F_{CO_2}/E$, is commonly referred to as the carbon intensity. It is the average amount of $CO_2$ released per unit of energy

consumed. To offset population and economic growth a significant lowering of the global carbon intensity is required.[15] This can be done by increasing the share of energy supplied from non-fossil sources such as nuclear fission, hydro, biomass, photovoltaics, concentrated solar, geothermal, and wind power. In 2014 non-fossil sources accounted for 18.9 % of the total energy supply.[2] The largest contributions were from biomass (10.3 %), nuclear (4.8 %), and hydro (2.4 %) with the remaining 1.4 % coming from the other less mature sources. The cost of energy production from these other sources is decreasing[18,19] and in 2015 a record 153 GW increase in global electricity capacity from renewable sources took place accounting for 55 % of total growth in electricity capacity.[19]

### 1.2.1 The Transport Sector Challenge

Even though options to reduced dependency on fossil fuels are available on a total energy supply level and in particular in electricity generation, utilizing these energy sources in the transportation sector is an additional challenge. Currently, 92.5 % of energy consumption in the transport sector is based on oil with an additional 3.7 % from natural gas.[2] In oil derived transportation fuels, such as gasoline and diesel, the energy is stored as chemical energy in liquid phase. These transportation fuels have large gravimetric and volumetric energy densities, are easy to handle, simple to convert into propulsion using a combustion engine, and relatively cheap.

For most sustainable energy sources the raw energy input, e.g. solar radiation, kinetic wind energy, or potential energy of water in a reservoir, has to be converted to electricity at some stationary facility such as a wind turbine of hydro power plant before it can be utilized. With the exception of few cases where transportation can be powered directly by the electrical grid, e.g. railroads, electrical energy must be converted and stored in an energy carrier to be useful in our current transportation infrastructure and in particular for use in personal vehicles.[20]

The exception is biomass, where plant photosynthesis has already performed the conversion from solar radiation to chemical energy. Biomass can be converted into biofuels such as bioethanol, which can be used in a similar manner as the oil derived liquid fuels. However, the transportation sector account for 27.9 % of the total energy consumption.[2] Supplying energy for the transport sector solely from biomass is problematic as there is a limited amount of arable land on earth for both food and energy crops.[20–22] Further, plants are not particularly efficient at converting solar energy to chemical energy. An energy carrier based on electrical energy as input is thus a key element in moving towards a fossil

fuel free transportation sector.[20] This will also allow better usage of the electricity generated from intermittent sources such as wind and solar power at times where supply exceeds demand.

## 1.3 Sustainable Energy Carriers

This thesis examines three different potential energy carriers for the transportation sector. They can all use electrical energy from sustainable sources as input.

### 1.3.1 Metal-Air Batteries

Metal-air batteries are attractive as both the gravimetric and volumetric energy density of such batteries can surpass state–of–the–art Li-ion batteries by approximately an order of magnitude.[23–25] Both the theoretical and the estimated practical energy density is comparable to that of gasoline used as fuel in an internal combustion engine.[23] The general concept is that a pure metal anode is reacted with oxygen either already present at the cathode of the system (metal-$O_2$ battery) or entering the electrochemical cell from ambient air (metal-air battery) to form an oxide. Some of the most promising chemistries are Li-air, Na-air, Zn-air and Mg-air batteries.[23,25,26]

For a battery to act as major transport sector energy carrier it must be secondary, i.e. electrochemically rechargeable. Further, both discharge and charge should occur at low overpotentials to ensure high cycle energy efficiency. For these reasons, reducing $O_2$ to peroxide $O_2^{2-}$ or superoxide $O_2^{-}$ ions rather than the full reduction to $O^{2-}$ ions can be advantageous and is attempted in Li-air and Na-air batteries. Other requirements include large practical discharge capacity, high power densities for fast discharge and charge rates, stability to obtain sufficient cycle and shelf life, and low to moderate cost.[23–26] All metal-air battery chemistries have in common that fundamental understanding of reaction processes is limited.

### 1.3.2 Synthetic Fuels from Electrocatalytic $CO_2$ Reduction

Replacement of liquid fossil fuels with (liquid) synthetic fuels is very attractive from an infrastructural standpoint. In contrast to most alternatives, it can utilize the already existing infrastructure for distribution and consumption.[27–29] $CO_2$ captured either directly from the atmosphere or from a highly concentrated steam, e.g. exhaust gases, is electrochemically reduced. The electricity required to drive the energetically uphill reduction process can be supplied from sustainable sources.

$CO_2$ can be reduced to CO, which in combination with electrochemically produced $H_2$ from water-splitting can be converted into long chain liquid fuels in the Fischer-Tropsch process. $CO_2$ can also be further electrocatalytically reduced directly to fuels or other valuable chemicals. The produced synthetic fuels will upon oxidation in an internal combustion engine or fuel cell release the originally captured $CO_2$. Many of the advantages of fossil transportation fuels can be obtained this way with zero net $CO_2$ emission by cycling $CO_2$.

For the method to be viable, electrocatalysts able to catalyze $CO_2$ reduction at a reasonable rate, low overpotentials, and high selectivity towards a specific product are required.[30] This is especially challenging for direct electrocatalytic reduction to fuels or chemicals. Further, the catalyst should be stable under operating conditions and ideally be composed of only abundant non-toxic elements. Atomic scale knowledge of catalytic processes on different heterogeneous catalysts can prove essential in development of commercial $CO_2$ reduction electrocatalysts.

### 1.3.3 Hydrogen

A third alternative is using hydrogen as energy carrier. Electricity from renewable sources can be used to generate $H_2$ by water splitting in electrolyzer cells. The energy stored in $H_2$ molecules can be converted back to electricity on demand electrochemically in a PEM hydrogen fuel cell.[31,32] In contrast to metal-air batteries and synthetic fuels from $CO_2$ reduction, the technology is commercially available. Hydrogen cars are being mass produced and the required infrastructure is under development.[33–35] The gravimetric energy density of pure $H_2$ is roughly three times as large as that of gasoline.[31] However, including the mass of the system required to store the hydrogen, the gravimetric energy density is reduced by more than one order of magnitude.[36–39] Combined with modest volumetric energy densities for both highly pressurized hydrogen gas and liquid hydrogen, it is essential that the energy efficiency is high.

Energy conversion in electrolyzers and fuel cells is not limited by the Carnot efficiency and can in theory be highly efficient.[40,41] To obtain high efficiency and fast reaction rates, the reactions must be catalyzed. The oxygen reduction reaction (ORR) at the fuel cell cathode and the oxygen evolution reaction (OER) at the electrolyzer cell anode are challenging to catalyze efficiently.[40,42,43] With commercial Pt catalysts the majority of the total overpotential in fuel cell operation is found to be caused by the ORR overpotential.[42] For hydrogen fuel cells to be dominant in the transportation sector, catalysts either composed of abundant elements or with higher mass activity than the current Pt catalyst and preferably with reduced overpotentials need to be developed.[40,44,45]

## 1.4 Motivation

Numerous experimental and theoretical methods can be applied to obtain the fundamental understanding required for efficient development of energy carrier systems. One such theoretical method is Density Functional Theory (DFT), an electronic structure method capable of providing fundamental knowledge at the atomic level. It is described further in Section 2.1. DFT has been found useful in research of many technologies including those mentioned above in Section 1.3, as described in Chapters 3-5. It is in particular useful when applied in combination with experimental methods.[46–52] To obtain optimal synergetic effects from DFT combined with experimental methods, the resource requirement, the accuracy, and the atomic structure transferability in calculations must be considered and balanced carefully.

The atomic structures studied should be sufficiently complex, so that knowledge gained from DFT calculations is transferable to and useful for understanding observed phenomena or hold predictive power. How complex atomic structures need to be varies immensely. In some cases knowledge and insight gained from relatively small idealized model structures will translate well into application, e.g. for establishing catalytic trends. In other cases much larger or more complex atomic structures are required, e.g. for determining the effect of trace amounts of elemental doping in composite materials or effects at interfaces.

DFT calculations can be performed at different levels of accuracy. The level is fundamentally adjusted by use of different exchange-correlation functionals as described in Chapter 2. The used exchange-correlation functional must be chosen such, that the resulting accuracy is sufficient for obtaining the desired understanding or making the desired predictions. For instance, predicting which catalyst is more reactive will generally require lower accuracy than predicting accurate reaction rates or product selectivity.

For DFT calculations to be an integrated part in applied research and rapid development of emerging technologies, calculations should be relatively fast such that experiments and calculations can continuously be compared and the synergetic benefits realized. The computational cost should be kept low compared to available resources for efficient use in applied research.

Increasing the structure complexity and accuracy will in general make calculations more resource demanding. The three factors must be balanced to the point where the system complexity, accuracy, and computational cost are all at a sufficient level for addressing a given research question. This balance is illustrated in Figure 1.2. The situation where all three considerations are met is marked as

the "triple sufficiency". The triple sufficiency requirement restricts which research questions can reliably and efficiently be addressed using DFT.

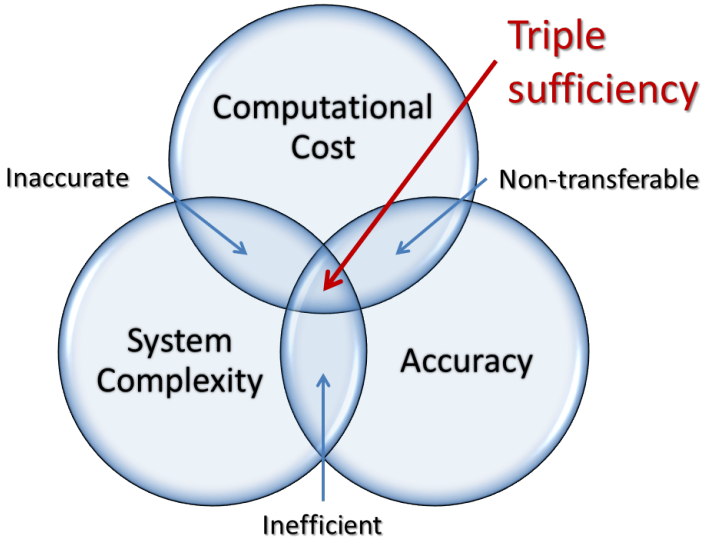


Figure 1.2: System complexity, calculational accuracy, and computational cost must be balanced in DFT calculations to ensure they are all sufficient to answer a given research question.

This thesis describes previously documented and newly discovered systematic errors in DFT when applied in metal-air battery, $CO_2$ reduction, and ORR/OER catalysis research. These errors are all observed with the GGA class of exchange-correlation functionals described in Section 2.2. This class of functionals is the workhorse theoretical surface science.[53] The systematic errors can prevent DFT calculations from being performed at triple sufficiency. The sources of systematic errors are identified through analysis of error correlations in a set of GGA type functionals. Errors are reduced either by applying alternative energy reference systems or transferable empirical corrections. Inspired by this approach a method for estimating the validity of neural networks able to emulate more computationally demanding atomic scale methods such as DFT is developed.

## 1.5 Outline of Thesis

This thesis includes the following chapters:

- Chapter 1 – Introduction
  The global energy supply and the challenge of limiting emissions are discussed with focus on the transport sector. Challenges in research and development of sustainable energy carriers are stated along with requirements for efficient use of DFT in solution of these.

- Chapter 2 – Applied Theory and Method
  The fundamentals of DFT, different exchange-correlation functionals, and the methods generally applied in this thesis are discussed.

- Chapter 3 – Metal-air Batteries
  The systematic errors in calculation of formation enthalpies for alkali and alkaline earth metal oxides are studied. It is shown how using a metal chloride reference instead of pure metal can lead to cancellation of the majority of the systematic error.

- Chapter 4 – $CO_2$ Reduction
  Systematic errors in $CO_2$ reduction reactions are found to be caused by carbon-oxygen double bonds and not an oxygen-carbon-oxygen structure as previously claimed. This improves the correctional approach and allows it to be extended to adsorbates.

- Chapter 5 – Oxygen Evolution and Reduction Reactions
  A systematic error is identified for peroxide bonds and found also to be present in OOH* adsorbates. The systematic error, which could potentially alter the previously determined OOH*/OH* scaling relation, is found to be largely canceled when previously neglected van der Waals interactions are included.

- Chapter 6: Error Ensemble for Neural Networks
  A neural network can upon training be used as a significantly less computationally demanding emulator of DFT calculations. A computationally efficient method for determining validity of neural network calculations is developed and exemplified.

- Chapter 7: Conclusion and Outlook
  Findings are summarized and possible future studies are proposed based on the presented results and applied method.

CHAPTER 2

# Applied Theory and Method

This chapter gives an introduction to density functional theory. It proceeds to present and discuss different exchange–correlation functional approximations with emphasis on those central to this thesis. Finally, the general computational method, the applied thermochemistry approach, an alternative oxygen reference, and an exemplification of ensemble–based error estimation and correlation is presented.

## 2.1 Density Functional Theory

A brief and by no means comprehensive introduction to density functional theory (DFT) is given in this section. It begins with a short introduction to the fundamentals of modern DFT inspired by the textbooks of Kohanoff and Burke.[54,55] This is followed by a discussion of different exchange–correlation functional approximations. The reader is referred to the given references and general literature for further details. Spin has for the sake of simplicity been omitted in the following introduction.

### 2.1.1 Fundamentals for DFT

With the discovery and formulation of quantum mechanics in the early 20th century a theoretical foundation for determining the electronic structure of a material was laid. In principle, the electronic structure of a system can be determined by solving the time–independent Schrödinger equation published in 1926:

$$\hat{H}\Psi_n(\mathbf{R},\mathbf{r}) = E_n\Psi_n(\mathbf{R},\mathbf{r}), \tag{2.1}$$

where $E_n$ are the energy eigenvalues of the eigenstates $\Psi_n(\mathbf{R},\mathbf{r})$. $\Psi_n(\mathbf{R},\mathbf{r})$ are wave functions depending on nuclear coordinates $\mathbf{R}$ and electron coordinates $\mathbf{r}$. The

Hamiltonian for a system consisting of $P$ nuclei and $N$ electrons, each with kinetic energy and interacting through electrostatic forces, can be expressed as:

$$\begin{aligned}\hat{H} = &- \sum_{I=1}^{P} \frac{\hbar^2}{2M_I} \nabla_I^2 - \sum_{i=1}^{N} \frac{\hbar^2}{2m} \nabla_i^2 + \frac{e^2}{2} \sum_{I=1}^{P} \sum_{J \neq I}^{P} \frac{Z_I Z_J}{|\mathbf{R}_I - \mathbf{R}_J|} \\ &+ \frac{e^2}{2} \sum_{i=1}^{N} \sum_{j \neq i}^{N} \frac{1}{|\mathbf{r}_i - \mathbf{r}_j|} - e^2 \sum_{I=1}^{P} \sum_{i=1}^{N} \frac{Z_i}{|\mathbf{R}_I - \mathbf{r}_i|}.\end{aligned} \tag{2.2}$$

$M_I$ are the masses and $Z_I$ the charges of the nuclei. For even a modest number of nuclei and electrons the pairwise interactions will leave the electronic structure problem practically unsolvable as shown below.

### The Born–Oppenheimer approximation

The extent of the problem can be reduced by decoupling the electrons and nuclei using the Born–Oppenheimer approximation.[56] Since the electron mass is much smaller than the mass of the nuclei, the motion of electrons will be significantly faster than that of nuclei. It can be argued[54] that electrons can be treated as instantaneously moving into the ground state for a given set of nuclear positions $\mathbf{R}$. This is commonly referred to as the adiabatic approximation. Secondly, as the nuclear wave functions are localized in space with a narrow width, e.g. of the order of 0.25 Å for a proton, they can be treated as classical particles. These two approximations constitute the Born–Oppenheimer approximation. For a given set of nuclei with coordinates $\mathbf{R}$, the electronic structure can be determined. The Hamiltonian is now reduced to

$$\hat{H} = - \sum_{i=1}^{N} \frac{\hbar^2}{2m} \nabla_i^2 - e^2 \sum_{I=1}^{P} \sum_{i=1}^{N} \frac{Z_i}{|\mathbf{R}_I - \mathbf{r}_i|} + \frac{e^2}{2} \sum_{i=1}^{N} \sum_{j \neq i}^{N} \frac{1}{|\mathbf{r}_i - \mathbf{r}_j|}. \tag{2.3}$$

The interaction between nuclei and electrons can be considered as electrons interacting with an external potential $v_{\text{ext}}$ provided by the nuclei. Once the electronic structure has been determined for a given $\mathbf{R}$, the force acting on each classically treated nuclei can be used to propose a new set of nuclei positions with a lower potential energy.

### The Quantum Many–Body Problem

Although the Born–Oppenheimer approximation does simplify the problem, it continues to be practically unsolvable for all but the most simple cases. The electrons cannot be treated as classical point charges in the same way as the nuclei.

They must be represented by a wave function. Since all electrons interact pair–wise, the total electronic wave function cannot be obtained from the product of wave functions for each individual electron. Each electron has 3 spatial degrees of freedom. This turns the problem into one of $3N$ dimensions. In the case where each individual degree of freedom is sampled on a rather coarse grid of 10 points, a total of $10^{3N}$ grid points are required to represent the wave function. For the relatively simple case of a $F_2$ molecule with 18 electrons, the number of required grid points is thus $10^{54}$. In comparison, the total number of nucleons on earth, which can be estimated from the total mass of earth,[57] is of the order of $10^{51}$.

Various approaches have been developed in the effort to circumvent this mathematical obstacle. As early as 1927 and 1928, Thomas and Fermi independently proposed a method for obtaining the electronic energy through the electron density rather than the total wave function.[54] Considering the electron density rather than the wave function reduces the dimensionality of the problem to 3 degrees of freedom.

### 2.1.2 Modern DFT

The Hohenberg–Kohn theorems published in 1964 provides the formal theoretical basis for obtaining electronic energies through the electronic density.[58] The first theorem states that the external potential and hence energy can be determined univocally from the electronic density of a system. The second theorem states that the ground state energy of a system can be obtained from the electronic density with a universal functional by application of the variational principle. The universal functional remains unknown.

The theorems do not by themselves provide a practical method for obtaining the electronic energy from the density. The Kohn–Sham equations published the following year provided such a scheme.[59] Rather than considering the system of fully interacting electrons, a reference system with non–interacting electrons but identical electron density is used. For such a reference system the Hamiltonian is given by

$$\hat{H}_{\mathrm{R}} = \sum_{i=1}^{N} \left[ -\frac{\hbar^2}{2m} \nabla_i^2 + v_{\mathrm{R}}(\mathbf{r}_i) \right]. \tag{2.4}$$

The kinetic energy is calculated as that of non–interacting electrons. $v_{\mathrm{R}}$ is the reference potential, which makes the electron density for the reference system identical to that of the fully interacting system, such that the ground state energy

will also be identical. This greatly simplifies the eigenvalue problem as no direct electron–electron interaction is present.

$$\hat{H}_{\mathrm{R}}\phi_i(\mathbf{r}) = \varepsilon_i\phi_i(\mathbf{r}). \tag{2.5}$$

The solutions are the energies $\varepsilon_i$ of the single electron Kohn–Sham orbitals $\phi_i(\mathbf{r})$. Given a set of Kohn–Sham orbitals the density $\rho(\mathbf{r})$ can be obtained through

$$\rho(\mathbf{r}) = 2\sum_{i=1}^{N} |\phi_i(\mathbf{r})|^2. \tag{2.6}$$

The total energy of the system is given by

$$E[\rho] = T_{\mathrm{R}}[\rho] + V_{\mathrm{ext}}[\rho] + E_{\mathrm{H}}[\rho] + E_{xc}[\rho]. \tag{2.7}$$

$T_{\mathrm{R}}[\rho]$ is the kinetic energy of the non–interacting particles and obtainable from the Kohn–Sham orbitals $\phi_i(\mathbf{r})$. $V_{\mathrm{ext}}[\rho]$ is energy from interaction with the external potential presented by the nuclei. The electron–electron interaction energy is now separated into the Hartree energy, $E_{\mathrm{H}}[\rho]$, which is simply the classical electrostatic or Coulomb repulsion energy. It is given by

$$E_{\mathrm{H}}[\rho] = \frac{1}{2}\int\int \frac{\rho(\mathbf{r})\rho(\mathbf{r}')}{|\mathbf{r}-\mathbf{r}'|} d\mathbf{r}\, d\mathbf{r}'. \tag{2.8}$$

The last term is the exchange–correlation energy, $E_{xc}[\rho]$. All other electron–electron interactions are included in this term, which is non–trivial. In practice exchange–correlation functionals must be approximated as discussed further in Section 2.2. From the energy expression the potential $v_{\mathrm{R}}(\mathbf{r}_i)$ in equation (2.4) can be determined to be

$$v_{\mathrm{R}}(\mathbf{r}) = v_{\mathrm{ext}}(\mathbf{r}) + \int \frac{\rho(\mathbf{r}')}{|\mathbf{r}-\mathbf{r}'|} d\mathbf{r}' + \frac{\delta E_{xc}[\rho]}{\delta\rho(\mathbf{r})}. \tag{2.9}$$

This new reference potential can be used to calculate new Kohn–Sham orbitals using equations (2.4) and (2.5). The density and ground state energy can thus be obtained by solving the equations iteratively until convergence is achieved.

## 2.2 Exchange–Correlation Functionals

In Kohn–Sham DFT the approximations beyond the Born–Oppenheimer approximation are accumulated in the exchange–correlation functional. From an application standpoint, the optimal exchange–correlation functional should be sufficiently accurate for its intended use while remaining simple enough to limit the

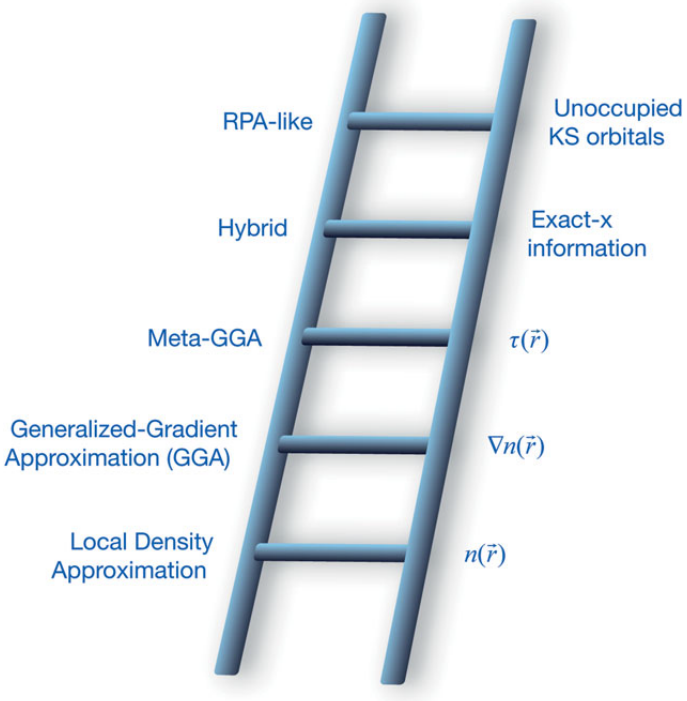


Figure 2.1: Different classes of DFT approximations ordered by increasing levels sophistication going up the ladder. Rungs are named on the left and the added components noted on the right. $n$ is electron density. Reprinted with permission.[61]

amount of required computational resources as discussed in Section 1.4. Functionals can in general be grouped by the components used to evaluate the exchange–correlation energy. This can be visualized with a Jacob's ladder, a biblical analogy, as presented by Perdew and Schmidt and depicted in Figure 2.1.[60,61]

Different classes of functionals and methods correspond to different rungs on the ladder visually lifting the accuracy of DFT approximations from the so–called "Hartree world", where exchange and correlation energies are neglected altogether as in the Hartree approximation,[61] towards chemical accuracy "heaven". In this simplistic ranking of methods more advanced higher rung methods will in general demand more computational resources in return for increased accuracy of calculations. In practice this is not strictly true as functionals often perform well for determining specific properties and worse for other.

In this section the four lower rungs of the ladder, the localized density approximation (LDA), the generalized–gradient approximation (GGA), the meta–GGA, and the hybrid exchange–correlation functionals, will be briefly discussed. Emphasis is on GGA functionals, as calculations presented in the following chapters have predominantly been performed at this level of applied theory.

### 2.2.1 Local Density Approximation (LDA)

In the local density approximation (LDA) the exchange and correlation energies depend solely on the local density $\rho(\mathbf{r})$. The total exchange–correlation energy is given by

$$E_{xc}^{\mathrm{LDA}} = \int \rho(\mathbf{r}) \epsilon_{xc}^{\mathrm{LDA}}[\rho] d\mathbf{r}. \tag{2.10}$$

$\epsilon_{xc}^{\mathrm{LDA}}[\rho]$ is the exchange–correlation energy for a homogeneous electron gas (HEG) with electron density $\rho$. It is thus assumed that at any position $\mathbf{r}$ the electron density can be treated as locally homogeneous. The total exchange–correlation energy is determined as the sum of the exchange and the correlation energy,

$$E_{xc}^{\mathrm{LDA}} = E_{x}^{\mathrm{LDA}} + E_{c}^{\mathrm{LDA}}. \tag{2.11}$$

For the HEG the exchange energy as function of the local density is known analytically.

$$\epsilon_{x}^{\mathrm{LDA}}[\rho] = -\frac{3}{4}\left(\frac{3}{\pi}\right)^{1/3} \rho^{1/3}. \tag{2.12}$$

An equally simple analytical expression is not available for the correlation energy $\epsilon_{c}^{\mathrm{LDA}}$. Instead several approximations have been proposed based on, e.g., quantum Monte Carlo simulations.[62] Some advantages of LDA functionals are the relatively modest computational cost and the fairly good description of systems with slowly varying electron densities such as many solids. When large variations in the electron density are present, as is the case for many systems of chemical interest, the LDA approximation can be expected to perform worse. The calculational accuracy for gas–phase and adsorbed chemical species has been found to often be prohibitively low for studying e.g. catalytic reactions.[63–66]

### 2.2.2 Generalized Gradient Approximation (GGA)

The second rung of the ladder is the Generalized Gradient Approximation (GGA), in which not only the local density but also the density gradient is used as input to calculate exchange and correlation energies. With this addition, chemistry and surface science can be studied with in many cases reasonable accuracy while remaining relatively computationally inexpensive.[64,65,67] This has made this class of functionals the workhorse in theoretical heterogeneous catalysis.[53]

An often used strategy for formulating GGA functionals has been to build on LDA. LDA expressions for $\epsilon_x$ and $\epsilon_c$ are modified by addition of a term or

multiplication with a factor commonly referred to as the enhancement factor. These additive terms or enhancement factors will be a function of the density gradient and in most cases also the density itself. In the limit of relatively small gradients compared to the density, the LDA expressions will be re–obtained.

The mathematical expressions of the additive terms or the enhancement factors are often lengthy and will in most part not be reproduced here. Two commonly used GGA functionals, the BLYP functional[68,69] and the PBE functional,[70] are examples of the two main approaches to determining these mathematical expressions. The BLYP exchange enhancement factor contains parameters, which are fitted to reproduce empirical data for molecules. The PBE functional is constructed such that it abides a range of formal properties and limits. For later reference, the exchange energy is given by

$$E_x^{\mathrm{PBE}} = \int \rho(\mathbf{r}) \epsilon_x^{\mathrm{LDA}}[\rho] F_x^{\mathrm{PBE}}(s) \mathrm{d}\mathbf{r}. \tag{2.13}$$

$F_x^{\mathrm{PBE}}(s)$ is the exchange enhancement factor given by

$$F_x^{\mathrm{PBE}}(s) = 1 + \kappa - \frac{\kappa}{1 + \mu s^2/\kappa}. \tag{2.14}$$

$\mu$ and $\kappa$ are constants. $s$ is the unitless reduced density gradient given by

$$s = \frac{|\nabla \rho|}{2(3\pi)^{1/3} \rho^{4/3}}. \tag{2.15}$$

$s$ thus depends on both the density and the density gradient and will tend to zero both when the gradient does and when the density itself is significantly larger than the gradient. The PBE functional has been modified multiple times to perform better in the description of a specifically desired property. One such case is the functional known as revPBE,[71] where the value of $\kappa$ is changed to improve atomization energies of molecules at the cost of less strict convergence to the large gradient limit known as the Lieb–Oxford bound. This revision was also found to perform well for determining chemisorption energies.[72] This led to formulation of the RPBE functional with a different mathematical expression but numerically similar enhancement factor for low to moderate values of $s$ as the revPBE functional. For large $s$ the enhancement factor converges to the local Lieb–Oxford bound.[72]

#### Non–Local van der Waals Correlation

The LDA and GGA approximations are in nature local and semi–local. They are unable to describe long–range non–local van der Waals (vdW) interactions.

The method primarily used in this thesis is that of Dion et al.[73] in various forms. It has the advantage over post–processing methods for including vdW interactions, that it can be applied in the Kohn–Sham scheme to obtain a self–consistent solution including non–local vdW interactions. It further has the advantage that it makes no prior assumptions about the interacting atomic structures, e.g., surfaces and molecules. It can thus be viewed as a "general purpose method" for including vdW interactions.[74] The vdW–DF,[73] vdW–DF2,[75] and BEEF–vdW[64] functionals are applied frequently in this thesis. In general, the vdW functionals can be expressed as

$$E_{xc}^{\mathrm{vdW}}[\rho] = E_{xc}^{0}[\rho] + E_{c}^{nl}[\rho]. \tag{2.16}$$

$E_c^{nl}[\rho]$ is the non–local vdW correlation energy, and $E_{xc}^{0}[\rho]$ is the exchange and local correlation energy. For both the vdW–DF and vdW–DF2 functionals the local correlation is given by the LDA expression and the exchange by a GGA. Determining the non–local vdW correlation energy can be rather cumbersome. However, once a general kernel describing the interaction between densities $\rho_1(\mathbf{r})$ and $\rho_2(\mathbf{r'})$ separated by distance $|\mathbf{r} - \mathbf{r'}|$ is determined, calculations can be performed at a total computational cost often similar to that of a standard GGA functional. In vdW–DF the used GGA exchange is that of revPBE. In vdW–DF2 it is a revised version of the PW86 functional[76] known as PW86R or rPW86.[77] The vdW–DF and vdW–DF2 functionals also differ slightly in $E_c^{nl}[\rho]$ as a different numerical value of the so–called "exchange gradient coefficient" is used. This improves the description of vdW interactions for molecules in vdW–DF2 in comparison to vdW–DF.

**BEEF–vdW Functional**

The BEEF–vdW functional is another GGA functional with added vdW interaction.[64] Since it, and in particular its ensemble property, is essential for methods presented in this work, it is described in more detail than the other functionals.

The BEEF–vdW functional has an energy expression following the general form in equation (2.16).

$$E_{xc} = \sum_{m=0}^{M-1} a_m E_m^{\mathrm{GGA-x}} + \alpha_c E^{\mathrm{LDA-c}} + (1-\alpha_c) E^{\mathrm{PBE-c}} + E^{\mathrm{nl-c}}. \tag{2.17}$$

The non–local correlation $E^{\mathrm{nl-c}}$ is identical to that of the vdW–DF2 functional. The total correlation is a linear combination of LDA and PBE correlation. The parameter $\alpha_c$ determines the ratio of LDA and PBE correlation in such a manner

that the sum of the correlation prefactors is always 1. The exchange is unlike that of prior functionals. The basic concept is as in BLYP to fit parameters to reproduce desired reference data. For each term in the exchange energy sum, $E_m^{\mathrm{GGA-x}}$, the energy is calculated as in (2.13) with an enhancement factor given by

$$F_m^{\mathrm{GGA-x}}(s) = P_m[t(s)], \tag{2.18}$$

where $P_m[t(s)]$ is the Legendre polynomial of order $m$ in a so–called transformed reduced density gradient $t$ given by

$$t(s) = \frac{2s^2}{4+s^2} - 1, \quad -1 \leq t \leq 1. \tag{2.19}$$

The total enhancement factor is thus given by

$$F^{\mathrm{GGA-x}}(s) = \sum_{m=0}^{M-1} a_m P_m[t(s)], \tag{2.20}$$

The total enhancement factor can thus be viewed as an expansion of Legendre polynomials. 30 Legendre polynomials have been used, i.e., $M = 30$. Expansion coefficients are fitted to obtain the total enhancement factor which best reproduces reference data. Representing the enhancement factor as an expansion of 30 Legendre polynomials does result in a very long mathematical expression. It does, however, allow the individual terms $E_m^{\mathrm{GGA-x}}$ to be calculated independently using (2.18),

$$E_x^{\mathrm{BEEF-vdW}} = \sum_{m=0}^{29} a_m E_m^{\mathrm{GGA-x}} = \sum_{m=0}^{29} a_m \int \rho(\mathbf{r}) \epsilon_x^{\mathrm{LDA}}[\rho] P_m[t(s)] d\mathbf{r}. \tag{2.21}$$

For small changes to these fitted expansion coefficients, such that the density and thus individual $E_m^{\mathrm{GGA-x}}$ can be assumed constant, the resulting change in the total energy can be calculated at very low computational cost.

In the making of the BEEF–vdW functional, an objective has been to formulate a functional which performs well for a range of important properties in surface science and catalysis. The reference data includes gas–phase molecular formation and reaction energies, gas–phase molecular reaction barriers, non–covalent interactions, solid–state cohesive energies and lattice constants, and chemisorption energies.

The fitting procedure is somewhat complicated and ensures the following: (1) The parameters are not overfitted. (2) The obtained exchange enhancement factor will be relatively smooth as function of $s$. (3) The exchange enhancement factor will not be very qualitatively different from that of PBE. The ideal parameters

of $a_m$ and $\alpha_c$ differ for each type of reference data. A compromise weighing the importance of each set of reference data was made to determine the global optimal values for $a_m$ and $\alpha_c$ used in the BEEF–vdW functional. The optimal local correlation is 0.6 LDA correlation and 0.4 PBE correlation. The exchange enhancement factor is depicted in Figure 2.2. It is seen to be similar to the RPBE enhancement factor but slightly larger in the, for application purposes, relevant region $s < 2.5$.[71] In addition to the main BEEF–vdW functional an ensemble of

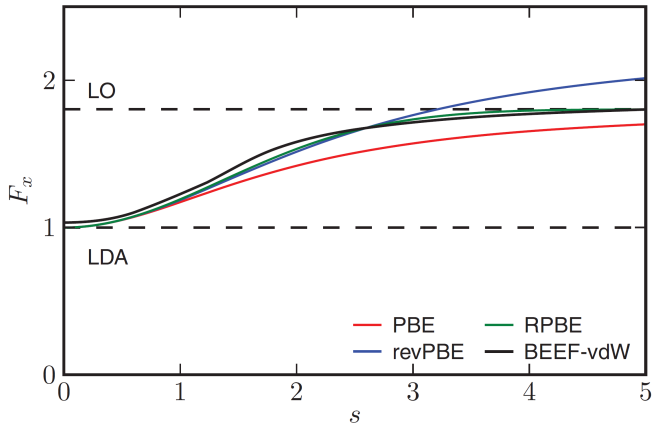


Figure 2.2: The exchange enhancement factor for different GGA functionals. Reprinted with permission.[64]

functionals are also formed in a process "inspired by Bayesian statistics".[64] The ensemble is constructed in such a way that the uncertainty of the calculation can be quantified. When calculating an energy for one of the properties the functional has been fitted to, it can be done not only with the main BEEF–vdW functional but also a large number of ensemble functionals. The standard deviation in calculated energies acts as a quantitative error estimate. The method can be viewed as a formalized way of calculating an energy of interest with a "mindfully selected range of functionals" as proposed by Sabbe, Reyniers and Reuter.[49] The method will in most cases produce an uncertainty estimate, which is equal to or larger than the calculational error.[64,65]

Besides being useful for quantitative error estimation, the BEEF ensemble is in this thesis also used as a computationally highly efficient method of obtaining e.g. reaction enthalpies with several thousand GGA+vdW level functionals. Although some randomness goes into the creation of the ensemble, functionals are accepted into the ensemble with a probability based on how well they reproduce the reference data. The ensemble will thus mostly consist of functionals, which perform reasonably well in calculation of the used reference data. The ensemble

functionals differ only from the main BEEF–vdW functional in the expansion coefficients $a_m$ and the correlation balancing parameter $\alpha_c$. The individual energy contributions $E_m^{\mathrm{GGA-x}}$ for $m$=0,1,..,29, $E^{\mathrm{LDA-c}}$, $E^{\mathrm{PBE-c}}$, and $E^{\mathrm{nl-c}}$ can be evaluated based on the density obtained from a calculation where the Kohn–Sham equations have been solved self–consistently using the BEEF–vdW functional. Single-point energy calculations based on this density can then be obtained for ensemble functionals by simply multiplying the energy terms with the prefactors in Equation (2.17) determine for a given ensemble functional before summation. The BEEF–vdW functional form thus eliminates the need to calculate energies from the density independently for each ensemble functional. Such calculations would be significantly more resource demanding considering that more than a thousand ensemble functionals can be required for convergence of the standard deviation. BEEF ensembles consist of 2000 functionals in the calculations presented in this thesis.

**Hubbard U Correlation**

Another approach to optimize LDA and GGA class functionals at modest additional computational cost is the addition of Hubbard U correlation.[78,79] With such addition the functional is referred to as the old functional abbreviation +U, e.g. PBE+U. It punishes fractional orbital occupation and can mitigate some of the negative effects of electrons interacting with their own electron density, the so–called self–interaction error. Self–interaction is in particular problematic for highly localized electrons. The Hubbard U correlation is only applied to selected orbitals. In most cases the U correlation is applied to atomic orbitals and the method used to improve description of localized $f$– and $d$–electrons. It can also be applied to, e.g., Wannier orbitals.[80] In this thesis it is applied to oxygen $p$–orbitals. The strength of the added correlation is decided by the value of the parameter U. A theoretically sound value of U can be calculated,[80] but is in practice often determined by tuning the parameter until some desired empirical result is reproduced, e.g., a specific band gap.

### 2.2.3 Meta–GGA

The functionals on the third rung of the ladder are the meta–GGA functionals. In meta–GGA's the kinetic energy density $\tau$ is considered in addition to the density and density gradient.

$$\tau(\mathbf{r}) = \sum_{i}^{occ.} \frac{1}{2} |\nabla \phi_i(\mathbf{r})|^2. \tag{2.22}$$

$\tau$ is preferred as extension over the perhaps more intuitive Laplacian $\nabla^2\rho$ as it allows fulfillment of more fundamental constraints.[81] Where GGA functionals will often be unable to describe many different properties very well simultaneously and have to be optimized for a specific use, meta–GGA functionals do not seem to suffer as severely from this.[64,82] It is not evident that they are significantly and systematically better than GGA functionals for catalysis and surface science.[49] They will, however, require more computational resources. Meta–GGA functionals have not been used to obtain results presented in this thesis.

### 2.2.4 Hybrid Functionals

The fourth rung on the ladder are hybrid functionals. In these a lower rung exchange–correlation density functional is combined with exact exchange energy calculated as in the Hartree–Fock method. An example is the PBE0 functional,[83] where the exchange–correlation energy is given by

$$E_{xc}^{\mathrm{PBE0}} = \alpha E_x^{\mathrm{HF}} + (1-\alpha)E_x^{\mathrm{PBE}} + E_c^{\mathrm{PBE}}. \tag{2.23}$$

The value of $\alpha$ is 0.25. Including exact exchange can be very computationally demanding. This is especially true for solid–state systems. The HSE functional is similar to the PBE0 functional but is a "screened Coulomb potential" functional meaning that exact exchange is only considered for short–range interactions.[84] Long–range interactions are treated purely with the PBE functional. This decreases the computational cost for condensed matter.[84,85] An improved numerical value of the so–called exchange screening parameter, $\omega$, separating short–range and long–range interactions was determined in 2006 by Krukau et al.[85] This version of the HSE functional referred to as HSE06 with $\alpha = 0.25$ and $\omega = 0.2$ Å$^{-1}$ has been used in this thesis.

## 2.3 General Computational Method

In the making of this thesis, the VASP computational code[86–89] with plane–wave basis sets has been used as the main electronic–structure code. In general, relatively large plane–wave cut–off energies and projector–augmented wave (PAW) potentials with higher accuracy than those recommended[90] and typically found in literature have been applied as specified in the individual Chapters 3–5. This improves calculational accuracy but increases computational cost. The motivation for this is to reduce errors related to the choice of computational code, basis set, and potentials to better be able to identify and quantify errors intrinsic to the used

exchange–correlation functionals. For consistency, all calculations are performed with the PAW potentials optimized for the PBE functional distributed with the VASP code. This is expected to cause only minor errors when other functionals than PBE are used. The applied fast Fourier transform mesh could have been increased with a similar argument but has been kept at the default setting. The Atomic Simulation Environment (ASE) has been used as interface to the VASP calculator and for initial and post–processing of atomic structures and computed data.[91]

Ionic positions are optimized until the maximum force is at most 0.05 eV/Å and 0.01 eV/Å when vibrational frequencies are subsequently calculated. vibrations are calculated using the harmonic approximation for small ionic displacements. Lattice constants have been determined independently for each applied self–consistent functional for periodic systems. Lattice constants pertaining to each specific functional have thus been used in slab systems. For oxide species, lattice constants and ionic positions have been optimized simultaneously without use of internal VASP optimizers, as they are prone to error for small cell volume changes.[90]

Various slab systems are used throughout this thesis. They have in common, that they are periodic in the two directions parallel to the surface with amble vacuum in the direction perpendicular to the surface. They are initialized with bulk crystal structure and interatomic distances. The lower layers are immobilized during ionic optimization to simulate a large underlying bulk. Molecules are calculated in relatively large cells such that the interatomic distances through periodic boundary conditions are 10 Å or larger. A single $k$–point, the Γ–point, is used in all gas–phase calculations. Dipole corrections are applied for both molecules and slabs to reduce the amount of required vacuum. Energies are converged to within 10 meV with respect to the unit cell size.

### 2.3.1 Thermochemistry

This thesis relies heavily on comparisons between calculated and experimental enthalpies. In calculating these enthalpies, gaseous species have been treated as ideal gas. The enthalpy, $H$, is given by

$$H = E_{\text{elec}} + E_{\text{ZPE}} + \int_0^T C_P \mathrm{d}T, \tag{2.24}$$

where $E_{\text{elec}}$ is the electronic energy, and $E_{\text{ZPE}}$ is the vibrational zero–point energy. In the used approximation the heat capacity under constant pressure, $C_P$, is given

by

$$C_P = k_\mathrm{B} + C_{V,\mathrm{trans}} + C_{V,\mathrm{rot}} + C_{V,\mathrm{vib}}. \tag{2.25}$$

The translational contribution under constant volume,$C_{V,\mathrm{trans}}$ is $3/2\ k_\mathrm{B}$. The rotational contribution, $C_{V,\mathrm{rot}}$, is $k_\mathrm{B}$ and $3/2\ k_\mathrm{B}$ for linear and nonlinear molecules, respectively. They are constants of temperature leaving the integration of $C_{V,\mathrm{vib}}$ as the only nontrivial term.

$$\int_0^T C_{V,\mathrm{vib}} dT = \sum_i^{\text{vib DOF}} \frac{\epsilon_i}{e^{\epsilon_i/k_\mathrm{B}T} - 1}. \tag{2.26}$$

The sum is over all vibrational degrees of freedom with vibrational energies $\epsilon_i$.

Adsorbates are assumed constrained such that no translational and rotational degrees of freedom are present. All degrees of freedom are treated as vibrational with the harmonic approximation. The expression for $H$ in (2.24) is used with $C_P = C_{V,\mathrm{vib}}$, and the heat capacity integral given as in (2.26).

For the bulk enthalpies in Chapter 3, the heat capacity integral has been neglected, i.e., assumed to be 0, unless otherwise stated.

The enthalpy of a given reaction is calculated simply by subtracting the calculated enthalpy of all reactants from the calculated enthalpy of all products.

### 2.3.2 Alternative Oxygen Reference

To avoid the known significant error in the calculated energy of $O_2$(g),[92] an alternative oxygen reference is applied.[93,94] The reference enthalpy for $O_2$ is inferred from the calculated enthalpies of $H_2O$ and $H_2$. This is done through the water formation reaction.

$$2\ \mathrm{H_2(g)} + \mathrm{O_2(g)} \rightarrow 2\ \mathrm{H_2O(g)}. \tag{2.27}$$

The standard enthalpy of reaction, $\Delta H_r^\circ$, is given by

$$\Delta H_r^\circ = 2\ H^\circ[\mathrm{H_2O}] - H^\circ[\mathrm{O_2}] - 2H^\circ[\mathrm{H_2}]. \tag{2.28}$$

$H^\circ[X]$ is the standard enthalpy of species $X$ calculated as in (2.24). Using the experimental standard enthalpy of formation for gaseous water, $\Delta H^\circ_{f,\,\mathrm{exp}}[\mathrm{H_2O}]$, which is -2.506 eV[95] and per definition half of the enthalpy of the reaction in (2.27), (2.28) can be rewritten

$$H^\circ[\mathrm{O_2}] = 2\left( H^\circ[\mathrm{H_2O}] - H^\circ[\mathrm{H_2}] - \Delta H^\circ_{f,\,\mathrm{exp}}[\mathrm{H_2O}] \right). \tag{2.29}$$

The RHS of (2.29) can thus be used as an alternative to calculating the enthalpy of gaseous $O_2$.

## 2.4 BEEF Ensemble Error Correlation

Error correlations between functionals in the BEEF ensemble are frequently determined in this thesis. The basic principle is exemplified below and in Paper VI. The enthalpy of reaction is calculated for two CO reduction reactions, A and B, which can occur in the Fischer–Tropsch process,

$$\mathrm{CO(g)} + 3\ \mathrm{H_2(g)} \rightarrow \mathrm{CH_4(g)} + \mathrm{H_2O(g)}. \qquad \text{(Reaction A)}$$

$$\mathrm{CO(g)} + \tfrac{5}{2}\ \mathrm{H_2(g)} \rightarrow \tfrac{1}{2}\ \mathrm{C_2H_6(g)} + \mathrm{H_2O(g)}. \qquad \text{(Reaction B)}$$

Written in this form, both reactions involve one reactant CO and one product $H_2O$. An additional reaction given by the net difference, Reaction B - Reaction A, is also considered,

$$\mathrm{CH_4(g)} \rightarrow \tfrac{1}{2}\ \mathrm{C_2H_6(g)} + \tfrac{1}{2}\ \mathrm{H_2(g)}. \qquad \text{(Reaction B-A)}$$

The BEEF–vdW functional is used to calculate the enthalpies of reactions as described in Section 2.3.1. The BEEF ensemble standard deviations, $\sigma_{\mathrm{BEEF}}$, are determined and used as uncertainty estimates. They are reported in Table 2.1.

Table 2.1: Enthalpies of reaction and errors in eV

| | Exp.[a] | BEEF–vdW | Error | $\sigma_{\mathrm{BEEF}}$ |
|---|---|---|---|---|
| Reaction A | -2.14 | -1.86 | -0.28 | $\pm$0.25 |
| Reaction B | -1.80 | -1.53 | -0.27 | $\pm$0.25 |
| Reaction B-A | 0.34 | 0.33 | 0.02 | $\pm$0.02 |

[a] From NIST[95]

The estimated uncertainties are similar to the errors. The error is considerable for Reaction A and Reaction B. Both the predicted uncertainty and the calculated error are more than an order of magnitude smaller for Reaction B-A. To understand why, the enthalpies of Reaction A and Reaction B calculated not only with the self–consistent BEEF–vdW functional but also with five functionals from the BEEF ensemble are shown in Figure 2.3.

Considering only the self–consistent BEEF–vdW calculations and the error bars obtained from $\sigma_{\mathrm{BEEF}}$, it appears that the uncertainty is such, that it cannot be concluded which reaction has the lowest enthalpy of reaction. However, the calculated enthalpies of the two reactions are strongly correlated with any functional within the GGA+vdW class, as is illustrated with the ensemble functionals plotted in Figure 2.3. The relative uncertainty between reactions is thus significantly smaller.

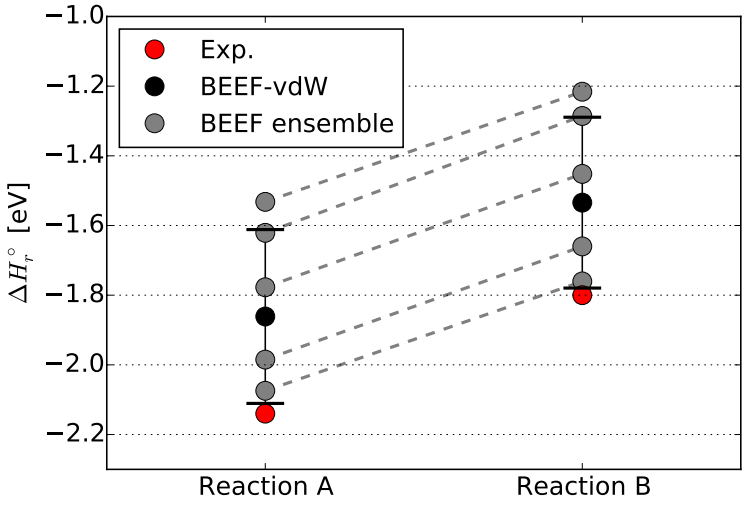


Figure 2.3: The enthalpy of Reaction A and Reaction B calculated with the self–consistent BEEF–vdW functional and five selected BEEF ensemble functionals. Error bars are given by $\sigma_{\text{BEEF}}$.

CO and $H_2O$ are absent in the net reaction difference, Reaction B-A. This absence could indicate that $\sigma_{\text{BEEF}}$ and the errors are mainly caused by CO and/or $H_2O$. Such conclusion can, however, not be drawn from two very similar reactions. After further analysis it appears that $\sigma_{\text{BEEF}}$ is mainly caused CO and $H_2O$. The errors are, however, caused by $H_2$. This is shown in Section 4.6.

CHAPTER 3

# Metal–Air Batteries

## 3.1 Introduction

DFT has been used in metal–air battery research to obtain fundamental understand at the atomic level. Several areas such as reaction processes in growth and dissolution of discharge product,[96–104] electron and ion conduction,[96,101,105–113] electrolyte effects,[114,115] and parasitic reactions[116] have been studied.

## 3.2 Challenge

A major challenge that limits application of DFT for metal–air battery research is documented systematic errors in the description of alkaline and alkaline earth bulk oxide species. The systematic errors are reproduced with several different exchange–correlation functionals.[97,104,117] They can be visualized with plots depicting the calculated versus experimental enthalpies of formation as shown in Figures 3.1 and 3.2.

The calculated enthalpies of formation have been found to differ systematically from experimental values depending on the ionic state of the oxygen.[104,117,118] In Figure 3.2 this is illustrated with three lines of the form,

$$\Delta H_f^{\circ\,\mathrm{calc}} = \Delta H_f^{\circ\,\mathrm{exp}} + b. \tag{3.1}$$

$b$ is a constant fitted independent for each of the three oxygen ion species, i.e. superoxides, $O_2^-$, peroxides, $O_2^{2-}$, and single atom oxygen ions, $O^{2-}$. Metal oxides containing $O^{2-}$ ions are for clarity here referred to as metal monoxides. The presence of an offset in comparison of calculated and experimental enthalpies is not surprising, as the enthalpy of gaseous $O_2$ is notoriously difficult to determine accurately with DFT.[92,117] This is probably at least in part due to the triplet spin

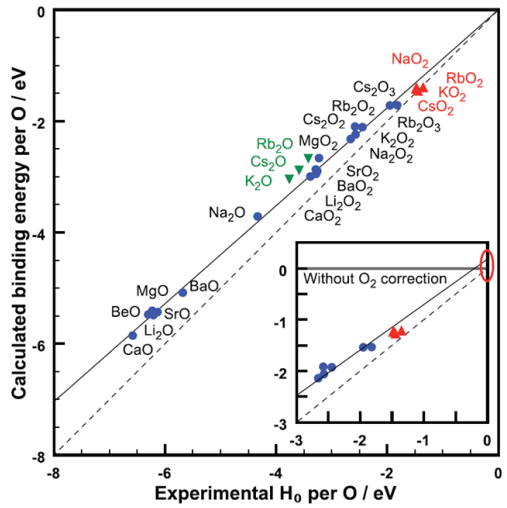


Figure 3.1: Comparison of experimental and calculated enthalpies of formation per oxygen atom. The RPBE functional has been used. Reprinted with permission.[97]

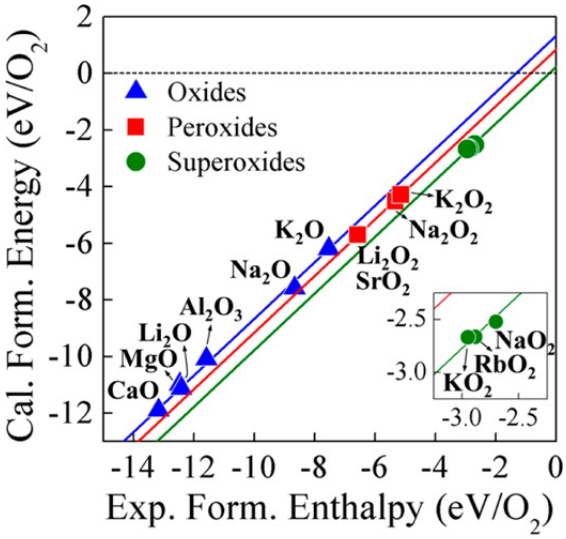


Figure 3.2: Comparison of experimental and calculated enthalpies of formation per $O_2$. The PBE functional has been used. Reprinted with permission.[104]

ground state of $O_2$. However, when the enthalpy of formation is calculated per O or $O_2$, the offset should be constant for all metal oxides if no other systematic errors were present. It has previously been suggested that the error for gaseous $O_2$ is in part also present in description of the superoxide ion, $O_2^-$, and peroxide ion, $O_2^{2-}$. The systematic differences in error are "due to the different degrees in which the O=O double bond is broken".[104] If this is the case, a functional with improved description of the $O_2$ bond should reduce the systematic error.

The systematic errors have previously been mitigated in studies by empirical corrections.[97,104] Alternatively, the systematic errors can be nearly removed by using the higher level Random–Phase Approximation (RPA) method.[118] This method is, however, too computationally demanding for many types of studies. The empirical corrections are non–ideal. They either do not treat the systematic difference in errors for different oxides, or require the oxygen ions in a calculation to be well defined for them to be applied.

In this Chapter and Paper I these systematic errors are studied to find ways to mitigate errors without use of corrections determined from fitting to empirical data. The role of electron localization is also examined.

## 3.3 Method

Enthalpies of formation are calculated with a range of different exchange–correlation functionals and compared to experimental enthalpies in search for a functional approach without the systematic errors. This approach is similar to the one applied previously by Christensen.[117] Several crude approximations in the previous study have not been made in the current study. As an example have lattice constants previously been assumed to be identical for all exchange–correlation functionals.

Table 3.1: Reference data for oxide species.[97]

| Oxide | Space group | $\Delta H_f^\circ$/f.u. [eV] | $\Delta H_f^\circ$/O [eV] |
|---|---|---|---|
| $Li_2O$ | $Fm\bar{3}m$ | -6.208 | -6.208 |
| $Li_2O_2$ | $P6_3/mmc$ | -6.561 | -3.280 |
| $LiO_2$ | $Pnnm$ | -2.995 | -1.498 |
| $Na_2O$ | $Fm\bar{3}m$ | -4.332 | -4.332 |
| $Na_2O_2$ | $P\bar{6}2m$ | -5.317 | -2.658 |
| $NaO_2$ | $Pnnm$ | -2.705 | -1.353 |
| $K_2O$ | $Fm\bar{3}m$ | -3.762 | -3.762 |
| $K_2O_2$ | $Ccme$ | -5.141 | -2.570 |
| $KO_2$ | $I4/mmm$ | -2.949 | -1.474 |
| $Rb_2O$ | $Fm\bar{3}m$ | -3.420 | -3.420 |
| $Rb_2O_2$ | $Immm$ | -4.892 | -2.446 |
| $RbO_2$ | $I4/mmm$ | -2.892 | -1.446 |
| $Rb_2O_3$ | $I\bar{4}3d$ | -5.462 | -1.821 |
| $Cs_2O$ | $R\bar{3}m$ | -3.586 | -3.586 |
| $Cs_2O_2$ | $Immm$ | -5.160 | -2.580 |
| $CsO_2$ | $I4/mmm$ | -2.966 | -1.483 |
| $Cs_2O_3$ | $I\bar{4}3d$ | -5.856 | -1.952 |
| $MgO$ | $Fm\bar{3}m$ | -6.229 | -6.229 |
| $MgO_2$ | $Pa\bar{3}$ | -6.457 | -3.228 |
| $CaO$ | $Fm\bar{3}m$ | -6.581 | -6.581 |
| $CaO_2$ | $I4/mmm$ | -6.768 | -3.384 |
| $SrO$ | $Fm\bar{3}m$ | -6.136 | -6.136 |
| $SrO_2$ | $I4/mmm$ | -6.571 | -3.285 |
| $BaO$ | $Fm\bar{3}m$ | -5.680 | -5.680 |
| $BaO_2$ | $I4/mmm$ | -6.519 | -3.260 |
| $H_2O_2$ | gaseous | -1.411 | -0.705 |

Calculations have been performed for the alkali metal and alkaline earth metal oxides seen in Table 3.1. The oxide species considered by Hummelshøj et al.[97] shown in Figure 3.1 are studied in this work except BeO, which has been omitted. The reference enthalpies of formation and crystal structures are the same as used

by Hummelshøj et al.[97] This is to ensure consistent comparison with previous findings. The used enthalpies of formation are given both per formula unit and per oxygen atom in Table 3.1. The space groups of the oxide structures used in calculations are also specified. Atomic structures can be obtained from various databases.[119–122]

The two sesquioxides, $Rb_2O_3$ and $Cs_2O_3$, differ from the other oxides by containing both peroxide and superoxide ions as shown in Figure 3.3. Other metal oxides will contain only one type of oxygen ion. Sesquioxides are particularly

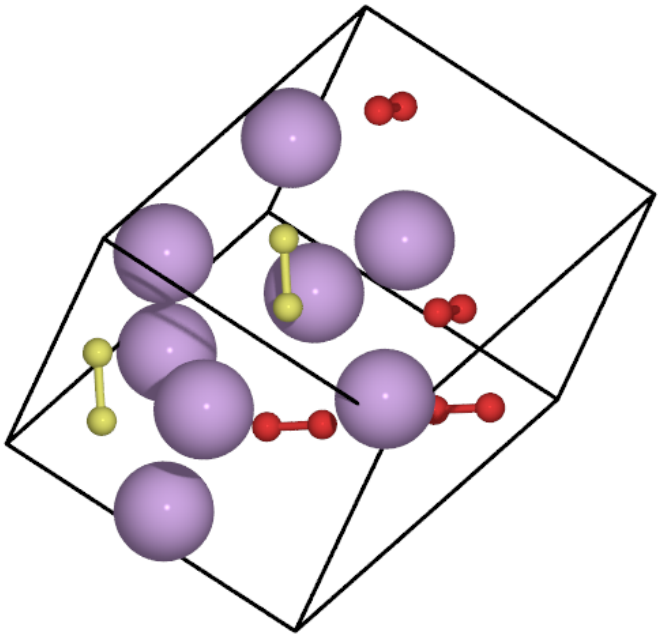

Figure 3.3: $Rb_2O_3$ unit cell containing 8 Rb atoms (purple) and 12 O atoms either as superoxide ions (red) or peroxide ions (yellow).

interesting, as they can be used to examine the ability of exchange–correlation functionals to converged the electron density into correctly localized election states. Further, they could potentially be used to decouple different systematic errors.

In addition to bulk metal oxides, the formation enthalpy of $H_2O_2$(g) has also been included for comparison. The inclusion of $H_2O_2$ introduces another peroxide species. Held against calculations for bulk metal peroxides it can be seen whether the presence of a peroxide bond will result in similar errors.

For a given oxide species $M_xO_y$, where M is the metal ion element, the standard enthalpy of formation is calculated as

$$\Delta H_f^\circ[\mathrm{M_xO_y}] = H^\circ[\mathrm{M_xO_y}] - xH^\circ[\mathrm{M}] - \frac{y}{2}H^\circ[\mathrm{O_2}]. \tag{3.2}$$

The individual enthalpies are calculated as described in Section 2.3.1. $H^{\circ}[\mathrm{M}]$ is the enthalpy of bulk crystalline metal M and $H^{\circ}[\mathrm{O_2}]$ the standard enthalpy of gaseous molecular oxygen. The enthalpies of formation are calculated per oxygen atom in order to reduce possible oxygen reference errors to a constant for all calculations,[97,117]

$$\Delta H_f^{\circ}[\mathrm{M_xO_y}]/\mathrm{O} = \frac{1}{y}H^{\circ}[\mathrm{M_xO_y}] - \frac{x}{y}H^{\circ}[\mathrm{M}] - \frac{1}{2}H^{\circ}[\mathrm{O_2}]. \tag{3.3}$$

Using the alternative oxygen reference described in Section 2.3.2, equation (3.3) can be rewritten as

$$\begin{aligned}\Delta H_f^{\circ}[\mathrm{M_xO_y}] =& \frac{1}{y}H^{\circ}[\mathrm{M_xO_y}] - \frac{x}{y}H^{\circ}[\mathrm{M}] \\ &- \Big( H^{\circ}[\mathrm{H_2O(g)}] - H^{\circ}[\mathrm{H_2(g)}] - \Delta H_{f,\,\mathrm{exp}}^{\circ}[\mathrm{H_2O(g)}] \Big).\end{aligned} \tag{3.4}$$

Using this expression the known error on $\mathrm{O_2(g)}$ is avoided. However, if the error in $\mathrm{O_2(g)}$ or part of it is present in the bulk oxygen ions, using the alternative water reference can prevent possible error cancellation.

The ratio of metal atoms to oxygen in the bulk oxide species depends directly on the type of oxygen ions present in the metal oxide. In equation (3.3) this can be seen by the factor in front of the enthalpy of the used reference metal $H^{\circ}[\mathrm{M}]$. As a result, systematic errors in the oxidation of metal atoms will correlate with the type of oxygen ion. Although the systematic errors appear to depend on the type of oxygen ion, this could be an indirect observation of systematic errors in the oxidation energy of alkali and alkaline earth metals. An alternative metal atom reference similar in principle to that applied for $\mathrm{O_2(g)}$ is introduced to examine this further.

Following the example of the $\mathrm{O_2(g)}$ reference in Section 2.3.2, the formation of alkali and alkaline earth metal chlorides are used as reference reactions.

$$\mathrm{M(s)} + \frac{z}{2}\mathrm{Cl_2(g)} \rightarrow \mathrm{MCl_z(s)}. \tag{3.5}$$

The enthalpy of reaction in (3.5) is identical to the enthalpy of formation for the general metal chloride $MCl_z$ given by

$$\Delta H_f^{\circ}[\mathrm{MCl_z}] = H^{\circ}[\mathrm{MCl_z}] - H^{\circ}[\mathrm{M}] - \frac{z}{2}H^{\circ}[\mathrm{Cl_2}]. \tag{3.6}$$

Using experimental enthalpies of formation $\Delta H_{f,\,\mathrm{exp}}^{\circ}[\mathrm{MCl_z}]$, which are readily available,[95] (3.6) can be rearranged

$$H^{\circ}[\mathrm{M}] = H^{\circ}[\mathrm{MCl_z}] - \frac{z}{2}H^{\circ}[\mathrm{Cl_2}] - \Delta H_{f,\,\mathrm{exp}}^{\circ}[\mathrm{MCl_z}]. \tag{3.7}$$

This expression can be inserted in (3.3) and (3.4).

$$\begin{aligned}\Delta H_f^\circ[\mathrm{M_xO_y}]/\mathrm{O} =& \frac{1}{y}H^\circ[\mathrm{M_xO_y}] \\ &-\frac{x}{y}\left(H^\circ[\mathrm{MCl_z}] - \frac{z}{2}H^\circ[\mathrm{Cl_2}] - \Delta H_{f,\,\mathrm{exp}}^\circ[\mathrm{MCl_z}]\right) \\ &-\frac{1}{2}H^\circ[\mathrm{O_2}]. \end{aligned} \tag{3.8}$$

$$\begin{aligned}\Delta H_f^\circ[\mathrm{M_xO_y}]/\mathrm{O} =& \frac{1}{y}H^\circ[\mathrm{M_xO_y}] \\ &-\frac{x}{y}\left(H^\circ[\mathrm{MCl_z}] - \frac{z}{2}H^\circ[\mathrm{Cl_2}] - \Delta H_{f,\,\mathrm{exp}}^\circ[\mathrm{MCl_z}]\right) \\ &-\left(\ H^\circ[\mathrm{H_2O(g)}] - H^\circ[\mathrm{H_2(g)}] - \ \Delta H_{f,\,\mathrm{exp}}^\circ[\mathrm{H_2O(g)}]\right). \end{aligned} \tag{3.9}$$

This gives in total 4 different combinations of reference systems for the calculation of $\Delta H_f^\circ[\mathrm{M_xO_y}]/\mathrm{O}$: (3.3), (3.4), (3.8), and (3.9). For $H_2O_2$, H takes the role of M. HCl(g) and $\frac{1}{2}H_2$(g) is used as reference states similarly to $MCl_z$ and M, respectively.

### 3.3.1 Functionals and Calculation Details

Calculations have been performed with three GGA functionals (PBE, RPBE, and rPW86), three GGA+vdW functionals (vdW–DF, vdW–DF2, and BEEF–vdW), a GGA functional with Hubbard U correction (PBE+U), and a hybrid functional (HSE06). They are all discussed in Section 2.2. The rPW86 functional is included to examine the difference between rPW86 and vdW–DF2, which have identical exchange and differ only in correlation. Different GGA+vdW functionals are included to determine whether a lack of van der Waals interaction in the standard GGA functionals is the cause of the systematic errors.

The addition of a Hubbard U has been shown to improve calculated enthalpies of formation for oxides.[123] That was, however, for transition metal oxides with U correlation applied to the localized *d*–orbitals. In this work the Hubbard U is applied to the *p*–orbitals of oxygen atoms. Such addition has proven useful for localizing polarons in peroxide and carbonate ions in $Li_2O_2$ and $Li_2CO_3$.[106] Enthalpies have been calculated with different values of U. In the used computational implementation of Hubbard correlation,[124] the parameter controlling the Hubbard correlation strength is $U_{eff}$=U - J. In this implementation negative values of U can in rare cases be optimal as discussed by Nakamura et al.[125] Negative values of U have thus also been considered for completeness. Hubbard correlation is implemented differently for different electronic structure codes. Optimal values of U obtained with one code might thus not be transferable to another code.

The HSE06 hybrid functional is the only non–second–rung functional applied. It is significantly more computationally demanding than the GGA–type functionals, but is also expected to give more accurate enthalpies of formation and be able to localize electrons on the ions. However, previous work did not find the systematic errors to be smaller with the HSE06 functional than with the GGA–type functionals.[117]

For non–metallic elements, O, H, and Cl, hard PAW potentials have been used. Potentials explicitly including semi–core *s*– and *p*–electrons ("sv" potentials) are used for metals with the exception of Mg, for which semi–core *p*–electrons but not semi–core *s*–electrons are included ("pv" potential). A plane wave basis set cut–off energy of 600 eV has been applied. An even number of k–points in each dimension distributed around the Γ–point in a Monkhorst–Pack grid with a spacing less than 0.05 $Å^{-1}$ has been used for the bulk species. As molecular oxygen and superoxide ions have a non–zero spin ground states, all calculations have been spin polarized. Magnetic moments for each atom are examined qualitatively to confirm convergence into the expected ground state spin configuration. Initial magnetic moments have been specified for few structures, e.g., the sesquioxides.

Vibrations have been calculated using the RPBE and PBE functionals. The two functionals yielded similar zero–point energies and integrated heat capacities for gas species. These energies have been used for all functionals to obtain enthalpies from the calculated electronic energies.

## 3.4 Enthalpies of Formation

Enthalpies of formation have been calculated with the different functionals. Plots similar to Figure 3.1 are displayed in Figure 3.4 for the PEB and RPBE functionals. Similar figures for the other applied functionals and for different values of U can be found in Appendix A. For each functional, the enthalpy of formation is plotted using the four different reference energy options. Since enthalpies are plotted per oxygen atom, the only difference between using a direct $O_2$ reference (solid points) or the water reference (hollow points) is a constant offset for all oxides. Comparing enthalpies calculated with a standard metal reference (circles) and with the metal chloride reference (diamonds) a difference in error pattern is observed.

The error pattern is similar to that previously observed[97,104,117] with the RPBE and PBE functionals and the metal reference (circles). Metal superoxides are calculated to be more stable relative to the experimental value, i.e., lower in energy relative to the ideal line $\Delta H_f^{\circ\,\mathrm{calc}} = \Delta H_f^{\circ\,\mathrm{exp}}$, than the metal peroxides, which in

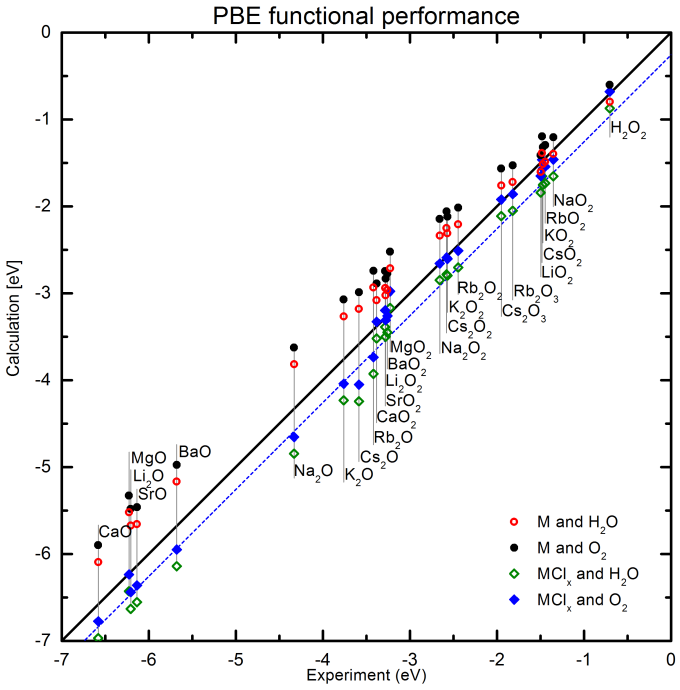


(a) PBE

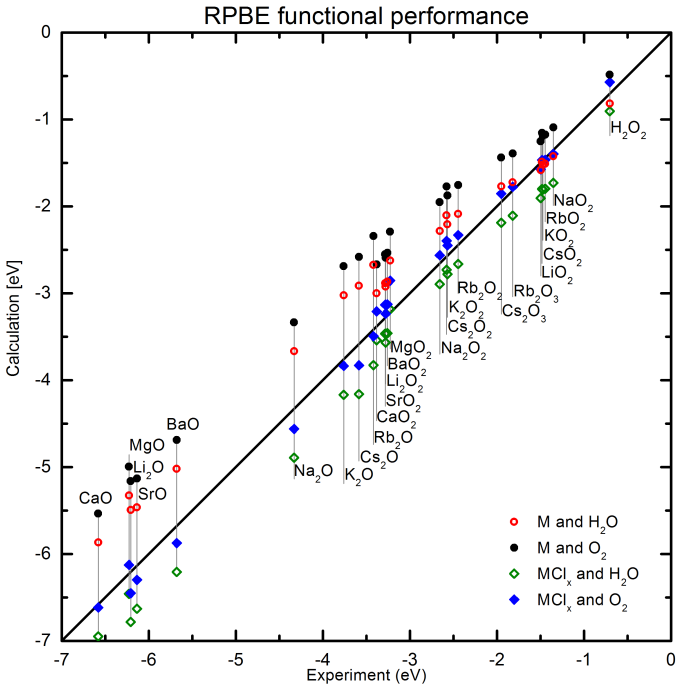


(b) RPBE

Figure 3.4: Calculated enthalpies of formation per oxygen atom, $\Delta H_f^\circ/\mathrm{O}$, for oxide species versus experimental enthalpies. The four different combinations of energy references are shown.

turn are more stable relative to experiment than the metal monoxides. $H_2O_2$ does not display a similar error as the metal peroxides.

Systematic differences in calculated stability compared to experiment, i.e., systematic difference in error, are summarized in Figure 3.5 for different functionals. An empirical correction has been applied to the oxygen reference energy to mini-

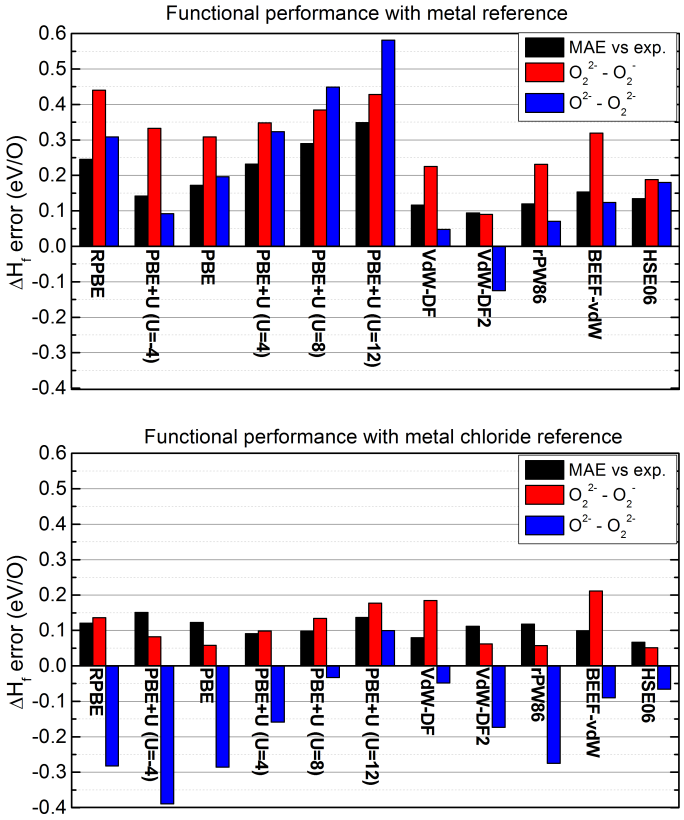


Figure 3.5: Performance of different functionals with fitted oxygen reference. Black bars are the post–fitting mean absolute error. Red bars are the differences in average error for peroxides and superoxide species. Blue bars are the differences in average error for monoxide and peroxides species. **Top:** Bulk metal reference. **Bottom:** Metal chloride reference.

mize the mean absolute error (MAE). The MAE is then a quantitative measure of the scatter around the best possible line given by Equation (3.1) with a single value of $b$ for all oxide species. The values of $b$ for each functional of choice of reference can be found in Appendix A. Similar results are obtained if the root mean square error (RMSE) is used instead of the MAE. With the bulk metal reference, the MAE is highly functional–dependent and is between 0.10 eV and 0.35 eV. Not only is the MAE in most cases significantly reduced with the metal chloride reference, the variation between functionals is also diminished. The MAE is in range 0.07–0.15 eV and reduced from 0.25 eV to 0.12 eV for the RPBE functional.

The red bars in Figure 3.5 are the differences in average error between alkali metal peroxides and superoxides. These average error differences correspond to the offset between the green and the red line in Figure 3.2. It is this systematic error which is particularly troublesome in studies of charge and discharge reactions. The systematic error is of considerable magnitude with the metal reference. The error is 0.44 eV and 0.31 eV for the RPBE and PBE functionals, respectively. Adding U correlation does not improve this, as the U is found to apply similarly to peroxide and superoxide ions. The systematic error is larger than 0.20 eV with all functionals except for vdW–DF2 and HSE06, where it is 0.09 eV and 0.19 eV, respectively. The systematic error is significantly reduced with the metal chloride reference. The error with the BEEF–vdW functional, 0.21 eV, is the only one larger than 0.20 eV. For several functionals, i.e., PBE, vdW–DF2, rPW86 and HSE06, the error is reduced to approximately 0.05 eV. This is within the normally expected accuracy for this type of DFT calculations.

The blue bars in Figure 3.5 are differences in average errors between alkali and alkaline earth metal monoxides and peroxides. These average error differences correspond to the offset between the red and the blue line in Figure 3.2. This systematic error changes significantly for different values of U. This can be understood from the absence of an oxygen–oxygen bond in the monoxides. This systematic error is highly functional–dependent regardless of the used metal reference. If the error from gaseous $O_2$ is also to some degree present in superoxide and peroxide ions but not in monoxide ions, as previously suggested,[104] this can explain such systematic errors. In Figure 3.4(a) it can be seen how the calculated enthalpies of formation for superoxides, sesquioxides and peroxides are similar to the experiment when a metal chloride and gaseous oxygen reference is used (blue diamonds). The monoxides fall on a straight line (dashed blue line) parallel to but below the ideal. The error in gaseous $O_2$ appear to be present to some degree until the oxygen–oxygen bond is fully broken. The reduction of systematic errors thus also pertains to a favorable error cancellation between superoxide and peroxide species. The offset for monoxides can be reduced by an addition of Hubbard U correlation.

The smallest differences are observed for the vdW functionals when the results with the bulk metal reference and metal chloride reference are compared. Although they have nearly identical exchange, the vdW–DF functional outperforms the RPBE functional significantly with the metal reference. The vdW–DF2 functional also appears better overall than the rPW86 functional. These findings agree with previous reports that van der Waals interactions have a considerable impact on bulk alkali and alkaline earth metal calculations.[89]

The HSE06 hybrid functional does not perform significantly better than the GGA functionals when the metal reference is used. It is the functional with the smallest MAE and systematic errors when the metal chloride reference is used. The detailed performance of HSE06 is shown in Figure 3.6. When a metal chloride and water reference is used (Equation 3.9), the MAE is obtained with $b = 0$ in Equation (3.1).

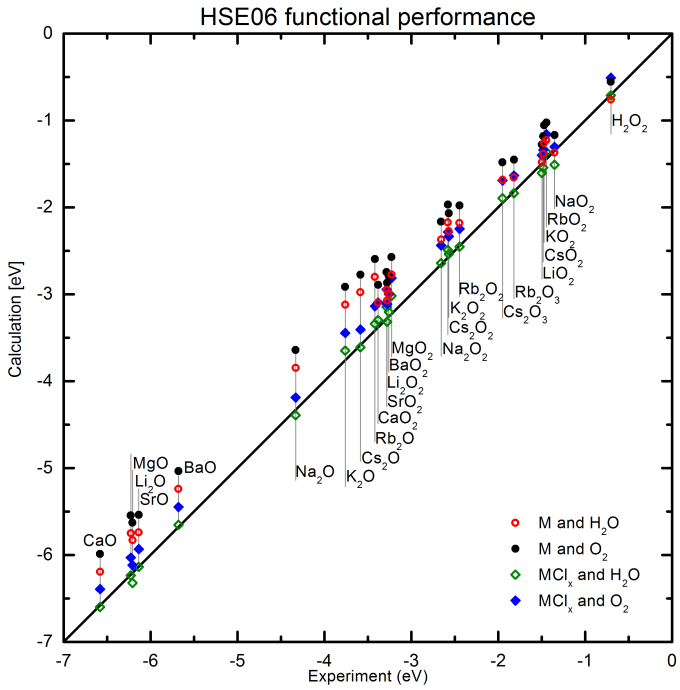


Figure 3.6: Enthalpies of formation per oxygen atom, $\Delta H_f^\circ/\mathrm{O}$, calculated with HSE06 versus experimental enthalpies for oxide species. The four different combinations of energy references are shown.

## 3.5 Error Correlation Analysis

Both the magnitude of errors and variation between the considered functionals are reduced when a metal chloride reference is used as compared to a bulk metal reference. The BEEF ensemble is used to test whether this is generally valid. The standard deviation in enthalpy of formation per oxygen is calculated with 2000 BEEF ensemble functionals. The standard deviations are presented for all oxide species in Figure 3.7. The standard deviations are approximately 2 times larger with the metal reference than with the metal chloride reference. Enthalpies are thus generally less functional–dependent when the metal chloride reference is used. Further, it can be seen that the standard deviation depends on the ratio of

metal to oxygen atoms. Metal monoxides have the largest standard deviation and the alkali superoxides have the smallest. This is true with either metal element references and shows that some functional–dependence caused by description of the metal atoms remain when the metal chloride reference is applied. $H_2O_2$

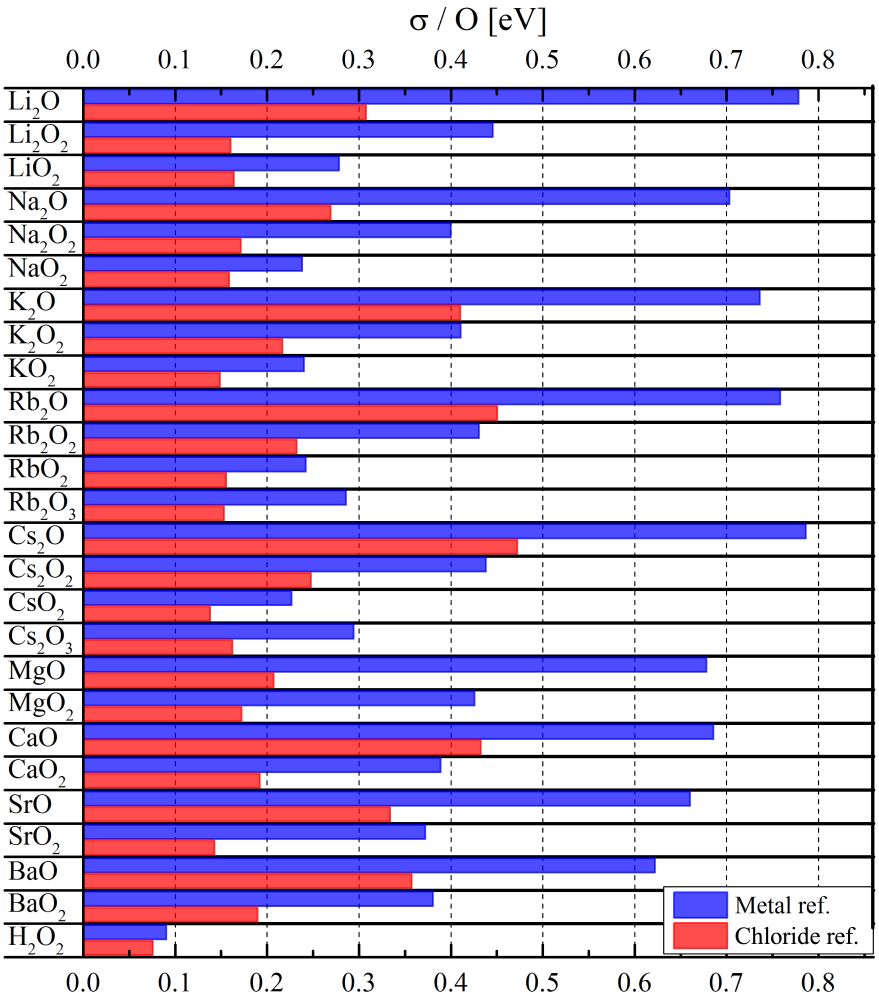


Figure 3.7: BEEF ensemble standard deviation for oxide species entahlpy of formation

does not display the same systematic errors as the metal peroxides calculated with the metal reference. Even with the metal chloride reference, $H_2O_2$ has a smaller standard deviation than the metal oxides. To examine this further, the experimental and calculated enthalpies of formation for $Na_2O_2$ and $H_2O_2$ are plotted versus each other in Figure 3.8. This type of plot is used extensively in Chapters 4 and 5. All axes in Figures 3.8(a) and 3.8(b) span 4.8 eV to illustrate the difference between the scatter in Figure 3.8(a) and in Figure 3.8(b). The experimental enthalpies of formation and enthalpies calculated with a number

of functionals are shown. The small semi–transparent gray points are 2000 BEEF ensemble functionals. A line with slope 1 is drawn through the BEEF–vdW functional point.

Similar variation along the x– and y–axis would be seen if the enthalpies of the two reactions were equally sensitive to the choice of exchange-correlation functional. If the functional–dependence for the two reactions were also correlated 1:1 as in the example presented in Section 2.4, the points would be located on the blue line. It can be seen how the points form a (wide) line. The general scatter around the line is caused by other contributions to functional–dependence than the most dominating one. The scatter is significant in Figure 3.8(a), where the metal reference is used. The scatter is smaller in Figure 3.8(b), where the metal chloride reference is used. There is no common feature dominating functional–dependence in the two reactions when the metal reference is used. The functional–dependence is significantly larger for the calculated enthalpy of formation for $Na_2O_2$ than for $H_2O_2$.

The enthalpy of reaction for $Na_2O_2$ formation is significantly less functional–dependent using the NaCl and HCl references as seen in Figure 3.8(b). The points, especially those for the self–consistent functionals, are much closer to the line with slope 1. The significant functional–dependence in formation enthalpy of $Na_2O_2$ is not caused by the formation of a peroxide ion when the Na metal reference is used. The functional–dependence is reduced considerably with the NaCl reference, and a reasonable correlation between the two reactions is established. The remaining error and functional–dependence seen in Figure 3.8(b) can be attributed to similar features in the two reactions, e.g., the formation of a peroxide.

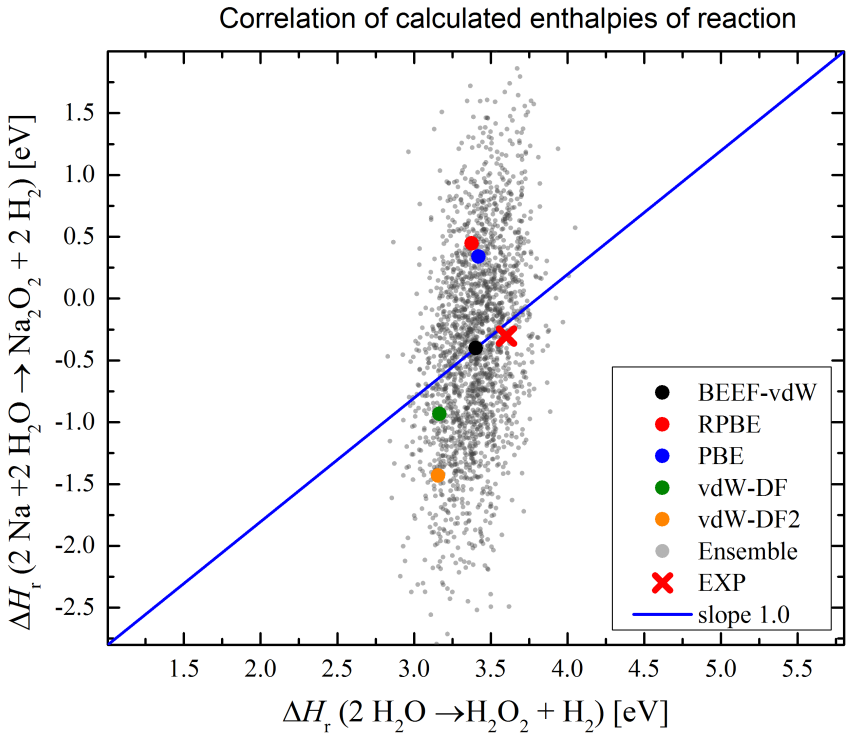


(a) Metal and water reference

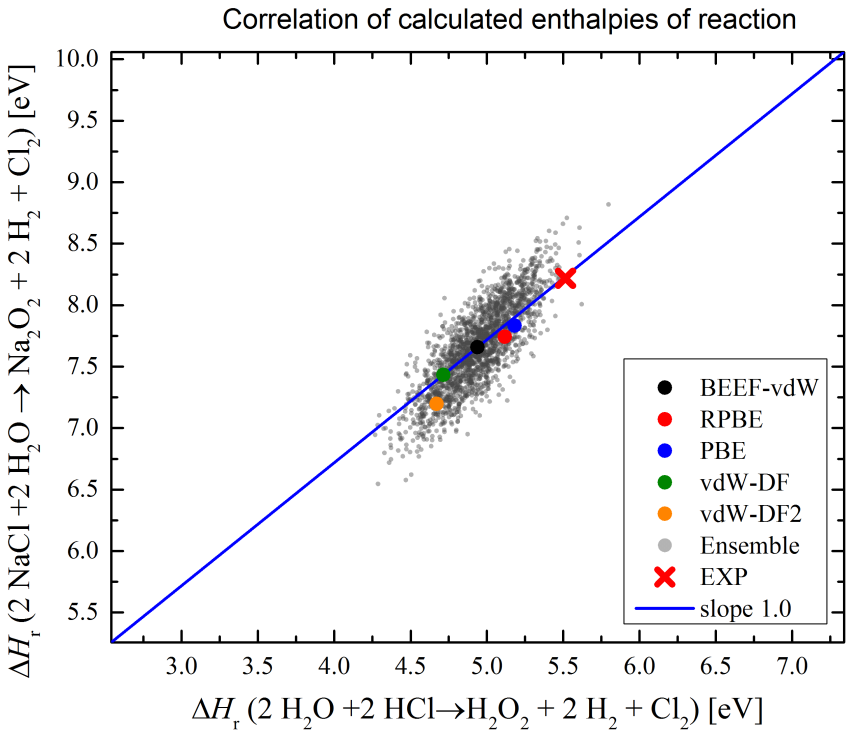


(b) Metal chloride and water reference

Figure 3.8: The experimental and calculated enthalpies of formation for $H_2O_2$ and $Na_2O_2$ plotted versus each other for multiple functionals including 2000 BEEF ensemble functionals (semi–transparent gray points).

## 3.6 Electron Localization

The ability to localize electrons with different functionals is also examined. Such ability is essential for calculation of electron conductivity. It can also be important in growth and depletion reactions of $Li_2O_2$, where an intermediate reaction can involve the formation of a superoxide ion on the surface of $Li_2O_2$.[97] The ability of different functionals to describe localized electrons can also indicate, whether such ability is important for further reduction of the above discussed systematic errors.

The $Rb_2O_3$ structure seen in Figure 3.3 is used to test the ability to localize electrons. The unit cell contains distinct superoxide and peroxide ions. The challenge is to localize an electron on each peroxide ion rather than having it delocalized over 3 oxygen ions. The ability to localize the electron can be evaluated from differences between the oxide ions such as the oxygen–oxygen bond length and the local magnetic moment of each atom.

All functionals have a tendency to convergence the electronic density in a delocalized state with equal partial electron charge on all oxygen ions, $O_2^{1.33-}$. The lattice constants of the $Rb_2O_3$ structure is optimized in this delocalized state. Subsequently, the oxygen–oxygen distances are changed for peroxide and superoxide ions to the distances in the optimized $Rb_2O_2$ and $RbO_2$ structures, respectively. Calculations are initialized with magnetic moments of 0.5 $\mu_B$ for oxygen atoms in superoxide ions.

With this initial configuration, the HSE06 functional is the only functional capable of producing the localized electron state with distinct peroxide and superoxide ions. It is expected that such a state can be obtained with HSE06, as hybrid functionals have previously been found to be able to capture electron localization in $Rb_2O_3$.[126] Bond lengths of 1.32 Å and 1.49 Å are obtained for superoxide and peroxide ions, respectively. These lengths are in agreement with experimental data within 0.01 Å.[127]

Most functionals will continue to converge into the delocalized state if the atomic configuration and wave function obtained using HSE06 functional is used as starting point. The exception is the PBE+U functional for sufficiently large values of U. As observed in Figure 3.9, localization begins to occur at values of U between 6 eV and 7 eV. This can be seen from the difference in oxygen–oxygen bond for peroxide and superoxide ions (Figure 3.9(a)). A difference in local magnetic moment is also observed for oxygen atoms in the two different ions (Figure 3.9(b). At U = 10 eV the difference in oxygen–oxygen bond length converges to 0.15 Å as compared to 0.17 Å for the HSE06 functional. The local

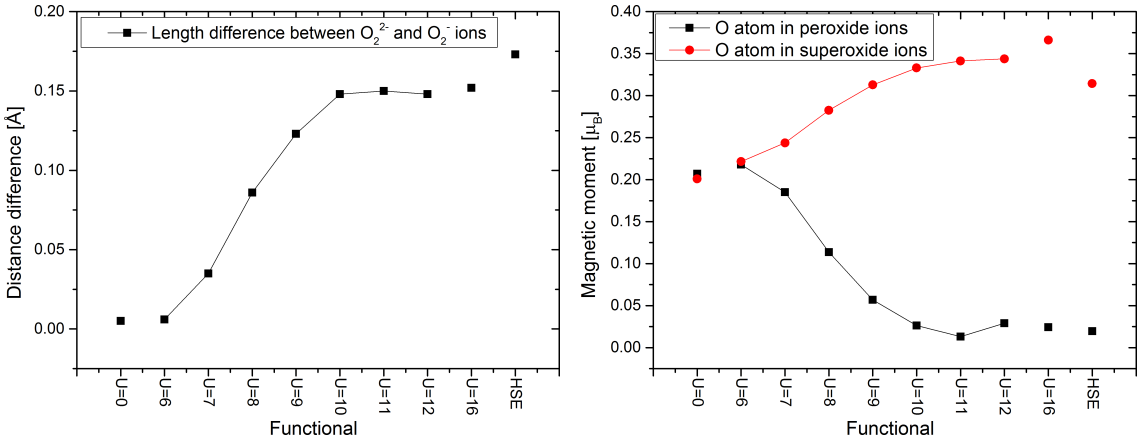


(a) Difference in oxygen–oxygen bond length for designated $O_2^-$ and $O_2^{2-}$ ions for HSE06 and PBE+U using different values of U.

(b) Difference in local magnetic moment for atoms in designated $O_2^-$ and $O_2^{2-}$ ions for HSE06 and PBE+U using different values of U.

Figure 3.9: Gradual electron localization for increasing values of U.

magnetic moments for oxygen atoms in the delocalized case, e.g. obtained with PBE, are not 0.33 $\mu_B$, as predicted, but 0.20–0.22 $\mu_B$. An explanation is that the volume around each nuclei, in which the magnetic moment is evaluated, does not fully cover the spatial distribution of the electron. For the oxygen atoms in superoxide ions, the magnetic moment when increasing U up to U=12 eV appears to converge at $\approx$ 0.34 $\mu_B$. For U=16 eV and HSE06 the magnetic moment is 0.37 $\mu_B$ and 0.32 $\mu_B$, respectively. The value is below the expected 0.5 $\mu_B$ by approximately a third, just as the magnetic moment in the delocalized case.

The HSE06 functional can capture the correct electron localization and outperforms the GGA level functionals when the metal chloride reference is used. They ability of a functional to describe localization thus appears the influence the errors in enthalpies of formation. PBE+U with values of U=8–12 eV gave modest systematic errors with the metal chloride reference (Figure 3.5). As it also capable of localizing electrons it will in many cases be the best compromise of accuracy and computational cost.

## 3.7 Application

The metal chloride reference is useful for calculating the energy of intermediate reactions in growth of $Na_2O_2$ and $NaO_2$ as done in Paper II. The equilibrium potentials are predicted from experimental standard free energies of formation of bulk $Na_2O_2$ and $NaO_2$. The equilibrium potentials are very close at -2.33 V and -2.27 V for $Na_2O_2$ and $NaO_2$, respectively. $Na_2O_2$ is thermodynamically preferred

over $NaO_2$. High charging overpotentials (¿ 1.3 V) and poor rechargeability (¡ 10 cycles) is observed in experiments where $Na_2O_2$ is found to be the main discharge product.[128–131] $NaO_2$ is observed to be the main discharge product in some experiments.[132–135] Rechargeability and overpotentials are improved when $NaO_2$ is the main discharge product.[136] Thermodynamic energy barriers for intermediate charge and discharge reactions can be determined from the energies of intermediate reactions. Such barriers can cause overpotentials and can prevent the formation of $Na_2O_2$.

With a small difference in equilibrium potential at 0.06 V, a systematic error over–stabilizing $NaO_2$ versus $Na_2O_2$ might lead to a wrong conclusion. Applying empirical corrections based on the type of oxygen ion is difficult, as molecular oxygen and Na atoms are gradually added such that the ionic state of the oxygen at the surface is not always well defined. Using the metal chloride reference to reduce systematic errors, the thermodynamic overpotentials for the growth of $Na_2O_2$ and $NaO_2$ can be consistently compared.

Equilibrium potentials are calculated and compared with experimental references. Calculations presented in this section have been performed with the PBE functional and the GPAW computational code[137,138] using a real–space basis with a grid spacing of 0.18 Å. Bulk free energies of formation can be converted to potentials using the Na equivalent of the computational hydrogen electrode.[139] The equilibrium potential, $U_0$, can be calculated as

$$U_0 = \Delta G/ne. \tag{3.10}$$

$\Delta G$ is the free energy of the considered reaction, which in this case is identical to the free energies of formation for $Na_2O_2$ and $NaO_2$. $n$ is the number of electrons transferred in the process. That is 2 and 1 for $Na_2O_2$ and $NaO_2$, respectively. Free energies are given by

$$G = H - TS. \tag{3.11}$$

Enthalpies have been calculated as described in Section 2.3.1. The entropies are obtained experimental reference data.[95]

An energy correction is applied to the $O_2$(g) reference energy. The reference energy correction is fitted to reduce errors in enthalpies of formation. Calculated standard enthalpies and equilibrium potentials are presented in Table 3.2. Calculations are observed to compare reasonably well with experiments giving the correct quantitative behavior without individual corrections for the $NaO_2$ and $Na_2O_2$ species. Considering $\Delta H_f^\circ$, the errors correspond to an overstabilization of $NaO_2$ vs $Na_2O_2$ by 0.03 eV/O. This is slightly lower but similar to the average

Table 3.2: Calculated enthalpies of formation, $\Delta H_f^\circ$, and equilibrium potentials, $U_0$, for $NaO_2$ and $Na_2O_2$ are compared with experimental values.[95] This is done with both a Na metal reference and a NaCl reference.

| | | $\Delta H_{f,\mathrm{exp}}^\circ$ [eV] | | | $U_0$[V] | | |
|---|---|---|---|---|---|---|---|
| | Space group | exp. | NaCl ref. | Na ref. | exp. | NaCl ref. | Na ref. |
| $Na_2O_2$ | $P\bar{6}2m$ | -5.32 | -5.29 | -5.01 | -2.33 | -2.32 | -2.18 |
| $NaO_2$ | $Pa\bar{3}$ | -2.71 | -2.74 | -3.05 | -2.27 | -2.30 | -2.61 |

overstabilization between superoxides and peroxides of 0.05 eV/O seen in Figure 3.5. A metal reference applied in an otherwise identical approach yields predicted enthalpies of formation of -5.01 eV and -3.05 eV for $Na_2O_2$ and $NaO_2$, respectively. This will result in both quantitative and a qualitative error for equilibrium potentials.

## 3.8 Chapter Conclusion

Systematic errors in calculation of enthalpies of formation for alkali and alkaline earth metal superoxides, peroxides, and monoxides were found using a range a exchange–correlation functionals. The errors are caused primarily by the difference in metal atom oxidation state in oxides and bulk crystalline metals. This error and the functional–dependence of results can be significantly reduced by applying a metal chloride reference as replacement for the bulk metals in a scheme similar to one previously used to circumvent known errors on the $O_2$ molecule. A smaller residual error related to the oxygen–oxygen bond is present for many GGA functionals. The hybrid HSE06 functional is seen to perform very well when the metal chloride reference is applied and is further able to capture the localization of electrons. It is, however, computationally demanding for calculation of surface reactions. The PBE+U functional with a value of U in range 8–12 eV appears to provide a good balance between accuracy, ability to localize electrons and computation cost.

CHAPTER 4

# $CO_2$ Reduction

## 4.1 Introduction

DFT can aid in the search for efficient and selective $CO_2$ reduction electrocatalysts.[140–163] DFT can among other applications be used to estimate the catalytic properties for a range of different materials and propose candidates for experimental testing. DFT can also be used to explain and understand experimental findings at an atomic level. DFT has, e.g., been used to investigate why copper as the only transition metal electrocatalysts is found to reduced $CO_2$ to a range of different products.[141,142,160,164,165]

## 4.2 Challenge

Enthalpies of gas-phase $CO_2$ reduction reactions have previously been found to be significantly different from experimental enthalpies[95] when calculated with the RPBE and BEEF–vdW functionals.[141,166,167] The functionals are optimized for heterogeneous catalysis and found the perform well for calculation of adsorption energies.[64,65,168] The significant gas-phase errors were first identified for the RPBE functional by Peterson at al.[141] They proposed the error to be caused by a systematic error on gas–phase molecules with a so–called O–C–O backbone structure, e.g., $CO_2$ and HCOOH. An empirical energy correction was added to the calculated energy of molecules with a O–C–O backbone. A correction of 0.45 eV was found through a minimization of the mean absolute error (MAE) for $CO_2$ and CO reduction reactions. The PBE functional did not cause systematic errors for molecules with O–C–O backbones, but a significant error of 0.51 eV was found for the calculated energy of CO(g).[141] An empirical correction to CO calculated with the PBE functional has subsequently been applied.[169]

A similar approach has been taken by Studt et al. for the BEEF–vdW functional.[166,167] A 0.09 eV energy correction was applied to the energy of $H_2$ in addition to a 0.33 eV[166] or 0.41 eV[167] correction of the O–C–O backbone depending on the used computational code. Although the magnitude of optimal corrections vary, significant and qualitatively similar errors are found with the DACAPO,[141] GPAW,[166] Quantum Espresso,[167] and VASP computational codes. This confirms that the error is intrinsic to the functionals. The correction approach is easy to apply in data treatment. It has been accepted and applied in a number of scientific papers with more than 20 directly citing Peterson at al.[141] or Studt et al.[166] for use of the O–C–O correction including some articles with very high impact.[142,170]

A noteworthy case where this correction does not perform well is the reduction of $CO_2$ to HCOOH. The enthalpy of reaction has been calculated to 0.26 eV,[141] 0.30 eV,[166] and 0.32 eV[167] with the corrections applied. The experimental enthalpy is 0.15 eV.[95] Errors of this magnitude will influence prediction of theoretical limiting potentials as exemplified in Section 4.8.

Electrocatalytic reduction of $CO_2$ to formic acid is of commercial interest for a number of reasons.[28,171,172] The direct reduction of $CO_2$ to formic acid is endothermic. Formic acid is industrially produced from methanol and CO. Electrocatalytic reduction of $CO_2$ to formic acid is in theory a simple two electron process able to run at an applied potential of 0.08 eV. The electricity cost is low compared to other possible electrocatalytic products and the commercial value of formic acid at a level, where operation could be profitable even without considering potential environmental benefits.[171] In the future, formic acid can also be used in transportation as a liquid phase hydrogen carrier or directly as a fuel in a formic acid fuel cell.[28,171,172]

It can be problematic to determine energy corrections through minimization of the MAE. The minimized MAE can vary by as little as 0.01 eV for different possible corrections.[166] This leaves the method sensitive to minor calculational and experimental uncertainties. An energy correlation scheme is used instead. The objective is to identify the dominant cause of errors and introduce an improved energy correction such that errors can be consistently reduced.

## 4.3 Method

### 4.3.1 Reactions

The enthalpies of the reactions in Table 4.1 have been calculated. All reactions have been normalized to one $CO_2$ reactant molecule as done previously.[141,166,167] This simplifies data treatment and comparison of errors.

Table 4.1: $CO_2$ reduction reactions and the used experimental enthalpy of reaction, $\Delta H_r^\circ$, in eV.

| Primary set | | | Reac | $\Delta H_r^\circ$ [eV][a] |
|---|---|---|---|---|
| $H_2$+$CO_2$ | → | CO+$H_2O$ | (0) | 0.43 |
| 4 $H_2$+$CO_2$ | → | $CH_4$+2 $H_2O$ | (1) | -1.71 |
| $H_2$+$CO_2$ | → | HCOOH | (2) | 0.15 |
| 3 $H_2$+$CO_2$ | → | $CH_3OH$+$H_2O$ | (3) | -0.55 |
| 3 $H_2$+$CO_2$ | → | $\frac{1}{2}$ $C_2H_5OH$+$\frac{3}{2}$ $H_2O$ | (4) | -0.89 |
| $\frac{10}{3}$ $H_2$+$CO_2$ | → | $\frac{1}{3}$ $C_3H_8$+2 $H_2O$ | (5) | -1.30 |
| $\frac{7}{2}$ $H_2$+$CO_2$ | → | $\frac{1}{2}$ $C_2H_6$+2 $H_2O$ | (6) | -1.37 |
| 3 $H_2$+$CO_2$ | → | $\frac{1}{2}$ $C_2H_4$+2 $H_2O$ | (7) | -0.66 |
| $\frac{11}{4}$ $H_2$+$CO_2$ | → | $\frac{1}{4}$ $C_4H_6$[b]+2 $H_2O$ | (8) | -0.65 |
| 2 $H_2$+$CO_2$ | → | $\frac{1}{2}$ $CH_3COOH$+$H_2O$ | (9) | -0.67 |
| 2 $H_2$+$CO_2$ | → | $\frac{1}{2}$ $HCOOCH_3$[c]+$H_2O$ | (10) | -0.17 |
| Verification set | | | | |
| 2 $H_2$+$CO_2$ | → | $CH_2O$[c]+$H_2O$ | (11) | 0.37 |
| $\frac{3}{2}$ $H_2$+$CO_2$ | → | OCHCHO+$H_2O$ | (12) | 0.47 |
| $\frac{7}{3}$ $H_2$+$CO_2$ | → | $\frac{1}{3}$ $C_2H_5COOH$[d]+$\frac{4}{3}$ $H_2O$ | (13) | -0.84 |
| $\frac{7}{3}$ $H_2$+$CO_2$ | → | $\frac{1}{3}$ $CH_3COOCH_3$+$\frac{4}{3}$ $H_2O$ | (14) | -0.68 |
| 3 $H_2$+$CO_2$ | → | $\frac{1}{2}$ $CH_3OCH_3$+$\frac{3}{2}$ $H_2O$ | (15) | -0.64 |
| $\frac{5}{2}$ $H_2$+$CO_2$ | → | $\frac{1}{2}$ $CH_3CHO$+$\frac{3}{2}$ $H_2O$ | (16) | -0.57 |
| Adsorbate set | | | | |
| 2 $H_2O$+$CH_4$ | → | HCOOH + 3 $H_2$ | (*1a) | 1.86 |
| 2 $H_2O$+$CH_3$* | → | COOH* + 3 $H_2$ | (*1b) | – |

[a]Data from NIST;[95] [b]1,3-Butadiene; [c]Alternative reference available;[95,173] [d]Propanoic acid; *Adsorbate on Cu(111).

The molecular structures of the primary products are shown in Figure 4.1. The "Primary set" contains the $CO_2$ reduction reactions used previously to determine corrections.[141,166,167] Previously, reactions for reduction of CO to the main products of Reactions (1)-(10) were also included as separate reactions. They are just the a linear combination of Reaction (0), the reverse water-gas shift reaction, and one of the other reactions. They thus contain no additional information. Including such reactions will have no other impact on results than increasing the statistical weight of Reaction (0). They have thus been omitted here.

A "Verification set" has been added. With the exception of reduction to dimethyl ether, Reaction (15), the main products of the reactions in the "Verification set" contain at least one carbon-oxygen double (C=O) bond. By including these reactions it can be determined, whether the systematic errors are caused by the presence of an O–C–O backbone or individual C=O bonds. $CO_2$ is present

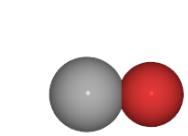

(a) CO
Reac (0)

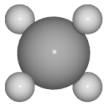

(b) $CH_4$
Reac (1)

(c) HCOOH
Reac (2)

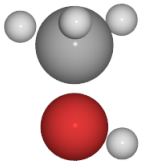

(d) $CH_3OH$
Reac (3)

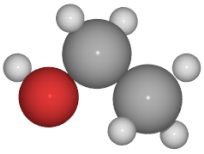

(e) $C_2H_5OH$
Reac (4)

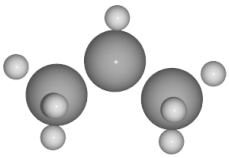

(f) $C_3H_8$
Reac (5)

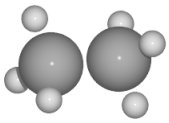

(g) $C_2H_6$
Reac (6)

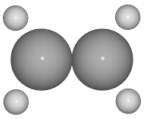

(h) $C_2H_4$
Reac (7)

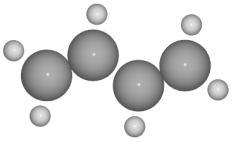

(i) $C_4H_6$
Reac (8)

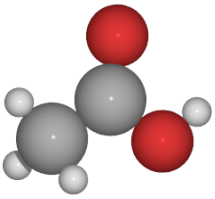

(j) $CH_3COOH$
Reac (9)

(k) $HCOOCH_3$
Reac (10)

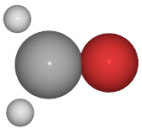

(l) $CH_2O$
Reac (11)

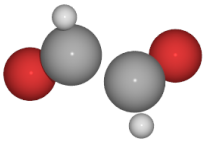

(m) OCHCHO
Reac (12)

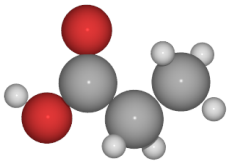

(n) $C_2H_5COOH$
Reac (13)

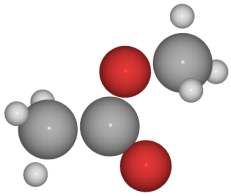

(o) $CH_3COOCH_3$
Reac (14)

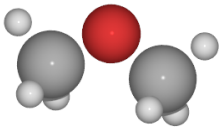

(p) $CH_3OCH_3$
Reac (15)

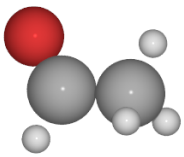

(q) $CH_3CHO$
Reac (16)

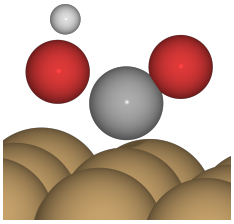

(r) COOH*
Reac (*1b)

Figure 4.1: Main reaction products in Reactions (0)–(16) and (*1b) in Table 4.1

in all reactions in the ”Primary set” and ”Verification Set” and will carry large statistical weight in corrections based on the MAE. As consequence, applying energy corrections to either the O–C–O backbone or individual C=O bonds will yield similar net energy correction to $CO_2$. The net energy correction for other molecules containing either a O–C–O backbone, one or more C=O bonds, or both but in a different ratio than $CO_2$(1:2) will depend on whether corrections are applied to O–C–O backbones or C=O bonds. The reactions in the ”Verification set” can be used to determine whether an applied energy correction does effectively counter the systematic error.

An ”Adsorbate set” consisting of two reactions is also included. They are in Section 4.7 used to establish whether systematic errors also apply to adsorbates, in this case specifically COOH* on a Cu(111) surface. This adsorbate is particularly interesting, as it is one of two possible first intermediate species for $CO_2$ reduction reactions. Enthalpies calculated for the gas–phase Reaction (*1a) and adsorbate Reaction (*1b) can be compared. This is based on the initial assumption, that the only difference between the two reactions is the replacement of a C-H bond with a C-Cu bond as both $CH_3$* and COOH* adsorbs ontop a copper atom.

Many of the reactions in Table 4.1 should not be viewed as likely outcomes of electrocatalytic $CO_2$ reduction. They can be viewed merely as a set of coupled linear equations, which allow calculated enthalpies to be compared against experimental enthalpies.

### 4.3.2 Computational Method

Enthalpies of reactions have been calculated with a number of GGA-level functionals (PBE, RPBE, BEEF–vdW, vdW–DF and vdW–DF2) all described in Section 2.2.2. Gas–phase calculations are routinely performed with higher level methods, but the ambition is to improve the accuracy of adsorption energies relative to gas–phase energies. The GGA-level often offers the best compromise between accuracy and computational cost for adsorption energies.[49,168]

Calculations in this chapter are with the exception of results in Section 4.8 obtained with the VASP code using a 650 eV plane–wave energy cut-off. Hard PAW potentials distributed with the code have been used for O, C, and H. Calculations are performed as described in Chapter 2. Vibrations calculated with the RPBE functional are in good agreement with those previously found.[141] Energies calculated from the vibrations have been used for functionals. The calculational slab used to model the Cu(111) surface consists of three closed pack $3\times3$ layers. The default PAW potential is used for Cu. A (4,4,1) k–point grid is used.

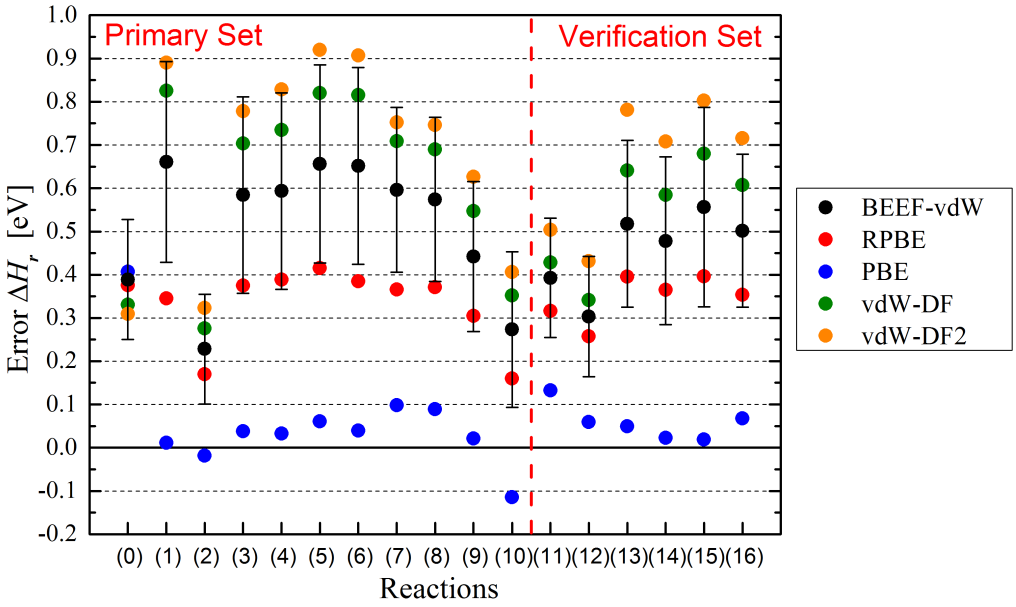


Figure 4.2: Errors, $\Delta H_r^{\circ\ \mathrm{DFT}}$ - $\Delta H_r^{\circ\ \mathrm{ref}}$, in calculated enthalpies of Reactions (0)–(16) in Table 4.1 with GGA-level exchange–correlation functionals. Error bars for the BEEF–vdW functional are the BEEF ensemble standard deviations.

## 4.4 Systematic Errors

The errors in calculated enthalpies of Reactions (0)–(16), $\Delta H_r^{\circ\ \mathrm{DFT}}$ - $\Delta H_r^{\circ\ \mathrm{ref}}$, are shown in Figure 4.2 for the different functionals. Reactions (1), (3)–(8), and (15) are simple in the sense that the product is not CO and contains neither an O–C–O backbone nor a C=O bond. Similar errors are observed for these reactions with a given functional. Notable outliers are Reaction (0), the reverse water gas shift reaction, and Reaction (2), formation of formic acid. Reactions (9)–(12) have lower but varying errors in comparison to the simple product reactions in the "Primary set". The error for Reactions (13)–(16) in the "Verification set" also appear systematic.

Error will generally be smaller than 0.1 eV with the PBE functional. The exceptions are Reaction (0), as expected from the previously found errors on CO with the PBE functional, and Reactions (10) and (11). The reason the latter two have larger errors might be the choice of reference enthalpy for $HCOOCH_3$ and $CH_2O$. Besides the newest reported and here used experimental gas–phase enthalpies, significantly different experimental enthalpies can be found for these molecules in the NIST database.[95]

For $HCOOCH_3$(g) the enthalpies in the NIST database span from -3.49 eV, which has been used here and in previous studies,[141,166,167] to -3.75 eV. Taking into account the stoichiometry of Reaction (10), using an alternative experimental

reference can shift the calculated enthalpies by as much as 0.13 eV. The errors for Reaction (10) then becomes similar to those observed in Reaction (9). The relatively large variation is caused by significantly different enthalpies for geometrical isomers. Consulting the ATcT database,[173–176] in which enthalpies are computed from an automated weighted average of a large amount of experimental data, the two possible geometrical isomers are reported to have enthalpies of -3.49 eV and -3.71 eV.

Two different enthalpies are reported in the NIST database for $CH_2O$(g). The enthalpy used as reference is -1.20 eV. The alternative enthalpy is -1.13 eV. The errors for Reaction (11) will be similar to those for Reaction (2) when the alternative enthalpy is used. The ATcT database[173–176] reports the enthalpy of $CH_2O$(g) to be -1.13 eV. Of all experimental enthalpies, those two molecules are the only cases with large variations in NIST database values. The errors with PBE for Reaction (10) and (11) can thus be explained as a consequences of erroneous reference data. The reference data is, however, not changed in the following analysis. This servers two purposes: Firstly, by using identical reference data as previous correction studies,[141,166,167] direct consistent comparisons can be made. Secondly, applying the erroneous reference data will illustrate how the correlation approach applied here to identify systematic errors is insensitive to errors in reference data in contrast to minimization of the MAE.

Comparing the different functionals in Figure 4.2, RPBE generally gives the second smallest errors followed by BEEF–vdW, vdW–DF and vdW–DF2. This order is true for all other reactions than Reaction (0). This once again indicates that the description of CO can be challenging. The errors are highly functional–dependent for all other reactions with variations as large as 0.9 eV. This is also reflected in the BEEF ensemble standard deviation plotted as error bars. They do, however, underestimate the errors. It is further observed, that the functional variation appears to be correlated with the magnitude of the error. A dominant systematic error, which is partially canceled in some of the reactions, can cause such correlation.

## 4.5 Error Correlation Analysis

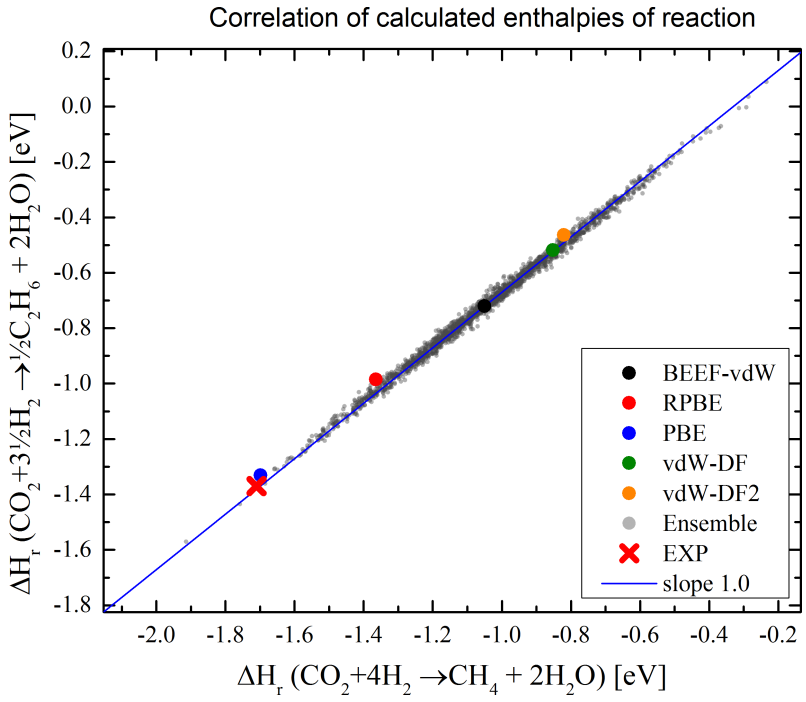


(a) Reaction (6) vs Reaction (1)

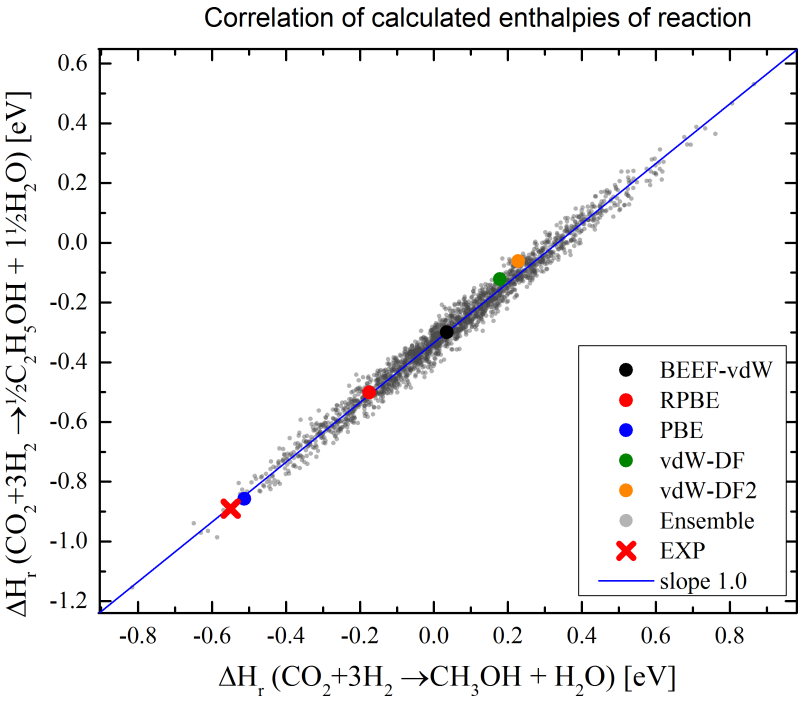


(b) Reaction (4) vs Reaction (3)

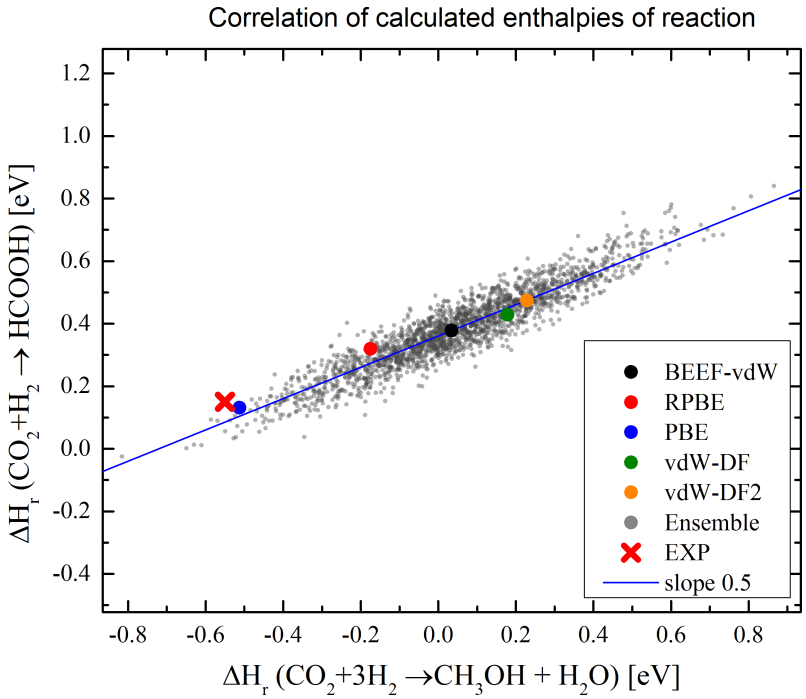


(c) Reaction (2) vs Reaction (3)

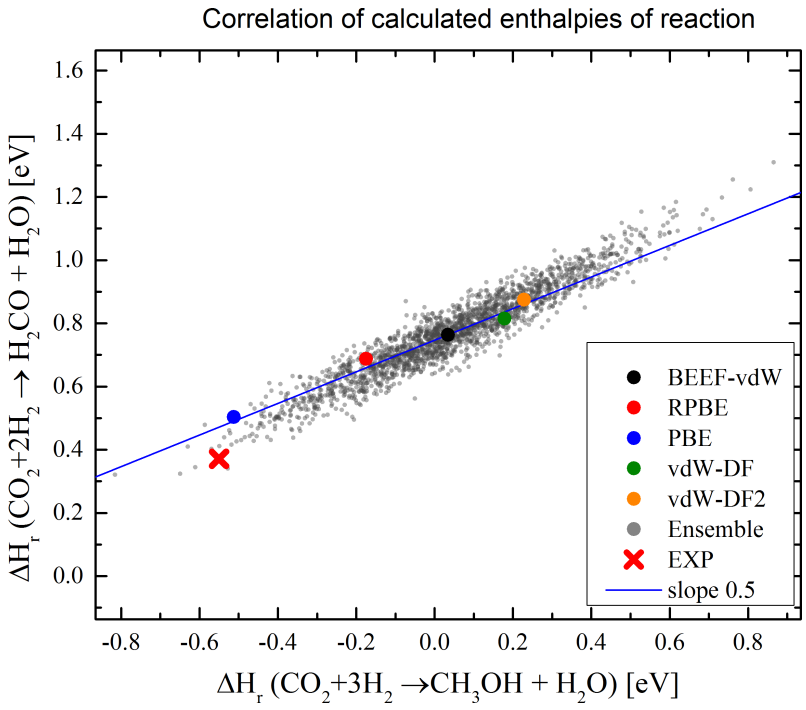


(d) Reaction (11) vs Reaction (3)

Figure 4.2: Correlations in calculated enthalpies of reaction for various gas–phase reactions in Table 4.1. Semi-transparent gray points are 2000 BEEF ensemble functionals. A blue line is drawn through the BEEF–vdW functional point with a slope determined by the change in number of C=O bonds in reactions.

Large differences in errors are obtained with PBE and RPBE. The only difference between PBE and RPBE is the exchange enhancement factor. The magnitude of the dominant systematic error must thus be highly dependent on the exchange enhancement factor. The BEEF ensemble contains functionals with different exchange enhancement factors. It can be used to examined correlations in the functional dependence of reaction enthalpies. The dominant systematic error can be deduced from these correlations. The enthalpies of reactions in Table 4.1 have been calculated with 2000 BEEF ensemble functionals in addition to the five self–consistent functionals.

Error correlations are examined graphically as in Section 3.5. The enthalpies calculated for one reaction are plotted versus those calculated for another reaction to identify pairwise correlation. The experimental reference enthalpies are also included. Plots is this type are shown in Figure 4.2. The calculated enthalpies are sensitive to choice of functional, as already seen in Figure 4.2. The points in Figure 4.2 tend to form a line. This will be the case if a common feature is dominating the functional–dependence in the two reactions making the errors strongly correlated. The slope of the line will be given by the ratio, in which the feature causing functional–dependence is present in the reactions. Additional minor contributions to functional–dependence can cause scatter which makes the line wider. An example of this can be seen by comparing Figure 4.3(a) and Figure 4.3(b). In Figure 4.3(a) strong correlation is observed with a very narrow correlation line when reduction to $C_2H_6$ is plotted versus reduction to $CH_4$. In Figure 4.3(b), where reduction to $C_2H_5OH$ is plotted versus reduction to $CH_3OH$, the scatter around the line is larger. This is likely due to the different amount of $H_2O$ in the balanced reactions. The energy of $H_2O$ is identified as functional–dependent in Chapter 5. A minor cause to functional–dependence can also influence the correlation line slope, if it is itself correlated with the dominating cause to functional–dependence as discussed further in Section 4.5.2. A likely error in the used experimental enthalpy of $CH_2O$ was discussed above. As a result of this, the experimental point does not fall on the correlation line in Figure 4.3(d).

Blue lines going through the BEEF–vdW points are drawn in all plots in Figure 4.2. The line has slope 1.0 in Figures 4.3(a) and 4.3(b) and slope 0.5 in Figures 4.3(c) and 4.3(d). In all cases, these drawn lines are seen to coincide with the trend lines formed by the functional points.

The products formed in reactions plotted in Figures 4.3(a), 4.3(b), and 4.3(d) do not contain an O–C–O backbone. All considered gas–phase reactions contain one O–C–O backbone in the reactant $CO_2$ molecule. The change in number of O–C–O backbones is thus 1 in all reactions plotted in Figures 4.3(a), 4.3(b),

and 4.3(d). The correlation lines would thus have slopes of 1.0 in these plots, if functional–dependence was caused by the O–C–O backbone. In Reaction (2), which is plotted as dependent reaction in Figure 4.3(b), the O–C–O backbone is retained in the product HCOOH (See Figure 4.1(c)). As a consequence, the correlation line slope should be near 0.0 if functional–dependence was caused by the O–C–O backbone. It could be non-zero if a minor cause to functional–dependence was present. However, the slopes predicted from O–C–O backbones are not observed for Figures 4.3(c) and 4.3(d).

The slopes are instead predicted under the assumption that individual C=O bonds are the dominating cause to functional–dependence. The number of individual C=O bonds on the reactant side is 2 for all considered reactions in the ”Primary” and ”Verification set”. In most reactions plotted in Figure 4.2, no C=O bonds are present in the products. The net change in number of C=O bonds is thus -2. Reactions (2) and (11) are plotted as independent reactions in Figures 4.3(c) and 4.3(d), respectively. The main products, HCOOH and $CH_2O$, are formed in a 1:1 ratio with reactant $CO_2$. Both contain a single C=O bond. The net change in number of C=O bonds is thus -1 for these reactions. The correlation line slopes, $a_{xy}$, can be predicted,

$$a_{xy} = \frac{\Delta(\mathrm{C{=}O})_y}{\Delta(\mathrm{C{=}O})_x}. \tag{4.1}$$

$\Delta(\mathrm{C{=}O})_y$ and $\Delta(\mathrm{C{=}O})_x$ are the net changes in number of C=O bonds in the dependent and independent reactions, respectively. The correlation slope will upon visual inspection be similar to the predicted for most pairwise correlations.

### 4.5.1 C=C Bond Error

Correlation line slopes are different from the predicted $a_{xy}$ when Reactions (7) and (8) are involved. An example is shown in Figure 4.3.

The main products in Reactions (7) and (8) are $C_2H_4$ and $C_4H_6$, respectively. They do not contain C=O bonds but do contain carbon-carbon double (C=C) bonds. C=C bonds are also cause to functional–dependence. The functional–dependence caused by C=O bonds and C=C bonds is correlated. This means, that any two functionals with a relatively large energy difference in the description of C=O bonds will also have a relatively large energy difference in the description of C=C bonds. The presence of a C=C bond will thus alter the correlation line slope and not simply increase the scatter. The correlation line slope is not 1.0, as predicted solely from the C=O bonds, but found with linear regression to be

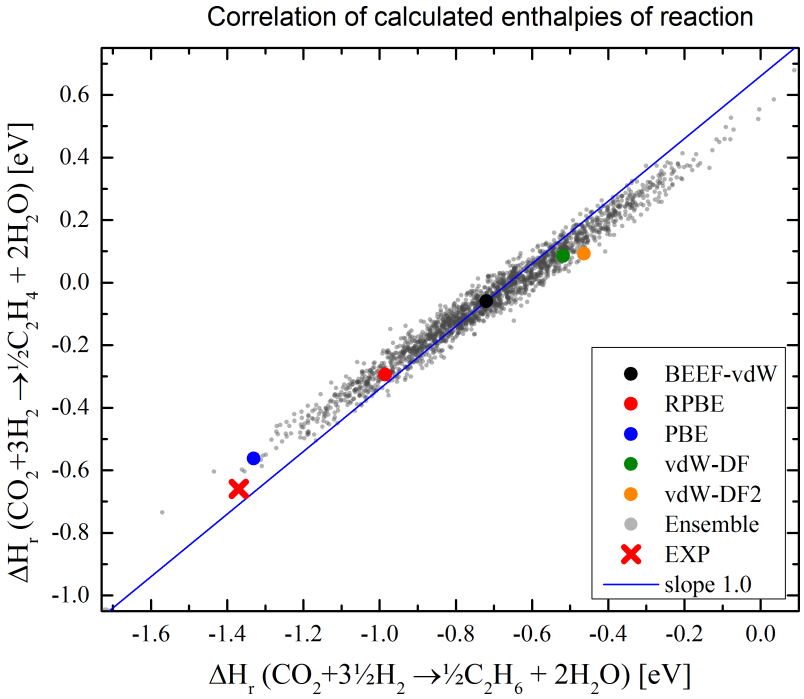


Figure 4.3: Error correlation for Reaction (7) versus Reaction (6) in Table 4.1. The plot is similar to those shown in Figure 4.2. The correlation line (gray points) is diffrent from the predicted (blue line).

0.83. By considering alternative reactions where $CO_2$ is removed as reactant and replaced by $CH_4$, the functional–dependence caused by the C=O bond and the C=C bond can be separated.

The reaction used as independent reaction in the LHS plot in Figure 4.4 is

$$2\ CH_4 \rightarrow C_2H_6 + H_2. \tag{4.2}$$

No C=C bonds are formed in this reaction. The functional–dependence for this reaction is small. One C=C bond is formed in the dependent reaction

$$2\ CH_4 \rightarrow C_2H_4 + 2H_2. \tag{4.3}$$

The functional–dependence is significantly larger for this reaction. A correlation line similar to those in Figure 4.2 is not present. The reaction in (4.3) is also used as dependent reaction in the RHS plot in Figure 4.4. The independent reaction in this plot is

$$4\ CH_4 \rightarrow C_4H_6 + 5H_2. \tag{4.4}$$

Two C=C bonds are formed in this reaction. A correlation line is observed. The self–consistent functionals, the BEEF ensemble, and the experimental reference are

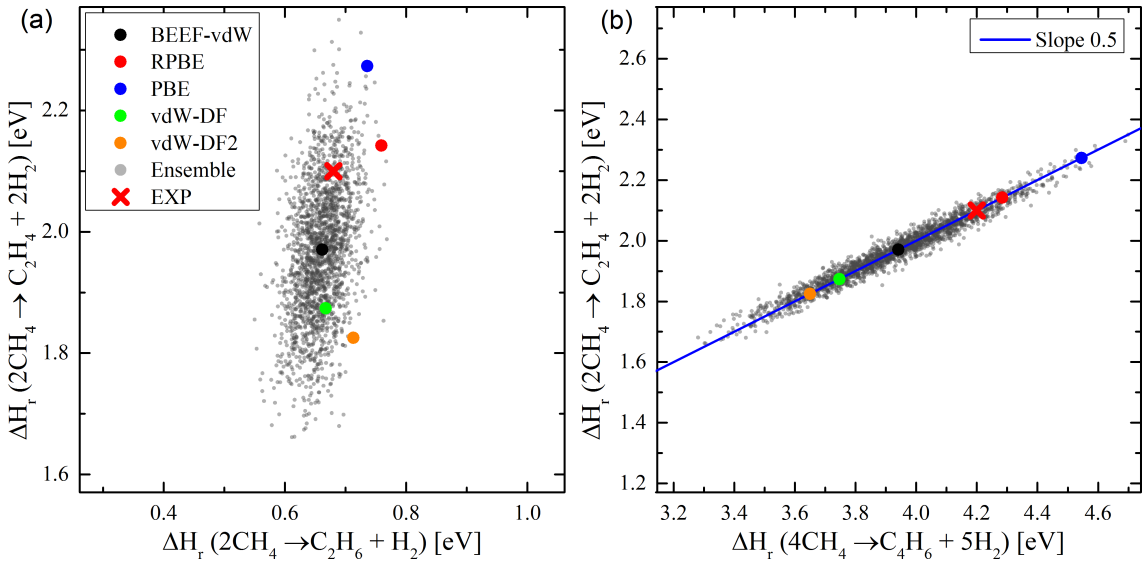


Figure 4.4: Error correlation for reactions where $CH_4$ is used to form other hydrocarbons as shown on the axes. The plot is similar to those shown in Figure 4.2. A blue line with slope 0.5 is drawn through the BEEF–vdW point in the RHS plot.

seen to all be located on the blue line drawn with slope 0.5 through the BEEF–vdW point. This is the expected slow if C=C bonds dominate the functional–dependence in these reactions. Although the C=C bond description is functional–dependent, the resulting systematic errors are smaller than observed for the C=O bond. The experimental point is for reactions in Figure 4.4 surrounded by functional points in contrast to the $CO_2$ reduction reactions, where all functionals (except PBE) overestimate the enthalpy. The functional–dependence on the energy of C=C bonds can be included in the prediction of correlation line slopes. The predicted slope $a_{xy}$ will be

$$_{xy} = \frac{\Delta(\mathrm{C{=}O})_y + \alpha\Delta(\mathrm{C{=}C})_y}{\Delta(\mathrm{C{=}O})_x + \alpha\Delta(\mathrm{C{=}C})_x}. \tag{4.5}$$

$\Delta(\mathrm{C{=}C})_x$ and $\Delta(\mathrm{C{=}C})_y$ are the number of C=C bonds formed in the independent and dependent reactions, respectively. $\alpha$ is a fitted parameter which quantifies the functional–dependence caused by the C=C bond relative to that cause by the C=O bond. It is fitted by minimized the difference between correlation line slopes predicted with Equation (4.5) and found with linear regression on BEEF ensemble functionals. $\alpha$ is 0.78.

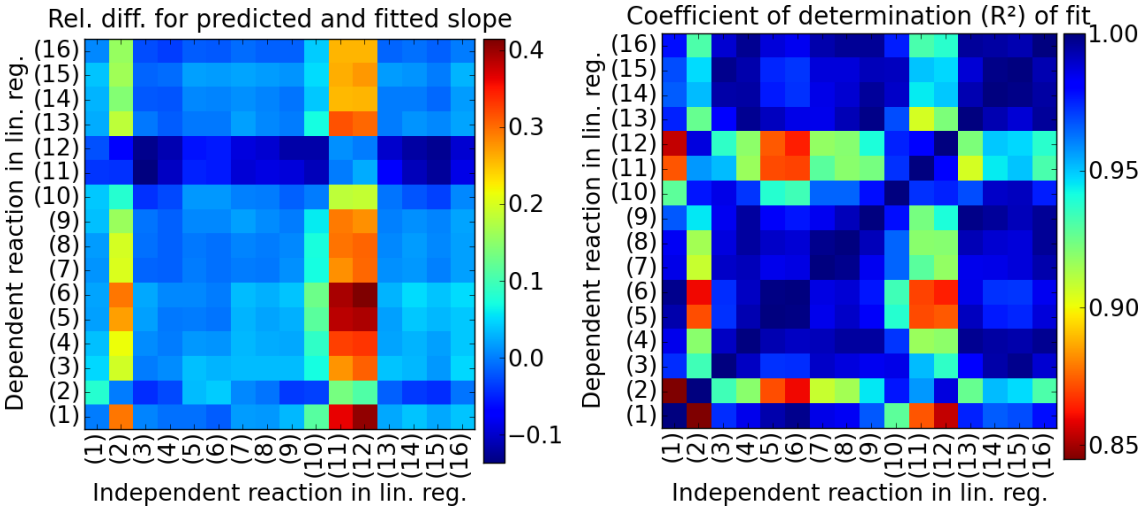


(a) Difference between predicted and fitted slopes.

(b) Coefficient of determination in linear regression.

Figure 4.5: Comparison of correlation line slopes predict and found with linear regression. The relative difference is calculated as $(a_{\text{predict}} - a_{\text{lin reg}})/a_{\text{lin reg}}$.

### 4.5.2 Slope Fitting

The difference between slopes predicted with Equation (4.5) and found with linear regression relative to the slopes found with linear regression, $(a_{\text{predict}} - a_{\text{lin reg}})/a_{\text{lin reg}}$, are shown for all possible combinations of Reactions (1)–(16) in Figure 4.5(a). 2/3 of the predicted slopes will be different from 1.

The predicted slope mostly agrees well with the slope found with linear regression on the BEEF ensemble data points. The predicted and fitted slopes are seen to be different if Reactions (2), (11), or (12) are involved. Reactions (2), (11), and (12) have the smallest change in number of C=O bonds. The differences between predicted and fitted slopes for these reactions are caused by lower "signal to noise ratio". The BEEF ensemble scatter in the correlation plots involving Reactions (2), (11), or (12) is large in comparison to the most dominant cause to functional–dependence. The scatter is quantified with the coefficient of determination ($R^2$) in the linear regression. The BEEF-ensemble data points generally follow correlation lines with relatively low scatter, and $R^2$ values are in most cases close to 1 as seen in Figure 4.5(b). The value of $R^2$ is lower for the correlations where the predicted and fitted slopes were most different. The differences between predicted and fitted slopes are caused by non-uniformity in the BEEF-ensemble. This is exemplify in Figure 4.6.

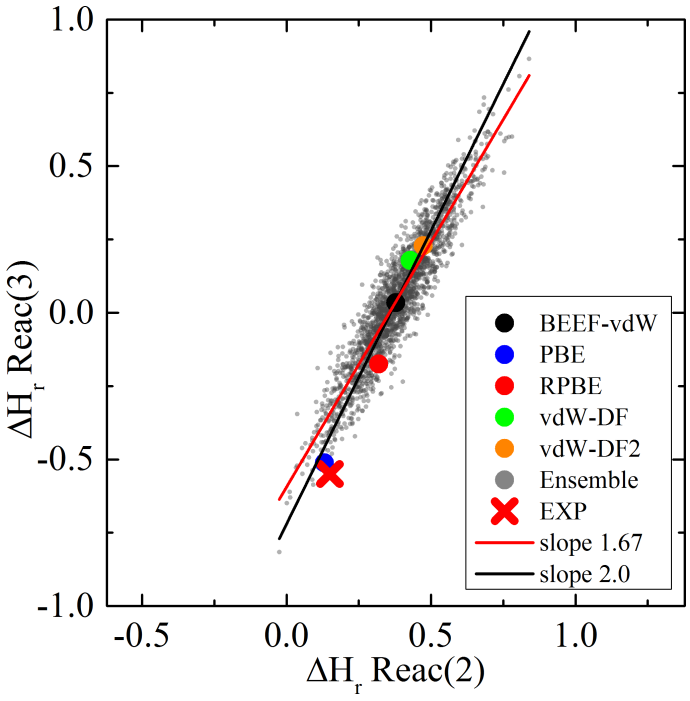


Figure 4.6: The predicted correlation line (black) for Reaction (3), [3 $H_2$ + $CO_2$ → $CH_3OH$ + $H_2O$], versus Reaction (2), [$H_2$ + $CO_2$ → HCOOH], visually follows the 2000 BEEF ensemble (semi-transparent gray), self–consistent functional, and experimental data points. The red line has been determined with linear regression on BEEF ensemble data points.

## 4.6 Energy Corrections

The energy correction per C=O bond is determined for the BEEF–vdW functional with the same procedure as used by Studt et al.[166,167] An energy correction is also applied to $H_2$ to make the performance of corrections 1:1 comparable with previous corrections. Applying a correction to C=C bonds will have close to no impact on errors. Although the C=C bond is functional–dependent, the BEEF–vdW functional describes it relatively well. Further, the total number of C=C bonds in the balanced gas–phase reactions is significantly smaller than the number of C=O bonds and $H_2$ molecules. The magnitudes of the energy corrections are fitted to minimize the MAE of reactions in the ”Primary set”. The difference between applying an energy correction to O–C–O backbones and individual C=O bonds can be seen in Figure 4.7.

The difference in MAE is small for the two different energy corrections. The MAE is 0.05 eV for O–C–O corrections and 0.03 eV for C=O corrections. Notable outliers with residual errors are present with correction of O–C–O backbones. This is in particular true for reactions in the ”Verification set”. The residual errors are smaller with the C=O correction. Reaction (10) is the only outlier. If the alternative

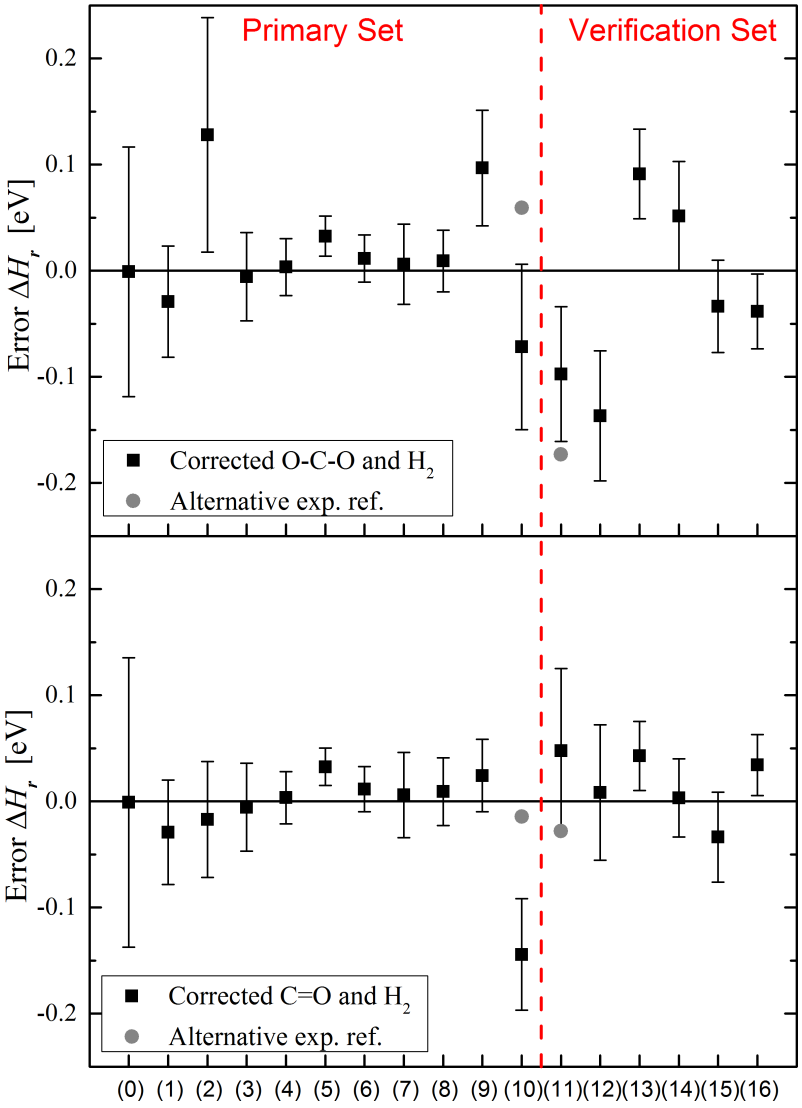


Figure 4.7: Residual errors after energy correction of $H_2$ and O–C–O backbones (top), and $H_2$ and individual C=O bonds (bottom). Error bars are the standard deviations in the BEEF ensembles after correction. Grey points mark alternative reference enthalpies as discussed in Section 4.4

enthalpy for $HCOOCH_3$(g) is used as discussed in Section 4.4, all residual errors are below 0.05 eV in magnitude.

Energy corrections are determined for all BEEF ensemble functionals. The standard deviations after energy correction are plotted as error bars. Standard deviations for the reactions with a C=O bond in the product are with the O–C–O energy correction larger than standard deviations for the reactions without a C=O bond in the product. The standard deviations after energy corrections show whether the applied correctional approach is universally applicable for GGA+vdW functionals. Standard deviations are generally reduced with the C=O

energy correction. The reduction in standard deviation is most notable for Reaction (2). The enthalpies of $CO_2$ and $H_2$ are corrected by 0.31 eV (0.15 eV for each C=O bond) and 0.09 eV, respectively, with both O–C–O and C=O energy corrections.

The post-correction results for Reaction (0) are interesting. The error for Reaction (0) with the BEEF-vdW functional is small but the functional–dependence significant after corrections of either O–C–O backbones or C=O bonds. It appears from the standard deviations that the energy of CO is functional–dependent, but that only a small error is present in calculations with the BEEF–vdW functional.

The error on $H_2$ is discussed in Section 5.4.1.

## 4.7 Adsorbates

It is next determined, whether the observed systematic error on C=O bonds is also present for adsorbates. The initial protonation of $CO_2$ results in either adsorbed carboxyl, COOH*, adsorbing through the carbon atom, or formate, OCHO*. Formate is on many surfaces found to be a bidentate adsorbate binding to the surface through both oxygen atoms. COOH* adsorbed in an ontop site on a Cu(111) surfaces can be seen in Figure 4.1(r). The adsorption energy of especially COOH* is often important in calculation of limiting potentials. A C=O bond appears to be present in COOH* by visual inspection. The presence of a C=O bond can be examined with a correlation plot for reactions in the "Adsorbate set" in Table 4.1.

The two reactions are in terms of chemical bonds very similar with one C-H bond in the gas–phase reaction (*1a) replaced by a C-Cu bond in reaction (*1b) on both reactant and product side. $CH_3$* is also adsorbed in an ontop site. The chemisorption energy is expected to be functional–dependent. However, the presence of the C-Cu bond on both reactant and product side of (*1b) with the C atom in identical adsorption sites leads to cancellation of the majority of the functional–dependence caused by chemisorption. The formation of one C=O bond in both reaction (*1a) and (*1b) is expected to dominate the correlation line slope.

In Figure 4.8 the correlation between reactions (*1a) and (*1b) can be seen. The BEEF ensemble and the self–consistent van der Waals functionals form a correlation line with slope 1. This line shows, that the systematic error on C=O found in the gas–phase species is also present for COOH*. An energy correction applied to the C=O bond in HCOOH should thus be equally applied to COOH*. The scatter around the correlation line is larger than previously observed. The increase in scatter is likely due to the chemisorption energies not fully canceling.

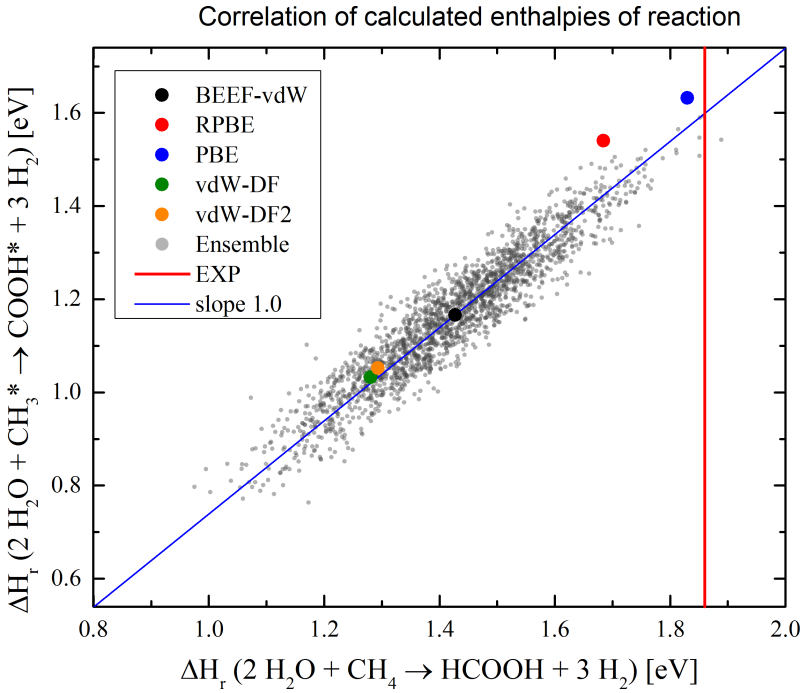


Figure 4.8: Error correlation for "Adsorbate set" reactions. The plot is similar to those shown in Figure 4.2. A blue line with slope 1.0 is drawn through the BEEF–vdW point. The red line marks the experimental enthalpy of reaction (*1a).

The GGA–functional points are located above the correlation line. This is because the van der Waals stabilization of COOH* and $CH_3$* does not cancel.

The functional–dependence of chemisorption must to large degree be canceled in reaction design to obtain a correlation between gas–phase reactions and adsorbates strong enough to determine whether similar systematic errors are present. This makes the approach difficult to apply for some adsorbates such as bidentate formate.

## 4.8 Application

The following study of electrocatalytic HCOOH formation on metal surfaces is discussed here to exemplify application of the C=O correction. See Paper IV for the full study.

Calculation of theoretical limiting potentials for reduction of $CO_2$ to HCOOH and CO as well as the hydrogen evolution reaction (HER) have been performed with the BEEF–vdW functional on various metal surfaces using the quantum espresso code.[177] The purpose is to identify catalysts, which could be both efficient and selective for reduction to HCOOH. This is not given but possible if the limiting potential for reduction to HCOOH is significantly (numerically) lower than the limiting potentials for reduction to CO and HER.

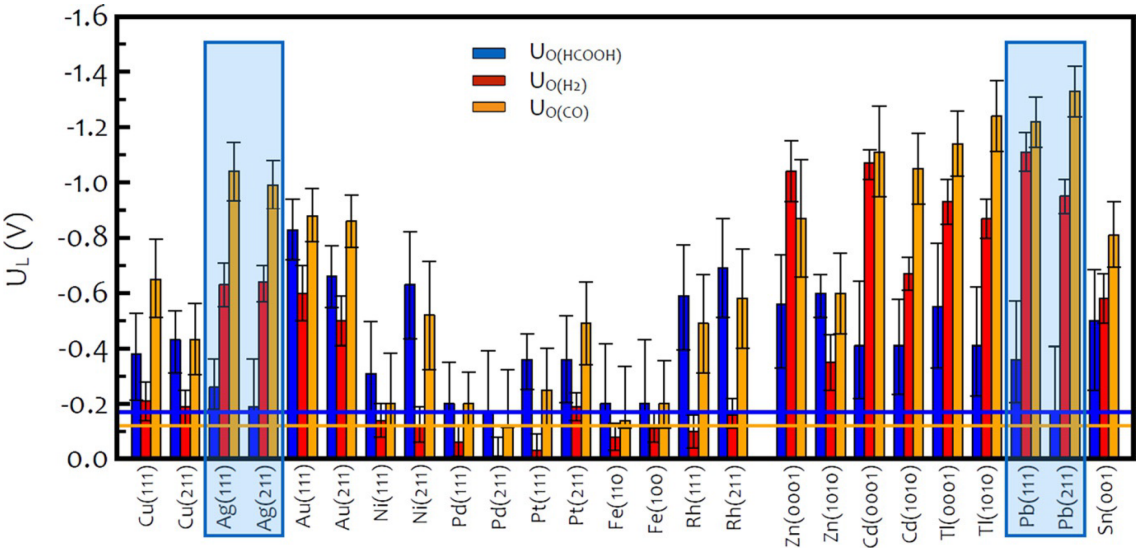


Figure 4.9: Theoretical limiting potentials vs RHE for $CO_2$ reduction to HCOOH (blue) and CO (orange) and for HER (red) on different metal surfaces. The blue and orange horizontal lines mark theoretical equilibirum potentials. Error bars are BEEF ensemble standard deviations.(Paper IV)

The considered reactions are two electron reactions. The energy of the intermediate adsorbates, i.e. H*, OCHO*, and COOH*, relative to the energy of the reactants and products calculated in gas–phase determines the limiting potential. The calculated limiting potentials are shown in Figure 4.9.

Systematic errors in energies must be mitigated for accurate comparison of limiting potentials for the different reactions. C=O energy corrections are applied to $CO_2$(g), COOH*, and HCOOH. The C=O correction will in comparison to the O–C–O correction increase the energy of COOH* and decrease the energy of HCOOH; both by 0.20 eV.[167] This will influence the theoretical limiting potentials for HCOOH and CO by as much as 0.4 V and 0.2 V, respectively. The change depends on the alignment of adsorption energies with the gas–phase energies. Differences in limiting potentials with a C=O energy correction and a O–C–O energy correction, $\Delta U_L$, can be seen in Table 4.2.

The blue horizontal line in Figure 4.9 marks the theoretical equilibrium potential for $CO_2$ reduction to HCOOH. It is here calculated to be -0.17 V. If the O–C–O backbone energy correction was used it would be -0.27 V.

The product formation trends agree with experiments performed by Hori et al.[164,165] for all other metals than Ag. The Ag and Pb surfaces marked in Figure 4.9 have low theoretical overpotentials for HCOOH formation on stepped surfaces and significantly lower theoretical limiting potentials for HCOOH formation than for CO formation and HER. They could thus be both efficient and selective

Table 4.2: Difference in limiting potential with a C=O energy correction and a O–C–O energy correction. The limiting potential is for negative values numerically smaller with the C=O energy correction.

| Surface | $\Delta U_{L(HCOOH)}$ [V] | $\Delta U_{L(CO)}$ [V] |
|---|---|---|
| Cu(111) | -0.07 | 0.20 |
| Cu(211) | 0.10 | 0.20 |
| Ag(111) | -0.02 | 0.20 |
| Ag(211) | -0.21 | 0.20 |
| Au(111) | 0.05 | 0.20 |
| Au(211) | 0.00 | 0.20 |
| Ni(111) | -0.40 | -0.19 |
| Ni(211) | -0.40 | -0.19 |
| Pd(111) | -0.09 | -0.05 |
| Pd(211) | -0.20 | -0.20 |
| Pt(111) | -0.06 | -0.20 |
| Pt(211) | -0.20 | -0.20 |
| Fe(110) | -0.40 | -0.16 |
| Fe(100) | -0.34 | -0.04 |
| Rh(111) | -0.26 | -0.19 |
| Rh(211) | -0.40 | -0.19 |
| Zn(0001) | -0.11 | 0.20 |
| Zn(1010) | 0.20 | 0.20 |
| Cd(0001) | -0.20 | 0.20 |
| Cd(1010) | -0.20 | 0.20 |
| Tl(0001) | -0.20 | 0.20 |
| Tl(1010) | -0.21 | 0.20 |
| Pb(111) | -0.21 | 0.20 |
| Pb(211) | -0.25 | 0.20 |
| Sn(001) | -0.10 | 0.17 |

catalysts for $CO_2$ reduction to HCOOH. For Ag(211), Pb(111), and Pb(211), the limiting potentials for CO formation were numerically increased by 0.20 eV with the C=O energy correction in comparison to the O–C–O energy correction. The limiting potentials for HCOOH were numerically decreased by $>$0.20 eV.

Pb surfaces have previously been found to reduce $CO_2$ to HCOOH with faradaic efficiencies $>$ 90 % at applied potentials of -0.7 $\sim$ -1.0 V vs. RHE.[178] Ag is experimentally found to produce mainly CO and small amounts of HCOOH at potentials of -0.6 $\sim$ -1.4 V vs. RHE.[179,180] The potential is relatively low (numerically large) compared to the theoretical limiting potential for HCOOH formation on Ag. Low potentials are applied experimentally to obtain sufficient current. It is possible that the thermodynamic limiting potential for HCOOH formation is numerically small, but the reaction limited by kinetic barriers. Calculations of

kinetic barriers are required to determine this.

## 4.9 Chapter Conclusion

Systematic errors have previously been identified for gas–phase $CO_2$ reduction reactions and an energy correction applied to molecules containing an O–C–O backbone. The errors are functional–dependent and through correlation analysis determined to be caused by individual C=O bonds. Applying an energy correction to C=O bonds rather than the O–C–O backbone, errors can be reduced, e.g., for the reduction of $CO_2$ to HCOOH. Correlation analysis is extended to adsorbates. An C=O bond error is present for COOH* adsorbed on a copper surface. The difference between applying C=O energy corrections and O–C–O energy corrections is exemplified in a study of formic acid formation trends on metal catalysts.

CHAPTER 5

# Oxygen Evolution and Reduction Reactions

## 5.1 Introduction

Development of inexpensive, stable, and efficient catalysts for the oxygen evolution reaction (OER) and oxygen reduction reaction (ORR) is a key challenge in the commercialization of hydrogen electrolyzers and fuel cells.[40,42–45,181–185] DFT has in recent years been applied in a number of studies to obtain fundamental knowledge and establish guiding principles in the search for better catalysts.[43,93,139,186–191] The energies of each intermediate reaction in the reaction processes are of particular interest, as they can be used to determine theoretical minimum overpotentials. The full ORR associative process catalyzed by a heterogeneous electrocatalyst consist of the following intermediate reactions,

$$O_2 + H^+ + e^- + * \rightarrow OOH* \tag{5.1}$$

$$OOH* + H^+ + e^- \rightarrow H_2O + O* \tag{5.2}$$

$$O* + H^+ + e^- \rightarrow OH* \tag{5.3}$$

$$OH* + H^+ + e^- \rightarrow H_2O + *. \tag{5.4}$$

Each reaction step includes both the transfer of a proton and an electron. $*$ denotes a catalyst adsorption site. The computational hydrogen electrode approach[139] can be used to calculated the energy of each intermediate reaction with DFT at certain reaction conditions.

$$G[H^+ + e^-] = \tfrac{1}{2}G[H_2]. \tag{5.5}$$

The OER intermediate reactions are the reverse of the ORR reactions.[189] The full net reaction of (5.1)–(5.4) is

$$O_2 + 4(H^+ + e^-) \rightarrow 2\ H_2O. \tag{5.6}$$

The free energy of the full reaction is -4.92 eV. The ideal catalyst does not have a thermodynamic overpotential. This requires the O*, OH* and OOH* adsorption energies to align such that the intermediate reactions (5.1)–(5.4) all have a free energy of -1.23 eV at zero applied potential.

Adsorption energies have been found to correlate for many species on catalytic surfaces. As a result, one adsorption energy can be predicted from another.[48] These relationships in adsorption energies are referred to as scaling relations and are very useful in the search for new catalysts. They can be used to construct so-called volcano plots, which simplify activity predictions by turning a multidimensional problem into one with fewer variables. Predicted volcano plots for ORR and OER activity have been shown to be in good agreement with experiment.[43,45,48,192]

A fundamental scaling relation in ORR and OER is that between the adsorption energies of OH* and OOH*.[48,93,187–190,193–195] Expressed in free energy[187,193](Appendix B) it is

$$\Delta G_{OOH^*} = \Delta G_{OH^*} + 3.2 \pm 0.2\ \text{eV}. \tag{5.7}$$

$\Delta G_{OOH^*}$ denotes the adsorption free energy of OOH*. The scaling relation is unchanged when expressed in electronic energies with an added correction for electrolyte stabilization.[189,190] The 1:1 change in OOH* and OH* adsorption energies (the scaling relation slope is 1) can be explained with bond order conservation,[196] as OH* and OOH* binds similarly to the surface. The scaling relation offset is 3.2 eV. The adsorption energy difference between OOH* and OH* will be 3.2 $\pm$ 0.2 eV on surfaces where the scaling relation applies. A 3.4 eV energy difference is observed experimentally between $OOH^-$(aq) and $OH^-$(aq).[197,198] The $\pm$ 0.2 eV does in this case not refer to calculational uncertainty of individual calculations but variations in the scaling relation offset for different catalytic surfaces.[48,189,190,193,194] Notable scatter is observed around the ”best fit” line when $\Delta G_{OOH^*}$ is plotted vs $\Delta G_{OH^*}$.[189,190,193,194] For a subclass of catalysts, e.g., Pt alloys, the deviation from the ”best fit” line is systematic. The $\pm$ 0.2 eV is the uncertainty introduced when the adsorption energies are predicted with a single universal scaling relation for a range of different catalytic surfaces.

The scaling relation dictates that the sum of reaction energies for reaction (5.2) and (5.3) will be -3.2 $\pm$ 0.2 eV at zero applied potential. The combined -3.2 eV energy of reactions (5.2) and (5.3) is significantly larger than the ideal -2.46 eV. The

scaling relation with slope 1 and offset 3.2 eV will thus for both ORR and OER force a minimum theoretical ovepotential of (3.2 $\pm$ 0.2 eV - 2.46 eV)/2$e$ = 0.4 $\pm$ 0.1 V for all intermediate reactions to become exergonic.

## 5.2 Challenge

The scaling relation in Equation (5.7) is determined from calculations performed with the RPBE functional. In Chapter 3 it was after removal of the metal oxidation state error shown, that a systematic error pertained to oxygen-oxygen bonds. The error was found for ions in metal peroxides and $H_2O_2$. An oxygen-oxygen bond is present in the OOH* adsorbate. This bond could be similar to the bond in $H_2O_2$. A systematic error on the oxygen-oxygen bond could cause the adsorption energy of OOH* to be systematically underestimated. The scaling relation offset will thus also by systematically underestimated. A larger offset will result in larger minimum thermodynamic overpotentials.

In this chapter it is examined whether systematic errors are present in peroxide bonds in gas–phase species with GGA–level functionals. It is determined whether systematic errors are also present for the OOH* adsorbate an various metal surfaces. The procedure is similar to that applied for $CO_2$ reduction reactions in Chapter 4.

## 5.3 Method

Enthalpies are calculated for a number of reactions shown in Table 5.1 with multiple GGA-level functionals including 2000 BEEF ensemble functionals. In the reactions in the ”Gas–phase set”, two O-H bonds are broken in the formation of a peroxide bond and a $H_2$ molecule. If a significant systematic error is present in the description of the peroxide bond, correlated errors in enthalpy of reaction can be expected.

A peroxide bond is not formed in the reactions in the ”Verification set”. Only common molecules, which are not expected to cause significant unknown errors, are part of these reactions. ”Verification set” reactions are used as accuracy reference to confirm that observed systematic errors in the ”Gas–phase set” reactions are only present when a peroxide bond is formed.

The ”Adsorbate set” consists of surface reactions between OH* and OOH* adsorbed on three different metal fcc(111) surfaces. The metals, i.e., Pt, Pd, and Ag, span the relevant reactivity range for ORR catalysts. Through correlation in

Table 5.1: Reaction sets and experimental enthalpies of gas–phase reactions.

| Gas–phase set | | | Reac | $\Delta H_r^\circ$ [eV][a] |
|---|---|---|---|---|
| $2\,H_2O$ | $\rightarrow$ | $H_2 + H_2O_2$ | (1) | 3.60 |
| $CH_3OH + H_2O$ | $\rightarrow$ | $H_2 + CH_3OOH$ | (2) | 3.23 |
| $C_2H_5OH + H_2O$ | $\rightarrow$ | $H_2 + C_2H_5OOH$[b] | (3) | 3.24 |
| $2\,CH_3OH$ | $\rightarrow$ | $H_2 + CH_3OOCH_3$ | (4) | 2.87 |
| $C_3H_7OH + H_2O$ | $\rightarrow$ | $H_2 + C_3H_7OOH$[b] | (5) | 3.25 |
| $(CH_3)_2CHOH + H_2O$ | $\rightarrow$ | $H_2 + (CH_3)_2CHOOH$ | (6) | 3.29 |
| $2\,C_2H_5OH$ | $\rightarrow$ | $H_2 + C_2H_5OOC_2H_5$ | (7) | 2.86 |
| $(CH_3)_3COH + H_2O$ | $\rightarrow$ | $H_2 + (CH_3)_3COOH$ | (8) | 3.31 |
| Adsorbate set | | | | |
| $OH^*_{Pt}$[a] $+ H_2O$ | $\rightarrow$ | $H_2 + OOH^*_{Pt}$[c] | (*1) | – |
| $OH^*_{Ag}$[b] $+ H_2O$ | $\rightarrow$ | $H_2 + OOH^*_{Ag}$[d] | (*2) | – |
| $OH^*_{Pd}$[a] $+ H_2O$ | $\rightarrow$ | $H_2 + OOH^*_{Pd}$[c] | (*3) | – |
| Verification set | | | | |
| $2\,CH_4$ | $\rightarrow$ | $H_2 + C_2H_6$ | (v1) | 0.69 |
| $CH_4 + H_2O$ | $\rightarrow$ | $H_2 + CH_3OH$ | (v2) | 1.20 |
| $CH_4 + C_2H_6$ | $\rightarrow$ | $H_2 + C_3H_8$ | (v3) | 0.56 |
| $C_2H_6 + H_2O$ | $\rightarrow$ | $H_2 + C_2H_5OH$ | (v4) | 0.94 |

[a]Data from NIST[95] unless otherwise specified; [b]$\Delta H^\circ$ from;[199]
[c]Ontop adsorption site; [d]hcp hollow adsorption site;

functional–dependence it can be established whether a systematic error in gas–phase species is also present in OOH* adsorbates. The enthalpies of reactions in the "Adsorbate set" is equal to the differences in adsorption enthalpies of OOH* and OH*. A systematic error in the reactions in the "Adsorbate set" is thus also a systematic error in the OH*/OOH* scaling relation offset.

Experimental enthalpies for gas–phase species have in most cases been obtained from the NIST database.[95] Experimental data with sufficient precision is not available for ethyl hydroperoxide, $C_2H_5OOH$, and n-propyl hydroperoxide, $C_3H_7OOH$. Cross–verified enthalpies calculated with high accuracy quantum chemistry methods have been used instead.[199] The combination of enthalpies obtained with experimental and higher level theoretical methods is an advantage. It can be difficult to determine standard enthalpies experimentally for molecules, which are in condensed phase at standard conditions and interact strongly, e.g., through hydrogen bonds. If identical systematic errors are observed for the reactions, in which experimental and quantum chemistry reference enthalpies are used, such methodological inaccuracies can be dismissed as cause.

### 5.3.1 Computational Method

As in Chapter 4, enthalpies of reaction are calculated with several GGA functionals (PBE, RPBE, BEEF–vdW, vdW–DF, vdW–DF2 ). The BLYP functional is also used. Calculations are performed as described in Section 2.3. A 650 eV plane–wave cut–off is used with hard PAW potentials for C, O, and H. Potentials explicitly including 4*p*-electrons are used for Pd and Ru (Section 5.8), i.e. the "pv" potentials. Default PAW potentials are used for Ag and Pt. All calculations allow spin polarization. Vibrations are calculated independently with the PBE, RPBE and BEEF–vdW functionals. The energies calculated from the vibrational frequencies are similar for the three functionals. These energies are also used for the vdW–DF, vdW–DF2, and BLYP functionals.

Metal slab structures consist of 5 closed pack layers with 4 atoms in each. The surface coverage is 1/4 monolayer. The two lower layers are constrained with interatomic distances as in bulk. A (4,4,1) k-point sampling is used for all slab structures.

## 5.4 Gas–Phase Errors

Table 5.2: Errors in $\Delta H_r^\circ$ [eV] with different exchange-correlation functionals for gas–phase reactions in Table 5.1.

| Reac | PBE | RPBE | BEEF–vdW | vdW–DF | vdW–DF2 | BLYP |
|---|---|---|---|---|---|---|
| (1) | 0.25 | 0.29 | 0.26 | 0.41 | 0.44 | 0.35 |
| (2) | 0.19 | 0.24 | 0.22 | 0.36 | 0.40 | 0.30 |
| (3) | 0.21 | 0.24 | 0.22 | 0.36 | 0.39 | 0.29 |
| (4) | 0.17 | 0.18 | 0.21 | 0.36 | 0.39 | 0.25 |
| (5) | 0.21 | 0.24 | 0.24 | 0.39 | 0.41 | 0.31 |
| (6) | 0.21 | 0.23 | 0.21 | 0.37 | 0.42 | 0.27 |
| (7) | 0.14 | 0.14 | 0.19 | 0.34 | 0.36 | 0.21 |
| (8) | 0.24 | 0.25 | 0.27 | 0.42 | 0.46 | 0.33 |
| avg.[a] | 0.20 | 0.22 | 0.23 | 0.38 | 0.41 | 0.29 |
| SD[b] | 0.03 | 0.04 | 0.02 | 0.03 | 0.03 | 0.04 |
| (v1) | 0.01 | -0.01 | -0.01 | 0.00 | -0.05 | -0.04 |
| (v2) | 0.05 | 0.05 | 0.06 | 0.11 | 0.10 | 0.07 |
| (v3) | -0.03 | -0.06 | -0.03 | -0.03 | -0.08 | -0.10 |
| (v4) | 0.02 | 0.00 | 0.03 | 0.08 | 0.08 | 0.03 |
| avg.[c] | 0.01 | -0.01 | 0.01 | 0.04 | 0.01 | -0.01 |

[a]Average error and [b]standard deviation for reactions (1)–(8).
[c] Average error for reactions (v1)–(v4).

Enthalpies of reactions are calculated for reactions in the "Gas–phase set" and Verification set" (Table 5.2). Both the average and individual errors are relatively small. This is especially true for the PBE, RPBE, and BEEF–vdW functionals, where the maximum error is 0.06 eV. A pattern in errors can be seen. The signed error is for all functionals smallest for reaction (v3) followed by reaction (v1), (v4), and (v2) in that order. The error pattern could be due to the used experimental references, but could also, at least in part, be due to a minor systematic error for $H_2O$, which is present in reactions (v2) and (v4).

Systematic errors are present for reactions (1)–(8) in the "Gas–phase set" where a peroxide ion is formed. The errors are nearly constant for the eight reactions with a given functional. The average error and the standard deviation in errors is calculated. The average error is 0.22 eV and the standard deviation in errors 0.04 eV for the RPBE functional used to determine the scaling relation offset to be 3.2 eV. Reaction (1) consistently gives a larger error than the average for reactions in the "Gas–phase set". The errors for reactions (4) and (7) are consistently below the average error. A minor error on $H_2O$ can explain this pattern, as two $H_2O$ molecules are present on the reactant side of reaction (1), and none present in reactions (4) and (7). One $H_2O$ molecule is present as reactant in the remaining reactions. An error for $H_2O$ is further discussed in Section 5.6.1.

### 5.4.1 $H_2$ Error

The energy of $H_2$ calculated with the BEEF–vdW functional is in Chapter 4 and literature[166,167] corrected by 0.09 eV to minimize $CO_2$ reduction reaction errors. A 0.09 eV energy correction is applied to $H_2$ energies calculated with all three vdW functionals. This correction decreases the errors in calculated enthalpies of reaction shown in Table 5.2. The enthalpy is changed by 0.09 for all reactions as one $H_2$ molecule is formed in all reactions. The $H_2$ energy correction will thus not impact the error pattern.

The average error for reactions in the "Verification set" is with the correction applied -0.01 eV to 0.01 eV for all other functionals than the vdW–DF functional, where it is 0.04 eV. It has previously been found that an energy correction to $H_2$ is not required with the RPBE functional.[141,166] Further, $H_2$ molecules do not appear to contribute significantly to functional–dependence within the BEEF ensemble. The non-local van der Waals correlation is identical in the vdW–DF2 and BEEF–vdW functionals. Applying the same energy correction to $H_2$ for these two functionals will reduce the average error of reactions in the "Verification set" to the average error of non–vdW functionals. A slightly different van der Waals

correlation is used in the vdW–DF functional. Here a slightly ($\approx$ 0.03 eV) larger energy correction would reduce the average "Verification set" errors to the average of the non–vdW functionals. All these findings point towards a systematic error on $H_2$ in large part caused by the non-local van der Waals correlation. As the non-local van der Waals correlation is identical in all BEEF ensemble functionals, it will not influence correlation line slopes. The error on $H_2$ will displace all the van der Waals functional points relative to the experimental point in correlation plots. The displacement is in the direction of the correlation line if the same number of $H_2$ is present in the two plotted reactions. The error on $H_2$ will cause the pure GGA functional data points to be located slightly of or towards one side of the BEEF ensemble correlation line in correlation plots, if the number of $H_2$ are different in the two plotted reactions. This can be observed, e.g., in Figure fig:chap4:scaling5.

The errors in Table 2.1 for reactions in Section 2.4 are reexamined. 3 and 2.5 $H_2$ are present as reactants in Reactions A and Reaction B, respectively. 0.5 $H_2$ is present as product in the net reaction, Reaction B-A. If errors in these reactions are solely cause by an error of 0.09 eV per $H_2$, the errors will be, -0.27 eV, -0.23 eV and 0.05 eV. For comparison, the calculated errors are -0.28 eV, -0.27 eV, and 0.2 eV. With the findings in this and the prior chapter, it thus seems that the BEEF ensemble standard deviations for reactions in Section 2.4 are caused primarily by CO and $H_2O$, whereas to errors in the reactions are caused by $H_2$. This example serves to show that the causes of functional–dependence and errors are not always identical and one should be careful drawing conclusions based on limited data.

## 5.5 Functional–Dependence

The errors in Table 5.2 are different for the six functionals. The variation in reaction enthalpies with choice of functional can be quantified with the BEEF ensemble standard deviation, $\sigma_{\mathrm{BEEF}}$. Standard deviations are calculated for all considered reactions including the reactions in the "Adsorbate set" and are reported in Table 5.3. $\sigma_{\mathrm{BEEF}}$ is similar for the reactions in the "Gas–phase set" and the "Adsorbate set". $\sigma_{\mathrm{BEEF}}$ is $0.19 \pm 0.02$ eV. The average error for the reactions in the "Gas–phase set" is 0.23 eV with the BEEF–vdW functional. Using the standard deviation as an error estimate will thus give slightly underestimated errors. The calculational uncertainty in the scaling relation offset is with the standard deviation estimated to be 0.19 eV. The same calculational uncertainty estimate is found by Deshpande, Kitchin and Viswanathan.[195] The calculational uncertainty is not to be confused with the previously discussed $\pm$ 0.2 eV uncertainty in the scaling relation.

Table 5.3: The standard deviation in reaction enthalpies calculated with the BEEF ensemble before and after an energy correction applied to the oxygen-oxygen bond.

| Reac | $\sigma_{\text{BEEF}}$ [eV] | $\sigma_{\text{BEEF, corrected}}$ [eV] |
|---|---|---|
| (1) | 0.17 | 0.04 |
| (2) | 0.19 | 0.04 |
| (3) | 0.19 | 0.04 |
| (4) | 0.20 | 0.06 |
| (5) | 0.18 | 0.04 |
| (6) | 0.19 | 0.05 |
| (7) | 0.20 | 0.05 |
| (8) | 0.19 | 0.05 |
| (*1) | 0.19 | 0.05 |
| (*2) | 0.19 | 0.04 |
| (*3) | 0.19 | 0.05 |
| (v1) | 0.03 | 0.03 |
| (v2) | 0.05 | 0.05 |
| (v3) | 0.05 | 0.05 |
| (v4) | 0.06 | 0.06 |

The calculated standard deviation is smaller for reaction (1) and larger for reactions (4) and (7) than for the other reactions in the ”Gas phase set” and the ”Adsorbate set”. These differences in standard deviations are in agreement with $H_2O$ as a minor cause of functional–dependence and error. The standard deviations for reactions in the ”Verification set” are significantly smaller at $0.05 \pm 0.02$ eV. The smaller standard deviations for the reactions in the ”Verification set” further indicates, that the energy of the oxygen-oxygen bond is functional–dependent.

An energy correction to cancel for functional–dependence cause by the oxygen-oxygen bond is determined independently for each BEEF ensemble functional. For a given ensemble functional $f$, the energy correction is $c_f$. The correction is calculated as

$$c_f = \frac{1}{11} \sum_r \left( E_{\text{BEEF}-\text{vdW},r} - E_{f,r} \right) . \tag{5.8}$$

$r$ denotes the 11 reactions in the ”Gas–phase set” and ”Adsorbate set”. $E_{\text{BEEF}-\text{vdW},r}$ is the electronic energy of reaction $r$ calculated with the self-consistent BEEF–vdW functional. $E_{f,r}$ is the electronic energy of reaction $r$ calculated with the ensemble functional $f$. The standard deviations decrease to $0.05 \pm 0.02$ eV when the energy corrections to the oxygen-oxygen bond are applied as seen in Table 5.3. After correction, the functional–dependence is the same for all reactions. The estimated calculational uncertainty and the functional–dependence of the scaling relation

offset is reduced from 0.19 eV to 0.05 eV when an energy correction is applied to oxygen-oxygen bond in OOH*.

## 5.6 Error Correlation

Error correlation plots as those presented in Chapter 4 are made to confirm that the systematic oxygen-oxygen bond error found for gas–phase species is the major cause of functional–dependence.

Error correlation plots for reactions in the ”Gas phase set” are shown in Figure 5.1. A linear regression line is calculated with the BEEF ensemble data points. Significant functional–dependence with only small scatter around the regression line is observed in both Figure 5.1(a) and 5.1(b). The scatter is larger in Figure 5.1(b) than in Figure 5.1(a). This is expected as the former includes $(CH_3)_3COOH$. This is a molecule of considerable size and complexity where many features can potentially be minor causes to functional–dependence and generate scatter. If the functional–dependencies in the dependent and independent reactions are correlated 1:1, the slope of the regression line will be 1. The fitted slopes are 0.99 and 1.02. The experimental point does not fall on the line in Figure 5.1(b). When errors versus experiment are calculated, reaction (8) will thus have slightly different errors than the other reactions in the ”Gas–Phase set” as can be seen in Table 5.2. However, the correlation plot reveals that the functional–dependence is the same in this reaction as in the other reactions in the ”Gas–Phase set”. This indicates that one of the experimental reference enthalpies used to calculate the enthalpy of reaction (8) can be inaccurate.

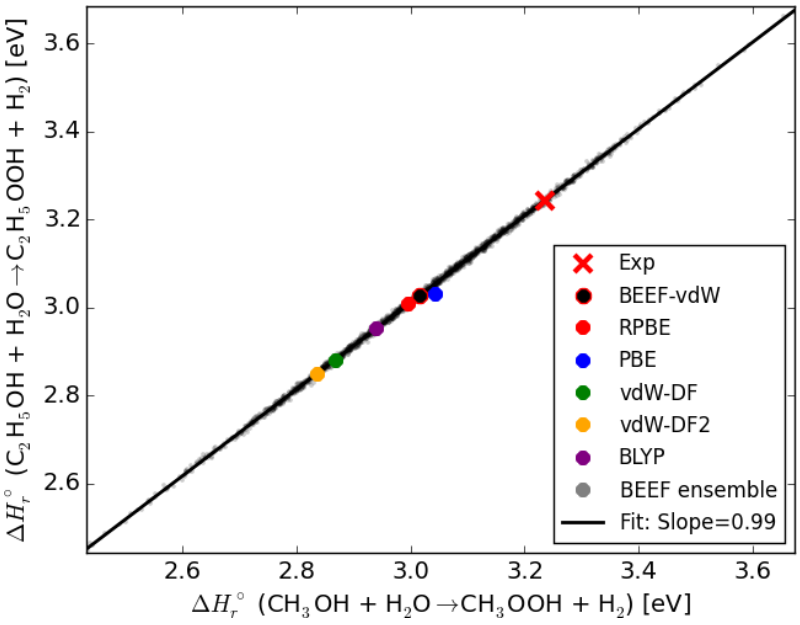


(a) Reaction (3) versus reaction (2)

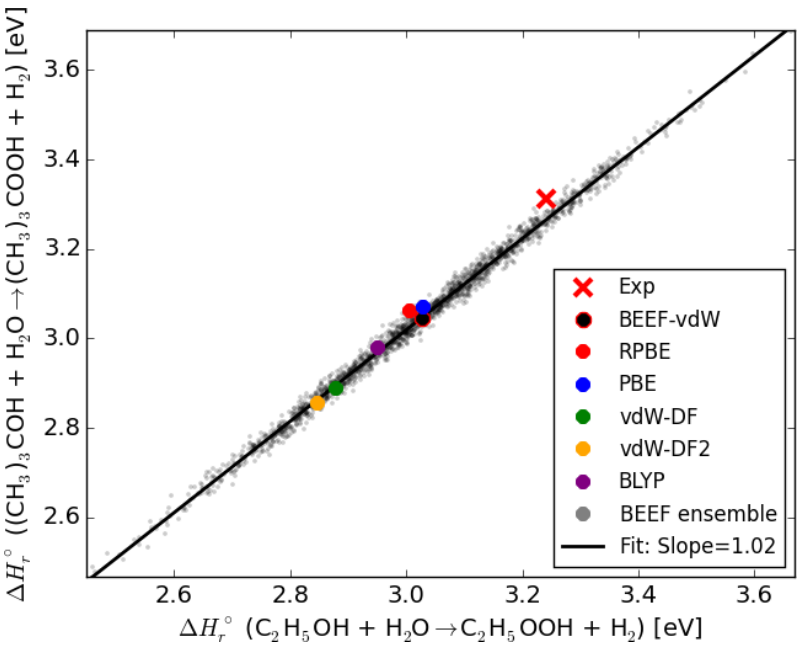


(b) Reaction (8) versus reaction (3)

Figure 5.1: Correlations in calculated enthalpies of reactions in the "Gas phase set" in Table 5.1. Semi-transparent gray points are 2000 BEEF ensemble functionals. A linear regression line is depicted and the slope obtained with linear regression noted in the legend.

### 5.6.1 $H_2O$ Error

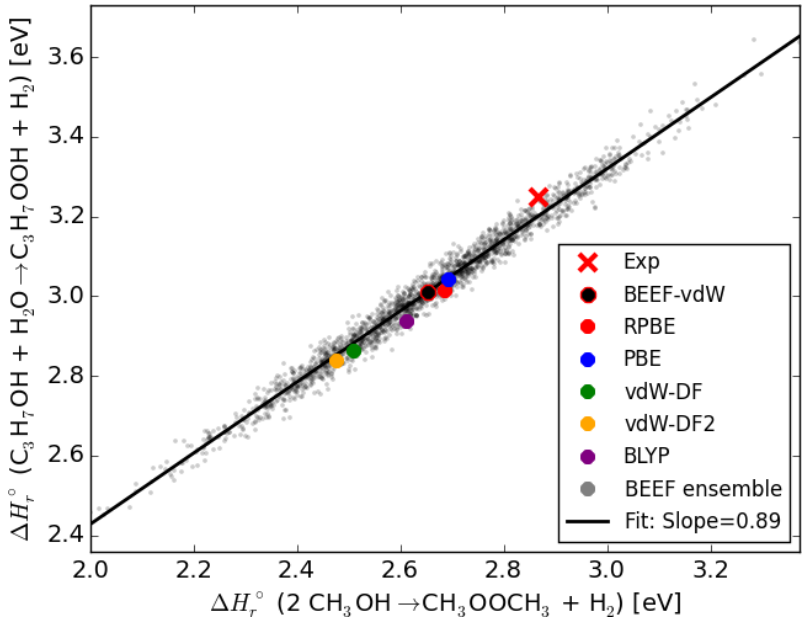


Figure 5.2: Correlation in calculated enthalpies of reaction for reaction (5) versus reaction (4) in the "Gas phase set" in Table 5.1. Semi-transparent gray points are 2000 BEEF ensemble functionals. A linear regression line with a slope of 0.89 is shown.

A correlation plot for reactions (4) and (5) can be seen in Figure 5.2. Reaction (4) does not contain $H_2O$. The linear regression line has a slope of 0.89. The slope is different from the slope of 1 expected, if the formation of an oxygen-oxygen bond was the only cause to functional–dependence. This is an additional indication that $H_2O$ can be a minor cause of functional–dependence.

Correlation line slopes are determined with linear regression for all pairwise combinations of reactions in the "Gas phase set". The difference from the expect slope of 1 is shown in Figure 5.3(a).

The correlation line slopes will for pair-wise correlations with reactions (1), (4) or (7) be different from 1.0. Correlation line slopes can be predicted with functional–dependence on $H_2O$ also taken into consideration. The predicted slopes, $a_{\text{predicted}}$, are given by

$$a_{\text{predicted}} = \frac{1 - \alpha n_{\text{H}_2\text{O},y}}{1 - \alpha n_{\text{H}_2\text{O},x}}. \tag{5.9}$$

The number of $H_2O$ molecules in the independent and dependent reaction is $n_{\text{H}_2\text{O},x}$ and $n_{\text{H}_2\text{O},y}$, respectively. $\alpha$ is fitted to reduce the differences between fitted and predicted slopes. $\alpha$ can be interpreted as the impact of $H_2O$ on the correlation

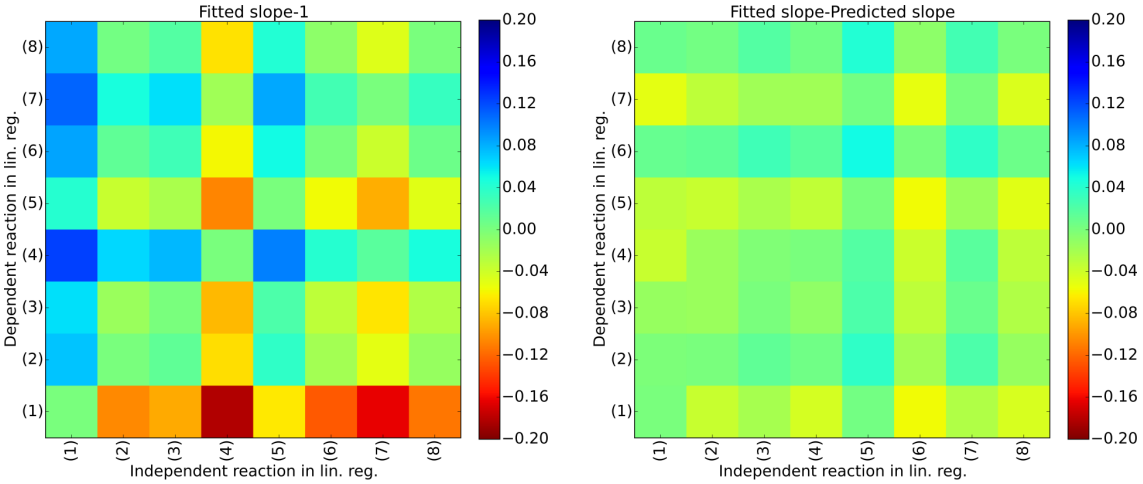


(a) Difference between fitted slopes and a slope of 1

(b) Difference between fitted slopes and slopes predicted with minor functional–dependence cause by $H_2O$

Figure 5.3: Differences between correlation line slopes from linear regression on BEEF ensemble functionals and expected/predicted correlation line slopes.

line slope relative to the impact of the oxygen-oxygen bond. $\alpha$=-0.08 has been used in Figure 5.3(b). The fitted and predicted slopes now agree significantly better.

## 5.7 Adsorbate Errors

Correlation line slopes are determined with linear regression for all pairwise combinations of reactions in Table 5.1. The slopes are shown in Figure 5.4.

With some exceptions due to $H_2O$ as discussed above, a correlation line slope close to 1 is found for pairwise correlations between reactions in the "Gas phase set" and "Adsorbate set". Reactions in the "Verification set", where an oxygen-oxygen bond is not formed, have significantly smaller functional–dependence than the other reactions. This causes the correlation line slopes obtained with linear regression to approach 0 or be large ($> 2$), when a reaction from the "Verification set" is used as either dependent or independent reaction, respectively.

The functional–dependence of reactions in the "Gas phase set", which contain a systematic error on the oxygen-oxygen bond, are seen to correlate with the functional–dependence of reactions in the "Adsorbate set". A correlation plot for reactions (2) and (*1) can be seen in Figure 5.5. The GGA+vdW functional points including the BEEF ensemble functionals fall on or near a line with a fitted slope of 1.01. The dominating cause to functional–dependence is identical in the two reactions. The systematic error on the oxygen-oxygen bond is thus present in

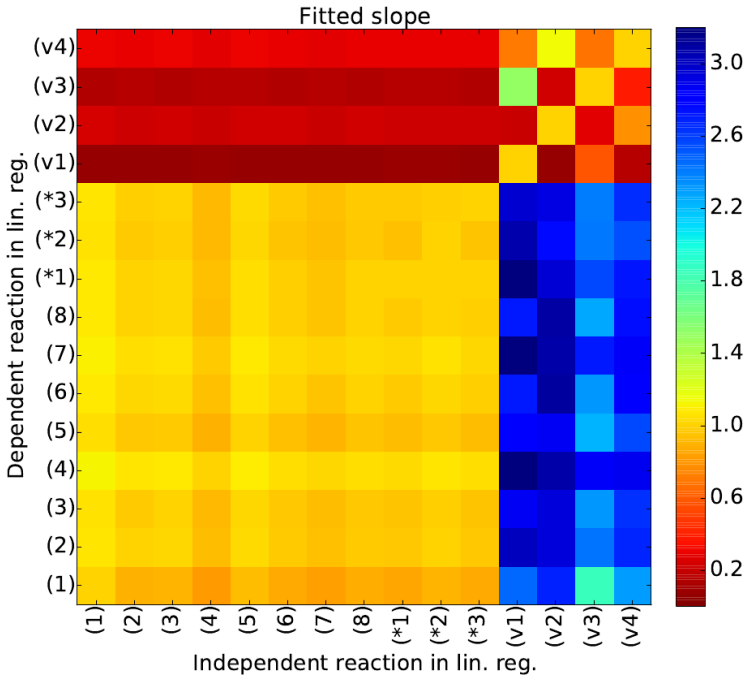


Figure 5.4: Correlation line slopes from linear regression on BEEF ensemble functionals for reactions in Table 5.1.

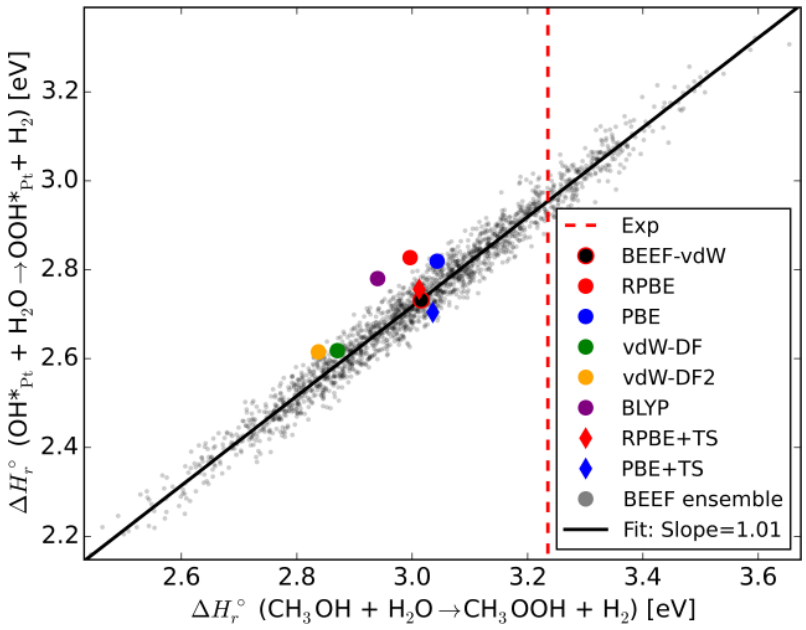


Figure 5.5: Correlations in calculated enthalpies of reaction (*1) versus reaction (2) in Table 5.1. A correlation line with a slope of 1.01 is found from linear regreesion on the BEEF ensemble functionals (semitransparent gray points). The experimental enthalpy of reaction (2) is marked by a red dashed line. Diamonds mark PBE and RPBE calculations with added vdW correlation using the Tkatchenko-Scheffler (TS) method.[200]

the OOH* adsorbate. Since a reliable high accuracy experimental energy is not available for reaction (*1), an experimental point cannot be plotted. It can not be concluded that an energy correction to the OOH* adsorbate will result in the correct enthalpy of reaction (*1), as other errors might be present.

The enthalpy of reaction is with the plain GGA functionals (PBE, RPBE, BLYP) overestimated relative to the GGA+vdW functional correlation line. Such relative overestimation is not seen for gas–phase reactions (Figures 5.1 and 5.2). Enthalpies have been recalculated with addition of van der Waals correlation to PBE and RPBE using the Tkatchenko-Scheffler (TS) method.[200,201] The inclusion of van der Waals interactions does not significantly change calculated enthalpies for gas–phase molecules. The adsorption enthalpies of OH* and OOH* are decreased by on average 0.15 eV and 0.25 eV, respectively, with inclusion of van der Waals interactions. The result is a net decrease of 0.1 eV in enthalpy of reactions in the "Adsorbate set". The RPBE+TS and PBE+TS points will with the van der Waals stabilization move to the GGA+vdW correlation line as seen in Figure 5.5.

The systematic error on the oxygen-oxygen bond in OOH* and the lack of van der Waals correlation in RPBE will both influence the scaling relation offset previously found to be 3.2 eV with the RPBE functional. Energy corrections to mitigate the systematic errors will make the energy of the scaling relation offset significantly less sensitive to the used exchange-correlation functional. The energy corrections can also improve the accuracy of individual calculations. The computational uncertainty will decrease from 0.19 eV to 0.05 eV, as seen in Table 5.3. The offset value of 3.2 eV obtained with the RPBE functional will, however, not be significantly changed. The systematic error on the oxygen-oxygen bond, which with RPBE is 0.22 eV, and the error caused by lack of van der Waals correlation in the RPBE functional will partly cancel. The scaling relation offset is changed by 0.1 eV to 3.3 eV by the energy corrections of systematic errors. Considering the $\pm$ 0.2 eV offset variations for different catalytic surfaces, the universal scaling relation is not a significant improved by the energy corrections. The RPBE scaling relation is thus found to be remarkably close to a scaling relation corrected for systematic errors.

## 5.8 Metal Oxide Catalysts

The functional–dependence is shown to correlation for gas–phase reactions and adsorbate reactions on metal surfaces. Functional–dependence is also examined for an adsorbate reaction on the (110) rutile $RuO_2$ surface. A correlation plot similar to Figure 5.5 is made for adsorbates on $RuO_2$ (Figure 5.6).

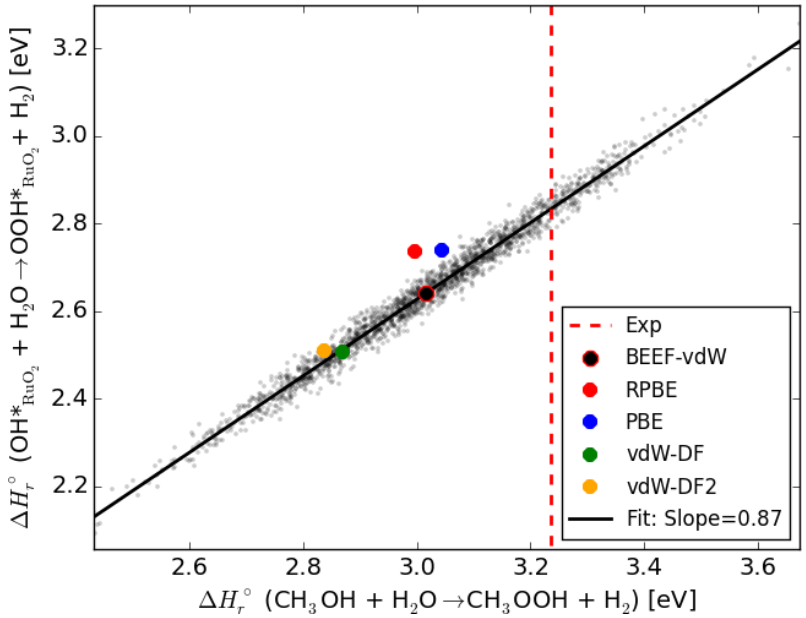


Figure 5.6: Correlations in calculated enthalpies of reaction for adsorbates on $RuO_2$ versus reaction (2) in Table 5.1. A correlation line with slope 0.87 is found with linear regreesion on the BEEF ensemble functionals (semitransparent gray points). The experimental enthalpy of reaction (2) is marked by a red dashed line.

A correlation line is present, but it does not have a slope of 1.0. The slope is with linear regression found to be 0.87. This slope could be due to a change in the oxygen-oxygen bond in OOH* adsorbed on $RuO_2$ in comparison to OOH* adsorbed on the metals and the peroxide bonds in gas–phase. If the oxygen-oxygen is changed, adsorption energies of OH* and OOH* might not follow an adsorption energy scaling relation with a slope of 1. It is thus possible that the scaling relation between OH* and OOH* adsorption energies is different on some oxide catalysts. Further studies are required to determine this.

## 5.9 Chapter Conclusion

An systematic error on peroxide bonds is identified for gas–phase reactions. The error is 0.22 eV with the RPBE functional. The systematic error was through correlations in functional–dependence found to be equally present in OOH* adsorbed on metal surfaces. An energy correction to mitigate the oxygen-oxygen bond will also change the scaling relation between OH* and OOH* adsorption energies. An error caused by lack of van der Waals correlation in the RPBE functional is, however, found to partly cancel the change in scaling relation. Considering the $\pm$ 0.2 eV variations in scaling relation offset for different catalysts, the scaling relation is not significantly changed by the energy corrections. The energy corrections

will decrease the calculational uncertainty in scaling relation offset from from 0.19 eV to 0.05 eV. It is possible that the error correlation approach can be used in future studies to identify metal oxides, which do not follow the OH*/OOH* scaling relation.

CHAPTER 6

# Error Ensemble for Neural Networks

## 6.1 Introduction

Although error cancellations and corrections to systematic errors in GGA functionals increase the applicability of DFT, there are still numerous cases where sufficient computational cost, accuracy, and system complexity cannot be obtained simultaneously. A plausible solution is to combine DFT with computationally less expensive methods, e.g., neural networks.[202–207] Neural networks require data for training. If the neural network is fitted to data obtained with a DFT calculator, a successfully trained neural network can be used as an emulator for the DFT calculator for atomic structures similar to those used in training.

Possible cases where a combination of DFT and neural network calculators could be advantageous include Nudged Elastic Band (NEB) calculations,[208,209] ionic optimization of large disordered structures, e.g. liquids, genetic algorithm calculations, e.g. to determine the structure and composition of large nanoparticles, and long molecular dynamics simulations.

## 6.2 Challenge

There are challenges associated with using neural networks as DFT emulators. Sufficient DFT data must be available to train the neural network. Training a neural network can be resource demanding. In addition, it can be very difficult to estimate the accuracy of a neural network for atomic structures not in the training data.

A committee approach can be used to estimate the accuracy of neural network calculations. Calculations are performed with a committee consisting several

individually trained neural networks. Discrepancies in the outputs are used to estimate the accuracy of the calculations.[202]

An alternative approach inspired by the BEEF functionals[64,65,210] is presented here. Rather than retraining a number of independent calculators, an ensemble of calculators can be made by perturbing the parameters of a single trained neural network. The ensemble can be used to qualitatively identify whether the neural network generates inaccurate results for a given atomic configuration. Forming an ensemble by perturbing the parameters in a single trained neural network will in many cases require significantly less computational resources than the committee approach.

The approach share some similarities with the "Bayes by Backprop" method,[211] in which an ensemble of neural networks is formed simultaneously during training of the neural network by assigning distributions rather than numerical values to parameters. The here presented approach has the advantage that it can be used as an add–on to a basic neural network when desired.

## 6.3 Atomistic Machine-learning Package

The Atomistic Machine-learning Package (AMP) is used to generate neural networks able to predict energy and forces for atomic structures.[202] Calculators trained with AMP can be used with the ASE[91] code. ASE makes it easy to switch between AMP calculators and calculators from a range of different DFT codes.

Neither the AMP code nor theoretical background on machine-learning and neural networks will be described in detail here. The interested reader is referred to Khorshidi and Peterson[202] and other literature. In the presented examples a Gaussian descriptor has been used to convert atomic positions into "fingerprint" vectors as described by Behler.[212] The Gaussian descriptor is a functional of pairwise atomic distances and three-atom angles within a cut-off radius of 6.5 Å. The fingerprints are used as input to a neural network.

A neural network consists of an input layer, a number of hidden layers, and an output layer. Relatively small neural networks with 5 hidden layers, each consisting of 5 nodes per element, have been used to exemplify the ensemble method. A neural network contains a number of parameters often referred to as weights and scalings. The parameters are optimized during a training process. After successful training, the neural network becomes an emulator for the calculator used to generate the training data. This has the distinct advantage that it allows seamless switching between the neural network calculator and the original calculator.

## 6.4 Ensemble Creation

There are certain parallels between the BEEF-vdW functional[64] and a neural network. They both have a fixed structure, i.e., the neural network architecture and the exchange-correlation functional form, in which a number of parameters are optimized to reproduce training data. An ensemble of functionals is made around the BEEF-vdW functional by perturbing the parameters. New functionals were included in the ensemble with a probability based on how well they were able to reproduce reference data.

A similar approach with perturbation of parameters is taken to create an ensemble of neural networks from a fully trained neural network. A training set of $N$ images is used to construct the ensemble. This training set can be identical to the training data used to optimize the first neural network calculator, as is the case in presented examples, but could be a subset of the training data to reduce computational cost. The goal is to form an ensemble of neural networks, where all neural networks perform well for atomic configurations similar to those in the training set. This ensures low variation in energy for atomic configurations, where the trained neural network calculator is expected to perform well. However, sufficiently large differences are required between the neural networks in the ensemble in order to ensure that they do not fail collectively when the main neural network does. In such a case the ensemble energy variation will be small even when the error is significant.

The potential energy error, $\epsilon_{0,i}$, is calculated with the AMP neural network calculator, $C_0(\boldsymbol{p})$, for each atomic configuration, $i$, in the training set. $\boldsymbol{p}$ is a list containing the parameters in the neural network, $p_0, p_1, ..., p_i, ..., p_M$. The probability of obtaining the error $\epsilon_{0,i}$ is determined for each individual error under the assumption that the errors are normally distributed with $\mu = 0$. The product of individual error probabilities is used as a baseline probability, $P_0$, in the formation of the ensemble,

$$P_0 = \prod_{i=1}^{N} \frac{1}{\sigma\sqrt{2\pi}} \mathrm{e}^{-\left(\epsilon_{0,i}^2/2\sigma^2\right)}. \tag{6.1}$$

Equation (6.1) can also be written as

$$P_0 = \frac{1}{\left(\sigma\sqrt{2\pi}\right)^N} \mathrm{e}^{-\left(\sum_{i=1}^{N} \epsilon_i^2/2\sigma^2\right)}. \tag{6.2}$$

At this point the standard deviation, $\sigma$, of the normal distribution is unknown. The $\sigma$ that maximizes the probability for a given set of errors is equal to the RMSE (See Appendix C) given by

$$\sigma = \sqrt{\sum_{i=1}^{N} \epsilon_{0,i}^2 / N}. \tag{6.3}$$

Inserting (6.3) into (6.2),

$$P_0 = \left( \frac{N}{2\pi \sum_{i=1}^{N} \epsilon_i^2} \right)^{N/2} \mathrm{e}^{-N/2}. \tag{6.4}$$

Once parameters are perturbed by $\boldsymbol{\gamma}$ as described in Section 6.4.1, the errors $\epsilon_{\boldsymbol{\gamma},i}$ are calculated with the new calculator $C(\boldsymbol{p} + \boldsymbol{\gamma})$. This calculator is included in the neural network error ensemble with probability

$$\frac{P_{\boldsymbol{\gamma}}}{P_0} = \left( \frac{\sum_{i=1}^{N} \epsilon_{0,i}^2}{\sum_{i=1}^{N} \epsilon_{\boldsymbol{\gamma},i}^2} \right)^{N/2}. \tag{6.5}$$

### 6.4.1 Parameter Perturbation

The magnitude of the proposed perturbations, $\boldsymbol{\gamma}$, to parameters is essential for obtaining an ensemble that can identify when the neural network is prone to errors. If too small perturbations are suggested, the ensemble will consist of calculators that are too similar to the main neural network calculator, $C_0(\boldsymbol{p})$, such that the variations in ensemble energies will not increase with the error. If too large perturbations are suggested, the probability of accepting a calculator with perturbed parameters into the ensemble becomes low and the computational cost advantage of forming the ensemble through perturbations of an already trained neural network will diminish.

An appropriate magnitude of perturbations is determined for each parameter by investigating how sensitive the acceptance probability is to changes in each parameter.

$$P_i = \frac{P[C(\boldsymbol{p} + \beta_i)]}{P[C_0(\boldsymbol{p})]} \tag{6.6}$$

The RHS is evaluated as in Equation (6.5). The perturbation $\beta_i$ is applied only to parameter $p_i$ while all other parameters are identical in the two calculators. $P_i$

is a target probability. The value of $\beta_i$ is optimized until the target probability is reached. This is done for all $M$ parameters to generate a list, $\boldsymbol{\beta}$, with appropriate perturbation magnitudes for each parameter. Once $\boldsymbol{\beta}$ is generated, parameter perturbations $\boldsymbol{\gamma}$ can be proposed. $\boldsymbol{\gamma}$ is a list of perturbations drawn from normal distributions with $\mu = 0$ and $\sigma^2 = \boldsymbol{\beta}^2$.

The target probability, $P_i$, depends on the desired average acceptance probability, $P_{\text{accp}}$, for a calculator with perturbations $\boldsymbol{\gamma}$. $P_{\text{accp}}$ is specified as a parameter when $\boldsymbol{\beta}$ is determined. The following crude assumptions are made: (1) All parameters influence the acceptance probability. (2) The influence is independent for each parameter. (3) The acceptance probability as a function of the magnitude of individual perturbations is normally distributed. In this case

$$P_i^M = P_{\text{accp}} \tag{6.7}$$

The crude approximations are rarely true, and the observed average acceptance probability when obtaining the error ensemble is rarely $P_{\text{accp}}$. However, $P_{\text{accp}}$ can be used as a parameter to tune the acceptance probability. For the error ensembles used in the examples below, the values of $P_{\text{accp}}$ are chosen such that 1 %–5 % of proposed perturbed calculators, $C(\boldsymbol{p} + \boldsymbol{\gamma})$, are accepted into the ensemble.

If a parameter $p_i$ has a low impact on the output energy it will also have little influence on the acceptance probability. It might not be possible to find a value of $\beta_i$ which can fulfill Equation (6.6). In such cases $\beta_i = 1000 \times p_i$. Instead of assuming the probability $P[C(\boldsymbol{p} + \beta_i)]$ to be symmetric around $\beta_i = 0$, two different values can be found for $\beta_i$; a negative $\beta_i^-$ and a positive $\beta_i^+$. $\gamma_i$ can then be drawn from $\mathcal{N}(0, (\beta_i{}^-)^2)$ for $\gamma_i < 0$ and $\mathcal{N}(0, (\beta_i{}^+)^2)$ for $\gamma_i > 0$.

## 6.5 Examples

Two examples are used to assess the applicability of the method. The standard deviation in the calculated energies for 50 ensemble calculators, $\sigma_E$, has been used to quantify the ensemble variation. Other statistical measures, e.g., the 90% percentile, could also be used.

### 6.5.1 $H_2$ Dissociation

$H_2$ dissociation is used to exemplify the method. The energy has been calculated for 25 images with H-H distances near the bond length and 25 images with H-H distances larger than 3 Å. A VASP calculator with the PBE functional and default parameter values are used. The 50 images are used to train an AMP neural

network. The neural network has 82 parameters. It is trained to a RMSE in energy of 0.8 meV and a 2.6 meV maximum error on any image. The potential energy is calculated for a range of H-H distances with both the neural network and the VASP calculator. The potential energy can be seen in Figure 6.1.

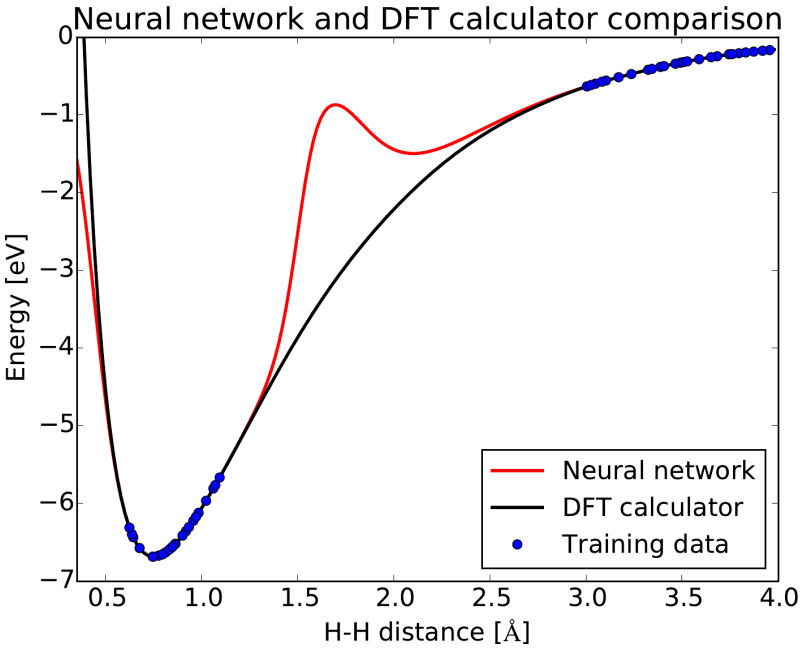


Figure 6.1: Potential energies at various H-H distances calculated with VASP and a neural network trained on images with distances marked by blue points.

The neural network is seen to perform well in the regions where the training data are present. It gives a correct energy in the region around the minimum and for distances above 3.0 Å. For regions with no nearby training points the neural network and DFT calculator give very different results. The neural network underestimates the repulsion at short distances and is different from the DFT calculator from 1.3 Å to 2.5 Å.

An ensemble of 50 neural networks is trained. 4 % of perturbed calculators were accepted into the ensemble. Training the independent neural network requires 1500 iterations, in which the errors on all training images are calculated. A similar number of iterations is required to construct the ensemble. The absolute error and $\sigma_E$ are shown in Figure 6.2. The absolute error and $\sigma_E$ correlate. Unlike the BEEF ensembles, the neural network error ensemble is bot a quantitative method for error estimation. $\sigma_E$ differs from zero when the error is zero. A baseline ensemble variation can be established from images known to be very similar to the training images.

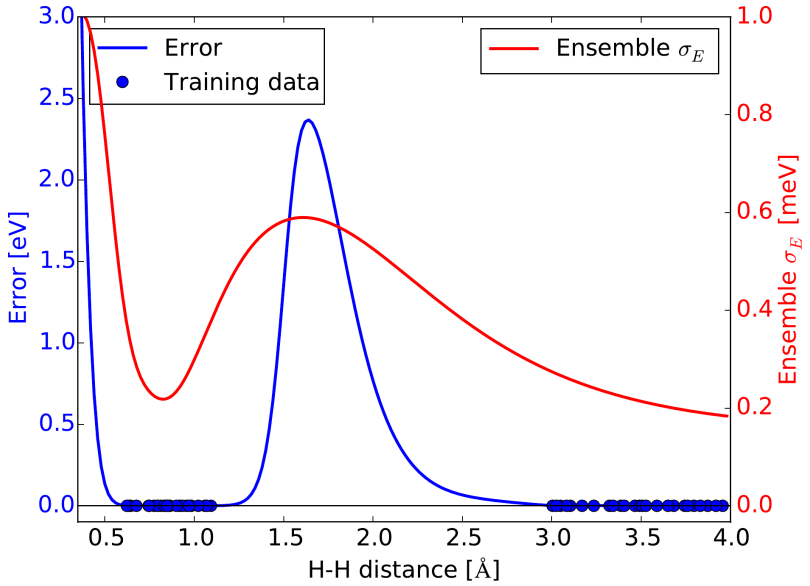


Figure 6.2: Absolute error (blue left axis) and $\sigma_E$ (red right axis) for $H_2$ dissociation. The training data is marked as blue points.

### 6.5.2 Pd Adatoms on a Pt Surface with Vacancies

A series of molecular dynamics (MD) simulations at 500 K for adatoms on a surface is performed. The simulations are performed at constant total energy with a time step of 5 fs. The momenta of atoms in the initial configuration are decided from a Boltzmann distribution. The EMT calculator, which is an integrated part of ASE,[91] is used as a computationally efficient method to obtain the training data and to determine the accuracy.

The initial structure is shown in Figure 6.3. The surface is a 6×6 Pt(111) surface with two vacancies in the top layer. The slab consists of two Pt layers and 4 Pd adatoms. The positions of all Pt atoms in the surface are fixed. 500 K is a relatively high temperature for such an unphysical system, where the Pd atoms are not able to transfer kinetic energy to the surrounding atoms. With this structure, a relative small neural network with 5 nodes for each element in 5 hidden layers can be used and easily trained. Using Pd adatoms rather than Pt adatoms has the advantage that the two types of atoms are considered separately in the inputs. A larger neural network is required to accommodate a good description of the Pt atoms in the surface and Pt adatoms simultaneously. Interesting trends in the selectivity of $CO_2$ reduction to HCOOH as a function of pH have been observed for Pd deposited on a Pt electrode.[213] Such a phenomenon are very computationally demanding to examine with DFT calculations but can possibly be addressed with a neural network. The procedure outline in the flowchart in Figure 6.4 is followed.

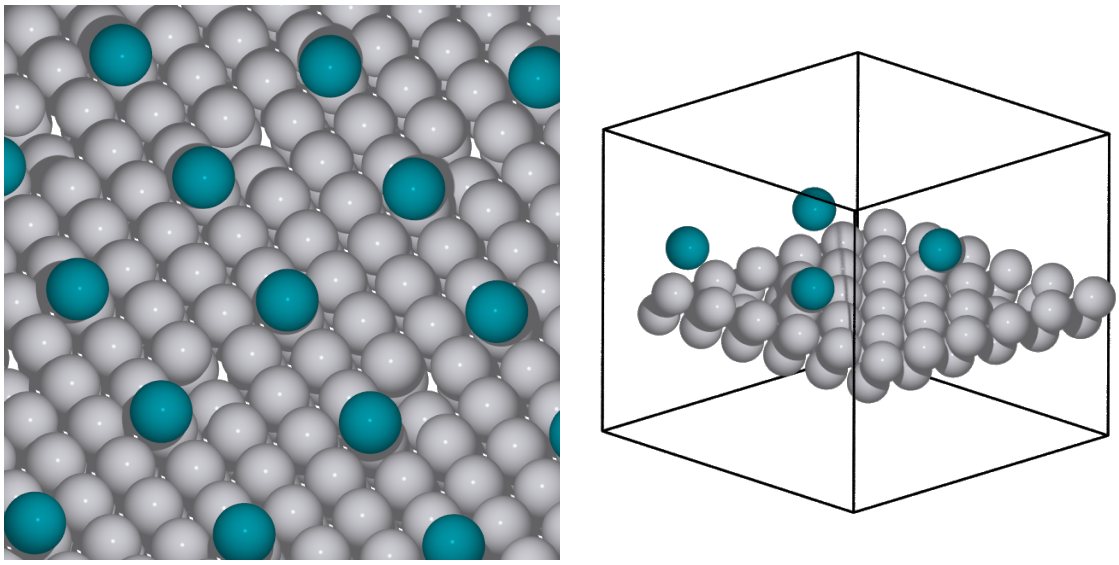

(a) Seen from top. (b) Unit cell seen from side.

Figure 6.3: The used initial atomic configuration for molecular dynamics of Pd adatom defusion on a Pt(111) surface with vacancies.

The initial atomic configuration is added to the MD trajectory file. A MD simulation starting with this atomic configuration has been run for 500 steps with the EMT calculator. The images and energies obtained with EMT are stored in a training set file and used to train the AMP neural network calculator and an error ensemble. Training the ensemble of 50 neural networks requires approximately as many iterations as training a single independent neural network.

The initial atomic configuration stored in the MD trajectory file is used as the starting point for a MD simulation with the AMP neural network calculator. This simulation runs for 200 steps. The potential energy is subsequently calculated on the 200 images with the error ensemble. The implementation could easily be changed such that the ensemble calculations are performed immediately after each MD step. The potential energy is also calculated for each image with the EMT calculator to determine the error.

The absolute error is at most 40 meV for the first 200 steps (Figure 6.5). $\sigma_E$ is below 0.50 meV. The 200 images are added to the MD trajectory file. We wish to continue the MD simulation. The MD simulation is resumed from the last image in the MD trajectory file.

Two Pd atoms come close to each other during the next ps of the MD simulation. Such a situation has not occurred in the training set. The neural network calculator is unable to predict a repulsion force between the two Pd atoms as they approach each other. As a result, the two nuclei will move very close to each other. This

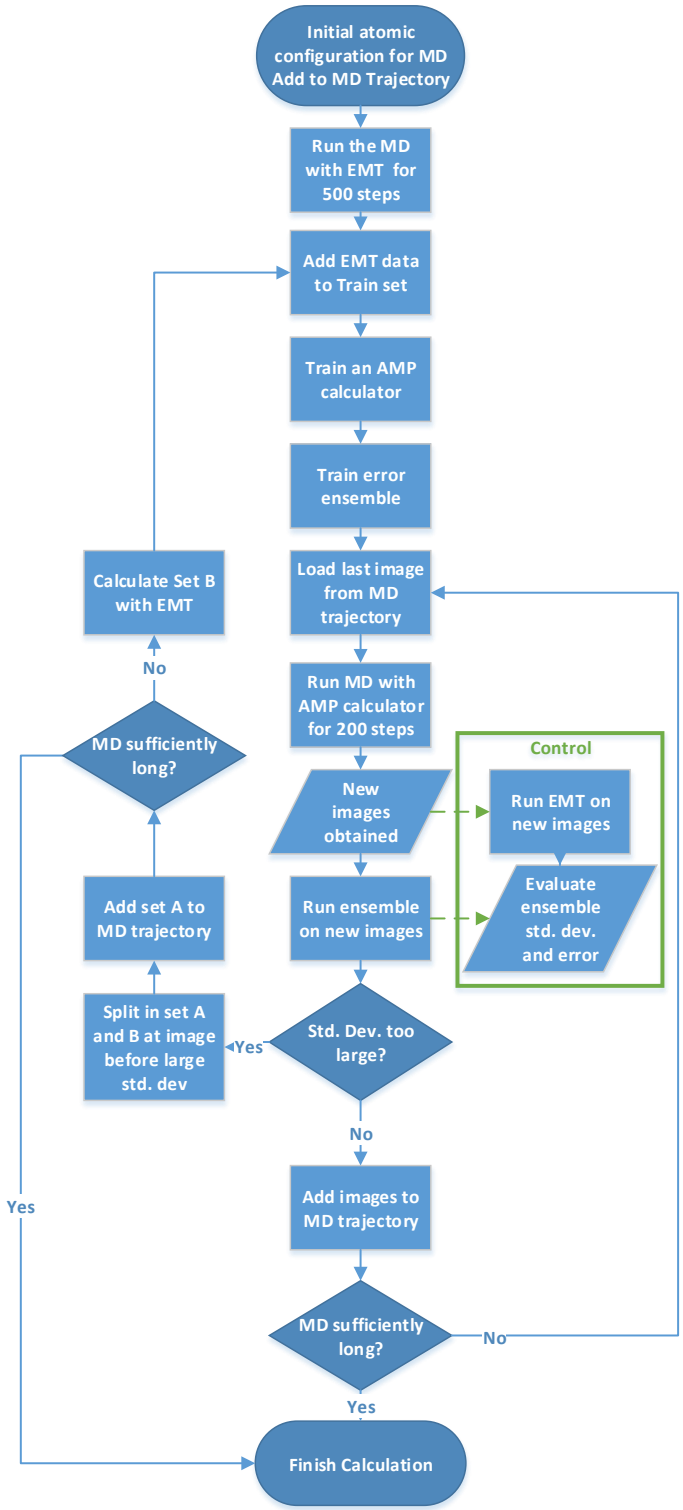


Figure 6.4: Flowchart of the molecular dynamics procedure.

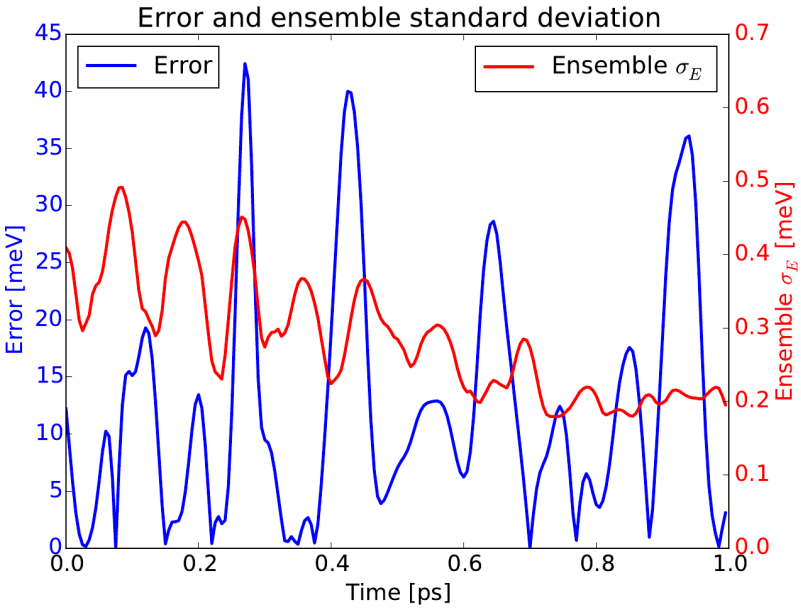


Figure 6.5: Absolute error versus EMT (left, blue) and ensemble standard deviation (right, red) for the MD simulation.

situation can be seen in Figure 6.6. This is followed by one of the Pd atoms leaving the surface.

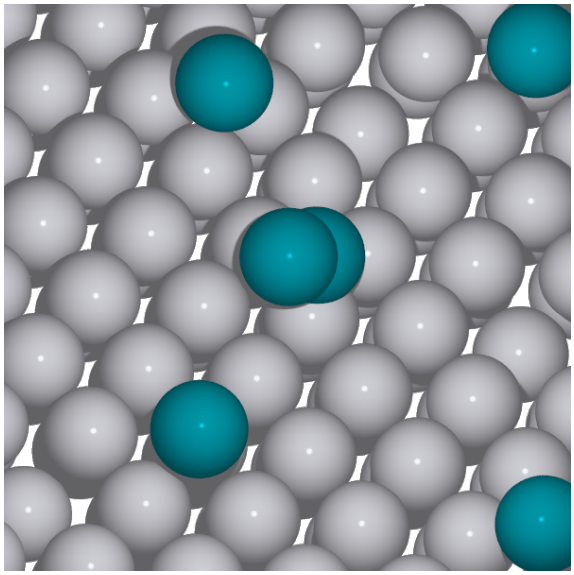

Figure 6.6: Atomic configuration obained in MD simulation with neural network. The nuclei of two Pd atoms (green) are seperated by a short distance.

The short distance between the two nuclei will obviously result in a large potential energy with the EMT calculator and a large error. The potential energy can be seen in Figure 6.7(a). The EMT calculator predicts a large (70 eV) increase in potential energy. The neural network predicts the potential energy to decrease as

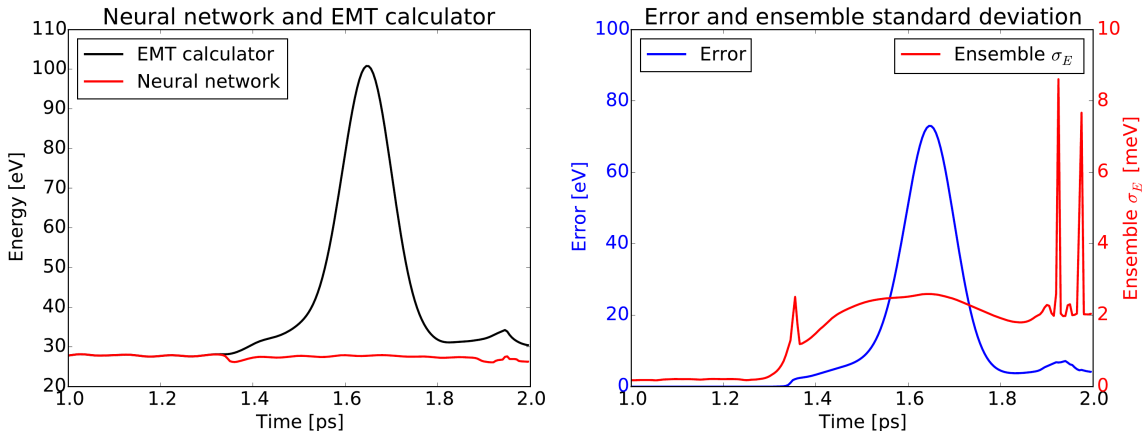


(a) Potential energy calculated with EMT and the neural network.

(b) Absolute error versus EMT (left, blue) and ensemble $\sigma_E$ (right, red)

Figure 6.7: MD simulation from 1.00 ps to 2.00 ps.

the two Pd atoms collide. The absolute error and $\sigma_E$ are shown in Figure 6.7(b). $\sigma_E$ increases at approximately the same time as a significant error begins to appear.

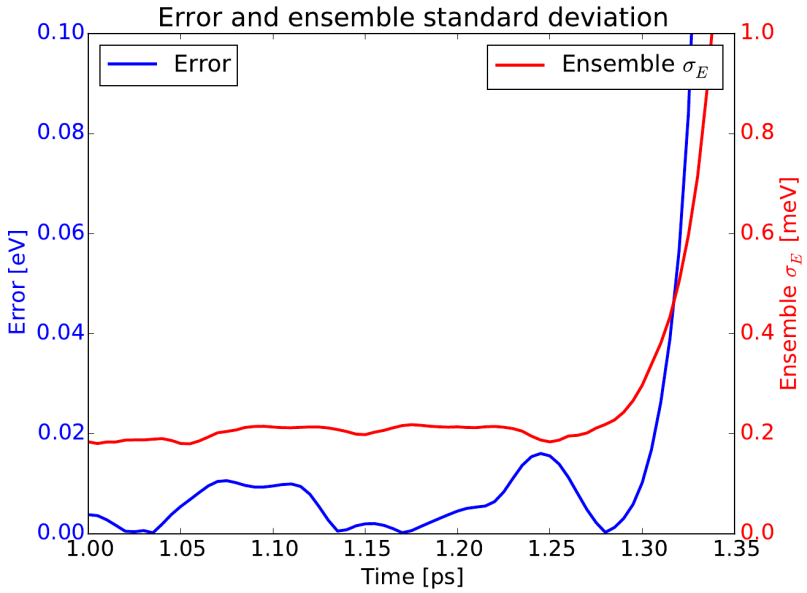


Figure 6.8: Absolute versus EMT (left, blue) and ensemble $\sigma_E$ (right, red) for the MD simulation from 1.00 ps to 1.35 ps.

Figure 6.8 shows the absolute error and $\sigma_E$ for the MD simulation from 1.00 ps to 1.35 ps. From 1.00 ps to 1.25 ps the error is lower than 20 meV and $\sigma_E$ remains approximately constant at 0.2 meV. After 1.28 ps the error begins to increase as the two Pd atoms should begin to repel each other. $\sigma_E$ increases with the error. $\sigma_E$ has a minimum at 1.25 ps. The images from 1.00 ps to 1.25 ps are stored in the MD

trajectory file. We would like to continue the MD simulation beyond 1.25 ps. The potential energy of the 150 images from 1.25 ps to 2.00 ps has been calculated with EMT. The images are added to the training set and the neural network calculator retrained. A new error ensemble is constructed for the retrained neural network and increased training set. The MD simulation is restarted from 1.25 ps. The

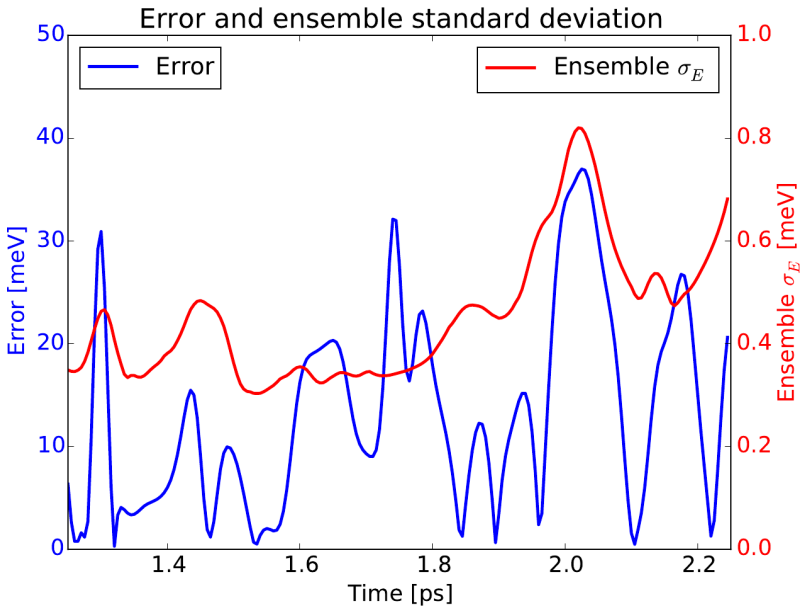


Figure 6.9: Absolute versus EMT (left, blue) and ensemble $\sigma_E$ (right, red) for the MD simulation from 1.25 ps to 2.25 ps with retrained neural network.

Pd atoms now repel each other at shorter distances. They continue to be single adatoms for the next 1.00 ps. The absolute error and $\sigma_E$ are shown in Figure 6.9. The errors are larger (up to 35 meV) with the retrained neural network. This is likely because the neural network has been retrained to a less homogeneous set of training images. Errors can be reduced by increasing the size of neural network. $\sigma_E$ fluctuates between 0.3 and 0.8 meV.

The procedure of retraining when a large standard deviation is observed can be continued until the MD simulation has run as long as desired. When applied in practice, the initial training set should contain atomic configurations that the user expects to be important. The error ensemble approach should not be viewed as a replacement for mindful selection of training data. Images with Pd dimers on the Pt surface could have been included in the initial training data to avoid the errors observed in this example.

## 6.6 Chapter Conclusion

Neural networks trained to DFT data can be used as DFT emulators. Neural networks are useful when many similar calculations are required. An error ensemble method has been developed. This method can determine when low accuracy should be expected for neural network calculations. The method has been demonstrated for $H_2$ dissociation and a molecular dynamics simulation of Pd adatoms on a Pt surface.

CHAPTER 7

# Conclusion and Outlook

## 7.1 Conclusion

The global energy supply is highly reliant on fossil fuels. Non-fossil energy sources are required to curb $CO_2$ emissions. In the transport sector it is particularly difficult to replace fossil fuels, as oil derived products have large gravimetric and volumetric energy densities. DFT can be used in research and development of new energy carriers based on sustainable electrical energy.

It can be difficult to balance computational cost and accuracy of DFT calculations for large atomic structures. The accuracy of the workhorse class of functionals for surface science, i.e., the GGA–level functionals, is hampered by systematic errors. Systematic errors have previously been found for metal-air battery discharge products and $CO_2$ reduction reactions. A systematic error is also found in the OOH* intermediate in the oxygen reduction and oxygen evolution reactions.

The BEEF-vdW functional and its ensemble have been used extensively. The BEEF ensemble formalism enables calculations with 2000 different ensemble functionals at low computational. Correlations in functional dependence have been used to identify dominating systematic errors.

The dominating error in metal-air battery discharge products is identified. The error is caused by the different oxidation state of metal elements in the metal oxides and the bulk crystalline metals used as reference states. By using metal chlorides as reference states the systematic errors in metal superoxides, peroxides, and monoxides are reduced. This allows, e.g., significantly better prediction of equilibrium potentials.

In gas–phase $CO_2$ reduction reactions the dominating systematic error is caused by C=O bonds. Energy corrections applied on a C=O bond basis give

significantly smaller residual errors than the previously applied energy corrections. Energy corrections can be extended to adsorbates through correlations in functional–dependence. The improvement in energy correction approach will change predicted limiting potentials, e.g., for $CO_2$ reduction to formic acid.

The adsorption energy difference between the OOH* and OH* intermediates in ORR and OER is 3.2 $\pm$ 0.2 eV on a range of catalytic surfaces. The constant adsorption energy difference dictates a theoretical minimum overpotential of 0.4 V for both ORR and OER. Systematic errors found in gas–phase peroxides are also present in OOH*. The change in the adsorption energy difference between OOH* and OH* caused by the systematic error is, however, almost canceled by inclusion of van der Waals interactions.

Neural networks can be used to emulate DFT calculations for large systems and long simulations. An ensemble method inspired by the BEEF ensemble is developed. The method can identify when a given neural network can no longer be used to emulate DFT calculations.

## 7.2 Outlook

The neural network ensemble method is in its current form computationally inefficient. The code has been written in an easily readable and adaptable from with python during development. The computational efficiency can be improved with fortran modules and by removing redundant operations. The ensemble construction can in theory be as computationally efficiently as training an independent neural network with AMP. Training an independent neural network is currently several orders of magnitude faster per iteration. Once the computational efficiency is improved the error ensemble method can be used for larger and more advanced systems.

The methodology used to identify dominant errors in $CO_2$ reduction reactions and the systematic error in gas–phase peroxides can be used for other reactions. Preliminary calculations show that systematic errors could also be present in large organic molecules and in particular aromatic molecules. Mitigating such errors could improve the accuracy of GGA–level DFT for heterogeneous catalysis of large organic molecules.

The correlation approach can also be used to reveal when the functional–dependencies for systems do not correlate as expected. This can be used to identify subtle fundamental differences, which could otherwise not be resolved with the accuracy of GGA–level DFT. An example is correlations in the OH*/OOH* adsorption energy differences on metal and metal oxide surfaces. If the correlation

is not 1:1 it could be because the oxygen-oxygen bond in OOH* is either weaker or stronger on the metal oxide than on the metal. This type of knowledge can be used in strategies to discover catalysts which break to OH*/OOH* scaling relation.

The main differences between the GGA–level functionals used in this thesis are the exchange enhancement factors and whether non–local van der Waals correlation is included. The exchange enhancement factors vary most when the reduced density gradient, $s$, is larger than 1, as can be seen in Figure 2.2. If an obtained electronic density at some point in space has both a significant density and $s > 1$, the energy contribution from this point in space will vary more with choice of exchange–correlation functional than energy contributions from other points in space. The converged electronic density could thus potentially be used to identify large functional–dependence for the energy of a given atomic structure. The specific part of an atomic structure causing the energy to be functional–dependent could be identified with a single calculation and without use of reference data. This method for identifying functional–dependence and thus also possible errors remains to be tested.

# Bibliography

[1] V. Smil, *Energy Transitions: History, Requirements, Prospects*. Praeger, 2010.

[2] International Energy Agency/OECD, "Key world energy statistics 2016," Paris, France, 2016.

[3] International Energy Agency/OECD, "Key World Energy STATISTICS 2015," Paris, France, 2015.

[4] World Economic Forum, "Energy Vision 2013, Energy Transistions: Past and Future," 2013.

[5] S. Shafiee and E. Topal, "When will fossil fuel reserves be diminished?," *Energy Policy*, vol. 37, no. 1, pp. 181 – 189, 2009.

[6] Q. Wang, X. Chen, A. N. Jha, and H. Rogers, "Natural gas from shale formation – The evolution, evidences and challenges of shale gas revolution in United States," *Renewable and Sustainable Energy Reviews*, vol. 30, pp. 1 – 28, 2014.

[7] S. Sorrell, R. Miller, R. Bentley, and J. Speirs, "Oil futures: A comparison of global supply forecasts," *Energy Policy*, vol. 38, no. 9, pp. 4990 – 5003, 2010. Special Section on Carbon Emissions and Carbon Management in Cities with Regular Papers.

[8] N. Lefèvre, "Measuring the energy security implications of fossil fuel resource concentration," *Energy Policy*, vol. 38, no. 4, pp. 1635 – 1644, 2010. Energy Security - Concepts and Indicators with regular papers.

[9] IPCC, *Climate Change 2013: The Physical Science Basis. Contribution of Working Group I to the Fifth Assessment Report of the Intergovernmental Panel on Climate*

*Change*. Cambridge, United Kingdom and New York, NY, USA: Cambridge University Press, 2013.

[10] GISTEMP Team, "2016: GISS Surface Temperature Analysis (GISTEMP). NASA Goddard Institute for Space Studies." Dataset accessed 2016-10-24 at http://data.giss.nasa.gov/gistemp/.

[11] J. Hansen, R. Ruedy, M. Sato, and K. Lo, "Global Surface Temperature Change," *Reviews of Geophysics*, vol. 48, no. 4, 2010.

[12] S. A. Marcott, J. D. Shakun, P. U. Clark, and A. C. Mix, "A Reconstruction of Regional and Global Temperature for the Past 11,300 Years," *Science*, vol. 339, no. 6124, pp. 1198–1201, 2013.

[13] J. Hansen, M. Sato, and R. Ruedy, "Perception of climate change," *Proceedings of the National Academy of Sciences*, vol. 109, no. 37, pp. E2415–E2423, 2012.

[14] Y. Kaya and K. Yokobori, *Environment, Energy and Economy; Strategies for Sustainability*. United Nations University Press, 1997.

[15] M. I. Hoffert, K. Caldeira, A. K. Jain, E. F. Haites, L. D. D. Harvey, S. D. Potter, M. E. Schlesinger, S. H. Schneider, R. G. Watts, T. M. L. Wigley, and D. J. Wuebbles, "Energy implications of future stabilization of atmospheric $CO_2$ content," *Nature*, vol. 395, pp. 881–884, Oct 1998.

[16] UN, *World population prospects: The 2015 revision*. New York: United Nations, 2015.

[17] European Environment Agency, "Correlation of energy consumption and GDP per person," 2014. Obtained 2016-10-24 at http://www.eea.europa.eu/data-and-maps/figures/correlation-of-per-capita-energy.

[18] IRENA, "Renewable Power Generation Costs in 2014," 2015.

[19] International Energy Agency/OECD, "Medium-Term Renewable Energy Market Report 2016," Paris, France, 2016.

[20] I. Ridjan, B. V. Mathiesen, D. Connolly, and N. Dui?, "The feasibility of synthetic fuels in renewable energy systems," *Energy*, vol. 57, pp. 76 – 84, 2013.

[21] N. S. Lewis and D. G. Nocera, "Powering the planet: Chemical challenges in solar energy utilization," *Proceedings of the National Academy of Sciences*, vol. 103, no. 43, pp. 15729–15735, 2006.

[22] H. Wenzel, "Breaking the biomass bottleneck of the fossil free society," tech. rep., Concito, 2010.

[23] M. A. Rahman, X. Wang, and C. Wen, "High Energy Density Metal-Air Batteries: A Review," *Journal of The Electrochemical Society*, vol. 160, no. 10, pp. A1759–A1771, 2013.

[24] G. Girishkumar, B. McCloskey, A. C. Luntz, S. Swanson, and W. Wilcke, "Lithium-Air Battery: Promise and Challenges," *The Journal of Physical Chemistry Letters*, vol. 1, no. 14, pp. 2193–2203, 2010.

[25] M. D. Radin and D. J. Siegel, "Non-aqueous Metal-Oxygen Batteries: Past, Present, and Future," in *Rechargeable Batteries: Materials, Technologies and New Trends* (Z. Zhang and S. Zhang, eds.), Green Energy and Technology, Springer International Publishing, 2015.

[26] M. Armand and J.-M. Tarascon, "Building better batteries," *Nature*, vol. 451, pp. 652–7, Feb. 2008.

[27] D. T. Whipple and P. J. A. Kenis, "Prospects of $CO_2$ Utilization via Direct Heterogeneous Electrochemical Reduction," *The Journal of Physical Chemistry Letters*, vol. 1, no. 24, pp. 3451–3458, 2010.

[28] E. V. Kondratenko, G. Mul, J. Baltrusaitis, G. O. Larrazabal, and J. Perez-Ramirez, "Status and perspectives of $CO_2$ conversion into fuels and chemicals by catalytic, photocatalytic and electrocatalytic processes," *Energy Environ. Sci.*, vol. 6, pp. 3112–3135, 2013.

[29] G. A. Olah, "Beyond Oil and Gas: The Methanol Economy," *Angewandte Chemie International Edition*, vol. 44, no. 18, pp. 2636–2639, 2005.

[30] J. Qiao, Y. Liu, F. Hong, and J. Zhang, "A review of catalysts for the electroreduction of carbon dioxide to produce low-carbon fuels," *Chem. Soc. Rev.*, vol. 43, pp. 631–675, 2014.

[31] L. Schlapbach and A. Zuttel, "Hydrogen-storage materials for mobile applications," *Nature*, vol. 414, pp. 353–358, Nov 2001.

[32] G. Cipriani, V. D. Dio, F. Genduso, D. L. Cascia, R. Liga, R. Miceli, and G. R. Galluzzo, "Perspective on hydrogen energy carrier and its automotive applications," *International Journal of Hydrogen Energy*, vol. 39, no. 16, pp. 8482 – 8494, 2014.

[33] T. Yoshida and K. Kojima, "Toyota MIRAI Fuel Cell Vehicle and Progress Toward a Future Hydrogen Society," *The Electrochemical Society Interface*, vol. 24, no. 2, pp. 45–49, 2015.

[34] T. Moriya, "(Invited Plenary) Honda Fuelcell Vehicle Development and Toward the Hydrogen Society," *Meeting Abstracts*, vol. MA2016-02, no. 38, p. 2409, 2016.

[35] Y. Nagai, T. Ikeda, F. Yamanashi, Y. Sone, M. Hirose, T. Abe, A. Okamoto, K. Matsuda, S. Kaneko, and H. Ito, "Activities of FCV/Infrastructure Demonstration Program in Japan," *ECS Transactions*, vol. 71, no. 1, pp. 65–84, 2016.

[36] S. Satyapal, J. Petrovic, C. Read, G. Thomas, and G. Ordaz, "The U.S. Department of Energy's National Hydrogen Storage Project: Progress towards meeting hydrogen-powered vehicle requirements," *Catalysis Today*, vol. 120, no. 3?4, pp. 246 – 256, 2007.

[37] J. M. Pasini, C. Corgnale, B. A. van Hassel, T. Motyka, S. Kumar, and K. L. Simmons, "Metal hydride material requirements for automotive hydrogen storage systems," *International Journal of Hydrogen Energy*, vol. 38, no. 23, pp. 9755 – 9765, 2013.

[38] U.S. DRIVE, "Target Explanation Document:Onboard Hydrogen Storage for Light-Duty Fuel Cell Vehicles," tech. rep., U.S. Department of Energy, 2015.

[39] R. Ahluwalia, T. Hua, and J. Peng, "On-board and Off-board performance of hydrogen storage options for light-duty vehicles," *International Journal of Hydrogen Energy*, vol. 37, no. 3, pp. 2891 – 2910, 2012.

[40] P. C. K. Vesborg, B. Seger, and I. Chorkendorff, "Recent Development in Hydrogen Evolution Reaction Catalysts and Their Practical Implementation," *The Journal of Physical Chemistry Letters*, vol. 6, no. 6, pp. 951–957, 2015.

[41] S. G. Chalk and J. F. Miller, "Key challenges and recent progress in batteries, fuel cells, and hydrogen storage for clean energy systems," *Journal of Power Sources*, vol. 159, no. 1, pp. 73 – 80, 2006.

[42] H. A. Gasteiger, S. S. Kocha, B. Sompalli, and F. T. Wagner, "Activity benchmarks and requirements for Pt, Pt-alloy, and non-Pt oxygen reduction catalysts for PEMFCs," *Applied Catalysis B: Environmental*, vol. 56, no. 1?2, pp. 9 – 35, 2005.

[43] J. Greeley, I. E. L. Stephens, A. S. Bondarenko, T. P. Johansson, H. A. Hansen, T. F. Jaramillo, J. Rossmeisl, I. Chorkendorff, and J. K. Nørskov, "Alloys of platinum and early transition metals as oxygen reduction electrocatalysts," *Nat Chem*, vol. 1, pp. 552–556, Oct 2009.

[44] P. C. K. Vesborg and T. F. Jaramillo, "Addressing the terawatt challenge: scalability in the supply of chemical elements for renewable energy," *RSC Adv.*, vol. 2, pp. 7933–7947, 2012.

[45] I. E. L. Stephens, A. S. Bondarenko, U. Grønbjerg, J. Rossmeisl, and I. Chorkendorff, "Understanding the electrocatalysis of oxygen reduction on platinum and its alloys," *Energy Environ. Sci.*, vol. 5, pp. 6744–6762, 2012.

[46] J. K. Nørskov, T. Bligaard, J. Rossmeisl, and C. H. Christensen, "Towards the computational design of solid catalysts," *Nat. Chem.*, vol. 1, pp. 37–46, Apr 2009.

[47] J. Greeley and N. M. Markovic, "The road from animal electricity to green energy: combining experiment and theory in electrocatalysis," *Energy Environ. Sci.*, vol. 5, pp. 9246–9256, 2012.

[48] J. Greeley, "Theoretical Heterogeneous Catalysis: Scaling Relationships and Computational Catalyst Design," *Annual Review of Chemical and Biomolecular Engineering*, vol. 7, no. 1, pp. 605–635, 2016.

[49] M. K. Sabbe, M.-F. Reyniers, and K. Reuter, "First-principles kinetic modeling in heterogeneous catalysis: an industrial perspective on best-practice, gaps and needs," *Catal. Sci. Technol.*, vol. 2, pp. 2010–2024, 2012.

[50] K. Kalz, R. Kraehnert, M. Dvoyashkin, R. Dittmeyer, R. Gläser, U. Krewer, K. Reuter, and J.-D. Grunwaldt, "Future Challenges in Heterogeneous Catalysis: Understanding Catalysts under Dynamic Reaction Conditions," *ChemCatChem*, pp. n/a–n/a, 2016.

[51] J. Greeley, J. K. Nørskov, and M. Mavrikakis, "ELECTRONIC STRUCTURE AND CATALYSIS ON METAL SURFACES," *Annual Review of Physical Chemistry*, vol. 53, no. 1, pp. 319–348, 2002.

[52] K. Reuter, "Ab Initio Thermodynamics and First-Principles Microkinetics for Surface Catalysis," *Catalysis Letters*, vol. 146, no. 3, pp. 541–563, 2016.

[53] R. Peverati and D. G. Truhlar, "Exchange–Correlation Functional with Good Accuracy for Both Structural and Energetic Properties while Depending Only on the Density and Its Gradient," *Journal of Chemical Theory and Computation*, vol. 8, no. 7, pp. 2310–2319, 2012.

[54] J. Kohanoff, *Electronic Structure Calculations for Solids and Molecules: Theory and Computational Methods*. Condensed matter physics, nanoscience and mesoscopic physics, Cambridge University Press, 2006.

[55] K. Burke, *The ABC of DFT*. Department of Chemistry, Rutgers University, 2003.

[56] M. Born and R. Oppenheimer, "Zur Quantentheorie der Molekeln," *Annalen der Physik*, vol. 389, no. 20, pp. 457–484, 1927.

[57] U.S. Nautical Almanac Office, *Astronomical Almanac for the Year 2013 and Its Companion, the Astronomical Almanac Online*. "Astronomical Almanac For the Year", U.S. Government Printing Office, 2012.

[58] P. Hohenberg and W. Kohn, "Inhomogeneous Electron Gas," *Phys. Rev.*, vol. 136, no. 3B, p. B864, 1964.

[59] W. Kohn and L. J. Sham, "Self-consistent equations including exchange and correlation effects," *Phys. Rev.*, vol. 140, no. 4A, p. A1133, 1965.

[60] J. P. Perdew and K. Schmidt, "Jacob's ladder of density functional approximations for the exchange-correlation energy," *AIP Conference Proceedings*, vol. 577, no. 1, pp. 1–20, 2001.

[61] J. P. Perdew, "Climbing the ladder of density functional approximations," *MRS Bulletin*, vol. 38, pp. 743–750, 9 2013.

[62] D. M. Ceperley and B. J. Alder, "Ground State of the Electron Gas by a Stochastic Method," *Phys. Rev. Lett.*, vol. 45, pp. 566–569, Aug 1980.

[63] P. Ziesche, S. Kurth, and J. P. Perdew, "Density functionals from LDA to GGA," *Computational Materials Science*, vol. 11, no. 2, pp. 122 – 127, 1998.

[64] J. Wellendorff, K. T. Lundgaard, A. Møgelhøj, V. Petzold, D. D. Landis, J. K. Nørskov, T. Bligaard, and K. W. Jacobsen, "Density functionals for

surface science: Exchange-correlation model development with Bayesian error estimation," *Phys. Rev. B*, vol. 85, p. 235149, Jun 2012.

[65] J. Wellendorff, T. L. Silbaugh, D. G. Pintos, J. K. Nørskov, T. Bligaard, F. Studt, and C. T. Campbell, "A benchmark database for adsorption bond energies to transition metal surfaces and comparison to selected DFT functionals," *Surf. Sci.*, vol. 640, no. 0, pp. 36–44, 2015.

[66] F. Favot, A. Dal Corso, and A. Baldereschi, "CO adsorbed on Cu(001): A comparison between local density approximation and Perdew, Burke, and Ernezerhof generalized gradient approximation," *The Journal of Chemical Physics*, vol. 114, no. 1, pp. 483–488, 2001.

[67] A. D. Becke, "Perspective: Fifty years of density-functional theory in chemical physics," *The Journal of Chemical Physics*, vol. 140, no. 18, p. 301, 2014.

[68] A. D. Becke, "Density-functional exchange-energy approximation with correct asymptotic behavior," *Phys. Rev. A*, vol. 38, pp. 3098–3100, Sep 1988.

[69] C. Lee, W. Yang, and R. G. Parr, "Development of the Colle-Salvetti correlation-energy formula into a functional of the electron density," *Phys. Rev. B*, vol. 37, pp. 785–789, Jan 1988.

[70] J. P. Perdew, K. Burke, and M. Ernzerhof, "Generalized Gradient Approximation Made Simple," *Phys. Rev. Lett.*, vol. 77, pp. 3865–3868, Oct 1996.

[71] Y. Zhang and W. Yang, "Comment on "Generalized Gradient Approximation Made Simple"," *Phys. Rev. Lett.*, vol. 80, pp. 890–890, Jan 1998.

[72] B. Hammer, L. B. Hansen, and J. K. Nørskov, "Improved adsorption energetics within density-functional theory using revised Perdew-Burke-Ernzerhof functionals," *Phys. Rev. B*, vol. 59, p. 7413, 1999.

[73] M. Dion, H. Rydberg, E. Schröder, D. C. Langreth, and B. I. Lundqvist, "Van der Waals Density Functional for General Geometries," *Phys. Rev. Lett.*, vol. 92, p. 246401, Jun 2004.

[74] K. Berland, V. R. Cooper, K. Lee, E. Schröder, T. Thonhauser, P. Hyldgaard, and B. I. Lundqvist, "van der Waals forces in density functional theory: a review of the vdW-DF method," *Reports on Progress in Physics*, vol. 78, no. 6, p. 066501, 2015.

[75] K. Lee, E. D. Murray, L. Kong, B. I. Lundqvist, and D. C. Langreth, "Higher-accuracy van der Waals density functional," *Phys. Rev. B*, vol. 82, p. 081101, Aug 2010.

[76] J. P. Perdew and W. Yue, "Accurate and simple density functional for the electronic exchange energy: Generalized gradient approximation," *Phys. Rev. B*, vol. 33, pp. 8800–8802, Jun 1986.

[77] E. D. Murray, K. Lee, and D. C. Langreth, "Investigation of Exchange Energy Density Functional Accuracy for Interacting Molecules," *Journal of Chemical Theory and Computation*, vol. 5, no. 10, pp. 2754–2762, 2009.

[78] J. Hubbard, "Electron Correlations in Narrow Energy Bands. IV. The Atomic Representation," *Proceedings of the Royal Society of London. Series A. Mathematical and Physical Sciences*, vol. 285, no. 1403, pp. 542–560, 1965.

[79] V. I. Anisimov, F. Aryasetiawan, and A. I. Lichtenstein, "First-principles calculations of the electronic structure and spectra of strongly correlated systems: the LDA+U method," *Journal of Physics: Condensed Matter*, vol. 9, no. 4, p. 767, 1997.

[80] B. Himmetoglu, A. Floris, S. de Gironcoli, and M. Cococcioni, "Hubbard-corrected DFT energy functionals: The LDA+U description of correlated systems," *International Journal of Quantum Chemistry*, vol. 114, no. 1, pp. 14–49, 2014.

[81] J. P. Perdew, A. Ruzsinszky, J. Tao, V. N. Staroverov, G. E. Scuseria, and G. I. Csonka, "Prescription for the design and selection of density functional approximations: More constraint satisfaction with fewer fits," *The Journal of Chemical Physics*, vol. 123, no. 6, 2005.

[82] J. Wellendorff, K. T. Lundgaard, K. W. Jacobsen, and T. Bligaard, "mBEEF: An accurate semi-local Bayesian error estimation density functional," *The Journal of Chemical Physics*, vol. 140, no. 14, 2014.

[83] C. Adamo and V. Barone, "Toward reliable density functional methods without adjustable parameters: The PBE0 model," *The Journal of Chemical Physics*, vol. 110, no. 13, pp. 6158–6170, 1999.

[84] J. Heyd, G. E. Scuseria, and M. Ernzerhof, "Hybrid functionals based on a screened Coulomb potential," *The Journal of Chemical Physics*, vol. 118, no. 18, pp. 8207–8215, 2003.

[85] A. V. Krukau, O. A. Vydrov, A. F. Izmaylov, and G. E. Scuseria, "Influence of the exchange screening parameter on the performance of screened hybrid functionals," *The Journal of Chemical Physics*, vol. 125, no. 22, p. 224106, 2006.

[86] G. Kresse and J. Furthmüller, "Efficient iterative schemes for *ab initio* total-energy calculations using a plane-wave basis set," *Phys. Rev. B*, vol. 54, pp. 11169–11186, Oct 1996.

[87] P. E. Blöchl, "Projector augmented-wave method," *Phys. Rev. B*, vol. 50, pp. 17953–17979, Dec 1994.

[88] G. Kresse and D. Joubert, "From ultrasoft pseudopotentials to the projector augmented-wave method," *Phys. Rev. B*, vol. 59, pp. 1758–1775, Jan 1999.

[89] J. c. v. Klimeš, D. R. Bowler, and A. Michaelides, "Van der Waals density functionals applied to solids," *Phys. Rev. B*, vol. 83, p. 195131, May 2011.

[90] G. Kresse, M. Marsman, and J. Furthmüller, *VASP the GUIDE.* Vienna, 2016.

[91] S. R. Bahn and K. W. Jacobsen, "An object-oriented scripting interface to a legacy electronic structure code," *Comput. Sci. Eng.*, vol. 4, no. 3, p. 56, 2002.

[92] R. O. Jones and O. Gunnarsson, "The Density Functional Formalism, Its Applications and Prospects," *Rev. Mod. Phys.*, vol. 61, pp. 689–746, Jul 1989.

[93] J. Rossmeisl, A. Logadottir, and J. Nørskov, "Electrolysis of Water on (Oxidized) Metal Surfaces," *Chem. Phys.*, vol. 319, no. 1–3, pp. 178–184, 2005.

[94] J. I. Martínez, H. A. Hansen, J. Rossmeisl, and J. K. Nørskov, "Formation Energies of Rutile Metal Dioxides using Density Functional Theory," *Phys. Rev. B*, vol. 79, p. 045120, Jan 2009.

[95] P. Linstrom and W. Mallard, eds., *NIST Chemistry WebBook, NIST Standard Reference Database Number 69*. National Institute of Standards and Technology, Gaithersburg MD, 20899, 2016.

[96] J. S. Hummelshøj, J. Blomqvist, S. Datta, T. Vegge, J. Rossmeisl, K. S. Thygesen, A. C. Luntz, K. W. Jacobsen, and J. K. Nørskov, "Communications: Elementary oxygen electrode reactions in the aprotic Li-air battery," *The Journal of Chemical Physics*, vol. 132, no. 7, p. 071101, 2010.

[97] J. S. Hummelshøj, A. C. Luntz, and J. K. Nørskov, "Theoretical evidence for low kinetic overpotentials in Li-$O_2$ electrochemistry," *The Journal of Chemical Physics*, vol. 138, no. 3, p. 034703, 2013.

[98] L. D. Chen, J. K. Nørskov, and A. C. Luntz, "Al-Air Batteries: Fundamental Thermodynamic Limitations from First-Principles Theory," *The Journal of Physical Chemistry Letters*, vol. 6, no. 1, pp. 175–179, 2015.

[99] J. G. Smith, J. Naruse, H. Hiramatsu, and D. J. Siegel, "Theoretical Limiting Potentials in $Mg/O_2$ Batteries," *Chemistry of Materials*, vol. 28, no. 5, pp. 1390–1401, 2016.

[100] L. D. Chen, J. K. Nørskov, and A. C. Luntz, "Theoretical Limits to the Anode Potential in Aqueous Mg-Air Batteries," *The Journal of Physical Chemistry C*, vol. 119, no. 34, pp. 19660–19667, 2015.

[101] B. Lee, J. Kim, G. Yoon, H.-D. Lim, I.-S. Choi, and K. Kang, "Theoretical Evidence for Low Charging Overpotentials of Superoxide Discharge Products in Metal-Oxygen Batteries," *Chemistry of Materials*, vol. 27, no. 24, pp. 8406–8413, 2015.

[102] Y. Mo, S. P. Ong, and G. Ceder, "First-principles study of the oxygen evolution reaction of lithium peroxide in the lithium-air battery," *Phys. Rev. B*, vol. 84, p. 205446, Nov 2011.

[103] Y. Sun and H. Zhou, "Facilitating the Oxygen Evolution Reaction of Lithium Peroxide via Molecular Adsorption," *The Journal of Physical Chemistry C*, vol. 120, no. 19, pp. 10237–10243, 2016.

[104] S. Kang, Y. Mo, S. P. Ong, and G. Ceder, "Nanoscale Stabilization of Sodium Oxides: Implications for $Na\text{-}O_2$ Batteries," *Nano Lett.*, vol. 14, no. 2, pp. 1016–1020, 2014.

[105] B. D. McCloskey, A. Speidel, R. Scheffler, D. C. Miller, V. Viswanathan, J. S. Hummelshøj, J. K. Nørskov, and A. C. Luntz, "Twin Problems of Interfacial Carbonate Formation in Nonaqueous $Li\text{-}O_2$ Batteries," *The Journal of Physical Chemistry Letters*, vol. 3, no. 8, pp. 997–1001, 2012.

[106] J. M. Garcia-Lastra, J. S. G. Myrdal, R. Christensen, K. S. Thygesen, and T. Vegge, "DFT+U Study of Polaronic Conduction in $Li_2O_2$ and $Li_2CO_3$: Implications for Li-Air Batteries," *The Journal of Physical Chemistry C*, vol. 117, no. 11, pp. 5568–5577, 2013.

[107] M. Radin, J. Rodriguez, and D. Siegel, "Lithium Peroxide Surfaces and Point Defects: Relevance for Li-air Batteries," in *Proceedings of the Battery Congress* (N. Uddin, T. Tang, J. Thompson, and R. Uddin, eds.), vol. 60, pp. 1–6, 2011. ISBN: 978-1-61782-843-0.

[108] Y. S. Mekonnen, J. M. Garcia-Lastra, J. S. Hummelshøj, C. Jin, and T. Vegge, "Role of $Li_2O_2$@$Li_2CO_3$ Interfaces on Charge Transport in Nonaqueous Li-Air Batteries," *The Journal of Physical Chemistry C*, vol. 119, no. 32, pp. 18066–18073, 2015.

[109] F. Tian, M. D. Radin, and D. J. Siegel, "Enhanced Charge Transport in Amorphous $Li_2O_2$," *Chemistry of Materials*, vol. 26, no. 9, pp. 2952–2959, 2014.

[110] A. C. Luntz, V. Viswanathan, J. Voss, J. B. Varley, J. K. Nørskov, R. Scheffler, and A. Speidel, "Tunneling and Polaron Charge Transport through $Li_2O_2$ in Li-$O_2$ Batteries," *The Journal of Physical Chemistry Letters*, vol. 4, no. 20, pp. 3494–3499, 2013.

[111] J. B. Varley, V. Viswanathan, J. K. Nørskov, and A. C. Luntz, "Lithium and oxygen vacancies and their role in $Li_2O_2$ charge transport in Li-$O_2$ batteries," *Energy Environ. Sci.*, vol. 7, pp. 720–727, 2014.

[112] M. D. Radin and D. J. Siegel, "Charge transport in lithium peroxide: relevance for rechargeable metal-air batteries," *Energy Environ. Sci.*, vol. 6, pp. 2370–2379, 2013.

[113] M. D. Radin, F. Tian, and D. J. Siegel, "Electronic structure of $Li_2O_2$ {0001} surfaces," *Journal of Materials Science*, vol. 47, no. 21, pp. 7564–7570, 2012.

[114] J. Scheers, D. Lidberg, K. Sodeyama, Z. Futera, and Y. Tateyama, "Life of superoxide in aprotic Li-$O_2$ battery electrolytes: simulated solvent and counter-ion effects," *Phys. Chem. Chem. Phys.*, vol. 18, pp. 9961–9968, 2016.

[115] S. Kazemiabnavi, P. Dutta, and S. Banerjee, "Density Functional Theory Based Study of the Electron Transfer Reaction at the Lithium Metal Anode in a Lithium-Air Battery with Ionic Liquid Electrolytes," *The Journal of Physical Chemistry C*, vol. 118, no. 47, pp. 27183–27192, 2014.

[116] Y. S. Mekonnen, K. B. Knudsen, J. S. G. Mýrdal, R. Younesi, J. Højberg, J. Hjelm, P. Norby, and T. Vegge, "Communication: The influence of $CO_2$ poisoning on overvoltages and discharge capacity in non-aqueous Li-Air batteries," *The Journal of Chemical Physics*, vol. 140, no. 12, 2014.

[117] R. Christensen, "Investigation of systematic errors in density functional theory calculations for lithium-air battery reactions," Master's thesis, Technical University of Denmark, DTU, 2013. Master's thesis, http://findit.dtu.dk/en/catalog/2292742185.

[118] J. Yan, J. S. Hummelshøj, and J. K. Nørskov, "Formation energies of group I and II metal oxides using random phase approximation," *Phys. Rev. B*, vol. 87, p. 075207, Feb 2013.

[119] A. Jain, S. P. Ong, G. Hautier, W. Chen, W. D. Richards, S. Dacek, S. Cholia, D. Gunter, D. Skinner, G. Ceder, and K. A. Persson, "The Materials Project: A materials genome approach to accelerating materials innovation," *APL Materials*, vol. 1, no. 1, p. 011002, 2013.

[120] M. Hellenbrandt, "The Inorganic Crystal Structure Database (ICSD)– Present and Future," *Crystallography Reviews*, vol. 10, no. 1, pp. 17–22, 2004.

[121] J. E. Saal, S. Kirklin, M. Aykol, B. Meredig, and C. Wolverton, "Materials Design and Discovery with High-Throughput Density Functional Theory: The Open Quantum Materials Database (OQMD)," *JOM*, vol. 65, no. 11, pp. 1501–1509, 2013.

[122] S. Kirklin, J. E. Saal, B. Meredig, A. Thompson, J. W. Doak, M. Aykol, S. Rühl, and C. Wolverton, "The Open Quantum Materials Database (OQMD): assessing the accuracy of DFT formation energies," *NPJ Computational Materials*, vol. 1, p. 15010, 2015.

[123] G. Hautier, S. P. Ong, A. Jain, C. J. Moore, and G. Ceder, "Accuracy of density functional theory in predicting formation energies of ternary oxides from binary oxides and its implication on phase stability," *Phys. Rev. B*, vol. 85, p. 155208, Apr 2012.

[124] S. L. Dudarev, G. A. Botton, S. Y. Savrasov, C. J. Humphreys, and A. P. Sutton, "Electron-energy-loss spectra and the structural stability of nickel oxide: An LSDA+U study," *Phys. Rev. B*, vol. 57, pp. 1505–1509, Jan 1998.

[125] H. Nakamura, N. Hayashi, N. Nakai, and M. Machida, "First-Principle Electronic Structure Calculations For Iron-Based Superconductors: An LSDA+U Study," *J. Phys. Soc. Jpn.*, vol. 77, no. Suppl.C, pp. 153–154, 2008.

[126] S. S. Naghavi, *Theoretical Study of Correlated Systems Using Hybrid Functionals*. PhD thesis, Johannes Gutenberg-Universität, Mainz, 2010.

[127] R. D. J. III, ed., *NIST Computational Chemistry Comparison and Benchmark Database, NIST Standard Reference Database Number 101*. National Institute of Standards and Technology, Gaithersburg MD, 20899, 2016.

[128] J. Kim, H.-D. Lim, H. Gwon, and K. Kang, "Sodium-oxygen batteries with alkyl-carbonate and ether based electrolytes," *Phys. Chem. Chem. Phys.*, vol. 15, pp. 3623–3629, 2013.

[129] Y. Li, H. Yadegari, X. Li, M. N. Banis, R. Li, and X. Sun, "Superior catalytic activity of nitrogen-doped graphene cathodes for high energy capacity sodium-air batteries," *Chem. Commun.*, vol. 49, pp. 11731–11733, 2013.

[130] W. Liu, Q. Sun, Y. Yang, J.-Y. Xie, and Z.-W. Fu, "An enhanced electrochemical performance of a sodium-air battery with graphene nanosheets as air electrode catalysts," *Chem. Commun.*, vol. 49, pp. 1951–1953, 2013.

[131] Y. Hu, X. Han, Q. Zhao, J. Du, F. Cheng, and J. Chen, "Porous perovskite calcium-manganese oxide microspheres as an efficient catalyst for rechargeable sodium-oxygen batteries," *J. Mater. Chem. A*, vol. 3, pp. 3320–3324, 2015.

[132] P. Hartmann, C. L. Bender, M. Vracar, A. K. Dürr, A. Garsuch, J. Janek, and P. Adelhelm, "A rechargeable room-temperature sodium superoxide ($NaO_2$) battery," *Nat Mater*, vol. 12, pp. 228–232, Mar 2013.

[133] L. Lutz, W. Yin, A. Grimaud, D. Alves Dalla Corte, M. Tang, L. Johnson, E. Azaceta, V. Sarou-Kanian, A. J. Naylor, S. Hamad, J. A. Anta, E. Salager, R. Tena-Zaera, P. G. Bruce, and J.-M. Tarascon, "High Capacity Na?$O_2$ Batteries: Key Parameters for Solution-Mediated Discharge," *The Journal of Physical Chemistry C*, vol. 120, no. 36, pp. 20068–20076, 2016.

[134] P. Hartmann, C. L. Bender, J. Sann, A. K. Durr, M. Jansen, J. Janek, and P. Adelhelm, "A comprehensive study on the cell chemistry of the sodium superoxide ($NaO_2$) battery," *Phys. Chem. Chem. Phys.*, vol. 15, pp. 11661–11672, 2013.

[135] B. D. McCloskey, J. M. Garcia, and A. C. Luntz, "Chemical and Electrochemical Differences in Nonaqueous Li?$O_2$ and Na?$O_2$ Batteries," *The Journal of Physical Chemistry Letters*, vol. 5, no. 7, pp. 1230–1235, 2014. PMID: 26274476.

[136] N. Zhao, C. Li, and X. Guo, "Long-life Na–$O_2$ batteries with high energy efficiency enabled by electrochemically splitting $NaO_2$ at a low overpotential," *Phys. Chem. Chem. Phys.*, vol. 16, pp. 15646–15652, 2014.

[137] J. J. Mortensen, L. B. Hansen, and K. W. Jacobsen, "Real-space grid implementation of the projector augmented wave method," *Phys. Rev. B*, vol. 71, p. 035109, Jan 2005.

[138] J. Enkovaara, C. Rostgaard, J. J. Mortensen, J. Chen, M. Dułak, L. Ferrighi, J. Gavnholt, C. Glinsvad, V. Haikola, H. A. Hansen, H. H. Kristoffersen, M. Kuisma, A. H. Larsen, L. Lehtovaara, M. Ljungberg, O. Lopez-Acevedo, P. G. Moses, J. Ojanen, T. Olsen, V. Petzold, N. A. Romero, J. Stausholm-Møller, M. Strange, G. A. Tritsaris, M. Vanin, M. Walter, B. Hammer, H. Häkkinen, G. K. H. Madsen, R. M. Nieminen, J. K. Nørskov, M. Puska, T. T. Rantala, J. Schiøtz, K. S. Thygesen, and K. W. Jacobsen, "Electronic structure calculations with GPAW: a real-space implementation of the projector augmented-wave method," *Journal of Physics: Condensed Matter*, vol. 22, no. 25, p. 253202, 2010.

[139] J. K. Nørskov, J. Rossmeisl, A. Logadottir, L. Lindqvist, J. R. Kitchin, T. Bligaard, and H. Jónsson, "Origin of the Overpotential for Oxygen Reduction at a Fuel-Cell Cathode," *The Journal of Physical Chemistry B*, vol. 108, no. 46, pp. 17886–17892, 2004.

[140] Y. Li, S. H. Chan, and Q. Sun, "Heterogeneous catalytic conversion of $CO_2$: a comprehensive theoretical review," *Nanoscale*, vol. 7, pp. 8663–8683, 2015.

[141] A. A. Peterson, F. Abild-Pedersen, F. Studt, J. Rossmeisl, and J. K. Nørskov, "How copper catalyzes the electroreduction of carbon dioxide into hydrocarbon fuels," *Energy Environ. Sci.*, vol. 3, pp. 1311–1315, 2010.

[142] A. A. Peterson and J. K. Nørskov, "Activity Descriptors for $CO_2$ Electroreduction to Methane on Transition-Metal Catalysts," *J. Phys. Chem. Lett.*, vol. 3, no. 2, pp. 251–258, 2012.

[143] W. J. Durand, A. A. Peterson, F. Studt, F. Abild-Pedersen, and J. K. Nørskov, "Structure effects on the energetics of the electrochemical reduction of $CO_2$ by copper surfaces," *Surf. Sci.*, vol. 605, no. 15?16, pp. 1354 – 1359, 2011.

[144] H. A. Hansen, J. B. Varley, A. A. Peterson, and J. K. Nørskov, "Understanding Trends in the Electrocatalytic Activity of Metals and Enzymes for $CO_2$ Reduction to CO," *J. Phys. Chem. Lett.*, vol. 4, no. 3, pp. 388–392, 2013.

[145] V. Tripkovic, M. Vanin, M. Karamad, M. E. Björketun, K. W. Jacobsen, K. S. Thygesen, and J. Rossmeisl, "Electrochemical $CO_2$ and CO Reduction on Metal-Functionalized Porphyrin-like Graphene," *J. Phys. Chem. C*, vol. 117, no. 18, pp. 9187–9195, 2013.

[146] M. Z. Ertem, S. J. Konezny, C. M. Araujo, and V. S. Batista, "Functional Role of Pyridinium during Aqueous Electrochemical Reduction of $CO_2$ on Pt(111)," *J. Phys. Chem. Lett.*, vol. 4, no. 5, pp. 745–748, 2013.

[147] M. Karamad, V. Tripkovic, and J. Rossmeisl, "Intermetallic Alloys as CO Electroreduction Catalysts?Role of Isolated Active Sites," *ACS Catal.*, vol. 4, no. 7, pp. 2268–2273, 2014.

[148] K. Chan, C. Tsai, H. A. Hansen, and J. K. Nørskov, "Molybdenum Sulfides and Selenides as Possible Electrocatalysts for $CO_2$ Reduction," *ChemCatChem*, vol. 6, no. 7, pp. 1899–1905, 2014.

[149] W. Zhu, R. Michalsky, Ö. Metin, H. Lv, S. Guo, C. J. Wright, X. Sun, A. A. Peterson, and S. Sun, "Monodisperse Au Nanoparticles for Selective Electrocatalytic Reduction of $CO_2$ to CO," *J. Am. Chem. Soc.*, vol. 135, no. 45, pp. 16833–16836, 2013.

[150] A. S. Bandarenka, A. S. Varela, M. Karamad, F. Calle-Vallejo, L. Bech, F. J. Perez-Alonso, J. Rossmeisl, I. E. L. Stephens, and I. Chorkendorff, "Design of an Active Site towards Optimal Electrocatalysis: Overlayers, Surface Alloys and Near-Surface Alloys of Cu/Pt(111)," *Angew. Chem., Int. Ed.*, vol. 51, no. 47, pp. 11845–11848, 2012.

[151] R. Michalsky, Y.-J. Zhang, A. J. Medford, and A. A. Peterson, "Departures from the Adsorption Energy Scaling Relations for Metal Carbide Catalysts," *J. Phys. Chem. C*, vol. 118, no. 24, pp. 13026–13034, 2014.

[152] Y.-J. Zhang, V. Sethuraman, R. Michalsky, and A. A. Peterson, "Competition between $CO_2$ Reduction and $H_2$ Evolution on Transition-Metal Electrocatalysts," *ACS Catal.*, vol. 4, no. 10, pp. 3742–3748, 2014.

[153] C. Shi, C. P. O'Grady, A. A. Peterson, H. A. Hansen, and J. K. Nørskov, "Modeling $CO_2$ reduction on Pt(111)," *Phys. Chem. Chem. Phys.*, vol. 15, pp. 7114–7122, 2013.

[154] C. Shi, H. A. Hansen, A. C. Lausche, and J. K. Nørskov, "Trends in electrochemical $CO_2$ reduction activity for open and close-packed metal surfaces," *Phys. Chem. Chem. Phys.*, vol. 16, pp. 4720–4727, 2014.

[155] X. Nie, M. R. Esopi, M. J. Janik, and A. Asthagiri, "Selectivity of $CO_2$ Reduction on Copper Electrodes: The Role of the Kinetics of Elementary Steps," *Angew. Chem., Int. Ed.*, vol. 52, no. 9, pp. 2459–2462, 2013.

[156] X. Nie, W. Luo, M. J. Janik, and A. Asthagiri, "Reaction mechanisms of $CO_2$ electrochemical reduction on Cu(111) determined with density functional theory," *J. Catal.*, vol. 312, no. 0, pp. 108 – 122, 2014.

[157] H.-K. Lim, H. Shin, W. A. Goddard, Y. J. Hwang, B. K. Min, and H. Kim, "Embedding Covalency into Metal Catalysts for Efficient Electrochemical Conversion of $CO_2$," *J. Am. Chem. Soc.*, vol. 136, no. 32, pp. 11355–11361, 2014.

[158] N. J. Bernstein, S. A. Akhade, and M. J. Janik, "Density functional theory study of carbon dioxide electrochemical reduction on the Fe(100) surface," *Phys. Chem. Chem. Phys.*, vol. 16, pp. 13708–13717, 2014.

[159] S. Back, H. Kim, and Y. Jung, "Selective Heterogeneous $CO_2$ Electroreduction to Methanol," *ACS Catal.*, vol. 5, no. 2, pp. 965–971, 2015.

[160] J. H. Montoya, A. A. Peterson, and J. K. Nørskov, "Insights into C-C Coupling in $CO_2$ Electroreduction on Copper Electrodes," *ChemCatChem*, vol. 5, no. 3, pp. 737–742, 2013.

[161] S. Lysgaard, J. S. G. Myrdal, H. A. Hansen, and T. Vegge, "A DFT-based genetic algorithm search for AuCu nanoalloy electrocatalysts for $CO_2$ reduction," *Phys. Chem. Chem. Phys.*, pp. –, 2015.

[162] W. Luo, X. Nie, M. J. Janik, and A. Asthagiri, "Facet Dependence of $CO_2$ Reduction Paths on Cu Electrodes," *ACS Catalysis*, vol. 6, no. 1, pp. 219–229, 2016.

[163] S. A. Akhade, W. Luo, X. Nie, N. J. Bernstein, A. Asthagiri, and M. J. Janik, "Poisoning effect of adsorbed CO during $CO_2$ electroreduction on late transition metals," *Phys. Chem. Chem. Phys.*, vol. 16, pp. 20429–20435, 2014.

[164] Y. Hori, H. Wakebe, T. Tsukamoto, and O. Koga, "Electrocatalytic process of CO selectivity in electrochemical reduction of $CO_2$ at metal electrodes in aqueous media," *Electrochimica Acta*, vol. 39, no. 11, pp. 1833 – 1839, 1994.

[165] Y. Hori, "Electrochemical $CO_2$ Reduction on Metal Electrodes," in *Modern Aspects of Electrochemistry* (C. G. Vayenas, R. E. White, and M. E. Gamboa-Aldeco, eds.), vol. 42 of *Modern Aspects of Electrochemistry*, pp. 89–189, Springer New York, 2008.

[166] F. Studt, F. Abild-Pedersen, J. B. Varley, and J. K. Nørskov, "CO and $CO_2$ Hydrogenation to Methanol Calculated Using the BEEF-vdW Functional,"

*Catal. Lett.*, vol. 143, no. 1, pp. 71–73, 2013. Correctional approach documented in Supplementary material.

[167] F. Studt, M. Behrens, E. L. Kunkes, N. Thomas, S. Zander, A. Tarasov, J. Schumann, E. Frei, J. B. Varley, F. Abild-Pedersen, J. K. Nørskov, and R. Schlögl, "The Mechanism of CO and $CO_2$ Hydrogenation to Methanol over Cu-Based Catalysts," *ChemCatChem*, vol. 7, no. 7, pp. 1105–1111, 2015. Correctional approach documented in Supporting Information.

[168] B.-T. Teng, X.-D. Wen, M. Fan, F.-M. Wu, and Y. Zhang, "Choosing a Proper Exchange-Correlation Functional for the Computational Catalysis on Surface," *Phys. Chem. Chem. Phys.*, vol. 16, pp. 18563–18569, 2014.

[169] F. Calle-Vallejo and M. T. M. Koper, "Theoretical Considerations on the Electroreduction of CO to $C_2$ Species on Cu(100) Electrodes," *Angew. Chem., Int. Ed.*, vol. 52, no. 28, pp. 7282–7285, 2013.

[170] M. Behrens, F. Studt, I. Kasatkin, S. Kühl, M. Hävecker, F. Abild-Pedersen, S. Zander, F. Girgsdies, P. Kurr, B.-L. Kniep, M. Tovar, R. W. Fischer, J. K. Nørskov, and R. Schlögl, "The Active Site of Methanol Synthesis over $Cu/ZnO/Al_2O_3$ Industrial Catalysts," *Science*, vol. 336, no. 6083, pp. 893–897, 2012.

[171] A. S. Agarwal, Y. Zhai, D. Hill, and N. Sridhar, "The Electrochemical Reduction of Carbon Dioxide to Formate/Formic Acid: Engineering and Economic Feasibility," *ChemSusChem*, vol. 4, no. 9, pp. 1301–1310, 2011.

[172] X. Lu, D. Y. C. Leung, H. Wang, M. K. H. Leung, and J. Xuan, "Electrochemical Reduction of Carbon Dioxide to Formic Acid," *ChemElectroChem*, vol. 1, no. 5, pp. 836–849, 2014.

[173] B. Ruscic, R. E. Pinzon, G. von Laszewski, D. Kodeboyina, A. Burcat, D. Leahy, D. Montoy, and A. F. Wagner, "Active Thermochemical Tables: thermochemistry for the 21st century," *Journal of Physics: Conference Series*, vol. 16, no. 1, p. 561, 2005.

[174] B. Ruscic, "Uncertainty quantification in thermochemistry, benchmarking electronic structure computations, and Active Thermochemical Tables," *International Journal of Quantum Chemistry*, vol. 114, no. 17, pp. 1097–1101, 2014.

[175] B. Ruscic, D. Feller, and K. A. Peterson, "Active Thermochemical Tables: dissociation energies of several homonuclear first-row diatomics and related thermochemical values," *Theoretical Chemistry Accounts*, vol. 133, no. 1, p. 1415, 2013.

[176] B. Ruscic, R. E. Pinzon, M. L. Morton, G. von Laszevski, S. J. Bittner, S. G. Nijsure, K. A. Amin, M. Minkoff, and A. F. Wagner, "Introduction to Active Thermochemical Tables: Several "Key" Enthalpies of Formation Revisited," *The Journal of Physical Chemistry A*, vol. 108, no. 45, pp. 9979–9997, 2004.

[177] P. Giannozzi, S. Baroni, N. Bonini, M. Calandra, R. Car, C. Cavazzoni, D. Ceresoli, G. L. Chiarotti, M. Cococcioni, I. Dabo, A. Dal Corso, S. de Gironcoli, S. Fabris, G. Fratesi, R. Gebauer, U. Gerstmann, C. Gougoussis, A. Kokalj, M. Lazzeri, L. Martin-Samos, N. Marzari, F. Mauri, R. Mazzarello, S. Paolini, A. Pasquarello, L. Paulatto, C. Sbraccia, S. Scandolo, G. Sclauzero, A. P. Seitsonen, A. Smogunov, P. Umari, and R. M. Wentzcovitch, "QUANTUM ESPRESSO: a modular and open-source software project for quantum simulations of materials," *Journal of Physics: Condensed Matter*, vol. 21, no. 39, p. 395502 (19pp), 2009.

[178] C. H. Lee and M. W. Kanan, "Controlling $H^+$ vs $CO_2$ Reduction Selectivity on Pb Electrodes," *ACS Catalysis*, vol. 5, no. 1, pp. 465–469, 2015.

[179] T. Hatsukade, K. P. Kuhl, E. R. Cave, D. N. Abram, and T. F. Jaramillo, "Insights into the electrocatalytic reduction of $CO_2$ on metallic silver surfaces," *Phys. Chem. Chem. Phys.*, vol. 16, pp. 13814–13819, 2014.

[180] N. Hoshi, M. Kato, and Y. Hori, "Electrochemical reduction of $CO_2$ on single crystal electrodes of silver Ag(111), Ag(100) and Ag(110)," *Journal of Electroanalytical Chemistry*, vol. 440, no. 1, pp. 283 – 286, 1997.

[181] Y. Nie, L. Li, and Z. Wei, "Recent Advancements in Pt and Pt-Free Catalysts for Oxygen Reduction Reaction," *Chem. Soc. Rev.*, vol. 44, pp. 2168–2201, 2015.

[182] L. Trotochaud and S. W. Boettcher, "Precise Oxygen Evolution Catalysts: Status and Opportunities," *Scr. Mater.*, vol. 74, pp. 25–32, 2014.

[183] E. Fabbri, A. Habereder, K. Waltar, R. Kotz, and T. J. Schmidt, "Developments and Perspectives of Oxide-Based Catalysts for the Oxygen Evolution Reaction," *Catal. Sci. Technol.*, vol. 4, pp. 3800–3821, 2014.

[184] Y. Cheng and S. P. Jiang, "Advances in Electrocatalysts for Oxygen Evolution Reaction of Water Electrolysis - From Metal Oxides to Carbon Nanotubes," *Prog. Nat. Sci.: Mater. Int.*, vol. 25, no. 6, pp. 545–553, 2015.

[185] M. K. Debe, "Electrocatalyst Approaches and Challenges for Automotive Fuel Cells," *Nature*, vol. 486, no. 7401, pp. 43–51, 2012.

[186] J. A. Keith and T. Jacob, "Computational Simulations on the Oxygen Reduction Reaction in Electrochemical Systems," in *Theory and Experiment in Electrocatalysis* (B. P. Balbuena and R. V. Subramanian, eds.), vol. 50 of *Modern Aspects of Electrochemistry*, pp. 89–132, New York, NY: Springer New York, 2010.

[187] M. T. M. Koper, "Thermodynamic Theory of Multi-Electron Transfer Reactions: Implications for Electrocatalysis," *J. Electroanal. Chem.*, vol. 660, no. 2, pp. 254–260, 2011.

[188] J. Rossmeisl, Z.-W. Qu, H. Zhu, G.-J. Kroes, and J. Nørskov, "Electrolysis of Water on Oxide Surfaces," *J. Electroanal. Chem.*, vol. 607, no. 1?2, pp. 83–89, 2007.

[189] I. C. Man, H.-Y. Su, F. Calle-Vallejo, H. A. Hansen, J. I. Martínez, N. G. Inoglu, J. Kitchin, T. F. Jaramillo, J. K. Nørskov, and J. Rossmeisl, "Universality in Oxygen Evolution Electrocatalysis on Oxide Surfaces," *ChemCatChem*, vol. 3, no. 7, pp. 1159–1165, 2011.

[190] V. Viswanathan, H. A. Hansen, J. Rossmeisl, and J. K. Nørskov, "Universality in Oxygen Reduction Electrocatalysis on Metal Surfaces," *ACS Catal.*, vol. 2, no. 8, pp. 1654–1660, 2012.

[191] N. B. Halck, V. Petrykin, P. Krtil, and J. Rossmeisl, "Beyond the Volcano Limitations in Electrocatalysis - Oxygen Evolution Reaction," *Phys. Chem. Chem. Phys.*, vol. 16, pp. 13682–13688, 2014.

[192] V. Stamenkovic, B. S. Mun, K. J. Mayrhofer, P. N. Ross, N. M. Markovic, J. Rossmeisl, J. Greeley, and J. K. Nørskov, "Changing the Activity of Electrocatalysts for Oxygen Reduction by Tuning the Surface Electronic Structure," *Angewandte Chemie*, vol. 118, no. 18, pp. 2963–2967, 2006.

[193] Z. Zhao, L. Zhang, and Z. Xia, "Electron Transfer and Catalytic Mechanism of Organic Molecule-Adsorbed Graphene Nanoribbons as Efficient Catalysts for Oxygen Reduction and Evolution Reactions," *J. Phys. Chem. C*, vol. 120, no. 4, pp. 2166–2175, 2016.

[194] F. Calle-Vallejo, D. Loffreda, M. T. M. Koper, and P. Sautet, "Introducing Structural Sensitivity into Adsorption–Energy Scaling Relations by means of Coordination Numbers," *Nat. Chem.*, vol. 7, no. 5, pp. 403–410, 2015.

[195] S. Deshpande, J. R. Kitchin, and V. Viswanathan, "Quantifying Uncertainty in Activity Volcano Relationships for Oxygen Reduction Reaction," *ACS Catal.*, vol. 6, no. 8, pp. 5251–5259, 2016.

[196] R. A. van Santen, "On Shustorovich's Bond-Order conservation method as applied to chemisorption," *Recueil des Travaux Chimiques des Pays-Bas*, vol. 109, no. 2, pp. 59–63, 1990.

[197] M. T. M. Koper, "Theory of Multiple Proton-Electron Transfer Reactions and Its Implications for Electrocatalysis," *Chem. Sci.*, vol. 4, pp. 2710–2723, 2013.

[198] V. Viswanathan and H. A. Hansen, "Unifying Solution and Surface Electrochemistry: Limitations and Opportunities in Surface Electrocatalysis," *Top. Catal.*, vol. 57, no. 1, pp. 215–221, 2013.

[199] J. M. Simmie, G. Black, H. J. Curran, and J. P. Hinde, "Enthalpies of Formation and Bond Dissociation Energies of Lower Alkyl Hydroperoxides and Related Hydroperoxy and Alkoxy Radicals," *J. Phys. Chem. A*, vol. 112, no. 22, pp. 5010–5016, 2008.

[200] A. Tkatchenko and M. Scheffler, "Accurate Molecular Van Der Waals Interactions from Ground-State Electron Density and Free-Atom Reference Data," *Phys. Rev. Lett.*, vol. 102, p. 073005, Feb 2009.

[201] T. Bučko, S. Lebègue, J. Hafner, and J. G. Ángyán, "Tkatchenko-Scheffler van der Waals Correction Method with and without Self-Consistent Screening Applied to Solids," *Phys. Rev. B*, vol. 87, p. 064110, Feb 2013.

[202] A. Khorshidi and A. A. Peterson, "Amp: A modular approach to machine learning in atomistic simulations," *Computer Physics Communications*, vol. 207, pp. 310 – 324, 2016.

[203] N. Asproulis and D. Drikakis, "An artificial neural network-based multiscale method for hybrid atomistic-continuum simulations," *Microfluidics and Nanofluidics*, vol. 15, no. 4, pp. 559–574, 2013.

[204] J. Behler, "Constructing high-dimensional neural network potentials: A tutorial review," *International Journal of Quantum Chemistry*, vol. 115, no. 16, pp. 1032–1050, 2015.

[205] T. Morawietz and J. Behler, "A Density-Functional Theory-Based Neural Network Potential for Water Clusters Including van der Waals Corrections," *The Journal of Physical Chemistry A*, vol. 117, no. 32, pp. 7356–7366, 2013.

[206] H. Eshet, R. Z. Khaliullin, T. D. Kühne, J. Behler, and M. Parrinello, "*Ab initio* quality neural-network potential for sodium," *Phys. Rev. B*, vol. 81, p. 184107, May 2010.

[207] J. Behler, "Perspective: Machine learning potentials for atomistic simulations," *The Journal of Chemical Physics*, vol. 145, no. 17, 2016.

[208] G. Henkelman and H. Jónsson, "Improved tangent estimate in the nudged elastic band method for finding minimum energy paths and saddle points," *The Journal of Chemical Physics*, vol. 113, no. 22, pp. 9978–9985, 2000.

[209] G. Henkelman, B. P. Uberuaga, and H. Jónsson, "A climbing image nudged elastic band method for finding saddle points and minimum energy paths," *The Journal of Chemical Physics*, vol. 113, no. 22, pp. 9901–9904, 2000.

[210] K. T. Lundgaard, J. Wellendorff, J. Voss, K. W. Jacobsen, and T. Bligaard, "mBEEF-vdW: Robust fitting of error estimation density functionals," *Phys. Rev. B*, vol. 93, p. 235162, Jun 2016.

[211] C. Blundell, J. Cornebise, K. Kavukcuoglu, and D. Wierstra, "Weight uncertainty in neural networks," *Proceedings of the 32nd International Conference on Machine Learning, Lille, France, 2015. JMLR: W&CP volume 37*, 2015. Google DeepMind.

[212] J. Behler, "Atom-centered symmetry functions for constructing high-dimensional neural network potentials," *The Journal of Chemical Physics*, vol. 134, no. 7, p. 074106, 2011.

[213] R. Kortlever, C. Balemans, Y. Kwon, and M. T. Koper, "Electrochemical $CO_2$ reduction to formic acid on a Pd-based formic acid oxidation catalyst," *Catalysis Today*, vol. 244, pp. 58 – 62, 2015.

[214] B. Zhang, X. Zheng, O. Voznyy, R. Comin, M. Bajdich, M. García-Melchor, L. Han, J. Xu, M. Liu, L. Zheng, F. P. García de Arquer, C. T. Dinh, F. Fan, M. Yuan, E. Yassitepe, N. Chen, T. Regier, P. Liu, Y. Li, P. De Luna, A. Janmohamed, H. L. Xin, H. Yang, A. Vojvodic, and E. H. Sargent, "Homogeneously Dispersed, Multimetal Oxygen-Evolving Catalysts," *Science*, 2016.

# Appendix A

## Functional Performance for Oxides

Table 1: Oxygen reference correction [eV] to minimize MAE in enthalpies of formation of oxides in Chapter 3 for different functionals with the four different possible reference options.

| Functional | $O_2$, M ref. | $H_2O$, M ref. | $O_2$, $MCl_y$ ref. | $H_2O$, $MCl_y$ ref. |
|---|---|---|---|---|
| RPBE | -0.725 | -0.393 | -0.012 | 0.320 |
| PBE+U(-4) | -0.385 | -0.423 | 0.218 | 0.180 |
| PBE | -0.515 | -0.323 | 0.068 | 0.260 |
| PBE+U(4) | -0.630 | -0.174 | -0.051 | 0.405 |
| PBE+U(8) | -0.776 | -0.047 | -0.214 | 0.515 |
| PBE+U(12) | -0.941 | 0.078 | -0.407 | 0.612 |
| vdW-DF | -0.148 | 0.287 | -0.015 | 0.420 |
| vdW-DF2 | 0.181 | 0.576 | 0.245 | 0.640 |
| rPW86 | -0.329 | -0.074 | 0.094 | 0.350 |
| BEEF-vdW | -0.370 | 0.031 | -0.071 | 0.330 |
| HSE06 | -0.500 | -0.303 | -0.219 | -0.015 |

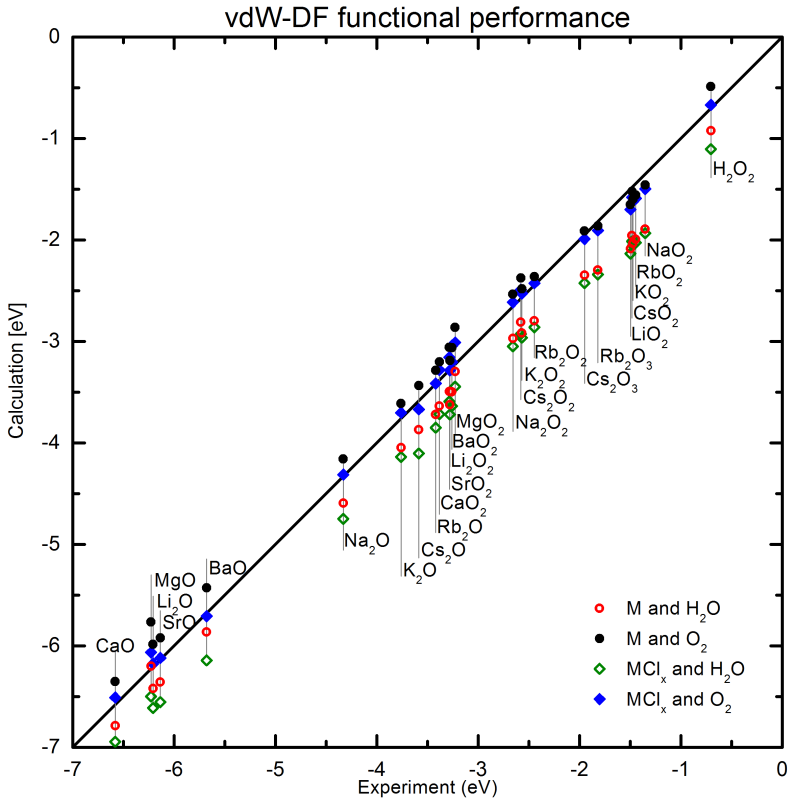


(a) vdW-DF

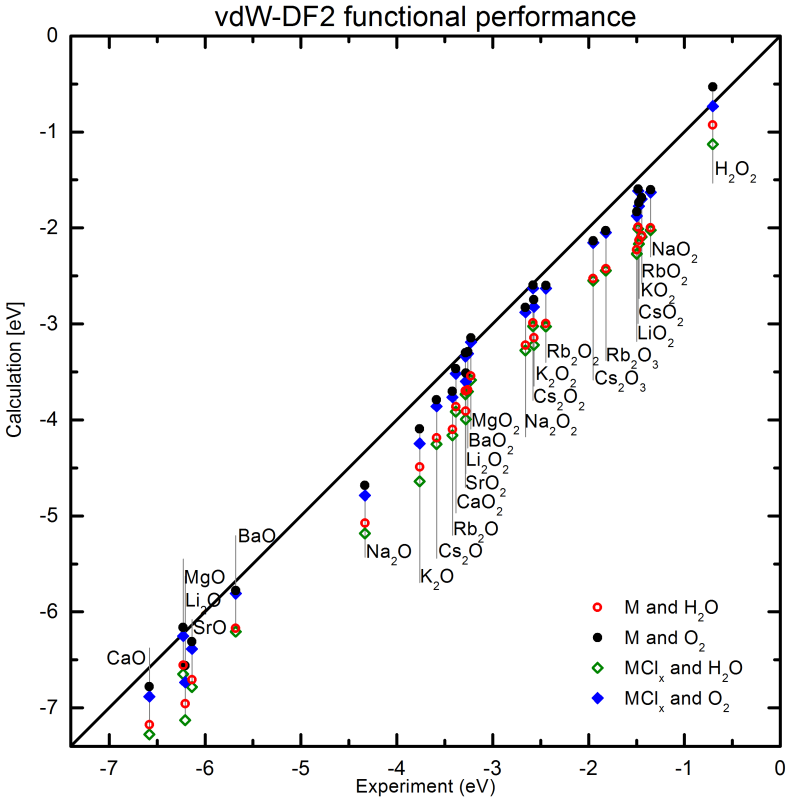


(b) vdW-DF2

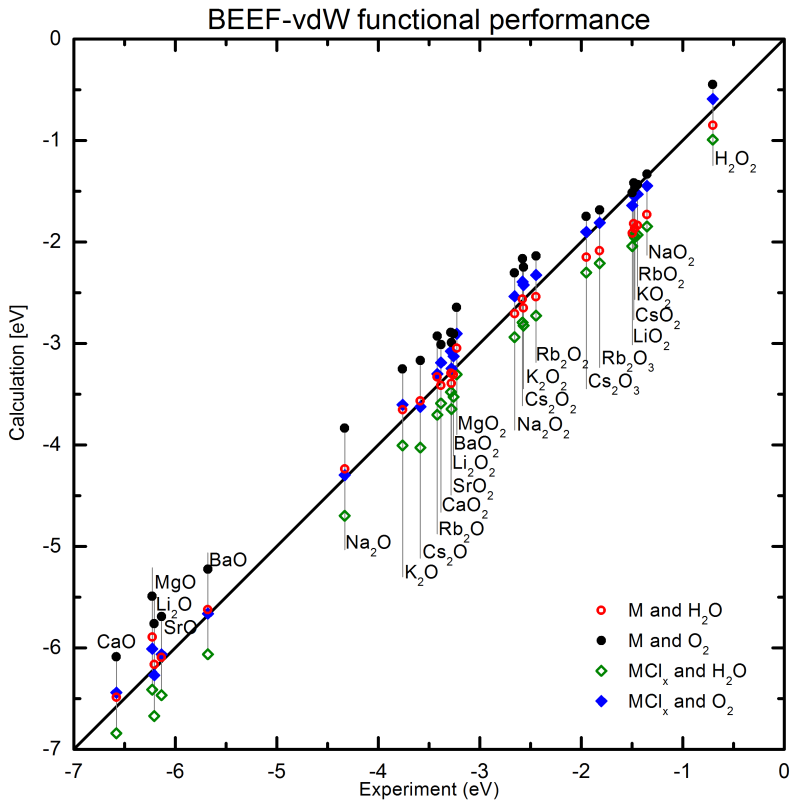


(a) BEEF-vdW

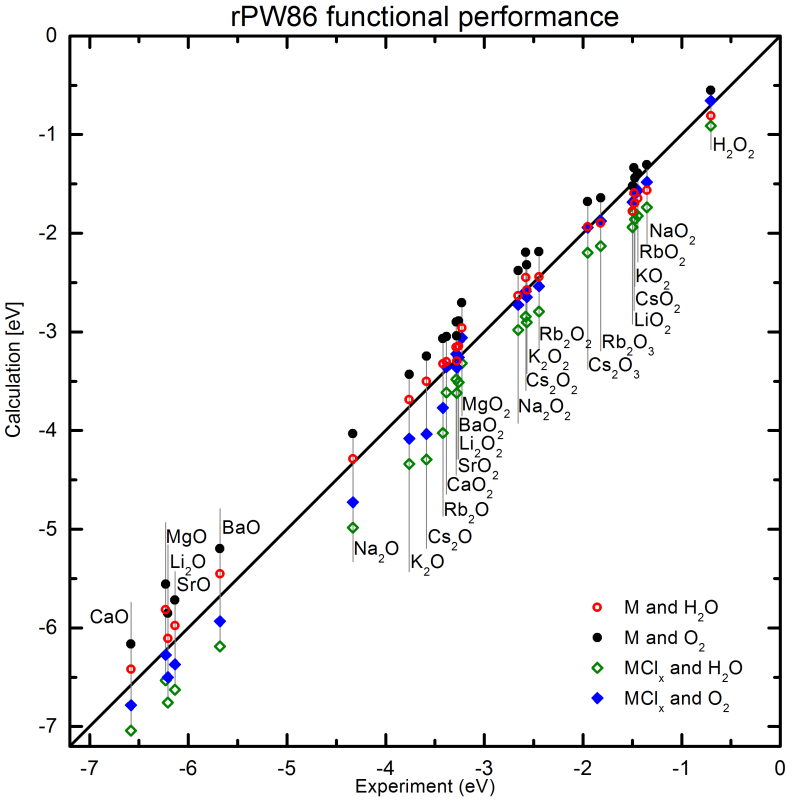


(b) rPW86

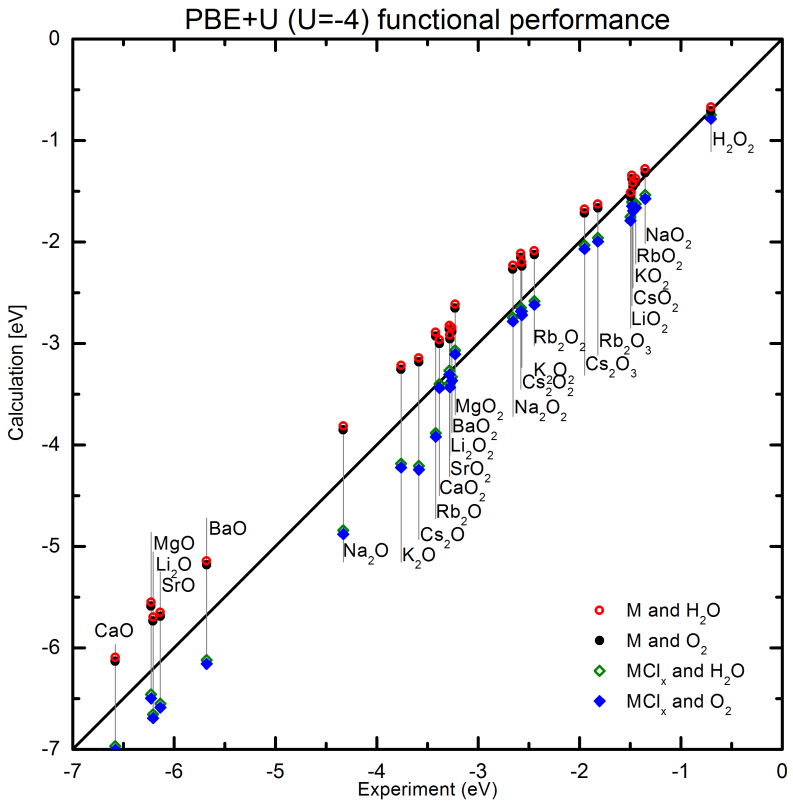


(c) PBE+U (U=-4)

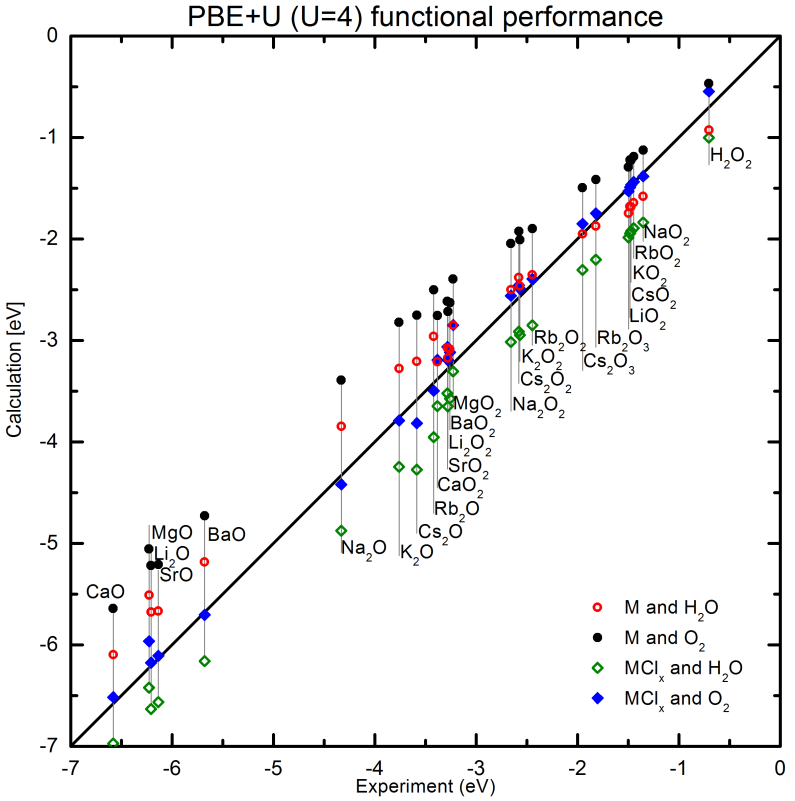


(d) PBE+U (U=4)

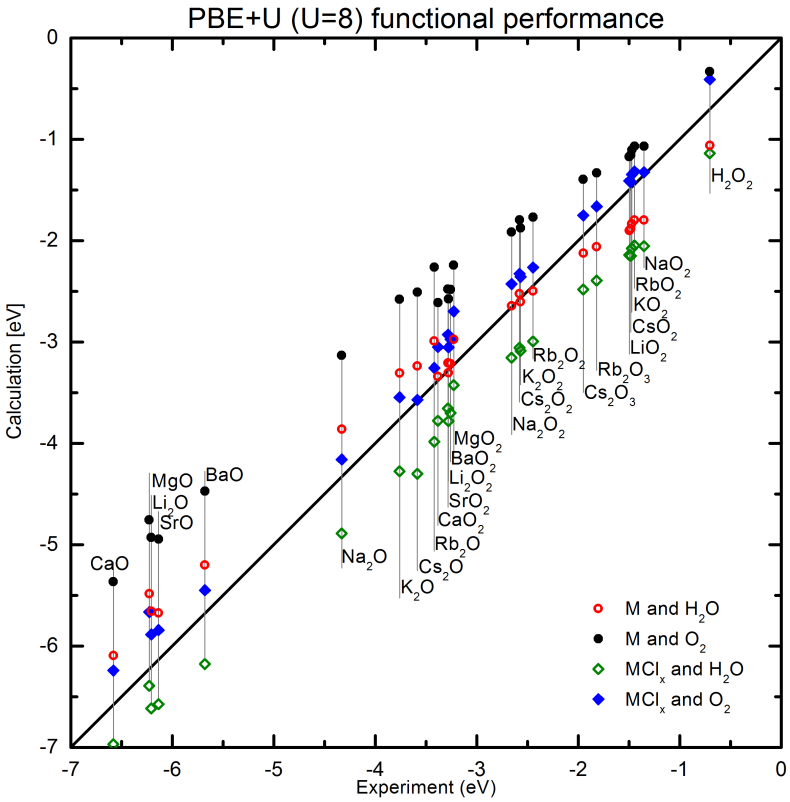


(e) PBE+U (U=8)

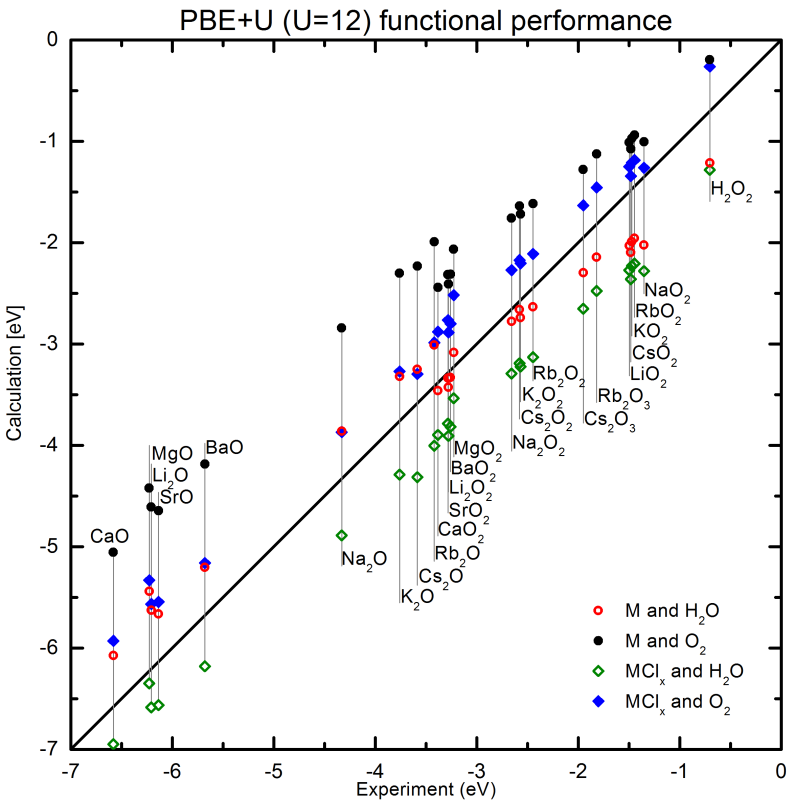


(f) PBE+U (U=12)

Figure 1: Calculated enthalpies of formation per oxygen atom, $\Delta H_f^\circ$/O, for oxide species versus experimental enthalpies.

# Appendix B

## Scaling Relation in Free Energy

The scaling relation between OH* and OOH* adsorption energies has previously mainly been given in electronic energies adjusted to included electrolyte stabilization of the adsorbates.[93,187–190]

$$E_{\mathrm{OOH}^*} = E_{\mathrm{OH}^*} + 3.2\ \mathrm{eV}\ \pm\ 0.2\ \mathrm{eV} \tag{1}$$

The following is used to convert it to Gibbs free energy:

$$G = H - TS = E_{\mathrm{elec}} + E_{\mathrm{ZPE}} + \int_0^T C_P dT - TS. \tag{2}$$

The scaling relation in free energy will be different from that expressed in electronic energies if inclusion of theses terms change the adsorption energy, $\Delta E_{\mathrm{ads}}$ of OH* relative to that of OOH*. The used values are seen in Table 2.

$E_{\mathrm{ZPE}}$ and $\int_0^T C_P dT$ are calculated as described in Section 2.3.1. For $TS$, experimental values have been used for the gas phase species.[95] For $H_2O$ the used

Table 2: Energies [eV] used for converting electronic energies to free energies.

| | $E_{\mathrm{ZPE}}$ | $\int_0^T C_P dT$ | $TS$ | $\Delta E_{\mathrm{ads}}$ |
|---|---|---|---|---|
| $H_2$ | 0.270 | 0.090 | 0.408 | – |
| $H_2O$ | 0.571 | 0.103 | 0.676 | – |
| $OH^*_{Pt}$ | 0.338 | 0.064 | 0.128 | 0.252 |
| $OOH^*_{Pt}$ | 0.44 | 0.095 | 0.204 | 0.263 |
| $OH^*_{Pd}$ | 0.323 | 0.074 | 0.178 | 0.197 |
| $OOH^*_{Pd}$ | 0.431 | 0.099 | 0.231 | 0.231 |
| $OH^*_{Ag}$ | 0.316 | 0.064 | 0.111 | 0.247 |
| $OOH^*_{Ag}$ | 0.407 | 0.110 | 0.251 | 0.198 |

entropy is for a pressure of 0.035 bar. This is approximately the room temperature equilibrium vapor pressure of $H_2O$. For adsorbates, the harmonic approximation is used to calculate $\int_0^T C_P dT$ and $TS$ from vibrational energies. They are thus given by

$$\int_0^T C_P dT = \sum_i^{\text{harm DOF}} \frac{\epsilon_i}{e^{\epsilon_i/k_B T} - 1}. \tag{3}$$

$$TS = Tk_B \sum_i^{\text{harm DOF}} \left[ \frac{\epsilon_i}{k_B T(e^{\epsilon_i/k_B T} - 1)} - \ln\left(1 - e^{-\epsilon_i/k_B T}\right) \right]. \tag{4}$$

The calculation of enthalpies is very sensitive to small errors in the low frequency vibrational modes. Using the values in Table 2, the scaling relation offset is found to change with values in the range -0.05 eV to 0.03 eV depending of the surface. This is in reasonable agreement with a previously found change of 0.04 eV on a Co-Fe-W oxy-hydroxide surface.[214]

Considering the relatively small and near zero average offset change as well as the calculational variation and uncertainty in calculations, the scaling relation expressed in free energies is taken to be identical to that expressed in electronic energies.

# Appendix C

## Most Probable $\sigma$ for Normally Distributed Errors

The product of individual probabilities for $N$ images with error $\epsilon_i$ can be written as

$$P = \prod_{i=1}^{N} \frac{1}{\sigma\sqrt{2\pi}} \, \mathrm{e}^{-\left(\epsilon_i^2/2\sigma^2\right)} \tag{5}$$

$$= \frac{1}{\left(\sigma\sqrt{2\pi}\right)^N} \, \mathrm{e}^{-\left(\sum_{i=1}^{N} \epsilon_i^2/2\sigma^2\right)} \tag{6}$$

To determine the most probable standard deviation based on the errors, the total probability is differentiated.

$$\frac{\mathrm{d}P_0}{\mathrm{d}\sigma} = \frac{1}{\left(\sigma\sqrt{2\pi}\right)^N} \, \mathrm{e}^{-\left(\sum_{i=1}^{N} \epsilon_i^2/2\sigma^2\right)} \frac{1}{\sigma} \left( \sum_{i=1}^{N} \epsilon_i^2/\sigma^2 - N \right). \tag{7}$$

The maximum probability can thus be found from

$$0 = \sum_{i=1}^{N} \epsilon_i^2/\sigma^2 - N \qquad \Leftrightarrow \tag{8}$$

$$N\sigma^2 = \sum_{i=1}^{N} \epsilon_i^2 \qquad \Leftrightarrow \tag{9}$$

$$\sigma = \sqrt{\sum_{i=1}^{N} \epsilon_i^2/N} \qquad \Leftrightarrow \tag{10}$$

the RHS of (10) is the root mean squared error (RMSE).

# Included publications

## Paper I

Reducing Systematic Errors in Oxide Species with Density Functional Theory Calculations

Rune Christensen, Jens S. Hummelshøj, Heine A. Hansen, and Tejs Vegge

*J. Phys. Chem. C*, **2015**, 119 (31), pp 17596–17601

THE JOURNAL OF PHYSICAL CHEMISTRY C

Article

pubs.acs.org/JPCC

# Reducing Systematic Errors in Oxide Species with Density Functional Theory Calculations

Rune Christensen,[†] Jens S. Hummelshøj,[‡] Heine A. Hansen,[†] and Tejs Vegge*[,†]

[†]Department of Energy Conversion and Storage, Technical University of Denmark, Fysikvej, Kgs. Lyngby DK-2800, Denmark

[‡]SUNCAT, SLAC National Accelerator Laboratory, Menlo Park, California 94025, United States

Supporting Information

**ABSTRACT:** Density functional theory calculations can be used to gain valuable insight into the fundamental reaction processes in metal−oxygen systems, e.g., metal−oxygen batteries. Here, the ability of a range of different exchange-correlation functionals to reproduce experimental enthalpies of formation for different types of alkali and alkaline earth metal oxide species has been examined. Most examined functionals result in significant overestimation of the stability of superoxide species compared to peroxides and monoxides, which can result in erroneous prediction of reaction pathways. We show that if metal chlorides are used as reference structures instead of metals, the systematic errors are significantly reduced and functional variations decreased. Using a metal chloride reference, where the metal atoms are in the same oxidation state as in the oxide species, will provide a computationally inexpensive and robust approach to significantly improve accuracy. The approach can potentially be applied to improve accuracy of calculations more generally.

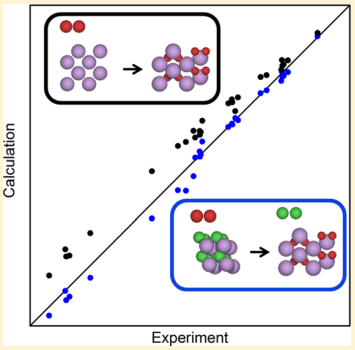


## INTRODUCTION

The potential for very large specific energy and the ability to possibly be operated as secondary batteries make metal-air batteries promising candidates for developing a battery technology for personal transportation truly competitive with fossil fuels. Some of the challenges for developing metal−air batteries include increasing round trip efficiency, stability, capacity, power density, and cyclability.[1]

Fundamental understanding of the reaction mechanisms at an atomic scale, which is currently infeasible from experimental methods, would be a great aid in the development of superior materials. Calculations based on density functional theory (DFT) have previously been applied to achieve such understanding.[2−18] However, the level of calculational accuracy prohibits detailed understanding of key processes in metal−air batteries. One example is the triplet ground state of the $O_2$ double bond, which is significantly overstabilized with common DFT methods.[19−24] This error can to some extent also be anticipated in superoxide ($O_2^-$) and peroxide ($O_2^{2-}$) ions.[25] As a result, calculational errors are expected to vary for peroxide, superoxide, and monoxide species; all of which are possible reaction intermediates. Although correction schemes to the calculated energy[2,16] can mitigate some of this error, it can still potentially cause errors in the description of charge and discharge reactions. Although surfaces and surface reactions are in many respects very different from bulk, the current relative understabilization of peroxide versus superoxide may result in intermediate reaction steps with formation of peroxide species being artificially unfavored in comparison to intermediate reactions with formation of superoxide species. This may result in erroneous prediction of overpotential, limiting reaction step, or even reaction path. As a specific example, the relative stability of $Li_2O_2$ facets with different surface terminations calculated by Hummelshøj, Luntz, and Nørskov[2] could change in favor of less oxygen rich surfaces.

In this work, we have applied an approach similar to those previously used, e.g., by Hummelshøj, Luntz, and Nørskov[2] as well as Kang et al.,[16] by calculating enthalpies of formation for various oxide species and comparing these to experimental data. It has previously been shown that significant improvements can be made using exact exchange followed by random phase approximation calculations.[26] These calculations are, however, computationally demanding. The purpose of this work is to determine the performance of different and less computationally demanding exchange-correlation functionals useful for extensive studies of large complex oxide structures, e.g., to obtain increased insight into reactions barriers in surface reactions. A functional with reduced systematic errors in the calculated enthalpies of formation for different bulk oxide species is expected to give improved accuracy in the determination of such reaction processes where oxygen changes oxidation state.

It is possible that a correct description of localized electrons will be decisive for reduction of systematic errors. For this reason the ability of the functionals to localize electrons properly in the superoxide and peroxide ions in cases where both are present has been examined to determine the importance of such ability for reducing systematic errors in enthalpies of formation. The ability of a functional to describe localized states is also among other properties important for studying polaronic conduction.[6,9]

**Received:** June 22, 2015
**Published:** July 14, 2015





DOI: 10.1021/acs.jpcc.5b05968
J. Phys. Chem. C 2015, 119, 17596−17601

## THEORETICAL METHODS

The VASP code has been applied with the projector augmented-wave (PAW) approach.[27−30] In the used implementation of PBE+U,[31] $U$ is an effective parameter, $U_{eff} = U - J$, and can in principle be negative as described by Nakamura et al.[32] Negative values of $U$ have been included for completeness. In general, computational parameters have been chosen such that as little error as possible will be related to parameters other than the exchange-correlation functional, while keeping calculations computationally feasible. Computational details can be found in Supporting Information.

The examined functionals include the common generalized gradient approximation (GGA) functionals, PBE[33] and RPBE;[20] van der Waals correlation functionals, vdW-DF,[34] vdW-DF2,[35] and BEEF-vdW;[36] and addition of Hubbard $U$ correlation, PBE+U.[31] These functionals are chosen for examination as they have GGA type exchange and thus are considered to be of sufficiently low computational cost for larger future studies.

In addition, a hybrid functional, HSE06,[37] with 25% exact exchange is also considered. Hybrid functionals are known to be able to describe localized electronic states.[38] The HSE06 functional has been included in the study despite its significantly higher computational cost in order to examine the importance of a correct description of localized states.

From evaluation of the ability of these functionals to reproduce experimental enthalpies of formation in a similar manner, it is not only possible to evaluate the performance of the functionals individually, but also to determine if increased accuracy can be achieved without increased computational cost.

The standard GGA functionals have been chosen due to their widespread use. Furthermore, a revised version of the PW86 functional,[39] rPW86, which constitutes the exchange part of the vdW-DF2 functional, has been included for comparison. Van der Waals correlation functionals and Hubbard correlation are examined as these represent relative computationally inexpensive methods to include additional correlation effects. The hybrid functional is included to determine if partial exact exchange can reduce errors and improve the description of localized electrons.

In order to depict systematic errors in the description of oxide, peroxide, and superoxide ions as thoroughly as possible, the, to our knowledge, most extensive set of non-transition-metal oxide species has been analyzed. Alkali metal (Li, Na, K, Rb, Cs) oxide, peroxide, and superoxide species and alkaline earth metal (Mg, Ca, Sr, Ba) oxide and peroxide species are included. In addition, rubidium and cesium sesquioxides have also been included. Sesquioxides, which have previously been studied mainly for their magnetic properties,[40,41] are particularly interesting as superoxide and peroxide ions are simultaneously present in the crystal structure in the ratio 2:1. The sesquioxides are thus also useful for investigating if proper localization of electrons can be described. Gaseous hydrogen peroxide is also included for comparison with the metal peroxides. An error intrinsic to the peroxide ion can be expected to be similar in metal peroxides and hydrogen peroxide. The use of the comprehensive set of different oxide species mitigates individual calculational or reference data uncertainties from skewing conclusions. As reference data originates from different sources, we do not expect large systematic errors to be present in the experimental reference data.

Previously, $H_2O$ has been used for gaseous reference in place of $O_2$ to avoid the known energy error for gaseous $O_2$.[3,23,42] In this work, both references for oxygen are applied as described below. Using the $O_2$ reference, error cancellation can possibly take place for the peroxide and superoxide ions. Enthalpies are all calculated per oxygen atom in the product oxide rather than per formula unit such that errors related to the oxygen reference will give a constant shift versus the experimental enthalpies for all oxide species as also discussed by Yan et al.[26] The relative stability between oxide species is thus unaffected by errors in this reference. In addition, an alternative to a standard metal reference is also considered. Metal chlorides, which have simple structures and are similar to oxides in terms of metal oxidation states, have been applied as metal atom reference using a similar approach as for the oxygen reference. By also using this reference, it can be examined whether the error caused by a change in the metal atom oxidation state or the different degrees in which the oxygen−oxygen double bond is broken in the different oxygen ions dominates the systematic errors. The latter has been suggested previously by Kang et al.[16] The expression for enthalpy of formation per oxygen $\Delta H'$ with $O_2$ and metal references is

$$\Delta H'_{M_xO_y} = \frac{1}{y}E(M_xO_y) - \frac{x}{y}E(M) - \frac{1}{2}E(O_2)$$

where $E(X)$ is the calculated energy per formula unit of X. Using the following expressions

$$\Delta H_{H_2O,exp} = E(H_2O) - E(H_2) - \frac{1}{2}E(O_2)$$

$$\Delta H_{MCl_z,exp} = E(MCl_z) - E(M) - \frac{z}{2}E(Cl_2)$$

where $\Delta H_{X,exp}$ are experimental enthalpies of formation,[43] the enthalpy of formation per oxygen using water and metal chlorides as references is thus given as

$$\Delta H'_{M_xO_y} = \frac{1}{y}E(M_xO_y) - \frac{x}{y}\left(E(MCl_z) - \frac{z}{2}E(Cl_2) - \Delta H_{MCl_z,exp}\right) - \left(E(H_2O) - E(H_2) - \Delta H_{H_2O,exp}\right)$$

Notice how pure metal and $O_2$ calculations are not used to determine $\Delta H_{M_xO_y}$. For $H_2O_2$, $^1/_2H_2$ replaces M, and HCl replaces $MCl_z$.

## RESULTS AND DISCUSSION

Using pure metal as reference, the discrepancy between experimental and calculated enthalpies of formation is, as previous studies also conclude,[16,26] found to depend on the oxidation state of the oxygen, i.e., $O^{2-}$, $O_2^-$, or $O_2^{2-}$. Experimental and calculated enthalpies of formation are compared for PBE in Figure 1. For similar figures for other functionals, see Supporting Information.

The previously observed behavior of calculated enthalpies of formation larger than the experimental values and the trend of increasing calculated stability relative to experimental values for monoxides, peroxides, and superoxides[2,16,25,26] is recognized for most functionals using the metal as reference. The error for sesquioxides falls in between that of superoxides and peroxides



DOI: 10.1021/acs.jpcc.5b05968
J. Phys. Chem. C 2015, 119, 17596−17601

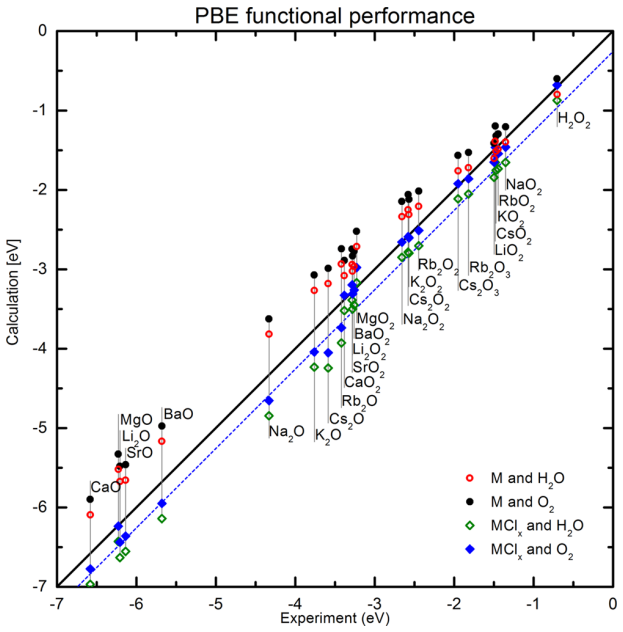


**Figure 1.** Experimental versus calculated enthalpies of formation using various references. The dashed blue line illustrates offset for monoxides using metal chloride and $O_2$ references.

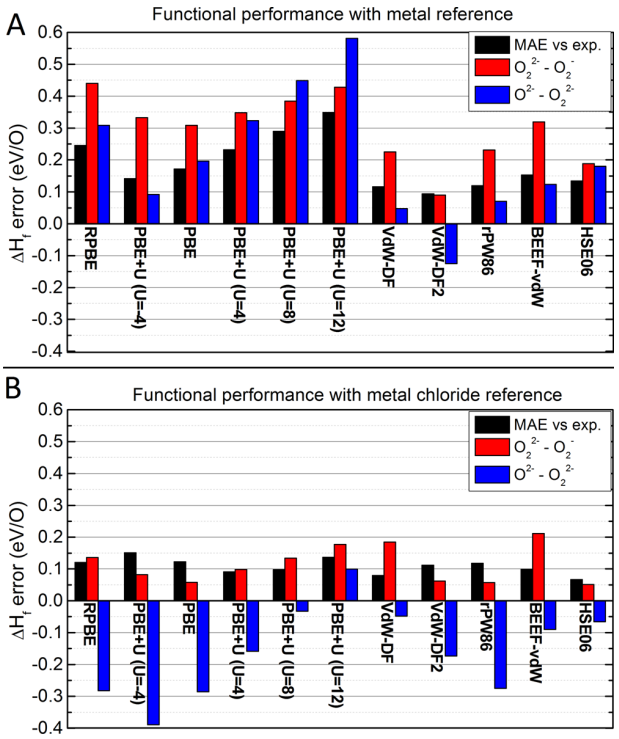


**Figure 2.** Performance of the functionals to reproduce experimental enthalpies of formation. The mean absolute error, MAE, (left black bars), has been calculated with the oxygen reference fitted to minimize MAE. Red bars (middle) show the average difference in error between alkali peroxides and alkali superoxides. Blue bars (right) similarly compare all metal peroxides with the monoxides. (A) Calculations using metal as reference. (B) Calculations using metal chlorides as reference.

as expected from their composition. With metal chlorides as reference, a different trend is observed. Now the differences between experiments and calculations are much more similar for superoxides, sesquioxides, and peroxides. For PBE, using $O_2$ as oxygen reference gives close to no error for these. Monoxides are calculated to be on average 0.26 eV/O more stable than the experimental values. This can be understood from cancellation of the error associated with the oxygen−oxygen bond.[25] A similar trend is observed for other examined functionals, i.e. RPBE, vdW-DF, rPW86, and BEEF-vdW (see Supporting Information).

The performance of each examined functional has been evaluated quantitatively using both metal and metal chlorides (Figure 2) as reference. Here, the oxygen reference has been fitted to minimize the mean absolute error (MAE). Using the metal reference, the MAE is between 0.1 and 0.4 eV and highly functional dependent. For the metal chloride reference, the MAE is in general significantly reduced, e.g., from 0.25 to 0.12 eV for the RPBE functional. The MAE also displays less variation from one functional to another. The same conclusions are reached using RMSE as measure of performance.

The MAE with corrected oxygen reference is a good measure of how consistently each functional is reproducing experimental data for the data set as one entity, i.e., how well a functional performs with a possible constant error on the oxygen reference accounted for. To reveal systematic errors within the data set and quantify these, the difference in average error for alkali peroxides and superoxides is compared (Figure 2, red bars). This reveals whether one oxide type systematically displays different errors than another. A similar comparison is made between alkali and alkaline earth monoxide and peroxide species (Figure 2, blue bars). The depicted average error differences are equivalent to the average error per oxygen atom for the oxidation reaction of superoxide to peroxide (red bars) and peroxide to monoxide (blue bars).

For the peroxide−superoxide comparison using the metal reference, the average difference is generally found to be larger than 0.2 eV with the exceptions of the vdW-DF2 and HSE06 functionals, where differences are 0.09 and 0.19 eV, respectively. It is noted that applying a Hubbard $U$ will in all cases increase this error difference. With metal chlorides as reference, much smaller and less functional dependent differences between the superoxides and peroxides are observed, with only the BEEF-vdW functional displaying a difference slightly larger than 0.20 eV. In a comparison of the peroxides with monoxides using the metal reference, the results are highly dependent on the functional with peroxides calculated to be more stable relative to experiment for all functionals except vdW-DF2. With the metal chloride reference, this pattern has been reversed, such that monoxides are now more stable compared to experiment.

The smallest difference between using the metal and metal chloride reference is observed for the van der Waals functionals. The vdW-DF2 functional is the best performing functional with the metal reference. This suggests that van der Waals interactions are important for a consistent description of oxide and metal structures. It has previously been found that inclusion of van der Waals interactions can significantly influence description of alkali and alkaline earth metals.[30] While the HSE06 functional only performs moderately well with the metal reference, it outperforms the less computationally demanding functionals with the metal chloride reference and only gives rise to systematic errors on the order of 0.05 eV


DOI: 10.1021/acs.jpcc.5b05968
J. Phys. Chem. C 2015, 119, 17596−17601

per oxygen. With a water reference, further fitting of the oxygen reference to minimize the MAE is not required. The errors for gaseous hydrogen peroxide and the bulk metal peroxides are similar, when the metal chloride reference is used. This further confirms the metal chlorides to be the better choice of reference. The better performance of the metal chloride reference can be viewed as error cancellation when comparing metal atoms of similar oxidation state. Delocalized conduction electrons are present in the metals where only relatively confined electronic orbitals are present around the metal ions in both metal oxides and metal chlorides.

The approach of using a reference with the metal atoms in similar oxidation state as in the system of interest is potentially able to generally improve accuracy of computationally inexpensive functionals. Multiple references, e.g., metal chlorides and pure metals, could be used simultaneously if metal atoms of the same element are present in different oxidation states.

The ensemble capability of the BEEF-vdW functional can be used to examine the robustness of results against functional changes at a low computational cost.[36] With the electron density obtained with the BEEF-vdW functional, non-self-consistent calculations are performed for a set of predefined ensemble functionals generated through perturbations of the BEEF-vdW functional. The ensemble has been created such that the ensemble standard deviation will represent the general uncertainty of a calculation. We refer to Wellendorff et al.[36] for further details regarding the ensemble. The functional dependence is here quantified using the standard deviation in calculated enthalpies of formation for an ensemble of 2000 functionals.

The ensemble standard deviations per oxygen atom are shown in Figure 3. In general, the metal references will result in

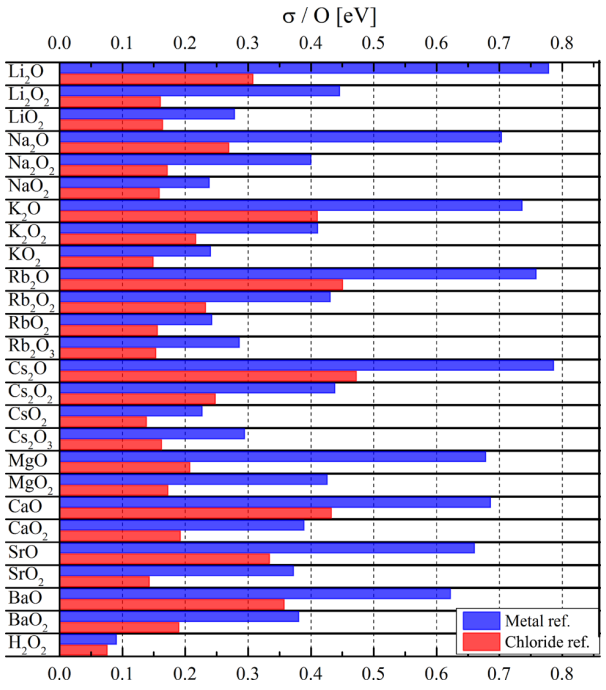


**Figure 3.** Standard deviations in the BEEF-vdW ensemble for calculation of enthalpy of formation per oxygen atom using metal (top, blue) and metal chloride (bottom, red) references.

significantly larger standard deviations than the metal chloride references. Thus, using metal chlorides as a reference will result in a smaller difference between functionals in accordance with Figure 2. Further, the standard deviations when using a metal reference (blue bars in Figure 3) will to a good approximation scale with the metal to oxygen ratio. This supports that much of the systematic error in the calculation of enthalpies of formation can be attributed to the metal reference. Using metal chlorides as a reference, the standard deviations shown on Figure 3 (red bars) are significantly reduced. For peroxides and superoxides they are in most cases between 0.15 and 0.20 eV, which is in the range of expected standard deviations using the BEEF-vdW ensemble method.[36] The standard deviations are approximately twice as large for the monoxides. With stoichiometry taken into account, the standard deviations are similar per formula unit using the metal chloride reference.

Localization of electrons can be obtained using the HSE06 functional for sesquioxides (see Supporting Information). For rubidium sesquioxide, the situation with properly localized electrons can be expressed as $Rb^{+4}(O_2^{-})_2O_2^{2-}$; i.e., two distinct superoxide ions and one peroxide ion are present for every four rubidium ions. Superoxide and peroxide ions are clearly distinguishable with significantly different bonding distances, 1.32 Å for $O_2^{-}$ and 1.49 Å for $O_2^{2-}$. The difference can also clearly be seen from a Bader charge analysis[44] and the magnetic moments, as oxygen atoms in superoxide and peroxide ions have nonzero and zero magnetic moment, respectively.

With the HSE06 optimized geometry and wave functions, it was possible to obtain proper localization of electrons with PBE +U. With ion bond lengths and local magnetic moments as measure, the degree of localization changes gradually from $U$ = 6 to $U$ = 10, where proper localization of electrons is obtained. For all other examined functionals it was not possible to obtain proper localization of the electrons. Although, PBE+U with large values of U can describe localization, this does not reduce systematic errors. Similarly, HSE06, which can also describe localization, does not reproduce experimental enthalpies of formation better than the GGA-exchange functionals with a metal reference. On the basis of this it is improbable that the correct description of electron localization alone is decisive for reduction of systematic errors.

## CONCLUSIONS

The ability to reproduce experimental enthalpies of formation for bulk alkali and alkaline earth oxide, peroxide, superoxide, and sesquioxide species has been examined for a large range of exchange-correlation functionals. With metal crystal structures as reference, systematic errors were observed as reported previously.[2,16] These were shown to be highly dependent on functional choice. However, when using metal chlorides for reference, it is found that calculated enthalpies are less functional dependent and the systematic error is significantly reduced. This shows that the systematic errors are dominated by changes in metal atom oxidation state rather than difference in oxygen ions. This insight provides a computationally fast and robust approach to improve calculational accuracy of the examined metal oxide species at the GGA level by using metal chlorides as reference species. The approach of adapting a metal reference with similar metal atom oxidation state as the structure of interest rather than a bulk metal reference can potentially improve calculational accuracy for a wider range of materials.



DOI: 10.1021/acs.jpcc.5b05968
J. Phys. Chem. C 2015, 119, 17596−17601

## ■ ASSOCIATED CONTENT

### Supporting Information

Computational details and figures similar to Figure 1 for performance of other examined functionals. Further results regarding general accuracy of different references and treatment of localization of electrons in sesquioxides. The Supporting Information is available free of charge on the ACS Publications website at DOI: 10.1021/acs.jpcc.5b05968.

## ■ AUTHOR INFORMATION


### Corresponding Author

*E-mail: teve@dtu.dk.


### Notes

The authors declare no competing financial interest.

## ■ ACKNOWLEDGMENTS

The authors acknowledge Prof. Alan C. Luntz for valuable discussions. The work has been conducted partly under the Catalysis for Sustainable Energy (CASE) initiative funded by The Danish Agency for Science, Technology and Innovation. The authors also acknowledge support from the ReLiable project (project no. 11-116792/0603-00462B) funded by the Danish Council for Strategic Research Programme Commission on Sustainable Energy and Environment under the Danish Innovation Foundation and from the European Union's Seventh Framework Programme (FP7/2007-2013) under grant agreement no. 608575.

## ■ REFERENCES


(1) Girishkumar, G.; McCloskey, B.; Luntz, A. C.; Swanson, S.; Wilcke, W. Lithium-Air Battery: Promise and Challenges. *J. Phys. Chem. Lett.* **2010**, *1*, 2193−2203.

(2) Hummelshøj, J. S.; Luntz, A. C.; Nørskov, J. K. Theoretical Evidence for Low Kinetic Overpotentials in Li-$O_2$ Electrochemistry. *J. Chem. Phys.* **2013**, *138*, 034703.

(3) Hummelshøj, J. S.; Blomqvist, J.; Datta, S.; Vegge, T.; Rossmeisl, J.; Thygesen, K. S.; Luntz, A. C.; Jacobsen, K. W.; Nørskov, J. K. Communications: Elementary Oxygen Electrode Reactions in the Aprotic Li-air Battery. *J. Chem. Phys.* **2010**, *132*, 071101.

(4) Mekonnen, Y. S.; Knudsen, K. B.; Myrdal, J. S. G.; Younesi, R.; Højberg, J.; Hjelm, J.; Norby, P.; Vegge, T. Communication: The Influence of $CO_2$ Poisoning on Overvoltages and Discharge Capacity in Non-aqueous Li-Air Batteries. *J. Chem. Phys.* **2014**, *140*, 121101.

(5) Myrdal, J. S. G.; Vegge, T. Selective Poisoning of Li-air Batteries for Increased Discharge Capacity. *RSC Adv.* **2014**, *4*, 15671−15674.

(6) Garcia-Lastra, J. M.; Myrdal, J. S. G.; Christensen, R.; Thygesen, K. S.; Vegge, T. DFT+U Study of Polaronic Conduction in $Li_2O_2$ and $Li_2CO_3$: Implications for Li-Air Batteries. *J. Phys. Chem. C* **2013**, *117*, 5568−5577.

(7) Garcia-Lastra, J. M.; Bass, J. D.; Thygesen, K. S. Communication: Strong Excitonic and Vibronic Effects Determine the Optical Properties of $Li_2O_2$. *J. Chem. Phys.* **2011**, *135*, 121101.

(8) Radin, M. D.; Rodriguez, J. F.; Tian, F.; Siegel, D. J. Lithium Peroxide Surfaces Are Metallic, While Lithium Oxide Surfaces Are Not. *J. Am. Chem. Soc.* **2012**, *134*, 1093−1103.

(9) Radin, M. D.; Siegel, D. J. Charge Transport in Lithium Peroxide: Relevance for Rechargeable Metal-air Batteries. *Energy Environ. Sci.* **2013**, *6*, 2370−2379.

(10) Radin, M.; Tian, F.; Siegel, D. Electronic Structure of $Li_2O_2${0001} Surfaces. *J. Mater. Sci.* **2012**, *47*, 7564−7570.

(11) Viswanathan, V.; Thygesen, K. S.; Hummelshøj, J. S.; Nørskov, J. K.; Girishkumar, G.; McCloskey, B. D.; Luntz, A. C. Electrical Conductivity in $Li_2O_2$ and Its Role in Determining Capacity Limitations in Non-aqueous Li-$O_2$ Batteries. *J. Chem. Phys.* **2011**, *135*, 214704.

(12) Albertus, P.; Girishkumar, G.; McCloskey, B.; Sánchez-Carrera, R. S.; Kozinsky, B.; Christensen, J.; Luntz, A. C. Identifying Capacity Limitations in the Li/Oxygen Battery Using Experiments and Modeling. *J. Electrochem. Soc.* **2011**, *158*, A343−A351.

(13) Chen, J.; Hummelshøj, J. S.; Thygesen, K. S.; Myrdal, J. S.; Nørskov, J. K.; Vegge, T. The Role of Transition Metal Interfaces on the Electronic Transport in Lithium-air Batteries. *Catal. Today* **2011**, *165*, 2−9.

(14) Varley, J. B.; Viswanathan, V.; Nørskov, J. K.; Luntz, A. C. Lithium and Oxygen Vacancies and Their Role in $Li_2O_2$ Charge Transport in Li-$O_2$ Batteries. *Energy Environ. Sci.* **2014**, *7*, 720−727.

(15) Wang, Z.; Sun, J.; Cheng, Y.; Niu, C. Adsorption and Deposition of $Li_2O_2$ on TiC{111} Surface. *J. Phys. Chem. Lett.* **2014**, *5*, 3919−3923.

(16) Kang, S.; Mo, Y.; Ong, S. P.; Ceder, G. Nanoscale Stabilization of Sodium Oxides: Implications for Na-$O_2$ Batteries. *Nano Lett.* **2014**, *14*, 1016−1020.

(17) Kang, J.; Jung, Y. S.; Wei, S.-H.; Dillon, A. C. Implications of the Formation of Small Polarons in $Li_2O_2$ for Li-air Batteries. *Phys. Rev. B: Condens. Matter Mater. Phys.* **2012**, *85*, 035210.

(18) Ong, S. P.; Mo, Y.; Ceder, G. Low Hole Polaron Migration Barrier in Lithium Peroxide. *Phys. Rev. B: Condens. Matter Mater. Phys.* **2012**, *85*, 081105.

(19) Jones, R. O.; Gunnarsson, O. The Density Functional Formalism, Its Applications and Prospects. *Rev. Mod. Phys.* **1989**, *61*, 689−746.

(20) Hammer, B.; Hansen, L. B.; Nørskov, J. K. Improved Adsorption Energetics within Density-functional Theory using Revised Perdew-Burke-Ernzerhof Functionals. *Phys. Rev. B: Condens. Matter Mater. Phys.* **1999**, *59*, 7413−7421.

(21) Klüpfel, S.; Klüpfel, P.; Jónsson, H. The Effect of the Perdew-Zunger Self-interaction Correction to Density Functionals on the Energetics of Small Molecules. *J. Chem. Phys.* **2012**, *137*, 124102.

(22) Blöchl, P. E. First-principles Calculations of Defects in Oxygen-deficient Silica Exposed to Hydrogen. *Phys. Rev. B: Condens. Matter Mater. Phys.* **2000**, *62*, 6158−6179.

(23) Rossmeisl, J.; Logadottir, A.; Nørskov, J. Electrolysis of Water on (Oxidized) Metal Surfaces. *Chem. Phys.* **2005**, *319*, 178−184.

(24) Kurth, S.; Perdew, J. P.; Blaha, P. Molecular and Solid-state Tests of Density Functional Approximations: LSD, GGAs, and meta-GGAs. *Int. J. Quantum Chem.* **1999**, *75*, 889−909.

(25) Wang, L.; Maxisch, T.; Ceder, G. Oxidation Energies of Transition Metal Oxides within the GGA + U Framework. *Phys. Rev. B: Condens. Matter Mater. Phys.* **2006**, *73*, 195107.

(26) Yan, J.; Hummelshøj, J. S.; Nørskov, J. K. Formation Energies of Group I and II Metal Oxides using Random Phase Approximation. *Phys. Rev. B: Condens. Matter Mater. Phys.* **2013**, *87*, 075207.

(27) Kresse, G.; Furthmüller, J. Efficient Iterative Schemes for *ab initio* Total-energy Calculations using a Plane-wave Basis Set. *Phys. Rev. B: Condens. Matter Mater. Phys.* **1996**, *54*, 11169−11186.

(28) Blöchl, P. E. Projector Augmented-wave Method. *Phys. Rev. B: Condens. Matter Mater. Phys.* **1994**, *50*, 17953−17979.

(29) Kresse, G.; Joubert, D. From Ultrasoft Pseudopotentials to the Projector Augmented-wave Method. *Phys. Rev. B: Condens. Matter Mater. Phys.* **1999**, *59*, 1758−1775.

(30) Klimeš, J. c. v.; Bowler, D. R.; Michaelides, A. van der Waals Density Functionals Applied to Solids. *Phys. Rev. B: Condens. Matter Mater. Phys.* **2011**, *83*, 195131.

(31) Dudarev, S. L.; Botton, G. A.; Savrasov, S. Y.; Humphreys, C. J.; Sutton, A. P. Electron-energy-loss Spectra and the Structural Stability of Nickel Oxide: An LSDA+U Study. *Phys. Rev. B: Condens. Matter Mater. Phys.* **1998**, *57*, 1505−1509.

(32) Nakamura, H.; Hayashi, N.; Nakai, N.; Okumura, M.; Machida, M. First-principle Electronic Structure Calculations for Magnetic Moment in Iron-based Superconductors: An LSDA+Negative U Study. *Phys. C* **2009**, *469*, 908−911.

(33) Perdew, J. P.; Burke, K.; Ernzerhof, M. Generalized Gradient Approximation Made Simple. *Phys. Rev. Lett.* **1996**, *77*, 3865−3868.




DOI: 10.1021/acs.jpcc.5b05968
J. Phys. Chem. C 2015, 119, 17596−17601

(34) Dion, M.; Rydberg, H.; Schröder, E.; Langreth, D. C.; Lundqvist, B. I. Van der Waals Density Functional for General Geometries. *Phys. Rev. Lett.* **2004**, *92*, 246401.
(35) Lee, K.; Murray, E. D.; Kong, L.; Lundqvist, B. I.; Langreth, D. C. Higher-accuracy van der Waals Density Functional. *Phys. Rev. B: Condens. Matter Mater. Phys.* **2010**, *82*, 081101.
(36) Wellendorff, J.; Lundgaard, K. T.; Møgelhøj, A.; Petzold, V.; Landis, D. D.; Nørskov, J. K.; Bligaard, T.; Jacobsen, K. W. Density Functionals for Surface Science: Exchange-correlation Model Development with Bayesian Error Estimation. *Phys. Rev. B: Condens. Matter Mater. Phys.* **2012**, *85*, 235149.
(37) Krukau, A. V.; Vydrov, O. A.; Izmaylov, A. F.; Scuseria, G. E. Influence of the Exchange Screening Parameter on the Performance of Screened Hybrid Functionals. *J. Chem. Phys.* **2006**, *125*, 224106.
(38) Kümmel, S.; Kronik, L. Orbital-dependent Density Functionals: Theory and Applications. *Rev. Mod. Phys.* **2008**, *80*, 3−60.
(39) Perdew, J. P.; Yue, W. Accurate and Simple Density Functional for the Electronic Exchange Energy: Generalized Gradient Approximation. *Phys. Rev. B: Condens. Matter Mater. Phys.* **1986**, *33*, 8800−8802.
(40) Naghavi, S. S. *Theoretical Study of Correlated Systems Using Hybrid Functionals*. Ph.D. Thesis, Johannes Gutenberg-Universität, Mainz, 2010.
(41) Winterlik, J.; Fecher, G. H.; Jenkins, C. A.; Medvedev, S.; Felser, C.; Kübler, J.; Mühle, C.; Doll, K.; Jansen, M.; Palasyuk, T.; et al. Exotic Magnetism in the Alkali Sesquioxides $Rb_4O_6$ and $Cs_4O_6$. *Phys. Rev. B: Condens. Matter Mater. Phys.* **2009**, *79*, 214410.
(42) Martínez, J. I.; Hansen, H. A.; Rossmeisl, J.; Nørskov, J. K. Formation Energies of Rutile Metal Dioxides using Density Functional Theory. *Phys. Rev. B: Condens. Matter Mater. Phys.* **2009**, *79*, 045120.
(43) *NIST Chemistry WebBook, NIST Standard Reference Database Number 69*; Linstrom, P. J., Mallard, W. G., Eds.; National Institute of Standards and Technology: Gaithersburg, MD, 2005.
(44) Tang, W.; Sanville, E.; Henkelman, G. A Grid-based Bader Analysis Algorithm without Lattice Bias. *J. Phys.: Condens. Matter* **2009**, *21*, 084204.



DOI: 10.1021/acs.jpcc.5b05968
*J. Phys. Chem. C* 2015, 119, 17596−17601

# Paper II

---

Thermodynamic and Kinetic Limitations for Peroxide and Superoxide Formation in $Na–O_2$ Batteries
Yedilfana S. Mekonnen, Rune Christensen, Juan M. Garcia-Lastra, and Tejs Vegge
*In preparation*

The author of this thesis contributed section 3.1 and applied metal-chloride references.

# Thermodynamic and Kinetic Limitations for Peroxide and Superoxide Formation in Na–$O_2$ Batteries

Yedilfana S. Mekonnen[2], Rune Christensen[1], Juan M. Garcia-Lastra[1], Tejs Vegge[1*]

[1]Department of Energy Storage, Technical University of Denmark, Fysikvej, Building 309, 2800 Kgs Lyngby, Denmark

[2]Center for Environmental Science, College of Natural and Computational Sciences, Addis Ababa University, Addis Ababa, Ethiopia

[*]Corresponding Author E-mail: teve@dtu.dk

## Abstract

The Na–$O_2$ system holds great potential as a low cost, high energy density battery, but under normal operating conditions, the discharge is limited to sodium superoxide ($NaO_2$), whereas the high capacity peroxide ($Na_2O_2$) remains elusive. Here, we apply density functional theory calculations with an improved error-correction scheme to determine equilibrium potentials and free energies as a function of temperature for the different phases of $NaO_2$ and $Na_2O_2$, identifying $NaO_2$ as the thermodynamically preferred discharge product up to ~120 K, after which $Na_2O_2$ is thermodynamically preferred. We also investigate the reaction mechanisms and resulting electrochemical overpotentials on stepped surfaces of the $NaO_2$ and $Na_2O_2$ systems, showing low overpotentials for $NaO_2$ formation ($\eta_{dis}$ = 0.14 V) and depletion ($\eta_{cha}$ = 0.19 V), whereas the overpotentials for $Na_2O_2$ formation ($\eta_{dis}$= 1.05 V) and depletion ($\eta_{cha}$ = 0.67 V) are found to be prohibitively high. These findings are in good agreement with experimental data on the thermodynamic properties of the $Na_xO_2$ species and provide a kinetic explanation for why $NaO_2$ is the main discharge product in Na–$O_2$ batteries under normal operating conditions.

**Key Words:** Na–$O_2$ batteries, DFT, Thermodynamic and Kinetic, Overpotential

# I. Introduction

In the last decade, significant efforts have been paid to the development of next generation battery technologies. In particular metal–air batteries (e.g. Li–, Na–, Mg–, Al–, Fe– and Zn–$O_2$ batteries) in either aqueous or non-aqueous (aprotic) electrolytes have gained significant attention,[1,2] especially for its possible use in electric vehicles. The cost of commercially available Li–ion batteries is generally too high and the energy storage capacity too low to solve the increasing demands on batteries for sustainable transportation [3]. Metal–air batteries have high theoretical specific energies since the technology, once mature, would apply metal as the anode and oxygen gas from air on the cathode side. The discharge products are generally peroxides and/or superoxides, depending on the experimental conditions and cell components used in the system. The oxygen reduction (ORR) and oxygen evolution reaction (OER) are the two main reactions taking place reversibly during discharge and charge, respectively. However, metal–air battery technologies are limited by a number of drawbacks and challenges, which must be resolved before becoming commercially viable, i.e. low accessible capacity (sudden death), poor electronic conductivity and rechargeability, limited chemical and electrochemical stability of electrodes [4,5], electrolytes [6] and salts [7], and high sensitivity to air impurities such as water and $CO_2$. [8–13]

Among the rechargeable metal-oxygen battery systems reported so far, the Li–$O_2$ couple offers higher equilibrium potential (~2.96 V) and specific capacity (~3,842 mAh/g), which is comparable to the gravimetric energy density of gasoline [14] and nearly an order of magnitude higher than current Li–ion batteries. [15] However, in practice, non-aqueous Li–$O_2$ batteries suffer from poor rechargeability and high overpotentials, particularly for the charging process. [16,17]Although the capacity and equilibrium potential is lower, the Na–$O_2$ battery system displays certain advantages over the Li–$O_2$ battery and similar batteries. The non-aqueous secondary Na–$O_2$ battery operates at low dis/charge overpotentials (< 200 mV) even at higher current densities (0.2 mA/cm$^2$) and yields high electrical energy efficiency (90 %), which can be observed over multiple cycles. [18–22] The theoretical specific capacity of the Na–$O_2$ battery is ~1,500 mAh/g [20], when $NaO_2$ is deposited on carbon nanotubes. If, however, the peroxide, $Na_2O_2$, could be formed reversibly as for Li–$O_2$, it would be possible to increase the specific capacity to ~2,800 mAh/g. [23]

Hartmann *et al*. [19,24], McCloskey *et al*. [25] and Tarascon *et al.* [26] have reported sodium superoxide ($NaO_2$) as the dominant reaction product. Whereas, Kim *et al.* [23], Li *et al*. [27], Lie *et al*. [28] and Hu *et al*. [29] have reported sodium peroxide ($Na_2O_2$) as the dominant discharge product. Poor rechargeability (< 10 cycles) and high charging overpotential (> 1.3 V) is exhibited when $Na_2O_2$ is formed at the cathode at room temperature, which are similar to the drawbacks observed in the

Li–$O_2$ system. However, sufficiently lower dis/charge overpotentials and higher rechargeability are observed when $NaO_2$ is formed. [20] Moreover, it has been also argued on the basis of density functional theory (DFT) calculations that the reason for $NaO_2$ formation over $Na_2O_2$ could be due to the poor conduction and differences in conduction mechanism [30], solvents[31] and the presence of proton sources like water. [32]

Scanning electron microscopy (SEM) images have revealed that highly ordered cubic $NaO_2$ particles are grown at the carbon cathode surface. [19, 24, 25] A computational study by Kang *et al.* reports that $NaO_2$ is more stable at the nanoscale level (up to about 5 nm), whereas bulk $Na_2O_2$ is thermodynamically stable at standard conditions (in agreement with experimental observations). For electrochemical growth during battery discharge, the size of the $NaO_2$ particles is, however, found in the micrometer range (1-50 μm).[19] The observed stoichiometry of the particles can therefore not be explained solely from the effect of the differences in surface energy, nor the effect of e.g. increased oxygen partial pressure or temperature, which may lead to the formation of somewhat larger $NaO_2$ particles (up to 20 nm based on the calculations by Kang *et al*. [33]). This is further supported by the reported effect of the discharge rate on the sizes and distribution of $NaO_2$ on carbon nanotubes, where relatively small sizes (~50–500 nm) with a wide distribution are observed at low rate and large sizes (~2 μm) with a narrow distribution are observed at higher rates. [34]

Regarding the $NaO_2$ charge/discharge mechanism, Hartmann *et al.* have reported computational and experimental work, which indicates that large amounts of $NaO_2$ can be formed at the cathode. This is due to high solubility of $NaO_2$ in the liquid electrolyte, i.e. forming superoxide ions ($O_2^-$), followed by precipitation in the presence of sodium ions to form solid sodium superoxide. Therefore, the discharge mechanism may also follow a solution-precipitation mechanism in addition to the direct electrochemical growth of $NaO_2$ investigated here.[26,35]

The reaction for non-aqueous Na–$O_2$ cathode electrochemistry using ether based electrolytes like diglyme, is shown below. [25]

$$Na^+ + e^- + O_2 \leftrightarrow NaO_2, \qquad E^o = 2.27 \text{ V vs. } Na/Na^+$$

Here, we apply DFT calculations to investigate the thermodynamic and kinetic properties of the materials and reactions in Na–$O_2$ batteries. We will discuss the thermodynamic stability and kinetic overpotentials for the growth/depletion pathways of $NaO_2$ and $Na_2O_2$ on selected stepped model surfaces, i.e. (001) for $NaO_2$ and $(1\bar{1}00)$ for $Na_2O_2$ and the equilibrium potential of different phases of bulk $NaO_2$ and $Na_2O_2$ as a function of temperature. The stepped surfaces are likely to give

accessible barriers and favorable nucleation sites for the minimum overpotential mechanism, as it has been reported in case of Li–$O_2$. [36]

It should be noted that the correct description of the thermodynamics of reactions involving superoxide vs. peroxide species (i.e. to describe the relative stability of $NaO_2$ vs. $Na_2O_2$ at finite temperatures) is computationally challenging, mainly due to the precession of misaligned superoxide species in the high temperature pyrite phase of $NaO_2$ (Fm3m above 231 K) relative to the low temperature pyrite phase ($Pa\bar{3}$, between 200 K and 231 K) (see Figure 1). Such effects and energetics are generally not accounted for in standard density functional theory (DFT) calculations, making it highly challenging to calculate the stability at finite temperatures. Systematic work on the modeling of alkali superoxides and peroxides using DFT+U and hybrid functional calculations is currently ongoing, but in the following, we describe a comparatively simple GGA-level computational approach using metal chloride reference energies [37], which yields excellent agreement with the experimental observations.

## II. COMPUTATIONAL METHODOLOGY

Calculations are performed using the PBE (Perdew-Burke-Ernzerhof) [38] exchange correlation functional as implemented in the GPAW package [39] using the Atomic Simulation Environment (ASE). [40] A real space grid basis set on the projector augmented wave (PAW) function method with frozen core approximation has been used with 0.18 Å grid point spacing. [41,42] Dipole corrections have been applied in the direction perpendicular to the slab surface and ionic optimization converged to a maximum residual force of 0.03 eV/Å. The $NaO_2$ growth/depletion mechanism is studied on the stepped (001) surface of $NaO_2$ in the $\mathrm{Pa}\bar{3}$ space group, thus neglecting the precession of the superoxide ions. We have used the ferromagnetic phase of $NaO_2$ in all the calculations (i.e., the initial magnetic moment value of each O atom in $NaO_2$ was set to 0.5 since previous theoretical studies reported it to be more stable than the antiferromagnetic phase by 15 meV per formula unit. [30] The k-points are sampled with a $2 \times 4 \times 1$ Monkhorst-Pack mesh and the supercell consists of 60-72 atoms. A vacuum layer of 21.2 Å is used. A stepped $(1\bar{1}00)$ surface of $Na_2O_2$ (space group $\mathrm{P}\bar{6}2\mathrm{m}$) with a super cell consisting of a 88-96 atoms slab with a 20 Å vacuum layer is used to study the $Na_2O_2$ growth/depletion mechanisms. This surface termination has been extensively studied in pristine form as well as in the presence of defects like steps and kinks for Li–$O_2$. [10,36,43–46] The k-points are sampled with a $2 \times 2 \times 1$ Monkhorst-Pack mesh.

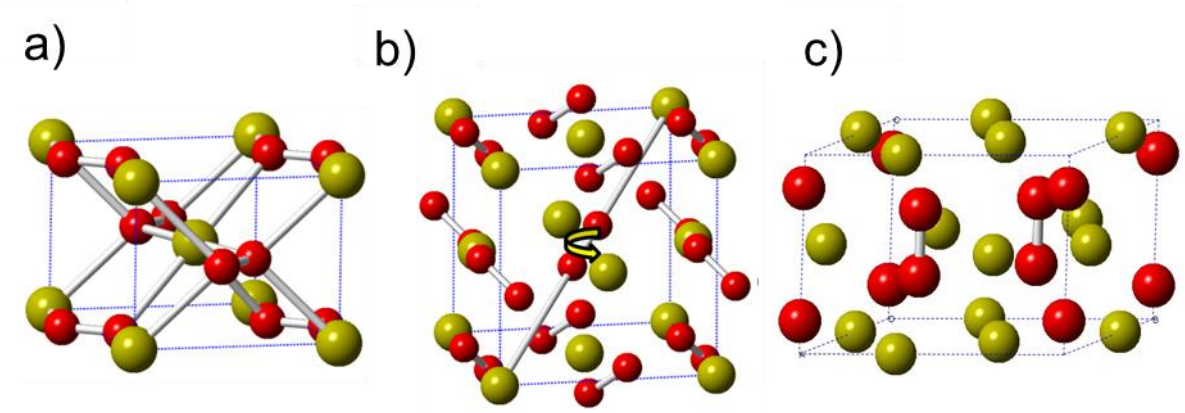


Figure 1: a) *Pnnm* $NaO_2$ orthorhombic structure (Marcasite) with lattice constants a = 4.26 Å, b = 5.44 Å, c = 3.36 Å. b) Face-centered cubic $\boldsymbol{Pa\bar{3}}$ $NaO_2$ structure (Pyrite) with lattice constant a = 5.523 Å. This phase occurs between 200 K and 231 K. Above 231 K the superoxide ions hop freely between the eight equivalent (111) orientations in a cube. Thus, the space group becomes Fm3m above 231 K. c) Hexagonal $Na_2O_2$ structure space group of $\boldsymbol{P\bar{6}_2m}$ with lattice constants of a = 6.39 Å, b = 6.39 Å and c = 4.6 Å. Color: Yellow (Sodium), Red (Oxygen).

The computational sodium electrode approach is used in the free energy calculations, analogous to the lithium electrode approach used for Li–air batteries. [43,47] At zero potential, U = 0, the bulk Na anode and Na ions in solution are assumed to be in equilibrium ($Na \leftrightarrow Na^+ + e^-$). The free energy change of the reaction is shifted by –neU at an applied bias, where n is the number of electrons transferred.

At neutral bias, all reaction steps are downhill in free energy, but at a given potential, the free energy difference changes for each step calculated as,

$$\Delta G_{i,U} = \Delta G_i - eU \quad (1)$$

The limiting discharge potential ($U_{discharge}$) is the lowest free energy step, $\Delta G_{i,min}$, along the reaction path, as this the first step to becomes uphill at a given potential. Likewise, the largest free energy step, $\Delta G_{i,max}$, that is last to become downhill for the reverse charging reaction giving the limited charge potential ($U_{charge}$):

$$U_{discharge} = \min[-\Delta G_i/e] \text{ and } U_{charge} = \max[-\Delta G_i/e] \quad (2)$$

The calculated effective equilibrium potential can be obtained as Uo = ΔG/ne.

Large systematic errors in the DFT description of superoxides, peroxides and monoxides have previously been documented by various groups and accounted for in various ways. [36,33,37] Here, we

adopt the recent approach of Christensen *et al*. [37] using NaCl as an indirect reference for sodium in order to better account for the oxidation state of Na in the Na–$O_2$ system. In line with Christensen *et al*. [37] an energy correction is applied to $O_2$ (g), which is notoriously difficult to describe correctly with DFT. With the computational approach used here, the optimal energy correction of $O_2$ (g) is −0.33 eV. The approach is chosen as it reduces the systematic errors significantly, while allowing consistent calculation of surfaces with oxide species in different oxidation states required for studying reactions in Na–$O_2$ batteries.

# III. RESULTS AND DISCUSSIONS

## 3.1. Enthalpy of Formation and Equilibrium Potential

To evaluate the accuracy of the calculations, bulk enthalpies of formation are compared with experiments [48] as seen in Table 1. The calculated formation enthalpies are converted to free energies at standard conditions ($\Delta H_{form} \rightarrow \Delta G_{form}$) using experimental entropies [48] and the equilibrium potentials are then calculated. As an alternative to using the experimental entropies, we also determine the equilibrium potentials using the simple approximation that the entropy can be described without explicitly considering the vibrational contributions to the entropy, as they are similar in $O_2$ (g) and the $O_2^-$ and $O_2^{2-}$ ions. As the superoxide ions are known to rotate easily in the $NaO_2$ pyrite phase at room temperature, the rotational degrees of freedom will to a good approximation also be similar for $O_2$ (g) and the superoxide ions. This is not the case for $Na_2O_2$, where the orientation of peroxide ions is well-defined at all relevant temperatures. This simple approximation has obvious flaws, e.g. will it not be able to capture the low temperature structural changes of $NaO_2$ due to differences in the rotational degrees of freedom of superoxide ions in different phases. It does, however, have the advantage of being simple to calculate with standard thermodynamic approaches. Comparison with experiment also proves the simple assumption to be reasonable (see Figure 2). It can also be seen that the experimental data for $NaO_2$ at 0 K is identical to the calculated result for the low temperature *Pnnm* structure.

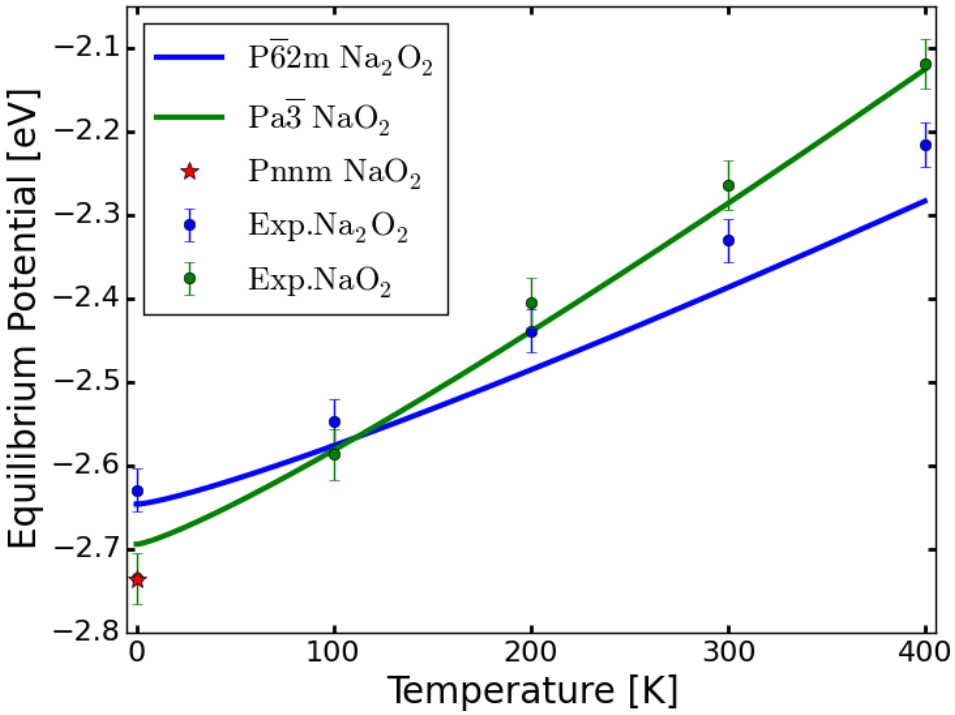


Figure 2: DFT-based equilibrium potentials predicted with the approximation that the temperature dependence is only due to the translational and rotational degrees of freedom for $O_2$ (g). This simple approximation is in good agreement with experimental data and reproduces relatively small free energy differences between $Na_2O_2$ and $NaO_2$.

As seen in Table 1, the difference in equilibrium potential for $NaO_2$ and $Na_2O_2$ at standard conditions is less than 0.1 V for the experimental results, the calculated enthalpies with experimental entropies, and the purely theoretical calculations with approximated entropies. This indicates that required overpotentials in the electrochemical reactions to $Na_2O_2$ and $NaO_2$ could be decisive for the product selectivity.

Table 1: Calculations for $Na_2O_2$ and the pyrite phase of $NaO_2$ are compared with experimental values [48] in parentheses. Equilibrium potentials are calculated both using experimental entropies ($U_{0,\ exp\ \Delta S}$) and with a simple approximation to temperature dependence ($U_{0,\ approx.\ \Delta S}$).

| | $\Delta_f H°$ [eV] ($\Delta_f H°_{exp}$) | $U_{0,\ exp.\ \Delta S}$ [V] ($U_{0,\ exp}$) | $U_{0,\ approx.\ \Delta S}$ [V] |
|---|---|---|---|
| $\boldsymbol{Pa\bar{3}}$ $NaO_2$ | -2.74 (-2.71) | -2.30 (-2.27) | -2.29 |
| $\boldsymbol{P\bar{6}2m}$ $Na_2O_2$ | -5.29 (-5.32) | -2.32 (-2.33) | -2.39 |

### 3.2. $NaO_2$ Growth/Depletion Mechanisms on Stepped Surfaces

The thermochemical properties of the four steps in the $NaO_2$ growth/depletion are investigated on a stepped $(001)$ $NaO_2$ surface. The method does not include specific effects of the electrolyte or possible kinetic barriers associated with the transport of the ions/molecules. DFT calculations can determine the preferred pathways for the discharge/charge mechanisms by comparing the free energies of the adsorbed species at every single step. The stepped surface is constructed from the bulk crystal in a specific direction in such a way that four sodium superoxide species are added (removed) at the step site for the complete pathways of growth (depletion).

In general, the $NaO_2$ growth/depletion mechanisms on stepped (001) $NaO_2$ surface follows a four step mechanism; each step involving the deposition (depletion) of either Na* or $NaO_2$* species (electrochemical steps) or $O_2$ species (chemical step) and both are taken into account to generate all likely pathways. The thermodynamically favorable path, i.e. the lowest overpotential path is selected. Thus, as shown in Figure 3, the first step for the (001) surface is the adsorption of $NaO_2$ at the bottom left site. This is the potential limiting step for discharge (-2.20 V) and is followed by adsorption of the second $NaO_2$ species at the bottom right site with a binding energy of -2.42 eV; the third and the fourth $NaO_2$ species are adsorbed by -2.22 eV and -2.54 eV, respectively. The fourth step is the limiting charge potential step and the growth mechanism is completed by forming 4 sodium superoxide species with equilibrium potential of -2.34 eV. The charging or desorption process follows the same reaction steps applied in reverse order (right to left), as shown in Figure 3 and Figure 4.

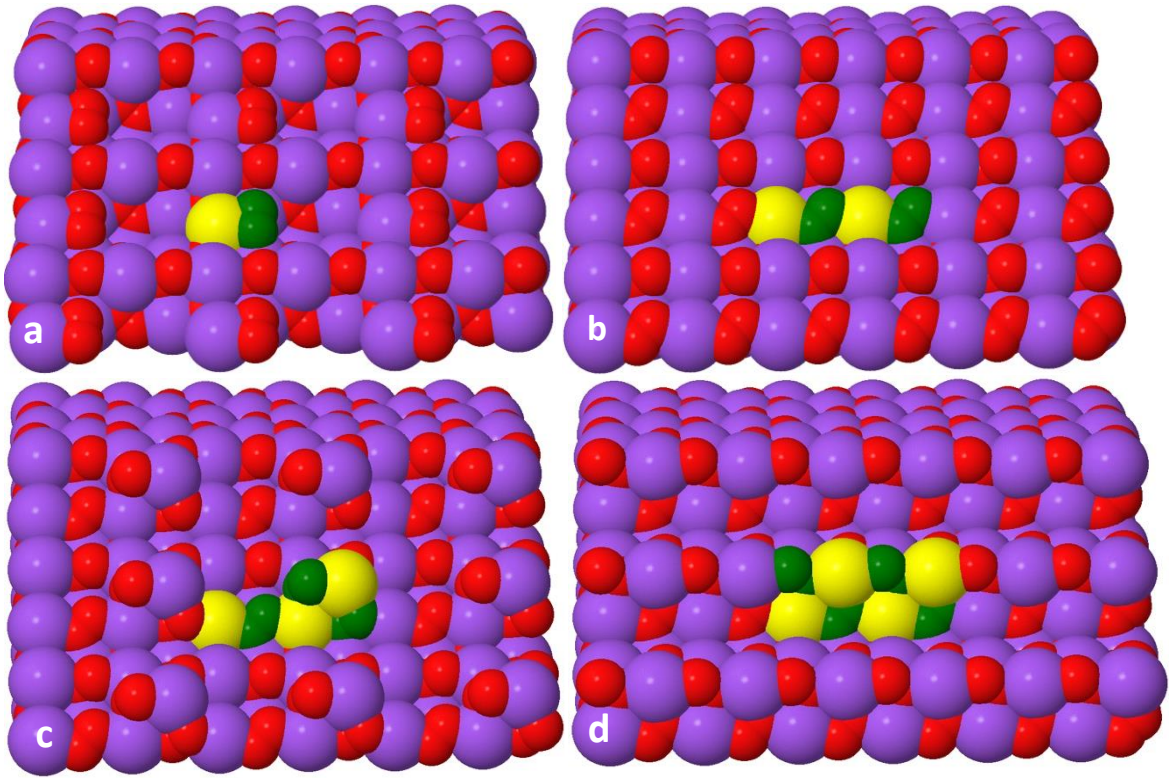


Figure 3: A 4 step growth/desorption mechanism on the (001) step surface of $NaO_2$. In a) and b) $NaO_2$ species adsorbs to the bottom site. In c) and d) $NaO_2$ adsorbs to the top site to complete the 4 formula units $NaO_2$ reaction mechanism. Color: Na (purple) and O (red). Highlighted deposited ions: Na (yellow) and O (green).

The studies of the growth/depletion mechanisms on the stepped $NaO_2$ surface revealed that the fundamental overpotentials for both charge and discharge are very low, which has also been observed experimentally <sup>25</sup><sup>25</sup><sup>25</sup><sup>25</sup>[25] A discharge (charge) overpotential of $\eta_{\mathrm{dis}} = 0.14$ V ($\eta_{\mathrm{cha}} = 0.19$ V) for the growth (depletion) mechanism is observed. The calculated equilibrium potential at the surface ($U_{o,surf}$ 2.34 V) is marginally higher than the calculated bulk value of $U_{o,bulk}$ = 2.30 V, which is expectedly a consequence of the size of the supercell.

All pathways involving a purely thermochemical step for $O_2$ ab/desorption are found to be inactive, due to high overpotential for the electrochemical steps (> 1.0 V).

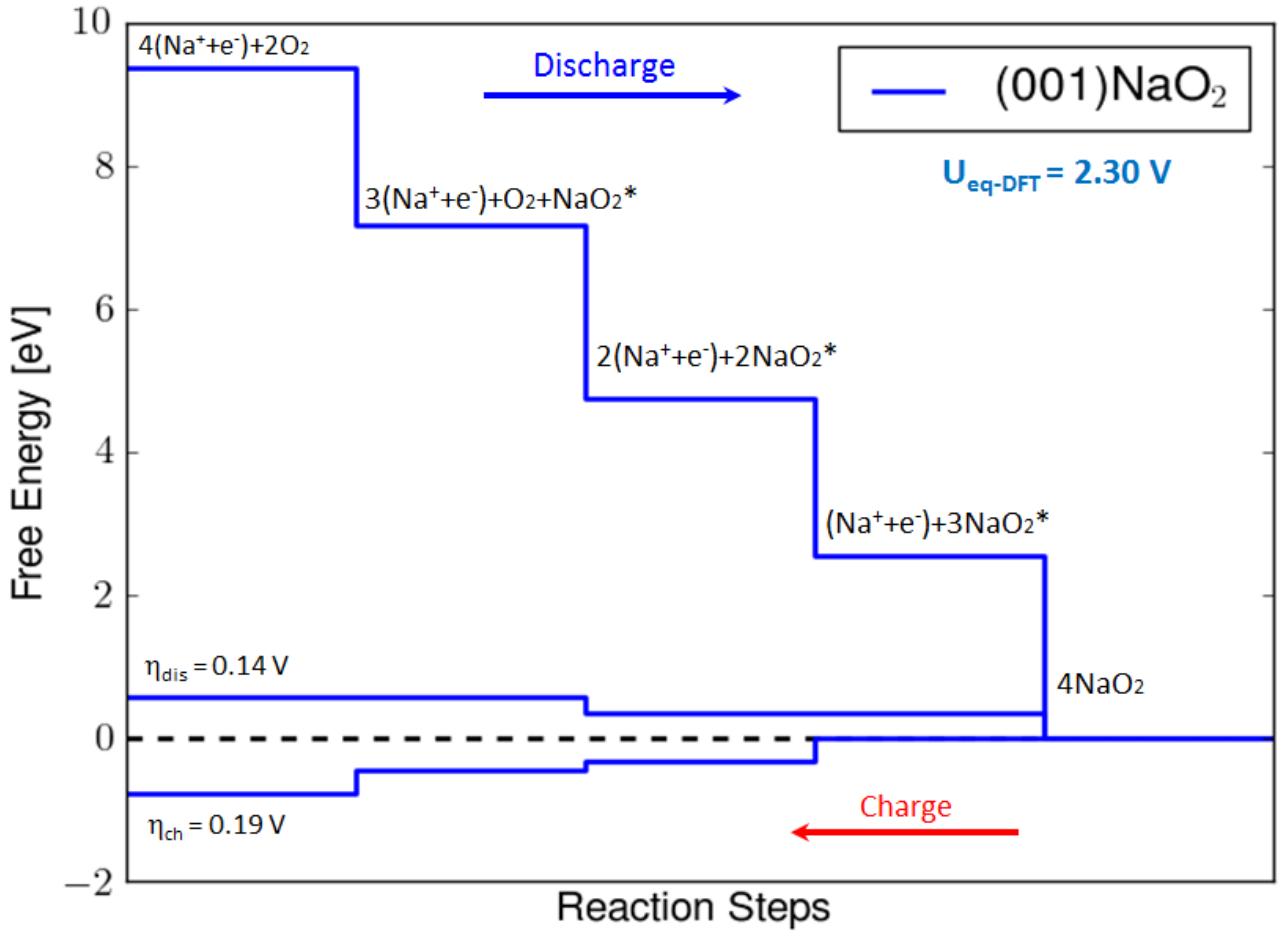


Figure 4: The calculated free energy diagram for $NaO_2$ growth/desorption mechanisms on stepped (001) $NaO_2$ surface.

### 3.3. $Na_2O_2$ Growth/Depletion Mechanisms on Stepped $(1\bar{1}00)$ Surfaces

The $Na_2O_2$ discharge and charge pathways are studied on a stepped $(1\bar{1}00)$ $Na_2O_2$ surface. Several pathways consisting of both chemical and electrochemical species have been investigated. As illustrated in Figure 5 and 6, the preferred growth (depletion) mechanism is found to be the path that has four electrochemical species, i.e. either Na* or $NaO_2$*, adsorbed to the step surface successively to grow (deplete) two formula units of $Na_2O_2$. This path becomes possible at minimum discharge (charge) overpotential of $\eta_{dis} = 1.05$ V ($\eta_{cha} = 0.67$ V). The first step is adsorption of Na* species (Figure 5a) with a binding energy of 2.67 eV and followed by the addition of $NaO_2$* (Figure 5b) with a binding energy of 3.00 eV, which is the potential limiting step for the charge process. The last two steps are additions of $NaO_2$* and Na*, respectively, with binding energies of 2.36 eV and 1.28 eV (the last step is the potential limiting step for discharge), as shown

in Figures 5c and 5d. The full growth mechanism is accomplished with the growth of two formula units of $Na_2O_2$ at the step surface with an equilibrium potential of $U_0$ = 2.32 V. The calculated equilibrium potential is here in agreement with that calculated for bulk $Na_2O_2$. The charging process follows the same reaction steps as the discharge but in reverse order (from d to a in Figure 5 and right to left in Figure 6). All pathways involving a purely thermochemical step are found to be inactive due to high overpotential for the electrochemical steps (> 1.5 V). The identified growth mechanism is similar to the one previously reported for $Li_2O_2$, [10,43] but the fundamental overpotentials for charge/discharge of $Na_2O_2$ are found to be substantially higher than those for $Li_2O_2$.

We thus find the overpotentials for growth (depletion) of $Na_2O_2$ of 1.05 V (0.67 V) to be prohibitively large compared to the low overpotential mechanism on $NaO_2$ (0.14 V and 0.19 V) and this therefore effectively blocks the formation of the thermodynamically preferred $Na_2O_2$, explaining why $NaO_2$ is the primary discharge product at standard conditions, as observed experimentally.

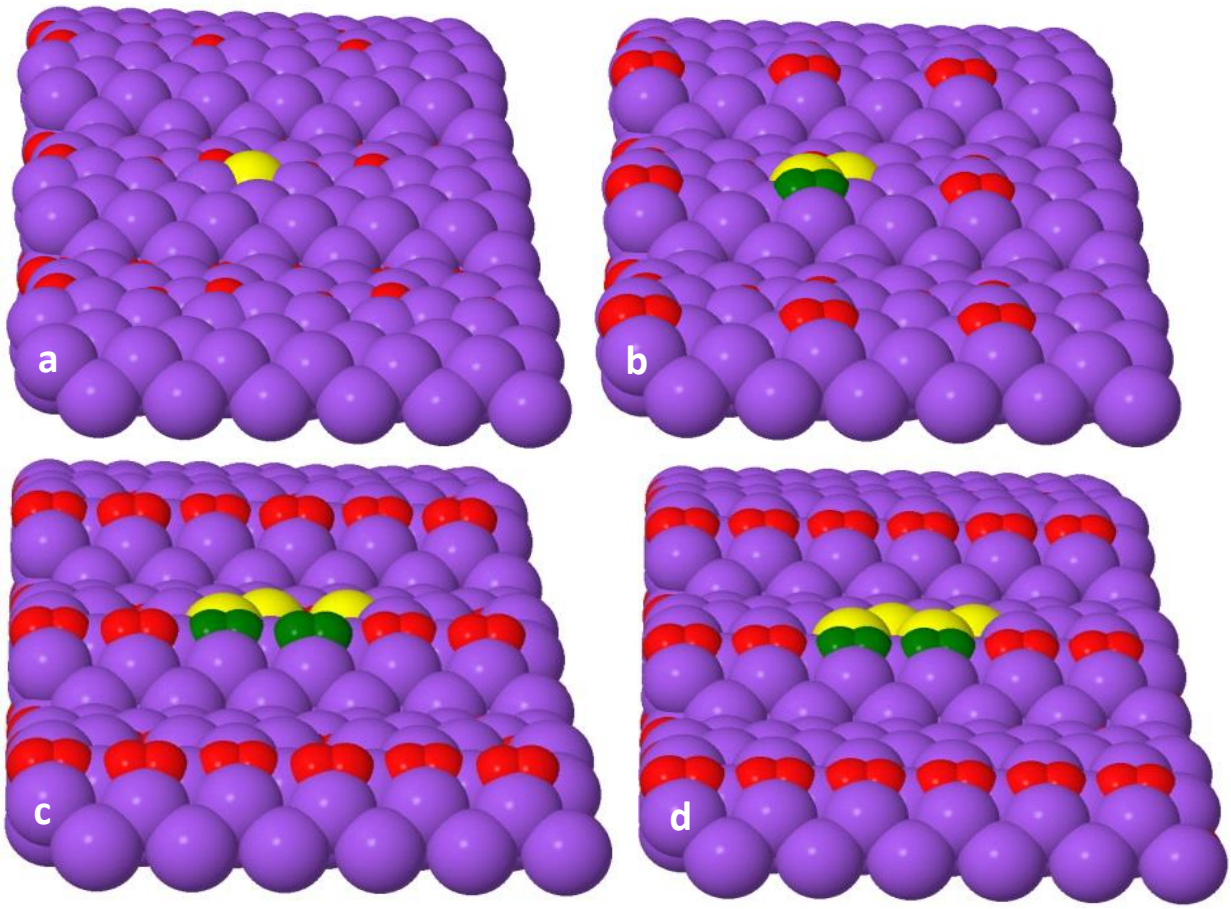


Figure 5: A 4 step $Na_2O_2$ growth pathway on a stepped $Na_2O_2$ $(1\bar{1}00)$ surface during discharge. a) Na b) $NaO_2$ c) $NaO_2$ and d) Na consecutively adsorbs to the step surface to complete the growth of 2 formula units of $Na_2O_2$. Color: Na (purple) and O (red). Highlighted deposited ions: Na (yellow) and O (green).

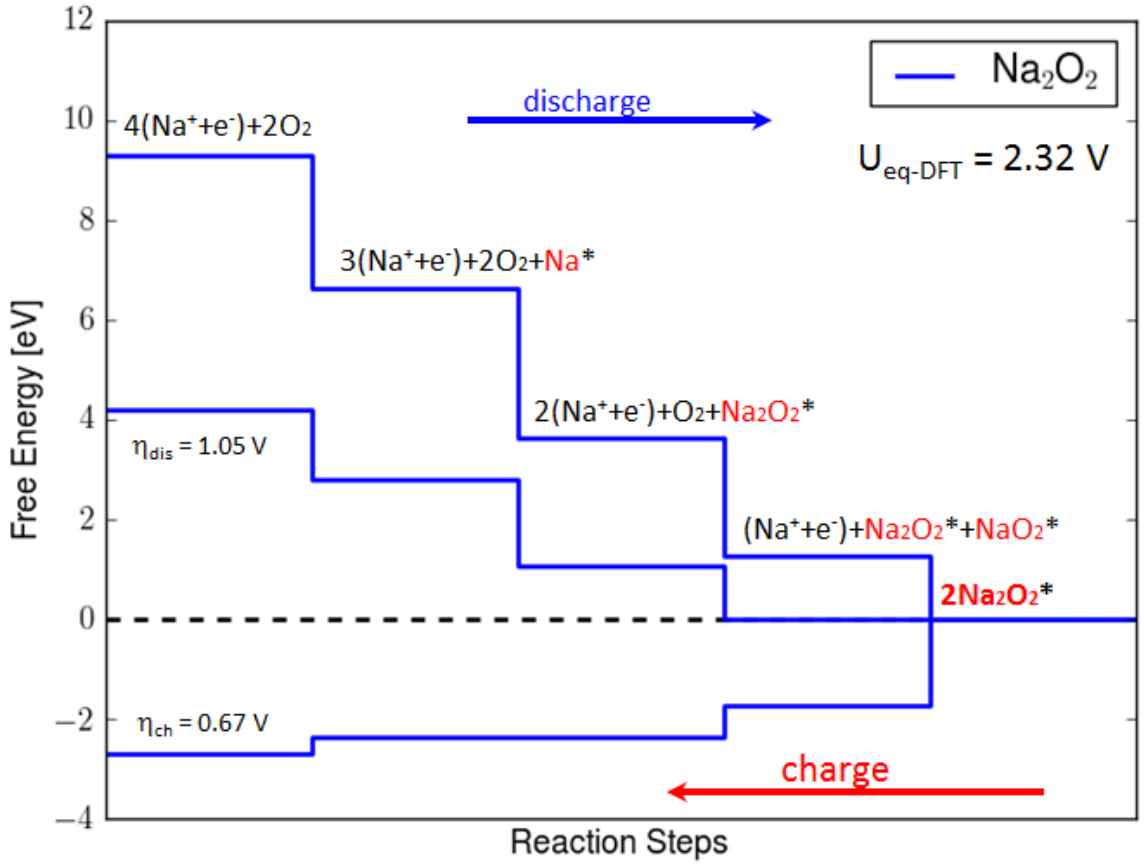


Figure 6: Calculated free energy diagrams for a four step $Na_2O_2$ growth mechanism on a stepped $(1\bar{1}00)$ $Na_2O_2$ surface, resulting in discharge (charge) overpotential of $\eta_{dis} = 1.05$ V ($\eta_{cha} = 0.67$ V).

## IV. CONCLUSIONS

The equilibrium potential and free energy as a function of temperature for different phases of $NaO_2$ and $Na_2O_2$, as well as the discharge and charge pathway mechanisms on selected stepped surfaces have been investigated computationally using DFT calculations. Using a new metal chloride reference scheme, which accounts for the change in the oxidation state of the metal atoms, and a simple approximation to the entropic contributions, it is possible to describe the free energies of formation as a function of temperature for $NaO_2$ and $Na_2O_2$ in good agreement with experimental data. The experimentally found reaction product at room temperature, i.e. $NaO_2$, is slightly less thermodynamically stable than the expected $Na_2O_2$ product, but we show that the formation and depletion of $Na_2O_2$ is limited by large discharge and charge overpotentials of $\eta_{dis}$= 1.05 V and $\eta_{cha}$ = 0.67 V), respectively. In contrast, the overpotentials for formation and dissolution of $NaO_2$ are small ($\eta_{dis}$= 0.14 V and $\eta_{cha}$= 0.19 V). The large difference in

overpotentials, compared to the small difference of 0.10 eV in equilibrium potential can explain how epitaxial growth during discharge of a Na–$O_2$ battery results in the formation of sodium superoxide ($NaO_2$) as a dominant discharge product over the thermodynamically more stable $Na_2O_2$ in non-aqueous Na–$O_2$ batteries as observed in experiments.

Finally, it is important to note that the effect of the solvent is not included in the present analysis and, e.g. the solvent-solute interaction and/or the interaction with water impurities will likely also influence the product formation.

## Acknowledgements

The authors acknowledge support of this work from the ReLiable project (project nr. 11-116792) funded by the Danish Council for Strategic Research Programme Commission on Sustainable Energy and Environment. J.M.G.-L. acknowledges support from the Spanish Ministry of Economy and Competitiveness under projects FIS2012-30996 and FIS2010-21282-C02-01 and from the Mat4Bat project founded by Villum Foundation Young Investigators Program (Project No.10096).

## References

(1) Lee, J.-S.; Tai Kim, S.; Cao, R.; Choi, N.-S.; Liu, M.; Lee, K. T.; Cho, J. Metal-Air Batteries with High Energy Density: Li-Air versus Zn-Air. *Adv. Energy Mater.* **2011**, 1, 34–50.

(2) Whittingham, M. S. *Metal-Air Batteries: A Reality Check. Meeting Abstract*; **2012**; 1099.

(3) Linden, D.; Reddy, T. B. *HANDBOOK OF BATTERIES*, Third Edit.; McGraw-Hill, **2001**.

(4) Mekonnen, Y. S.; Garcia-Lastra, J. M.; Hummelshøj, J. S.; Jin, C.; Vegge, T. Role of $Li_2O_2$@$Li_2CO_3$ Interfaces on Charge Transport in Non-Aqueous Li-Air Batteries. *J. Phys. Chem. C* **2015**, 119, 18066–18073.

(5) Mccloskey, B. D.; Speidel, A.; Scheffler, R.; Miller, D. C.; Viswanathan, V.; Hummelshøj, J. S.; Nørskov, J. K.; Luntz, A. C. Twin Problems of Interfacial Carbonate Formation in Nonaqueous. *J. Phys. Chem. Lett.* **2012**, 3, 997–1001.

(6) Younesi, R.; Norby, P.; Vegge, T. A New Look at the Stability of Dimethyl Sulfoxide and Acetonitrile in Li-$O_2$ Batteries. *ECS Electrochem. Lett.* **2014**, 3, A15–A18.

(7) Younesi, R.; Veith, G. M.; Johansson, P.; Edström, K.; Vegge, T. Lithium Salts for Advanced Lithium Batteries: Li–metal, Li–$O_2$ , and Li–S. *Energy Environ. Sci.* **2015**, 8, 1905–1922.

(8) Girishkumar, G.; McCloskey, B.; Luntz, a. C.; Swanson, S.; Wilcke, W. Lithium−Air Battery: Promise and Challenges. *J. Phys. Chem. Lett.* **2010**, 1, 2193–2203.

(9) Luntz, A. C.; Mccloskey, B. D. Nonaqueous Li − Air Batteries : A Status Report. *Chem. Rev.* **2014**, 114, 11721–11750.

(10) Mekonnen, Y. S.; Knudsen, K. B.; Mýrdal, J. S. G.; Younesi, R.; Højberg, J.; Hjelm, J.; Norby, P.; Vegge, T. Communication: The Influence of $CO_2$ Poisoning on Overvoltages and Discharge Capacity in Non-Aqueous Li-Air Batteries. *J. Chem. Phys.* **2014**, 140, 121101.

(11) Yang, S.; Knickle, H. Design and Analysis of Aluminum / Air Battery System for Electric Vehicles. **2002**, 112, 162–173.

(12) Tarascon, J. M.; Armand, M. Issues and Challenges Facing Rechargeable Lithium Batteries. *Nature* **2001**, 414, 359–367.

(13) Xu, S.; Lau, S.; Archer, L. $CO_2$ and Ambient Air in Metal-Oxygen Batteries: Steps towards Reality. *Inorg. Chem. Front.* **2015**.

(14) Balaish, M.; Kraytsberg, A.; Ein-Eli, Y. A Critical Review on Lithium-Air Battery Electrolytes. *Phys. Chem. Chem. Phys.* **2014**, 16, 2801–2822.

(15) Armand, M.; Tarascon, J. M. Building Better Batteries. *Nature* **2008**, 451, 652–657.

(16) Hojberg, J.; Knudsen, K. B.; Hjelm, J.; Vegge, T. Reactions and SEI Formation during Charging of Li-$O_2$ Cells. *ECS Electrochem. Lett.* **2015**, 4, A63–A66.

(17) Feng, N.; He, P.; Zhou, H. Critical Challenges in Rechargeable Aprotic Li- $O_2$ Batteries. *Adv. Energy Mater.* **2016**, 6, 1502303.

(18) Das, S. K.; Lau, S.; Archer, L. a. Sodium–oxygen Batteries: A New Class of Metal–air Batteries. *J. Mater. Chem.* A **2014**.

(19) Hartmann, P.; Bender, C. L.; Vračar, M.; Dürr, A. K.; Garsuch, A.; Janek, J.; Adelhelm, P. A Rechargeable Room-Temperature Sodium Superoxide ($NaO_2$) Battery. *Nat. Mater.* **2013**, 12, 228–232.

(20) Zhao, N.; Li, C.; Guo, X. Long-Life Na-$O_2$ Batteries with High Energy Efficiency Enabled by Electrochemically Splitting $NaO_2$ at a Low Overpotential. *Phys. Chem. Chem. Phys.* **2014**, 16, 15646–15652.

(21) Bender, C. L.; Hartmann, P.; Vračar, M.; Adelhelm, P.; Janek, J. On the Thermodynamics, the Role of the Carbon Cathode, and the Cycle Life of the Sodium Superoxide ($NaO_2$) Battery. *Adv. Energy Mater.* **2014**, 4, 1301863.

(22) Knudsen, K. B.; Nichols, J. E.; Vegge, T.; Luntz, A. C.; Mccloskey, B. D.; Hjelm, J. An Electrochemical Impedance Study of the Capacity Limitations in Na−$O_2$ Cells *J. Phys. Chem. C* **2016**, 120, 10799–10805.

(23) Kim, J.; Lim, H.-D.; Gwon, H.; Kang, K. Sodium-Oxygen Batteries with Alkyl-Carbonate and Ether Based Electrolytes. *Phys. Chem. Chem. Phys.* **2013**, 15, 3623–3629.

(24) Hartmann, P.; Bender, C. L.; Sann, J.; Dürr, A. K.; Jansen, M.; Janek, J.; Adelhelm, P. A Comprehensive Study on the Cell Chemistry of the Sodium Superoxide ($NaO_2$) Battery. *Phys. Chem. Chem. Phys.* **2013**, 15, 11661–11672.

(25) Mccloskey, B. D.; Garcia, J. M.; Luntz, A. C. Chemical and Electrochemical Differences in Nonaqueous Li−$O_2$ and Na−$O_2$ Batteries. *J. Phys. Chem. Lett.* **2014**, 5, 1230–1235.

(26) Lutz, L.; Yin, W.; Grimaud, A.; Corte, D. A. D.; Tang, M.; Johnson, L.; Azaceta, E.; Naylor, A. J.; Hamad, S.; Anta, J. A.; et al. High Capacity Na−$O_2$ Batteries: Key Parameters for Solution- Mediated Discharge *J. Phys. Chem. C* **2016**, 120, 20068-20076.

(27) Li, Y.; Yadegari, H.; Li, X.; Banis, M. N.; Li, R.; Sun, X. Superior Catalytic Activity of Nitrogen-Doped Graphene Cathodes for High Energy Capacity Sodium-Air Batteries. *Chem. Commun. (Camb).* **2013**, 49, 11731–11733.

(28) Liu, W.; Sun, Q.; Yang, Y.; Xie, J.-Y.; Fu, Z.-W. An Enhanced Electrochemical Performance of a Sodium-Air Battery with Graphene Nanosheets as Air Electrode Catalysts. *Chem. Commun. (Camb).* **2013**, 49, 1951–1953.

(29) Hu, Y.; Han, X.; Zhao, Q.; Du, J.; Cheng, F.; Chen, J. Porous Perovskite Calcium-Manganese Oxide Microspheres as Efficient Catalyst for Rechargeable Sodium-Oxygen Batteries. *J. Mater. Chem. A* **2015**, 3, 3320–3324.

(30) Yang, S.; Siegel, D. J. Intrinsic Conductivity in Sodium-Air Battery Discharge Phases: Sodium Superoxide vs. Sodium Peroxide. *Chem. Mater.* **2015**, 150508165039003.

(31) He, M.; Lau, K. C.; Ren, X.; Xiao, N.; Mcculloch, W. D.; Curtiss, L. A. Energy Storage Very Important Paper Concentrated Electrolyte for the Sodium –Oxygen Battery : Solvation Structure and Improved Cycle Life. *Angew. Chem. Int. Ed.* **2016**, 55, 1–6.

(32) Bender, C. L.; Schrçder, D.; Pinedo, R.; Adelhelm, P.; Janek, J. One- or Two-Electron

Transfer ? The Ambiguous Nature of the Discharge Products in Sodium–Oxygen Batteries Minireviews. *Angew. Chem. Int. Ed.***2016**, 55, 4640–4649.

(33) Kang, S.; Mo, Y.; Ong, S. P.; Ceder, G. Nanoscale Stabilization of Sodium Oxides: Implications for Na-O2 Batteries. *Nano Lett.* **2014**, 14, 1016–1020.

(34) Ortiz-Vitoriano, N.; Batcho, T. P.; Kwabi, D. G.; Han, B.; Pour, N.; Yao, K. P. C.; Thompson, C. V.; Shao-Horn, Y. Rate-Dependent Nucleation and Growth of $NaO_2$ in Na–$O_2$ Batteries. *J. Phys. Chem. Lett.* **2015**, 6, 2636–2643.

(35) Hartmann, P.; Heinemann, M.; Bender, C. L.; Graf, K.; Baumann, R.-P.; Adelhelm, P.; Heiliger, C.; Janek, J. Discharge and Charge Reaction Paths in Sodium-Oxygen Batteries: Does $NaO_2$ Form by Direct Electrochemical Growth or by Precipitation from Solution? *J. Phys. Chem. C* **2015**, 119, 22778–22786.

(36) Hummelshøj, J. S.; Luntz, A. C.; Nørskov, J. K. Theoretical Evidence for Low Kinetic Overpotentials in Li-$O_2$ Electrochemistry. *J. Chem. Phys.* **2013**, 138, 034703.

(37) Christensen, R.; Hummelshøj, J. S.; Hansen, H. A.; Vegge, T. Reducing Systematic Errors in Oxide Species with Density Functional Theory Calculations. *J. Phys. Chem. C* **2015**, 119, 17596–17601.

(38) Perdew, J. P.; Burke, K.; Ernzerhof, M. Generalized Gradient Approximation Made Simple. *Phys. Rev. Lett.* **1996**, 77, 3865–3868.

(39) Enkovaara, J.; Rostgaard, C.; Mortensen, J. J.; Chen, J.; Dułak, M.; Ferrighi, L.; Gavnholt, J.; Glinsvad, C.; Haikola, V.; Hansen, H. a; et al. Electronic Structure Calculations with GPAW: A Real-Space Implementation of the Projector Augmented-Wave Method. *J. Phys. Condens. Matter* **2010**, 22, 253202.

(40) Bahn, S. R.; Jaconsen, K. W. An Object-Oriented Scripting Interface to a Legacy Electronic Strcture Code. *Comput. Sci. Eng.* **2002**, 4, 56–66.

(41) Blochl, P. E. Projected Augmented-Wave Method. *Phys. Rev. B* **1994**, 50, 17953–17979.

(42) Mortensen, J. J.; Hansen, L. B.; Jacobsen, K. W. A Real-Space Grid Implementation of the Projector Augmented Wave Method. *Phys. Rev. B* **2005**, 71, 035109.

(43) Hummelshøj, J. S.; Blomqvist, J.; Datta, S.; Vegge, T.; Rossmeisl, J.; Thygesen, K. S.; Luntz, a C.; Jacobsen, K. W.; Nørskov, J. K. Communications: Elementary Oxygen Electrode Reactions in the Aprotic Li-Air Battery. *J. Chem. Phys.* **2010**, 132, 071101.

(44) Radin, M. D.; Rodriguez, J. F.; Tian, F.; Siegel, D. J. Lithium Peroxide Surfaces Are Metallic,

While Lithium Oxide Surfaces Are Not. *J. Am. Chem. Soc.* **2012**, 134, 1093–1103.

(45) Mýrdal, J. S. G.; Vegge, T. Selective Poisoning of Li–air Batteries for Increased Discharge Capacity. *RSC Adv.* **2014**, 4, 15671.

(46) Radin, M. D.; Rodriguez, J. F.; Siegel, D. J. Lithium Peroxide Surfaces and Point Defects: Relevance for Li-Air Batteries. *Batter. Congr.* **2011**, *6*, 1–6.

(47) Nørskov, J. K.; Rossmeisl, J.; Logadottir, A.; Lindqvist, L.; Lyngby, D.-; Jo, H. Origin of the Overpotential for Oxygen Reduction at a Fuel-Cell Cathode. *J.Phys. Chem. B* **2004**, 108, 17886–17892.

(48) Chase, M. W.; National Institute of Standards and Technology, NIST_JANAF Thermodynamical Tables. America Chemical society; American Institute of Physics for the National Institute of Standards and Technology: Washington, D.C., Woodbury. N.Y. **1998**.

# Paper III

---

Identifying systematic DFT errors in catalytic reactions
Rune Christensen, Heine A. Hansen, and Tejs Vegge
*Catal. Sci. Technol.*, **2015**, 5, pp 4946–4949

Catalysis Science & Technology

COMMUNICATION

View Article Online
View Journal | View Issue



Cite this: *Catal. Sci. Technol.*, 2015, 5, 4946

Received 14th August 2015,
Accepted 14th September 2015

DOI: 10.1039/c5cy01332a

www.rsc.org/catalysis

# Identifying systematic DFT errors in catalytic reactions†

Rune Christensen, Heine A. Hansen and Tejs Vegge*

Using $CO_2$ reduction reactions as examples, we present a widely applicable method for identifying the main source of errors in density functional theory (DFT) calculations. The method has broad applications for error correction in DFT calculations in general, as it relies on the dependence of the applied exchange–correlation functional on the reaction energies rather than on errors *versus* the experimental data. As a result, improved energy corrections can now be determined for both gas phase and adsorbed reaction species, particularly interesting within heterogeneous catalysis. We show that for the $CO_2$ reduction reactions, the main source of error is associated with the C=O bonds and not the typically energy corrected OCO backbone.

Electroreduction of $CO_2$ using electricity from renewable sources has the potential to supply carbon neutral transportation fuels, but improved electrocatalysts are needed. Although research within this area has been conducted for decades,[1,2] current challenges include low efficiency, product selectivity and stability of the catalysts. In recent years, significant progress in understanding catalytic activity from fundamental reaction mechanisms has been made for a variety of different heterogeneous electrocatalysts using density functional theory (DFT).[3,4] Within DFT, several levels of calculational complexity in describing the exchange–correlation functional exist. Although higher level methods can be used in some cases, computational cost will often limit treatment of the exchange energy to be performed using the Generalized Gradient Approximation (GGA) for extensive studies of heterogeneous catalysis.[5] For this reason, this work focuses solely on improving the accuracy of calculations relying on functionals with GGA type exchange.

*Department of Energy Conversion and Storage, Technical University of Denmark, Fysikvej Bldg. 309, DK-2800 Kgs. Lyngby, Denmark. E-mail: teve@dtu.dk; Fax: +45 46 77 57 58; Tel: +45 46 77 58 18*

† Electronic supplementary information (ESI) available: Computational details, extended ensemble correlation analysis, and atomic structures. See DOI: 10.1039/c5cy01332a

The RPBE[6] and BEEF-vdW[7] exchange–correlation functionals have been developed for catalysis studies and showed to be well-suited for determining chemisorption energies.[8,9] However, experimental gas phase reaction enthalpies for $CO_2$ reduction to products of interest can, in many cases, not be reproduced within an error of 0.5 eV per $CO_2$, due to significant systematic errors.[10–12] These inaccuracies can prevent, *e.g.*, accurate determination of product selectivity. To remain at a sufficiently low level of computational cost while improving accuracy, energy corrections have previously been applied in a fitting procedure, where the mean absolute error (MAE) *versus* experimental data has been minimized for a given set of reactions.[10–12] As a result, energy corrections were previously applied to molecules containing an oxygen–carbon–oxygen (OCO) backbone structure, *e.g.* $CO_2$ and HCOOH, for the RPBE functional[10] with an additional correction on the $H_2$ molecule for the BEEF-vdW functional.[11,12] This correction scheme has subsequently been widely accepted and applied in a large number of high impact papers.[10,13,14]

The minimized MAE can vary by as little as 0.01 eV for different choices of corrections,[11] making the choice of corrections based solely on the minimized MAE vulnerable to both minor calculational and experimental inaccuracies. Here, we present a new and robust approach for identification of the specific molecules or molecular components requiring an energy correction to obtain the needed accuracy. Here, we demonstrate it for $CO_2$ reduction reactions, but the approach is generally applicable, *e.g.* in studies of heterogeneous catalysis of organic compounds or oxygen reduction.

Although inferior to RPBE and BEEF-vdW for determination of chemisorption energies,[8,9] we find the PBE functional,[15] which is also frequently used within heterogeneous catalysis, able to reproduce most experimental gas phase enthalpies of reaction for $CO_2$ reduction reactions with sufficient accuracy. The PBE and RPBE functionals differ only in enhancement factor in the GGA exchange energy.[6] If the calculated energy of one specific molecule or molecular component is particularly sensitive towards changes in the

enhancement factor, it will dominate the ability to reproduce the experimental enthalpies of reaction. Sensitivity towards changes in the enhancement factor can be probed by calculating the enthalpies of reaction with GGA type functionals with different enhancement factors. The enhancement factor in the BEEF-vdW functional is composed of a sum of Legendre polynomials with expansion coefficients determined in a machine learning process to obtain the best GGA functional for a range of databases containing different data such as enthalpies of formation, chemisorption energies, reaction barriers and van der Waals interactions. Intrinsic to the functional is an ensemble of functionals with perturbed expansion coefficients. Perturbations are included in the ensemble of functionals based on how well the perturbed functional performs and a "temperature" parameter such that one standard deviation in a quantity calculated using the generated ensemble of functionals corresponds to the predicted calculational error.[7] The use of ensemble functionals is a computationally very efficient method for calculating enthalpies of formation with a large number of functionals with different enhancement factors. Here, 2000 different ensemble functionals have been examined. The vdW-DF[16] and vdW-DF2[17] functionals are also examined for comparison as they contain vdW correlation similar to that of BEEF-vdW.

Here, the reaction enthalpy is calculated for a range of different $CO_2$ reduction reactions listed in Table 1. The gas phase reactions in the 'primary set' are identical to those examined previously for establishing general energy corrections.†[10–12] In addition to the primary set, a 'verification set' is also introduced. With the exception of the reduction to dimethyl ether, *i.e.* reaction (15), the verification set consists of reactions with product molecules containing carbon–oxygen double bonds (C═O). The stoichiometry of all gas phase reactions is normalized to one $CO_2$ reactant molecule. This is not required but this simplifies data treatment.

In addition to gas phase molecules, functional dependent errors can, in contrast to previously used correctional approaches, also be examined for surface adsorbates. A highly important example – carboxyl (COOH*) adsorption on a Cu (111) surface – is presented. By comparing the functional dependence of a surface reaction with a similar gas phase reaction, it can be determined whether a similar correction should be applied for the two. To obtain functional dependence comparable to the gas phase, adsorbed methyl ($CH_3$*) has been used as the reactant as both COOH* and $CH_3$* bond to a single copper atom through a carbon atom with 3 additional covalent bonds. The compared reactions, (*1a) and (*1b), can be seen in Table 1.

All calculations have been performed using the Vienna *ab initio* Simulation Package (VASP)[18–21] and the Atomic Simulation Environment (ASE),[22] which has been used to generate the ensembles.†

Examples of correlated reaction enthalpies can be seen in Fig. 1. The observed linear correlations indicate that the functional dependence is dominated by a single molecule or molecular component, or by linearly dependent molecules or molecular components. By assuming a specific molecule or molecular component to dominate the functional dependence, it is possible to predict the slope by dividing the change in the number of occurrences in the *y*-axis reaction with the change in the *x*-axis reaction as exemplified below. The predicted slope can subsequently be validated against the observed slope. Assuming molecules with an oxygen–carbon–oxygen (OCO) backbone structure to be the major source of functional dependence and, thus, error,[10–12] the slope for the reactions in Fig. 1a is predicted to be 1.0 (−1/−1) since in both reactions an OCO backbone is present in the $CO_2$ reactant, but not in the product, giving a change of −1 in both reactions. This fits well with the observed slope.

Fig. 1b and c show the functional dependence approximately following lines with a slope of 0.5. This disagrees with the general assumption that the OCO backbone dominates the functional dependence, as this assumption predicts a slope of 0 for Fig. 1b, since the OCO backbone is present in both reactant and product (HCOOH), giving a change of 0 in the *y*-axis reaction (0/−1), and a slope of 1.0 for Fig. 1c, which is similar to Fig. 1a in terms of changes in the OCO backbones. The observed slopes do, however, fit with the C═O bonds dominating the functional dependence. In both reactions plotted on the *y*-axis, one of the double bonds in the $CO_2$ reactant is preserved in the product (HCOOH and $H_2CO$) and both are broken in reaction (3) plotted on the *x*-axis, resulting in a predicted slope of 0.5 (−1/−2). In a more in-depth quantitative analysis of the total reaction set, one can find the slopes obtained through linear regression to agree

**Table 1** Reactions examined

| | | | |
|---|---|---|---|
| **Primary set** | | | Reac |
| $H_2 + CO_2$ | → | $CO + H_2O$ | (0) |
| $4H_2 + CO_2$ | → | $CH_4 + 2H_2O$ | (1) |
| $H_2 + CO_2$ | → | $HCOOH$ | (2) |
| $3H_2 + CO_2$ | → | $CH_3OH + H_2O$ | (3) |
| $3H_2 + CO_2$ | → | $\frac{1}{2}C_2H_5OH + \frac{3}{2}H_2O$ | (4) |
| $\frac{10}{3}H_2 + CO_2$ | → | $\frac{1}{3}C_3H_8 + 2H_2O$ | (5) |
| $\frac{7}{2}H_2 + CO_2$ | → | $\frac{1}{2}C_2H_6 + 2H_2O$ | (6) |
| $3H_2 + CO_2$ | → | $\frac{1}{2}C_2H_4 + 2H_2O$ | (7) |
| $\frac{11}{4}H_2 + CO_2$ | → | $\frac{1}{4}C_4H_6{}^a + 2H_2O$ | (8) |
| $2H_2 + CO_2$ | → | $\frac{1}{2}CH_3COOH + H_2O$ | (9) |
| $2H_2 + CO_2$ | → | $\frac{1}{2}HCOOCH_3 + H_2O$ | (10) |
| **Verification set** | | | |
| $2H_2 + CO_2$ | → | $CH_2O + H_2O$ | (11) |
| $\frac{3}{2}H_2 + CO_2$ | → | $OCHCHO + H_2O$ | (12) |
| $\frac{7}{3}H_2 + CO_2$ | → | $\frac{1}{3}C_2H_5COOH^b + \frac{4}{3}H_2O$ | (13) |
| $\frac{7}{3}H_2 + CO_2$ | → | $\frac{1}{3}CH_3COOCH_3 + \frac{4}{3}H_2O$ | (14) |
| $3H_2 + CO_2$ | → | $\frac{1}{2}CH_3OCH_3 + \frac{3}{2}H_2O$ | (15) |
| $\frac{5}{2}H_2 + CO_2$ | → | $\frac{1}{2}CH_3CHO + \frac{3}{2}H_2O$ | (16) |
| **Adsorbate set** | | | |
| $2H_2O + CH_4$ | → | $HCOOH + 3H_2$ | (*1a) |
| $2H_2O + CH_3$* | → | $COOH^* + 3H_2$ | (*1b) |

[a] 1,3-Butadiene. [b] Propanoic acid. * Adsorbate on Cu(111).

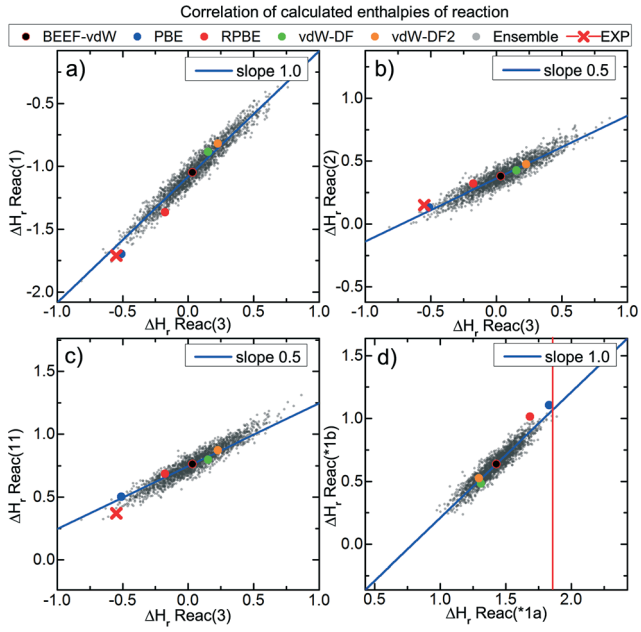


**Fig. 1** Correlations in the calculated enthalpies of reaction (eV) for various reactions (a–d). Functional dependence on energies is observed to correlate linearly for different reactions including surface reactions (d). Blue lines are drawn with predicted slopes equal to the ratio of broken/formed C═O bonds in the compared reactions. Larger points are self-consistent calculations using different functionals, crosses (red line in d) are the experimental reference values,[23] and the smaller grey semi-transparent points represent the values for the 2000 BEEF-ensemble functionals.

very well with the slopes predicted under the assumption that the C═O bonds dominate the functional dependence.†

Fig. 1d compares the two reactions in the adsorbate set. They are observed to show the same functional dependence, and COOH* (carboxyl) should thus be corrected with the same energy correction as HCOOH (formic acid). From the geometry and bond lengths, this is expected as the C═O bond appears to be present in COOH*.† Dispersion forces included in the vdW functionals have an effect on the adsorbate reactions as the vdW functionals appear to be on a lower but parallel line to the non-vdW functionals, although too few non-vdW data points are present for definite conclusions. The offset does not impact the analysis of the functional dependence.

Having identified the C═O bond to be dominating the functional dependence, energy corrections are applied based on the number of C═O bonds in a molecule rather than to molecules with an OCO backbone. The magnitude of the energy correction is then determined by minimizing the MAE *versus* the experimental data for the primary set of reactions shown in Table 1 in a procedure identical to the one previously applied for determining corrections using the same reference data.[10–12] To make a direct comparison with the previously used corrections for the BEEF-vdW functional, corrections are also applied to the $H_2$ molecules. A comparison of corrections can be seen in Fig. 2. For both types of corrections (C═O and OCO), the optimal magnitudes of corrections are 0.10 eV for the $H_2$ molecules and 0.29 eV for $CO_2$ (0.15 eV per C═O bond). These are similar although not identical to what have been found previously (0.09 eV and 0.33 eV,[11] and 0.09 eV and 0.41 eV (ref. 12)). The magnitude of corrections is the same within 0.01 eV per bond if the reactions in the verification set are included in the minimization of the MAE. By applying a correction to C═O instead of OCO, a significant reduction in post-correction errors are observed for the reactions, where the main product either has the OCO backbone but with only one C═O bond or has the C═O bond without the OCO backbone structure (see Fig. 2). This is seen to be the case in both the primary and the verification sets. This trend is also observed for the RPBE functional. In the case of the reduction to HCOOH (reaction (3)), the post-correction error in the calculations with BEEF-vdW changes from 0.13 eV to −0.02 eV. Previously, errors of 0.15 eV[11] and 0.17 eV[12] were obtained for this reaction using the OCO backbone and $H_2$ corrected BEEF-vdW functional. For $HCOOCH_3$ (reaction (10)) and $CH_2O$ (reaction (11)), significantly different experimental gas phase enthalpies of formation are available in the NIST database, which is used as the source for all reference data.[23] The previously used experimental value for $HCOOCH_3$ is by far the highest in the database and is extrapolated from the liquid phase enthalpy of formation.[23] Using one of the three alternative experimental

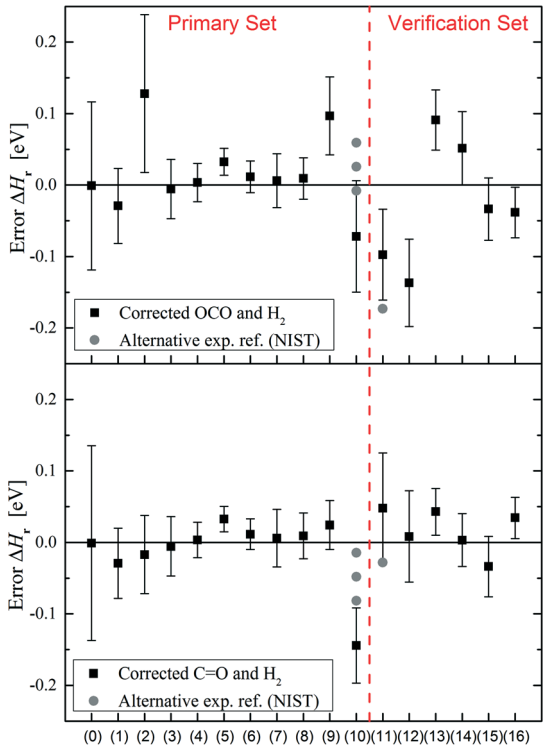


**Fig. 2** Comparison of remaining errors after correction of the OCO backbone (above) or the C═O bonds (below). Error bars show one standard deviation for the corrected ensemble. The grey points mark the error with alternative experimental references present in the NIST database.[23]

references in the NIST database, the error for reaction (10) follows the trend of the other reactions and can be decreased to a few meV after the C═O correction.

The effect of changing the correction scheme and applying corrections to the adsorbate can be very significant as exemplified by the reduction of COOH* to HCOOH. Computed using the BEEF-vdW functional, the reaction energy changes significantly from having a free energy change of −0.82 eV with OCO corrections, to −1.11 eV with C═O corrections.

Optimal magnitudes of corrections have been determined for all ensemble functionals. The standard deviation is then calculated for the ensemble of corrected functionals and plotted as error bars in Fig. 2. This can be used as a measure of how well the correction performs for the class of functionals. The ensemble standard deviation is generally decreased with the C═O correction for reactions where it applies differently than the OCO correction, *e.g.* for reaction (2), the reduction to formic acid. With the C═O corrections, the standard deviation for reaction (0) is significantly larger than for the other reactions. As this is the only depicted reaction including CO, the relatively large standard deviation suggests that the energy of CO could also be functional dependent and require correction on the order of 0.2 eV with certain functionals. CO has previously been found to require corrections using the PBE functional.[9,24] A functional dependent error is also found for carbon–carbon (C═C) double bonds, as described in the ESI.† It is, however, of minor importance for the reactions considered here.

The demonstrated method is not limited to the presented case or catalytic reactions and can be used to identify a dominating, error-causing structure, molecule or molecular component in other cases, where functional dependence is observed.

For the different GGA functionals, the difference in the enhancement factor will be small for low density gradients and increase as the density gradient increases.[7] This can explain why functional dependence is most notable for the C═O bond, the C═C bond, and the CO molecule, as they probably give rise to the largest density gradients for the species in the reactions. In the future, the reduced density gradient could potentially be used directly for qualitative identification of molecules or molecular components with large functional dependence.

## Acknowledgements

The authors acknowledge the support from the Catalysis for Sustainable Energy (CASE) initiative funded by The Danish Agency for Science, Technology and Innovation.

## References

1 Y. Hori, *Modern Aspects of Electrochemistry*, Springer, New York, 2008, vol. 42, pp. 89–189.
2 J. Qiao, Y. Liu, F. Hong and J. Zhang, *Chem. Soc. Rev.*, 2014, **43**, 631–675.
3 Y. Li, S. H. Chan and Q. Sun, *Nanoscale*, 2015, **7**, 8663–8683.
4 S. Lysgaard, J. S. G. Myrdal, H. A. Hansen and T. Vegge, *Phys. Chem. Chem. Phys.*, 2015, DOI: 10.1039/C5CP00298B.
5 M. K. Sabbe, M.-F. Reyniers and K. Reuter, *Catal. Sci. Technol.*, 2012, **2**, 2010–2024.
6 B. Hammer, L. B. Hansen and J. K. Nørskov, *Phys. Rev. B: Condens. Matter Mater. Phys.*, 1999, **59**, 7413–7421.
7 J. Wellendorff, K. T. Lundgaard, A. Møgelhøj, V. Petzold, D. D. Landis, J. K. Nørskov, T. Bligaard and K. W. Jacobsen, *Phys. Rev. B: Condens. Matter Mater. Phys.*, 2012, **85**, 235149.
8 B.-T. Teng, X.-D. Wen, M. Fan, F.-M. Wu and Y. Zhang, *Phys. Chem. Chem. Phys.*, 2014, **16**, 18563–18569.
9 J. Wellendorff, T. L. Silbaugh, D. Garcia-Pintos, J. K. Nørskov, T. Bligaard, F. Studt and C. T. Campbell, *Surf. Sci.*, 2015, **640**, 36–44.
10 A. A. Peterson, F. Abild-Pedersen, F. Studt, J. Rossmeisl and J. K. Nørskov, *Energy Environ. Sci.*, 2010, **3**, 1311–1315.
11 F. Studt, F. Abild-Pedersen, J. B. Varley and J. K. Nørskov, *Catal. Lett.*, 2013, **143**, 71–73.
12 F. Studt, M. Behrens, E. L. Kunkes, N. Thomas, S. Zander, A. Tarasov, J. Schumann, E. Frei, J. B. Varley, F. Abild-Pedersen, J. K. Nørskov and R. Schlögl, *ChemCatChem*, 2015, **7**, 1105–1111.
13 A. A. Peterson and J. K. Nørskov, *J. Phys. Chem. Lett.*, 2012, **3**, 251–258.
14 M. Behrens, F. Studt, I. Kasatkin, S. Kühl, M. Hävecker, F. Abild-Pedersen, S. Zander, F. Girgsdies, P. Kurr, B.-L. Kniep, M. Tovar, R. W. Fischer, J. K. Nørskov and R. Schlögl, *Science*, 2012, **336**, 893–897.
15 J. P. Perdew, K. Burke and M. Ernzerhof, *Phys. Rev. Lett.*, 1996, **77**, 3865–3868.
16 M. Dion, H. Rydberg, E. Schröder, D. C. Langreth and B. I. Lundqvist, *Phys. Rev. Lett.*, 2004, **92**, 246401.
17 K. Lee, E. D. Murray, L. Kong, B. I. Lundqvist and D. C. Langreth, *Phys. Rev. B: Condens. Matter Mater. Phys.*, 2010, **82**, 081101.
18 G. Kresse and J. Furthmüller, *Phys. Rev. B: Condens. Matter Mater. Phys.*, 1996, **54**, 11169–11186.
19 G. Kresse and D. Joubert, *Phys. Rev. B: Condens. Matter Mater. Phys.*, 1999, **59**, 1758–1775.
20 P. E. Blöchl, *Phys. Rev. B: Condens. Matter Mater. Phys.*, 1994, **50**, 17953–17979.
21 J. C. V. Klimeš, D. R. Bowler and A. Michaelides, *Phys. Rev. B: Condens. Matter Mater. Phys.*, 2011, **83**, 195131.
22 S. Bahn and K. W. Jacobsen, *Comput. Sci. Eng.*, 2002, **4**, 56–66.
23 NIST Chemistry WebBook, *NIST Standard Reference Database Number 69*, ed. P. J. Linstrom and W. G. Mallard, National Institute of Standards and Technology, 2005.
24 F. Calle-Vallejo and M. T. M. Koper, *Angew. Chem., Int. Ed.*, 2013, **52**, 7282–7285.

# Paper IV

---

Theoretical Insight into the Trends that Guide the Electrochemical Reduction of Carbon Dioxide to Formic Acid
Jong Suk Yoo, Rune Christensen, Tejs Vegge, Jens K. Nørskov, and Felix Studt
*ChemSusChem*, **2016**, 9 (4), pp 358–363

The author of this thesis applied energy corrections to data.

ChemPubSoc Europe

DOI: 10.1002/cssc.201501197

CHEMSUSCHEM Full Papers

# Theoretical Insight into the Trends that Guide the Electrochemical Reduction of Carbon Dioxide to Formic Acid

Jong Suk Yoo,[a, b] Rune Christensen,[c] Tejs Vegge,[c] Jens K. Nørskov,[a, b] and Felix Studt*[a, b]

The electrochemical reduction (electroreduction) of $CO_2$ to formic acid (HCOOH) and its competing reactions, that is, the electroreduction of $CO_2$ to CO and the hydrogen evolution reaction (HER), on twenty-seven different metal surfaces have been investigated using density functional theory (DFT) calculations. Owing to a strong linear correlation between the free energies of COOH* and H*, it seems highly unlikely that the electroreduction of $CO_2$ to HCOOH via the COOH* intermediate occurs without a large fraction of the current going to HER. On the other hand, the selective electroreduction of $CO_2$ to HCOOH seems plausible if the reaction occurs via the HCOO* intermediate, as there is little correlation between the free energies of HCOO* and H*. Lead and silver surfaces are found to be the most promising monometallic catalysts showing high faradaic efficiencies for the electroreduction of $CO_2$ to HCOOH with small overpotentials. Our methodology is widely applicable, not only to metal surfaces, but also to other classes of materials enabling the computational search for electrocatalysts for $CO_2$ reduction to HCOOH.

## Introduction

Modern society relies heavily on the utilization of fossil fuels to supply our high energy needs, particularly in the transportation sector. With the growing world population and rising standards of living, there has been an increased stress on our environment as expressed in, for example, elevated concentrations of $CO_2$ in the atmosphere. To curb $CO_2$ emissions and reduce our dependence on fossil fuels, we must turn to renewable energy sources such as wind, solar, and hydro power.[1–3] For the transportation sector, this accentuates the need to develop alternatives to the internal combustion engine. Hydrogen fuel cells offer such an alternative, generating electricity without pollution. However, several practical issues prevent the large-scale implementation of hydrogen fuel cells. One of the most critical ones is perhaps the storage of hydrogen in high volumetric and gravimetric capacities.[3–5]

Recently, formic acid (HCOOH) has been suggested as a suitable hydrogen storage material because it has a high volumetric (53.4 g $L^{-1}$) and a moderate gravimetric (4.4 wt%) hydrogen storage capacity in ambient conditions.[6,7] Hydrogen stored in HCOOH can be released on demand by selectively decomposing HCOOH into $CO_2$ and $H_2$ in the presence of a suitable catalyst.[8–10] Alternatively, HCOOH can be employed directly to generate electricity (and $CO_2$) using direct formic acid fuel cells.[11,12] However, these formic-acid-based technological solutions for hydrogen storage inevitably emit large quantities of $CO_2$. To achieve a $CO_2$-neutral hydrogen storage cycle, we must develop a sustainable process of producing HCOOH from $CO_2$.[13–16] Nowadays, HCOOH is mostly produced from CO and $CH_3OH$,[17] as its formation from $CO_2$ and hydrogen is relatively endothermic [see Equation (1)].

$$CO_2 + H_2 \rightarrow HCOOH \qquad \Delta H^{298\,K} = +14.8\ kJ\ mol^{-1} \qquad (1)$$

HCOOH production via the electrochemical reduction (electroreduction) of $CO_2$ is therefore attracting widespread interest, as the endothermicity of a catalytic reaction is often greatly alleviated by applying an electrochemical potential rather than thermal energy. In addition, the electroreduction of $CO_2$ to HCOOH is only a 2-proton/electron reaction that consists of two elementary steps. As a consequence, there should be no theoretical limit towards achieving catalyst materials with small overpotentials (see Supporting Information, Figure S1), as opposed to, for example, the 4-proton/electron $O_2$ oxygen reduction/evolution,[18,19] the 6-proton/electron reduction of $N_2$ to $NH_3$,[20,21] and the 8-proton/electron reduction of $CO_2$ to $CH_4$.[22] From a theoretical point of view, it should be less of a problem

[a] J. S. Yoo, Prof. Dr. J. K. Nørskov, Dr. F. Studt
SUNCAT Center for Interface Science and Catalysis
SLAC National Accelerator Laboratory
2575 Sand Hill Road, Menlo Park, CA 94025 (USA)
E-mail: studt@slac.stanford.edu

[b] J. S. Yoo, Prof. Dr. J. K. Nørskov, Dr. F. Studt
Department of Chemical Engineering
Stanford University
Stanford, CA 94305 (USA)

[c] R. Christensen, Prof. Dr. T. Vegge
Department of Energy Conversion and Storage
Technical University of Denmark
Fysikvej Bldg. 309, 2800 Kgs. Lyngby (Denmark)

Supporting Information and ORCIDs from the authors of this article are available on the WWW under http://dx.doi.org/10.1002/cssc.201501197.

This publication is part of a Special Issue on the "Chemistry for Energy Conversion and Storage" conference in Berlin, Germany. To view the complete issue visit: http://dx.doi.org/10.1002/cssc.v9.4.

to find good catalyst materials for the electroreduction of $CO_2$ to HCOOH, compared to other multi-proton/electron products.

Previously, Hori et al. conducted experiments of electroreduction of $CO_2$ on various metal electrodes in 0.1 M of $KHCO_3$ (pH 6.8), and the electrodes were classified according to their product selectivities.[23] Lead, mercury, thallium, indium, tin, cadmium, and bismuth electrodes produced mostly formate, whereas gold, silver, zinc, palladium, and gallium electrodes produced mostly CO gas and nickel, iron, platinum, and titanium electrodes were selective to hydrogen production.[23] However, it is important to note that the experiments were conducted at very negative potentials (−0.91 ~ −1.63 V vs. SHE), as the product distribution of a metal electrode can change greatly depending on the applied potential.[24,25] On copper electrodes, for example, $CH_4$ and $C_2H_4$ were the major products of $CO_2$ reduction at potentials more negative than −0.95 V vs. SHE, whereas hydrogen was dominantly produced at potentials more positive than −0.95 V vs. SHE.[26–28]

In this study, theoretical methods will outline important characteristics of catalyst materials that are selective for the electroreduction of $CO_2$ to HCOOH. The computational hydrogen electrode model[18] is used to obtain the theoretical limiting potentials for the electroreduction of $CO_2$ to HCOOH on twenty-seven different metal surfaces, and they will be compared to those for two competing reactions, namely electroreduction of $CO_2$ to CO, and the hydrogen evolution reaction (HER). By examining the thermochemical trends among different metal surfaces, we will discuss the necessary requirements for a catalyst material to be active and selective for the electroreduction of $CO_2$ to HCOOH, purely based on thermodynamic arguments. Because the requirements of an ideal catalyst material are obtained at the thermodynamic limit (i.e., by comparing the limiting potentials for different electrocatalytic reactions) they may not be sufficient to pinpoint only the best catalyst materials. More sufficient requirements can only be achieved by considering the electrochemical activation barriers. However, it is important to mention that the descriptors obtained purely based on the thermodynamics of electrocatalytic reactions (i.e., without considering the kinetics) have been shown to represent the catalytic trends in electroreduction of $CO_2$ to $CH_4$ and $CH_3OH$ on transition-metal surfaces reasonably well.[29–31]

## Results and Discussion

First, we start by identifying relevant reaction pathways for the electroreduction of $CO_2$ and the HER. As shown in Scheme 1, the transfer of a first proton/electron pair to $CO_2$ leads to a formation of either the formate (HCOO*) or carboxyl (COOH*) species. Both HCOO* and COOH* can be reduced to HCOOH upon the transfer of a second proton/electron pair. However, COOH* can also be reduced to CO (+$H_2O$), whereas HCOO* can also be reduced to biformate ($H_2COO$*), which competes with HCOOH formation. Both CO* and $H_2COO$* are often quoted to be reaction intermediates for other multi-proton/electron $CO_2$ reduction reactions, for example, $CO_2$ to $CH_4$, $C_2H_6$, or $CH_3OH$.[28–34] Therefore, we limit this study to consider

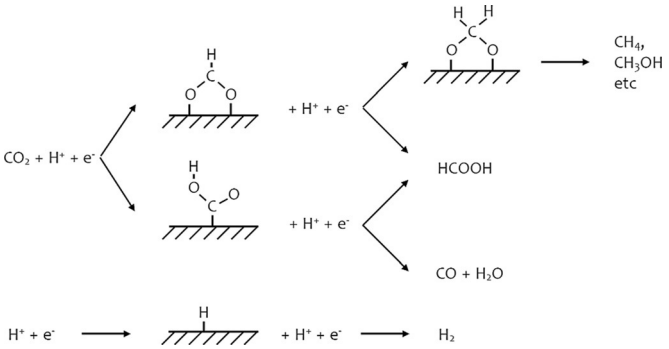


**Scheme 1.** Reaction pathways for the electroreduction of $CO_2$ to different products (top), and the competing hydrogen evolution reaction (bottom).

only the 2-proton/electron $CO_2$ reduction reactions (i.e., $CO_2$ to HCOOH, and that to CO) because the limiting potential for a full multi-proton/electron $CO_2$ reduction reaction cannot be less negative than that for the electroreduction of $CO_2$ to CO* (or $H_2COO$*). Finally, we consider another 2-proton/electron reduction reaction that is known to be parasitic in many electrochemical reduction reactions, namely the HER, which occurs via the H* intermediate (see Scheme 1).

In order to examine the preference of a catalyst surface towards the three different products (HCOOH, CO, and $H_2$), we need to compare the free energies of different reaction intermediates. However, these free energies are often not independent due to scaling relations between similar classes of adsorbates.[35–37] For example, Figure 1 shows the scaling relation between the free energies of COOH* and H* on various metal surfaces (see Supporting Information, Figures S2–S5 for other scaling relations). There is a scaling relation between the free energies of COOH* and H*, although non-transition-metals, such as zinc, cadmium, lead, thallium, and tin, tend to deviate

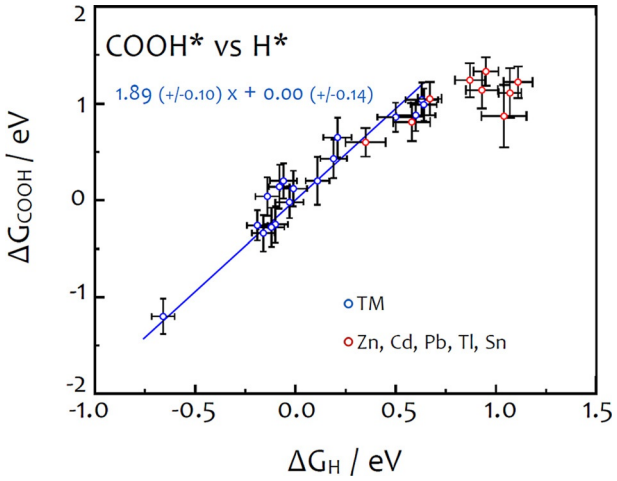


**Figure 1.** Scaling between the free energies of COOH* and H* on various transition-metal (blue circles) and non-transition-metal (red circles) surfaces. The free energies are given relative to gas-phase $H_2$ and $CO_2$, and the blue line indicates the scaling relation obtained when only the transition-metal surfaces have been used for the linear fit. The error bars are obtained using the ensemble of the BEEF-vdW exchange-correlation functionals (see Supporting Information, Table S2 for values). This ensemble has also been used to calculate the errors on the slope and y-intercept of the scaling line shown in blue.

from the scaling relation obtained by considering only the transition-metals. Interestingly, both the close-packed (fcc(111), hcp(0001) and bcc(110)) and stepped (fcc(211), hcp(1010) and bcc(100)) facets fall nearly on the same scaling line. On the other hand, the scaling relation is found to be extremely weak (or absent) between the free energies of HCOO* and H* (see Figure S2). The free energies of HCOO* scale well with only those species that bind to the surface through oxygen atoms (e.g., $H_2COO$*, as shown in Figure S3).[10] Thus, we conclude that it is more plausible to alter the free energies of HCOO* and H* independently than those of COOH* and H* by choosing different catalyst materials.

If the electroreduction of $CO_2$ to HCOOH occurs via the COOH* intermediate on a metal surface, the HER will always be a strongly competing sidereaction as the equilibrium potential for HER (0 V vs. RHE) is more positive than that for $CO_2$ to HCOOH (−0.17 V vs. RHE). Because the chemisorption energies for COOH* and H* are strongly linearly correlated, it would be difficult to find metals or alloys that can selectively produce HCOOH via the COOH* intermediate. Although lead, thallium, zinc, tin, and cadmium surfaces (see red circles in Figure 1) are not fully obeying the scaling relation shown in Figure 1, their $\Delta G_{COOH}$ values are extremely positive, indicating large overpotentials for the electroreduction of $CO_2$ to HCOOH via the COOH* intermediate. The selective production of HCOOH relative to HER seems much more plausible if the electroreduction of $CO_2$ to HCOOH occurs via the HCOO* intermediate for the following reasons: (1) the scaling relation between $\Delta G_H$ and $\Delta G_{HCOO}$ is extremely weak, thus there is a good chance of finding a metal surface whose $\Delta G_{HCOO}$ is close to the equilibrium potential for HCOOH production, while its $\Delta G_H$ is far from the equilibrium potential for HER (see Figure S2); (2) the reduction of HCOO* to $H_2COO$* instead of HCOOH is not favorable on most metal surfaces because $H_2COO$* is rather high in free energy compared to HCOOH (see Supporting Information, Table S1 for values). Thus, in order to obtain a high faradaic efficiency for the electroreduction of $CO_2$ to HCOOH, one would need to find a catalyst material that produces HCOOH via the HCOO* intermediate, while binding H* very weakly (to suppress HER).

Figure 2 shows the theoretical limiting potentials for electroreduction of $CO_2$ to HCOOH via the lowest energy pathway (i.e., COOH* vs. HCOO* pathway; see Supporting Information, Figure S6) vs. HER on various metal surfaces. The figure shows that there are many transition-metal surfaces whose limiting potential for HER is higher (more positive) than the equilibrium potential for the electroreduction of $CO_2$ to HCOOH (−0.17 V vs. RHE), thus showing a strong preference for HER compared to electroreduction of $CO_2$ to HCOOH. On the other hand, there are only a few surfaces (e.g., silver and lead) whose overpotential for electroreduction of $CO_2$ to HCOOH is small while that for HER is relatively large. However, we also need to check whether these metal surfaces prefer electroreduction of $CO_2$ to HCOOH over another competing reaction, namely the electroreduction of $CO_2$ to CO.

In this study, the theoretical limiting potentials for the electroreduction of $CO_2$ to CO on various metal surfaces are obtained based on the assumption that gas-phase CO is produced via only the electrochemical steps shown in Scheme 1 (i.e., $CO_2+H^++e^-\rightarrow COOH^*+H^++e^-\rightarrow CO+H_2O$). This approach excludes the pathway where gas-phase CO is produced via thermal desorption of CO*, which can be important for metals that bind CO* very strongly (i.e., nickel, palladium, platinum, rhodium, and titanium; see Supporting Information, Table S7 for the binding energies of CO* on various surfaces). However, under ambient reaction conditions these surfaces have a large coverage of CO*, and adsorbate-adsorbate interactions of CO* as well as between CO* and other intermediates have to be considered in order to more accurately determine their catalytic performance. This is beyond the scope of the current study, thus we choose to make the assumption above, while keeping in mind that the limiting potential for the electroreduction of $CO_2$ to CO is not well defined on some reactive metal surfaces.

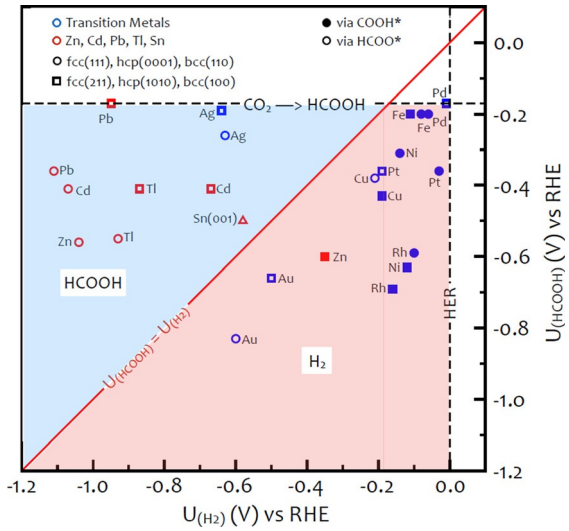


**Figure 2.** Theoretical limiting potentials (at pH 0) for the electroreduction of $CO_2$ to HCOOH vs. those for HER. The black dashed lines show the theoretical equilibrium potentials for electro-reduction of $CO_2$ to HCOOH and HER. The diagonal red line shows where the potential for HCOOH production equals that for HER, and the blue and red areas indicate where $U_{HCOOH} < U_{H_2}$ and $U_{HCOOH} > U_{H_2}$, respectively. Various transition-metal and non-transition-metal surfaces are depicted in blue and red, respectively. All metal surfaces have been calculated according to their corresponding crystal structures. The flat fcc(111), hcp(0001) and bcc(110) surfaces are shown as circles whereas the stepped fcc(211), hcp(1010) and bcc(100) surfaces are shown as squares. Full circles and squares indicate that formic acid production proceeds via the carboxyl intermediate whereas empty circles and squares indicate that it proceeds via the formate intermediate.

Figure 3 shows a comparison of the theoretical limiting potentials for all three 2-proton/electron reduction reactions on various metal surfaces (see also Figures S4 and S5 for separate comparisons). Note that the equilibrium potential (−0.12 V vs. RHE) for the electroreduction of $CO_2$ to CO is in between that for HER (0 V vs. RHE) and that for the electroreduction of $CO_2$ to HCOOH (−0.17 V vs. RHE). Therefore, from a thermodynamic point of view, HCOOH production is not only disadvantageous vs. HER but also vs. CO production. We find that silver, lead, cadmium, thallium, and tin favor the electroreduction of $CO_2$ to HCOOH, whereas platinum, rhodium, nickel, and titanium

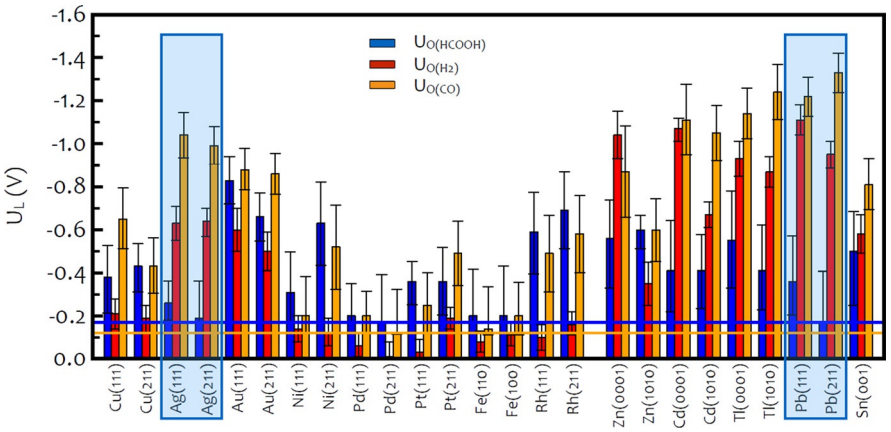


**Figure 3.** Theoretical limiting potentials (at pH 0) for the electroreduction of $CO_2$ to formic acid (blue bars), HER (red bars) and the electroreduction of $CO_2$ to CO (orange bars) on various metal surfaces (see Supporting Information, Table S3 for values). The blue and orange lines indicate theoretical equilibrium potentials for formic acid (−0.17 V vs. RHE) and carbon monoxide (−0.12 V vs. RHE), respectively (note that the equilibrium potential for hydrogen evolution is 0 V vs. RHE). The blue boxes highlight silver and lead surfaces because they show promising properties, that is, low overpotentials and high faradaic efficiencies for the electroreduction of $CO_2$ to formic acid. The error bars are obtained using the BEEF–vdW ensemble of exchange-correlation functionals (see Supporting Information, Table S4 for values).

favor HER, and palladium, gold, copper, and zinc do not particularly favor any one reaction. These results are generally in agreement with electrochemical measurements performed by Hori et al.,[42] although we find one major exception: the silver surfaces. However, one has to keep in mind that Hori et al. measured the performance of the electrodes at a high current density, hence at a very negative potential, and the faradaic efficiencies toward different products can change profoundly with the applied potential, as has been shown for copper electrodes.[26–28] We will discuss this in more detail below.

As can be seen from Figure 3, silver and lead surfaces are found to be the most promising monometallic surfaces for the electroreduction of $CO_2$ to HCOOH. Cadmium, thallium and tin surfaces are also found to be selective towards HCOOH production, but require relatively high overpotentials (0.2~0.4 V). Lead has indeed been shown to be a good catalyst for HCOOH production from $CO_2$ with faradaic efficiencies of >90% at potentials ($U$) between −0.7~−1.0 V vs. RHE.[38] This is in good agreement with the results of our calculations, that only −0.17 V vs. RHE is required for the electroreduction of $CO_2$ to HCOOH on lead, whereas a minimum of −1.22 or −0.95 V vs. RHE is required for the electroreduction of $CO_2$ to CO or HER, respectively, indicating that only HCOOH is produced under the experimental conditions of $U$=−0.7~−1.0 V vs. RHE. Previously, tin electrodes were also shown to exhibit steady-state faradaic efficiencies of 5~10% for CO formation, 19% for HCOOH formation, with the remainder of the current going to HER at $U$=−0.7 V vs. RHE.[39] This is also in good agreement with the results of our calculations, that only HCOOH formation and HER are feasible under the experimental condition of $U$=−0.7 V vs. RHE, because the calculated limiting potentials for the electroreduction of $CO_2$ to HCOOH and HER on Sn(001) are −0.50 V and −0.58 V vs. RHE (more positive than −0.7 vs. RHE), respectively, whereas that for the electroreduction of $CO_2$ to CO is −0.81 V vs. RHE (more negative than −0.7 V).

Although we predict silver to be a good catalyst for the electroreduction of $CO_2$ to HCOOH with an overpotential of ~0.1 V, silver is experimentally found to produce mostly CO with minor amounts of HCOOH at $U$=−0.6~−1.4 V vs. RHE.[25,40] This apparent discrepancy to our prediction can have multiple reasons: (1) the product selectivity of an electrocatalyst can change significantly with the applied potential, but electrocatalytic measurements are often performed with large overpotentials in order to obtain sufficient current;[23–25,40,41] (2) the kinetics for the reduction of $CO_2$ to HCOOH on silver may be slow, thus changing the reaction pathway. For example, although we predict the electroreduction of $CO_2$ to HCOOH to occur via HCOO* rather than COOH* on silver surfaces (see Supporting Information, Figure S6 and then Table S5 for values), the proton transfer to the carbon atom of $CO_2$ to form HCOO* may be kinetically hindered compared to the transfer to the oxygen atom of $CO_2$ to form COOH*, as shown to be the case for Pt(111).[42] If this is indeed the case for silver as well, the limiting potential for the electroreduction of $CO_2$ to HCOOH (now via COOH*) would be approximately −1.0 V vs. RHE, which is comparable to the limiting potential for the electroreduction of $CO_2$ to CO.

We just discussed the possibility of the electroreduction of $CO_2$ to HCOOH being more difficult on some surfaces due to kinetic reasons. The same argument may also apply regarding the limiting potentials of $H_2$ and CO formation. In this case, $H_2$ and CO formation would be kinetically hindered, thus favoring the formation of HCOOH. This may be the case for some palladium-based catalysts. Recently, it was found that Pd–H[43] and Pd–Pt nanoparticles[44,45] can reduce $CO_2$ to HCOOH with high faradaic efficiencies (80~100%) at $U$=−0.2~−0.4 V vs. RHE (note how the onset potential matches well with our limiting potential for HCOOH formation on palladium surfaces; see Figure 3 and Supporting Information, Table S3). This is partially in disagreement with our analysis of palladium as an active catalyst for both, the electroreduction of $CO_2$ to HCOOH and HER (Figure 3). It is likely that HER is kinetically suppressed on Pd–H and Pd–Pt catalysts despite its low limiting potential. A more detailed analysis of the selectivities of these catalysts

can only be obtained when electrochemical barriers are also considered. However, calculations of electrochemical barriers are considerably more complex, and approximation schemes need to be developed in order to quickly obtain electrochemical barriers for a large range of systems.[46]

Lastly, we turn our discussion to another important requirement a surface must satisfy in order to provide the free sites needed for the reduction of $CO_2$ in aqueous solutions. Figure 4 shows the coverages of oxygen and hydroxyl species on metal

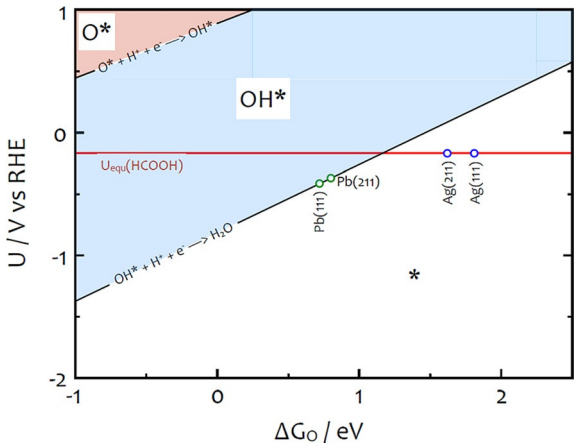


**Figure 4.** Coverages of surfaces as a function of potential ($U$) and the oxygen binding free energy ($\Delta G_O$), at pH 0 and $T = 300$ K. Different regions in the figure are determined by the most stable surface configuration at given variables, that is, $U$ and $\Delta G_O$, where the phase borders are defined by the equilibrium between different oxygen species. O*, OH* and * denote atomic oxygen, hydroxyl and free sites, respectively. $\Delta G_O$ for lead and silver surfaces are shown as green and blue circles, respectively. The red line indicates the equilibrium potential for the reduction of $CO_2$ to HCOOH.

surfaces as a function of the applied potential and $\Delta G_O$ of the corresponding metal surface (see Supporting Information, Table S6 for values). Since the free energies of O* and OH* scale linearly with each other (Figure S6),[35] one can derive the surface coverage as a function of $\Delta G_O$ only. It can be seen that metal surfaces are more easily covered by OH* than O* at negative potentials (i.e., under reducing conditions). Silver surfaces are calculated to be free of oxygen species at their limiting potentials for the electroreduction of $CO_2$ to HCOOH, thus providing the free sites needed to facilitate the catalytic reaction. On the other hand, lead surfaces require potentials slightly more negative than their limiting potentials for the electroreduction of $CO_2$ to HCOOH in order to be free of OH*. We can also see from Figure 4 that the surface poisoning by OH* can be severe for surfaces having very strong oxygen binding energies, requiring large overpotentials to be free of oxygen adsorbates in aqueous solutions.

## Conclusions

Theoretical methods were used to investigate the electroreduction of $CO_2$ to HCOOH on twenty-seven different metal surfaces. Our analysis is purely based on thermodynamic arguments, thus we have identified only the necessary (but not sufficient) requirements for catalyst materials to be suitable for the electroreduction of $CO_2$ to HCOOH competing with two other reactions, that is, the electroreduction of $CO_2$ to CO and the hydrogen evolution reaction. Due to a strong scaling between the free energies of carboxyl and hydrogen, it seems highly unlikely that a selective catalyst is designed based on optimal carboxyl binding energies. On the other hand, we find that the selective electroreduction of $CO_2$ to HCOOH via the formate intermediate is more plausible. Lead and silver surfaces are identified as the most promising among the twenty-seven different monometallic surfaces. Our methodology is widely applicable, not only to metal surfaces, but also to other classes of materials, enabling the computational search for electrocatalysts for $CO_2$ reduction to HCOOH.

## Computational Details

Periodic DFT calculations employing the BEEF–vdW functional[47] were carried out using the Atomic Simulation Environment (ASE)[48] in connection with the Quantum ESPRESSO code.[49] The BEEF–vdW functional was used here as it has been shown to describe the chemisorption and physisorption properties of adsorbates on transition-metal surfaces well.[50] For example, the BEEF–vdW functional has yielded quite accurate energetics of $CO_2$ hydrogenation to $CH_3OH$ via formic acid.[51–53] The BEEF–vdW functional is also capable of assessing the reliability of the calculated results through an ensemble of functionals representing its known computational errors.[54] A kinetic energy cut-off of 500 eV and a density energy cut-off of 5000 eV were used for all calculations. The ionic cores were described using Vanderbilt ultrasoft pseudopotentials.[55] The slab models were created by infinitely repeating a $2\times2\times4$ supercell, separated by more than 13 Å of vacuum space in the direction perpendicular to the surface plane. In the slab models, the top two atomic layers were allowed to relax whereas the bottom two layers were fixed at their bulk positions. The Brillouin zones were sampled using a $4\times4\times1$ Monkhorst–Pack k-point mesh.[56] The convergence criterion for the energy optimization was a maximum force of 0.03 eV Å$^{-1}$ per atom. Convergence with respect to the slab model thickness, k-point sampling, and cut-off energies has been confirmed as shown elsewhere.[10] The energies of the gas-phase $CO_2$, HCOOH, $H_2$ and the adsorbed COOH* were corrected by $+0.41$ eV, $+0.20$ eV, $+0.09$ eV, and $+0.20$ eV, respectively, in order to account for the systematic DFT errors that originate from inaccurate descriptions of carbon-oxygen double bonds as discussed elsewhere.[52,57] We also corrected the binding energies of COOH* and OH* by $-0.25$ eV and $-0.5$ eV, respectively, in order to roughly account for the stabilization of H-bonding species in aqueous solutions.[28,29]

## Supporting Information

The Supporting Information includes raw data for all figures shown here, scaling relations, and comparison of the theoretical onset potentials for $CO_2$ to formic acid, $CO_2$ to CO, and hydrogen evolution.

## Acknowledgements

*We gratefully acknowledge support from the U.S. Department of Energy, Office of Sciences, Office of Basic Energy Sciences to the SUNCAT Center for Interface Science and Catalysis. J.S.Y. gives special thanks to the U.S. Department of State for funding his studies through the International Fulbright Science&Technology Award program. We also acknowledge support from the Global Climate Energy Project (GCEP) at Stanford University, fund number 52454.*

**Keywords:** carbon dioxide · density functional calculations · heterogeneous catalysis · hydrogen evolution · transition metals

[1] N. S. Lewis, D. G. Nocera, *Proc. Natl. Acad. Sci. USA* **2006**, *103*, 15729 – 15735.
[2] N. S. Lewis, *ChemSusChem* **2009**, *2*, 383 – 386.
[3] G. Crabtree, J. Sarrao, *Phys. World* **2009**, *22*, 24 – 30.
[4] U. Eberle, M. Felderhoff, F. Schüth, *Angew. Chem. Int. Ed.* **2009**, *48*, 6608 – 6630; *Angew. Chem.* **2009**, *121*, 6732 – 6757.
[5] S. Satyapal, J. Petrovic, C. Read, G. Thomas, G. Ordaz, *Catal. Today* **2007**, *120*, 246 – 256.
[6] M. Grasemann, G. Laurenczy, *Energy Environ. Sci.* **2012**, *5*, 8171 – 8181.
[7] A. Boddien, F. Gärtner, C. Federsel, P. Sponholz, D. Mellmann, R. Jackstell, H. Junge, M. Beller, *Angew. Chem. Int. Ed.* **2011**, *50*, 6411 – 6414; *Angew. Chem.* **2011**, *123*, 6535 – 6538.
[8] F. Solymosi, Á. Koós, N. Liliom, I. Ugrai, *J. Catal.* **2011**, *279*, 213 – 219.
[9] Q.-Y. Bi, X.-L. Du, Y.-M. Liu, Y. Cao, H.-Y. He, K.-N. Fan, *J. Am. Chem. Soc.* **2012**, *134*, 8926 – 8933.
[10] J. S. Yoo, F. Abild-Pedersen, J. K. Nørskov, F. Studt, *ACS Catal.* **2014**, *4*, 1226 – 1233.
[11] C. Rice, S. Ha, R. I. Masel, A. Wieckowski, *J. Power Sources* **2003**, *115*, 229 – 235.
[12] X. Yu, P. G. Pickup, *J. Power Sources* **2008**, *182*, 124 – 132.
[13] W. Leitner, *Angew. Chem. Int. Ed. Engl.* **1995**, *34*, 2207 – 2221; *Angew. Chem.* **1995**, *107*, 2391 – 2405.
[14] F. Joó, *ChemSusChem* **2008**, *1*, 805 – 808.
[15] A. Boddien, H. Junge, *Nat. Nanotechnol.* **2011**, *6*, 265 – 266.
[16] J. F. Hull, Y. Himeda, W.-H. Wang, B. Hashiguchi, R. Periana, D. J. Szalda, J. T. Muckerman, E. Fujita, *Nat. Chem.* **2012**, *4*, 383 – 388.
[17] W. Reutemann, H. Kieczka, in *Ullmann's Encyclopedia of Industrial Chemistry, Vol. 16*, Wiley-VCH, Weinheim, **2012**.
[18] J. K. Nørskov, J. Rossmeisl, A. Logadottir, L. Lindqvist, J. R. Kitchin, T. Bligaard, H. Jónsson, *J. Phys. Chem. B* **2004**, *108*, 17886 – 17892.
[19] J. Rossmeisl, A. Logadottir, J. K. Nørskov, *Chem. Phys.* **2005**, *319*, 178 – 184.
[20] E. Skúlason, T. Bligaard, S. Gudmundsdóttir, F. Studt, J. Rossmeisl, F. Abild-Pedersen, T. Vegge, H. Jónsson, J. K. Nørskov, *Phys. Chem. Chem. Phys.* **2012**, *14*, 1235 – 1245.
[21] J. H. Montoya, C. Tsai, A. Vojvodic, J. K. Nørskov, *ChemSusChem* **2015**, *8*, 2180 – 2186.
[22] A. A. Peterson, J. K. Nørskov, *J. Phys. Chem. Lett.* **2012**, *3*, 251 – 258.
[23] Y. Hori, *Electrochemical $CO_2$ Reduction on Metal Electrodes, in Modern Aspects of Electrochemistry, No. 42* (Ed.: C. Vayenas), Springer, New York, **2008**.
[24] K. P. Kuhl, T. Hatsukade, E. R. Cave, D. N. Abram, J. Kibsgaard, T. F. Jaramillo, *J. Am. Chem. Soc.* **2014**, *136*, 14107 – 14113.
[25] T. Hatsukade, K. P. Kuhl, E. R. Cave, D. N. Abram, T. F. Jaramillo, *Phys. Chem. Chem. Phys.* **2014**, *16*, 13814 – 13819.
[26] K. P. Kuhl, E. R. Cave, D. N. Abram, T. F. Jaramillo, *Energy Environ. Sci.* **2012**, *5*, 7050 – 7059.
[27] Y. Hori, A. Murata, R. Takahashi, S. Suzuki, *J. Am. Chem. Soc.* **1987**, *109*, 5022 – 5023.
[28] A. A. Peterson, F. Abild-Pedersen, F. Studt, J. Rossmeisl, J. K. Nørskov, *Energy Environ. Sci.* **2010**, *3*, 1311 – 1315.
[29] C. Shi, H. A. Hansen, A. C. Lausche, J. K. Nørskov, *Phys. Chem. Chem. Phys.* **2014**, *16*, 4720 – 4727.
[30] W. J. Durand, A. A. Peterson, F. Studt, F. Abild-Pedersen, J. K. Nørskov, *Surf. Sci.* **2011**, *605*, 1354 – 1359.
[31] H. A. Hansen, J. B. Varley, A. A. Peterson, J. K. Nørskov, *J. Phys. Chem. Lett.* **2013**, *4*, 388 – 392.
[32] C. Cui, H. Wang, X. Zhu, J. Han, Q. Ge, *Sci. China Chem.* **2015**, *58*, 607 – 613.
[33] Y. Kwon, J. Lee, *Electrocatalysis* **2010**, *1*, 108 – 115.
[34] W. Li, *Electrocatalytic Reduction of $CO_2$ to Small Organic Molecule Fuels on Metal Catalysts, in Advances in $CO_2$ Conversion and Utilization* (Ed.: Y. Hu), ACS Symposium Series, American Chemical Society, Washington, DC, **2010**.
[35] F. Abild-Pedersen, J. Greeley, F. Studt, J. Rossmeisl, T. R. Munter, P. G. Moses, E. Skúlason, T. Bligaard, J. K. Nørskov, *Phys. Rev. Lett.* **2007**, *99*, 016105.
[36] G. Jones, F. Studt, F. Abild-Pedersen, J. K. Nørskov, T. Bligaard, *Chem. Eng. Sci.* **2011**, *66*, 6318 – 6323.
[37] S. Wang, V. Petzold, V. Tripkovic, J. Kleis, J. G. Howalt, E. Skúlason, E. M. Fernández, B. Hvolbæk, G. Jones, A. Toftelund, H. Falsig, M. Björketun, F. Studt, F. Abild-Pedersen, J. Rossmeisl, J. K. Nørskov, T. Bligaard, *Phys. Chem. Chem. Phys.* **2011**, *13*, 20760 – 20765.
[38] C. H. Lee, M. W. Kanan, *ACS Catal.* **2015**, *5*, 465 – 469.
[39] Y. Chen, M. W. Kanan, *J. Am. Chem. Soc.* **2012**, *134*, 1986 – 1989.
[40] N. Hoshi, M. Kato, Y. Hori, *J. Electroanal. Chem.* **1997**, *440*, 283 – 286.
[41] D. W. DeWulf, T. Jin, A. J. Bard, *J. Electrochem. Soc.* **1989**, *136*, 1686.
[42] C. Shi, C. P. O'Grady, A. A. Peterson, H. A. Hansen, J. K. Nørskov, *Phys. Chem. Chem. Phys.* **2013**, *15*, 7114 – 7122.
[43] X. Min, M. W. Kanan, *J. Am. Chem. Soc.* **2015**, *137*, 4701 – 4708.
[44] R. Kortlever, C. Balemans, Y. Kwon, M. T. M. Koper, *Catal. Today* **2015**, *244*, 58 – 62.
[45] R. Kortlever, I. Peters, S. Koper, M. T. M. Koper, *ACS Catal.* **2015**, *5*, 3916 – 3923.
[46] K. Chan, J. K. Nørskov, *J. Phys. Chem. Lett.* **2015**, *6*, 2663 – 2668.
[47] J. Wellendorff, K. T. Lundgaard, A. Møgelhøj, V. Petzold, D. D. Landis, J. K. Nørskov, T. Bligaard, K. W. Jacobsen, *Phys. Rev. B* **2012**, *85*, 235149.
[48] S. R. Bahn, K. W. Jacobsen, *Comput. Sci. Eng.* **2002**, *4*, 56 – 66.
[49] P. Giannozzi, S. Baroni, N. Bonini, M. Calandra, R. Car, C. Cavazzoni, D. Ceresoli, G. L. Chiarotti, M. Cococcioni, I. Dabo, A. Dal Corso, S. de Gironcoli, S. Fabris, G. Fratesi, R. Gebauer, U. Gerstmann, C. Gougoussis, A. Kokalj, M. Lazzeri, L. Martin-Samos, N. Marzari, F. Mauri, R. Mazzarello, S. Paolini, A. Pasquarello, L. Paulatto, C. Sbraccia, S. Scandolo, G. Sclauzero, A. P. Seitsonen, A. Smogunov, P. Umari, R. M. Wentzcovitch, *J. Phys. Condens. Matter* **2009**, *21*, 395502.
[50] J. Wellendorff, T. L. Silbaugh, D. Garcia-Pintos, J. K. Nørskov, T. Bligaard, F. Studt, C. T. Campbell, *Surf. Sci.* **2015**, *640*, 36 – 44.
[51] F. Studt, F. Abild-Pedersen, J. B. Varley, J. K. Nørskov, *Catal. Lett.* **2013**, *143*, 71 – 73.
[52] F. Studt, M. Behrens, E. L. Kunkes, N. Thomas, S. Zander, A. Tarasov, J. Schumann, E. Frei, J. B. Varley, F. Abild-Pedersen, J. K. Nørskov, R. Schlögl, *ChemCatChem* **2015**, *7*, 1105 – 1111.
[53] F. Studt, I. Sharafutdinov, F. Abild-Pedersen, C. F. Elkjær, J. S. Hummelshøj, S. Dahl, I. Chorkendorff, J. K. Nørskov, *Nat. Chem.* **2014**, *6*, 320 – 324.
[54] A. J. Medford, J. Wellendorff, A. Vojvodic, F. Studt, F. Abild-Pedersen, K. W. Jacobsen, T. Bligaard, J. K. Nørskov, *Science* **2014**, *345*, 197 – 200.
[55] K. Laasonen, R. Car, C. Lee, D. Vanderbilt, *Phys. Rev. B* **1991**, *43*, 6796.
[56] H. J. Monkhorst, J. D. Pack, *Phys. Rev. B* **1976**, *13*, 5188.
[57] R. Christensen, H. A. Hansen, T. Vegge, *Catal. Sci. Technol.* **2015**, *5*, 4946 – 4949.

Received: September 3, 2015
Revised: October 28, 2015
Published online on December 10, 2015

# Paper V

---

Functional Independent Scaling Relation for ORR/OER Catalysts
Rune Christensen, Heine A. Hansen, Colin F. Dickens, Jens K. Nørskov, and Tejs Vegge
*J. Phys. Chem. C*, **2016**, 120 (43), pp 24910–24916

THE JOURNAL OF PHYSICAL CHEMISTRY C

Article

pubs.acs.org/JPCC

# Functional Independent Scaling Relation for ORR/OER Catalysts

Rune Christensen,[†] Heine A. Hansen,[†] Colin F. Dickens,[‡,§] Jens K. Nørskov,[‡,§] and Tejs Vegge*[,†]

[†]Department of Energy Conversion and Storage, Technical University of Denmark, Fysikvej bld. 309, DK-2800 Kgs. Lyngby, Denmark

[‡]SUNCAT Center for Interface Science and Catalysis, SLAC National Accelerator Laboratory, 2575 Sand Hill Road, Menlo Park, California 94025, United States

[§]Department of Chemical Engineering, Stanford University, Stanford, California 94305, United States

Supporting Information

**ABSTRACT:** A widely used adsorption energy scaling relation between OH* and OOH* intermediates in the oxygen reduction reaction (ORR) and oxygen evolution reaction (OER), has previously been determined using density functional theory and shown to dictate a minimum thermodynamic overpotential for both reactions. Here, we show that the oxygen−oxygen bond in the OOH* intermediate is, however, not well described with the previously used class of exchange-correlation functionals. By quantifying and correcting the systematic error, an improved description of gaseous peroxide species versus experimental data and a reduction in calculational uncertainty is obtained. For adsorbates, we find that the systematic error largely cancels the vdW interaction missing in the original determination of the scaling relation. An improved scaling relation, which is fully independent of the applied exchange−correlation functional, is obtained and found to differ by 0.1 eV from the original. This largely confirms that, although obtained with a method suffering from systematic errors, the previously obtained scaling relation is applicable for predictions of catalytic activity.

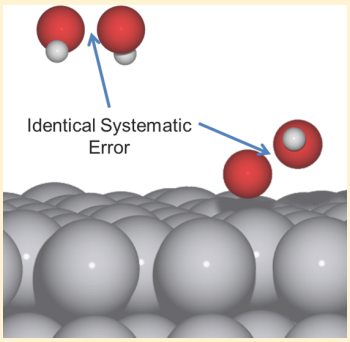


## INTRODUCTION

Development of efficient, highly stable, and inexpensive oxygen evolution reaction (OER) and oxygen reduction reaction (ORR) catalysts are key challenges in large scale commercialization of water electrolyzers and hydrogen fuel cells, respectively.[1−5] In these efforts detailed fundamental knowledge of the catalytic processes is required.

In recent years, a number of studies applying Density Functional Theory (DFT) has provided new insight into the fundamentals of OER and ORR.[6−13] A significant finding is a scaling relation between the adsorption energy of OH* and OOH* intermediates found for a large variety of catalysts and catalytic sites.[9−12,14−18] When expressed in terms of the free energy the scaling relation is $\Delta G_{OOH^*} = \Delta G_{OH^*} + 3.2 \pm 0.2$ eV[9,15] with the 3.2 eV offset determined using the RPBE exchange-correlation functional.[19] The 3.2 eV free energy difference compares favorably to an experimental free energy difference of 3.4 eV between $OH^-(aq)$ and $OOH^-(aq)$.[20,21] The optimal adsorption free energy difference between OH* and OOH* is 2.46 eV for both ORR and OER.[9,11,21] The scaling relation forces a minimum thermodynamic overpotential, at which all intermediate reaction steps are exergonic, of $(3.2 \pm 0.2\ \text{eV} - 2.46\ \text{eV})/2e = 0.4 \pm 0.1$ V for both reactions. Based on the scaling relation, it is possible to use adsorption free energies as predictors for catalyst activity. For ORR, the adsorption free energy of OH* can be used as predictor with the optimum at $(4.92\ \text{eV} - 3.2 \pm 0.2\ \text{eV})/2 = 0.9 \pm 0.1$ eV. Catalysts which adsorb OH* slightly (~0.1 eV) weaker than Pt have been found to display improved activity over Pt.[7,22] Predictions of catalyst activity based on the OH* adsorption free energy relative to Pt have been shown to agree well with experimental findings.[7,22] Similarly, the adsorption free energy difference between O* and OH* is used as a descriptor for highest OER activity.[11] The highest activity is predicted at a difference of $(3.2 \pm 0.2\ \text{eV})/2 = 1.6 \pm 0.1$ eV.

It is important to stress that the ±0.2 eV reported for the scaling relation does not refer to the calculation accuracy in any individual calculation but how well adsorption free energies calculated for a multitude of different surfaces follow the scaling relation.[11,12,15,16] Although the general trend is a 3.2 eV difference in adsorption energy between OH* and OOH*, there is notable scatter around this "best fit" trend line. The ±0.2 eV is thus an uncertainty introduced by considering the scaling relation as "universal"[11] for all surfaces and not to be confused with the general calculational uncertainty at the applied level of theory. When considering a narrow class of materials such as Pt skins on Pt alloys, the scatter is significantly less than 0.2 eV.[12]

The calculational accuracy for a given calculation is not known a priori. The largest contribution to the calculational uncertainty is expected to be the exchange−correlation functional. This has become increasingly true as electronic

Received: September 9, 2016
Revised: October 11, 2016
Published: October 11, 2016





DOI: 10.1021/acs.jpcc.6b09141
J. Phys. Chem. C 2016, 120, 24910−24916

structure codes have been developed to the point where results are largely converged across different codes.[23] The magnitude of the uncertainty related to the exchange-correlation functional can be difficult to estimate although methods for it have been developed as discussed below.[24] Recently, Deshpande et al.[18] have applied these methods to evaluate the calculational uncertainty in studies of heterogeneous ORR catalysts. An extension to the error estimation method is applied here to determine whether systematic errors are present when calculating the adsorption free energy difference between OH* and OOH* with the applied class of exchange-correlation functionals. The extended approach has previously been used for identifying systematic errors in calculated energies for $CO_2$ reduction reactions.[25] This knowledge improved accuracy of calculations and has been applied in studies of $CO_2$ reduction to formic acid.[26]

A major difference between OH* and OOH* is the presence of an oxygen−oxygen bond in the OOH* intermediate. This bond can to some extent be assumed to be similar to the oxygen−oxygen bond in a peroxide. The triplet ground state of molecular oxygen is known to be very difficult to describe using DFT.[27] Although peroxides are not spin polarized, systematic errors in calculated enthalpies of metal oxides and metal peroxides for several exchange−correlation functionals including the RPBE functional have been attributed to the difference in oxygen ions.[28−31] We here seek to determine whether a systematic error is indeed present and determine how it influences the OH*/OOH* scaling relation and predictions based on it. If a systematic error is present in the description of the oxygen−oxygen bond, the adsorption free energy of OOH* is likely also to be systematically inaccurate. The previously determined free energy difference between OH* and OOH*, i.e., the scaling relation offset of 3.2 eV, will thus also be systematically inaccurate and lead to inaccuracies in predictions of the minimum thermodynamic overpotentials and optimal adsorption free energies. By quantifying the systematic error not only can the calculational uncertainty for a given surface be reduced, but the accuracy of predictions previously made using the scaling relation also be evaluated.

## THEORETICAL METHODS

To test for systematic errors in the description of peroxide species, the enthalpy of reaction is calculated for different reactions with known reaction enthalpies. Eight representative gas phase reactions ("gas phase set" in Table 1), where a peroxide is formed, have been examined and the enthalpies of reaction have been compared to experimental values.[32]

In the case of ethyl hydroperoxide, $C_2H_5OOH$, and *n*-propyl hydroperoxide, $C_3H_7OOH$, experimental data obtained with sufficient precision is unavailable. Instead, cross verified enthalpies calculated using quantum chemistry methods, which are well suited for highly accurate description of gaseous molecules, are used for these species.[33] To test whether errors are related to the formation of a peroxide specie, four verification reactions similar to the others but without the formation of peroxide are examined in a similar manner ("verification set" in Table 1). We expect the enthalpy of reaction for the verification reactions to be well-described.

To determine whether systematic errors are not only present in gas phase peroxides, but also for surface bound OOH*, the difference in adsorption enthalpies of OH* and OOH* are calculated on different metal surfaces, which span the full range of relevant OH*/OOH* adsorption energies for ORR, i.e., the

**Table 1. Reaction Sets**

| | | | |
|---|---|---|---|
| gas phase set | | | reac |
| $2\,H_2O$ | $\rightarrow$ | $H_2 + H_2O_2$ | (1) |
| $CH_3OH + H_2O$ | $\rightarrow$ | $H_2 + CH_3OOH$ | (2) |
| $C_2H_5OH + H_2O$ | $\rightarrow$ | $H_2 + C_2H_5OOH$ | (3) |
| $2\,CH_3OH$ | $\rightarrow$ | $H_2 + CH_3OOCH_3$ | (4) |
| $C_3H_7OH + H_2O$ | $\rightarrow$ | $H_2 + C_3H_7OOH$ | (5) |
| $(CH_3)_2CHOH + H_2O$ | $\rightarrow$ | $H_2 + (CH_3)_2CHOOH$ | (6) |
| $2\,C_2H_5OH$ | $\rightarrow$ | $H_2 + C_2H_5OOC_2H_5$ | (7) |
| $(CH_3)_3COH + H_2O$ | $\rightarrow$ | $H_2 + (CH_3)_3COOH$ | (8) |
| adsorbate set | | | |
| $OH^*_{Pt}{}^a + H_2O$ | $\rightarrow$ | $H_2 + OOH^*_{Pt}{}^a$ | (*1) |
| $OH^*_{Ag}{}^b + H_2O$ | $\rightarrow$ | $H_2 + OOH^*_{Ag}{}^b$ | (*2) |
| $OH^*_{Pd}{}^a + H_2O$ | $\rightarrow$ | $H_2 + OOH^*_{Pd}{}^a$ | (*3) |
| verification set | | | |
| $2\,CH_4$ | $\rightarrow$ | $H_2 + C_2H_6$ | (v1) |
| $CH_4 + H_2O$ | $\rightarrow$ | $H_2 + CH_3OH$ | (v2) |
| $CH_4 + C_2H_6$ | $\rightarrow$ | $H_2 + C_3H_8$ | (v3) |
| $C_2H_6 + H_2O$ | $\rightarrow$ | $H_2 + C_2H_5OH$ | (v4) |

[a]Ontop adsorption site. [b]hcp hollow adsorption site.

(111) facets of Pt, Ag, and Pd.[8] The enthalpy is calculated for an "adsorbate set" (Table 1) of reactions similar to those in the "gas phase set". Important aspects such as coverage and electrolyte effects, which should be included to obtain adsorption free energies under realistic ORR/OER conditions, have purposely been disregarded as including these effects will make it difficult to isolate the oxygen−oxygen bond functional dependence.

The reaction enthalpies are calculated with a range of different generalized gradient approximation (GGA) functionals. Here, we focus on the GGA functionals, as this level of functional complexity is often the best applicable for practical trend studies of heterogeneous catalysis.[34] Besides the RPBE functional[19] originally used to establish the OH*/OOH* scaling relation, we also consider the common GGA functionals PBE[35] and BLYP.[36,37] In addition, three functionals with nonlocal van der Waals correlation, vdW-DF,[38] vdW-DF2,[39] and BEEF-vdW,[24] are included.

The BEEF-vdW functional is constructed with catalysis studies in mind and demonstrated to describe many adsorption energies well.[24,40] As the BEEF-vdW functional and the associated ensemble are critical to the applied method, it will here be presented in some detail. For a more thorough description of the functional and ensemble the reader is refereed to Wellendorff et al.[24]

The BEEF-vdW exchange−correlation energy is given by

$$E_{xc} = \sum_{m=0}^{29} a_m E_m^{\mathrm{GGA-x}} + \alpha_c E^{\mathrm{LDA-c}} + (1-\alpha_c)E^{\mathrm{PBE-c}} + E^{\mathrm{nl-c}} \quad (1)$$

$E_m^{\mathrm{GGA-x}}$ is the exchange energy obtained with the GGA approximation applying the Legendre polynomial of order $m$ as enhancement factor. $E^{\mathrm{LDA-c}}$ and $E^{\mathrm{PBE-c}}$ are LDA and PBE correlation energies. The $E^{\mathrm{nl-c}}$ term is nonlocal van der Waals correlation identical to that applied in the vdW-DF2 functional.

In a machine learning process, the exchange energy expansion parameters, $a_m$, and the correlation weighting, $\alpha_c$, are determined such that the functional is optimized to



DOI: 10.1021/acs.jpcc.6b09141
J. Phys. Chem. C 2016, 120, 24910−24916

reproduce energies in selected data set, i.e. formation and reaction energies, reaction barriers, chemisorption energies, van der Waals interactions, and cohesive energies. The optimal parameter values for $a_m$ and $\alpha_c$ determined in this approach are used for the main BEEF-vdW functional. In addition to the optimal parameters, an ensemble of functionals using suboptimal parameter values is created in a process inspired by Bayesian statistics. A set of suboptimal parameters, which reproduces database energies relatively well, is more likely to be accepted into the ensemble of functionals than a worse performing set of parameters.

The ensemble can be used to quantify an estimate of the error and thus also calculational uncertain related to the specific choice of exchange-correlation functional for a given calculation. This is done by computing the energy of interest with a number of ensemble functionals (generally convergence is reached at 2000).[24] The standard deviation in calculated energies across the ensemble has been shown to be a good quantitative error estimate.[24] The procedure can be viewed as an improved method for testing the robustness of the results by recalculating with a range of "mindfully selected" functionals, as discussed by Sabbe et al.[34]

All ensemble functionals differ from the main BEEF-vdW functional only in the weight given to the individual energy terms in (1). Once a self-consistent BEEF-vdW calculation has been performed and the energy of each term obtained, the energy for all ensemble functionals can easily be evaluated at single point level accuracy by simply multiplying a matrix containing the parameters $a_m$ and $\alpha_c$ for the ensemble functionals with a vector containing the individual energy terms. The method does not only help quantify error estimates but is also useful for obtaining energies computed with a large range of functionals very efficiently.

The VASP code using the projector augmented-wave (PAW) method has been used for all calculations.[41−44] To reduce errors related to choice of PAW potentials, high accuracy hard potentials distributed with the code have been used for H, O, and C. Default potentials have been used for Pt and Ag, and a potential treating the 4*p* electrons as valence electrons has been used for Pd (pv potential). A plane wave energy cutoff at 650 eV has been used. Both molecular oxygen and superoxide ions are spin polarized. Although the oxygen−oxygen bonds present in the examined structures are not expected to exhibit spin polarization, calculations allowing spin polarization were performed. See the Supporting Information for further calculational details.

## RESULTS AND DISCUSSION

The enthalpy of reaction has been calculated for the reactions in Table 1. The errors versus reference data are shown in Table 2 for reactions in the "gas phase set" and the "verification set".

The vdW functionals have been adjusted for a previously identified systematic error of 0.09 eV on the $H_2$ molecule using the BEEF-vdW functional.[25,26,45,46] This generally decreases the errors. Reactions 1−8 have similar errors with a given functional as seen in Table 2, where the average error (avg.) and the standard deviation on the error (SD) are also reported. The verification reactions v1−v4 do not display the same systematic error, indicating a systematic error related to the formation of a peroxide bond.

The error is consistently above the average in reaction 1 and below the average in reactions 4 and 7. A likely explanation is that the amount of reactant $H_2O$ is different for reaction 1 (two $H_2O$) and reactions 4 and 7 (no $H_2O$) as compared to the other reactions (one $H_2O$). For a given functional, the small variation in error within the "gas phase set" and the "verification set" can thus largely be explained by an error of 0.02−0.05 eV per $H_2O$ molecule. This is discussed further below.

Having established that the formation of a peroxide is the dominant reason for the systematic errors, it is examined whether such systematic errors are also present when comparing free energies of OH* and OOH* adsorbed on catalytic surfaces, where accurate experimental values remain elusive. First, calculational uncertainties are quantified using the BEEF ensemble. For each reaction, the enthalpy has been calculated with the ensemble of functionals and the standard deviation determined (Table 3). The standard deviation is 0.19 ± 0.02 eV for reactions in the "gas phase set" and "adsorbate set" and 0.05 ± 0.02 eV for the reactions in the Verification Set. The functional dependence of the result and thus the calculational uncertainty is found to be significantly larger for reactions in the "gas phase set" and the "adsorbate set" than for reactions in the Verification Set. Further, the functional dependence is seen to be similar in magnitude for the "gas

**Table 2. Errors in Calculated $\Delta H_r^\circ$ (eV) for Reactions in Table 1 with Diffferent Exchange-Correlation Functionals**

| reac | PBE | RPBE | BEEF-vdW | vdW-DF | vdW-DF2 | BLYP |
|---|---|---|---|---|---|---|
| (1) | 0.25 | 0.29 | 0.26 | 0.41 | 0.44 | 0.35 |
| (2) | 0.19 | 0.24 | 0.22 | 0.36 | 0.40 | 0.30 |
| (3) | 0.21 | 0.24 | 0.22 | 0.36 | 0.39 | 0.29 |
| (4) | 0.17 | 0.18 | 0.21 | 0.36 | 0.39 | 0.25 |
| (5) | 0.21 | 0.24 | 0.24 | 0.39 | 0.41 | 0.31 |
| (6) | 0.21 | 0.23 | 0.21 | 0.37 | 0.42 | 0.27 |
| (7) | 0.14 | 0.14 | 0.19 | 0.34 | 0.36 | 0.21 |
| (8) | 0.24 | 0.25 | 0.27 | 0.42 | 0.46 | 0.33 |
| avg.[a] | 0.20 | 0.22 | 0.23 | 0.38 | 0.41 | 0.29 |
| SD[b] | 0.03 | 0.04 | 0.02 | 0.03 | 0.03 | 0.04 |
| (v1) | 0.01 | -0.01 | -0.01 | 0.00 | -0.05 | -0.04 |
| (v2) | 0.05 | 0.05 | 0.06 | 0.11 | 0.10 | 0.07 |
| (v3) | -0.03 | -0.06 | -0.03 | -0.03 | -0.08 | -0.10 |
| (v4) | 0.02 | 0.00 | 0.03 | 0.08 | 0.08 | 0.03 |

[a]Average error. [b]Standard deviation for reactions 1−8.

**Table 3. BEEF Ensemble Standard Deviation (eV) before and after Correction of the O−O Bond**

| reac | std. dev. | std. dev. corrected |
|---|---|---|
| (1) | 0.17 | 0.04 |
| (2) | 0.19 | 0.04 |
| (3) | 0.19 | 0.04 |
| (4) | 0.20 | 0.06 |
| (5) | 0.18 | 0.04 |
| (6) | 0.19 | 0.05 |
| (7) | 0.20 | 0.05 |
| (8) | 0.19 | 0.05 |
| (*1) | 0.19 | 0.05 |
| (*2) | 0.19 | 0.04 |
| (*3) | 0.19 | 0.05 |
| (v1) | 0.03 | 0.03 |
| (v2) | 0.05 | 0.05 |
| (v3) | 0.05 | 0.05 |
| (v4) | 0.06 | 0.06 |



DOI: 10.1021/acs.jpcc.6b09141
J. Phys. Chem. C 2016, 120, 24910−24916

phase set" reactions and the "Adsorbate Set" reactions. We further note that 0.19 eV is comparable to the scaling relation offset uncertainty found by Deshpande et al.[18] calculated from separate uncertainties on OH* and OOH* using statistical measures. It is also worth noting that the ensemble standard deviation is a good quantitative estimate of the errors observed with the BEEF-vdW functional in Table 2, although it is slightly smaller than the on average 0.23 eV error for the "gas phase set" reactions.

To examine whether the increased functional dependence for the "gas phase set" and "adsorbate set" is due to the presence of an oxygen−oxygen bond, the effect of applying an energy correction to the oxygen−oxygen bond is examined. For each of the ensemble functionals, the average difference from the electronic energy calculated with the BEEF-vdW functional is determined for the reactions in the "gas phase set" and the "adsorbate set" and applied as an energy correction for that particular ensemble functional. The energy correction $c_f$ for a given ensemble functional $f$ is thus given by

$$c_f = \frac{1}{11}\sum_r \left(E_{\mathrm{BEEF-vdW},r} - E_{f,r}\right) \quad (2)$$

where $r$ is the 11 reactions in the "gas phase set" and the "adsorbate set". $E_{\mathrm{BEEF-vdW},r}$ and $E_{f,r}$ are the electronic energies of reaction $r$ calculated with the BEEF-vdW functional and the ensemble functional $f$, respectively. After a correction has been applied to each ensemble functional, $E_{f,r,\mathrm{corrected}} = E_{f,r} + c_f$, the standard deviation for each reaction is recalculated using the corrected energies and found to be significantly smaller and in agreement with those observed for the verification reactions (Table 3). It is thus shown to be generally valid for GGA-vdW type functionals that the functional dependence can be minimized effectively through an identical energy correction to the reactions in the "gas phase set" and the "adsorbate set" and be brought to the level of the reactions in the "verification set". The systematic error causing significant functional dependence observed for the reactions in the "gas phase set" hence applies identically to the reactions in the "adsorbate set".

An illustrative way to examine correlations in the functional dependence is by plotting the calculated enthalpies of reactions for two reactions versus each other with several functionals.[25] In Figure 1, the calculated enthalpies of the gas phase formation of methyl hydroperoxide from methanol (reaction 2) is compared to the enthalpy difference between OH* and OOH* adsorbed on Pt (reaction *1).

The 2000 functionals in the BEEF ensemble form a straight line with a slope of 1.01 determined through linear regression. The variation in the calculated enthalpy of reaction is as large as 1.0 eV. The presence of a straight line (coefficient of determination $R^2$ = 0.987) with slope 1 indicates that the feature dominating functional dependence is identical in the two reactions. The three primary vdW functionals are placed on or close to this line. The inclusion of vdW interactions will likely stabilize OOH* more than OH* due to the size difference.[47] This explains why the non-vdW functionals deviate slightly from the line toward a larger enthalpy of reaction for reaction *1. To examine this the isolated effect of vdW interactions has been probed by adding vdW interactions to RPBE and PBE using the Tkatchenko−Scheffler[48] (TS) method using a scaling parameter $s_R$ = 0.94 and reoptimizing geometries. The inclusion of the vdW interactions does not change the gas phase enthalpies significantly, but stabilizes

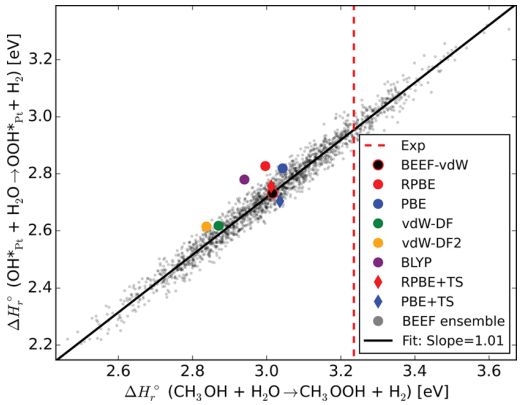


**Figure 1.** Enthalpies of reaction for reactions 2 and *1 calculated with various functionals and plotted versus each other. Diamonds mark functionals with added vdW correlation using the Tkatchenko−Scheffler (TS) method. The BEEF-ensemble functionals (semi-transparent gray points) fall on a straight line with a fitted slope of 1.01. The dashed red line marks the experimental enthalpy of reaction 2.

OH* by ∼0.15 eV and OOH* by ∼0.25 eV causing a relative downshift of ∼0.10 eV in $\Delta H_r^\circ$ for reaction *1. This downshift brings the non-vdW functionals onto the line.

Similar correlation analyses are made for all the considered reactions. The obtained slopes found through linear regression are depicted in Figure 2. A straight line with a slope close to 1 is

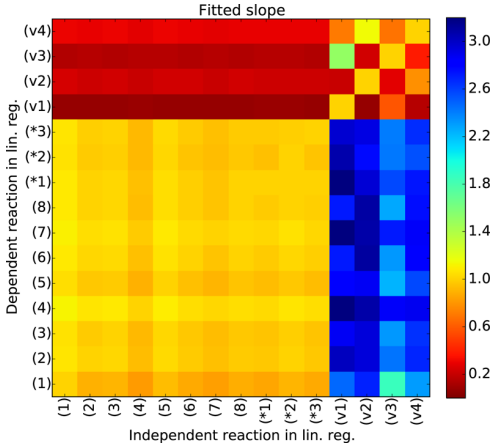


**Figure 2.** Heat plot depicting the slopes obtain through linear regression on the BEEF ensemble for all possible combinations with the 15 total reactions examined.

obtained for all possible combinations of reactions in the "gas phase set" and the "adsorbate set". When reactions from the "verification set" are compared in a similar manner to reactions in the "gas phase set" and the "adsorbate set", the results are significantly different. As the functional dependence is much smaller for reactions in the "verification set", which does not contain peroxide bonds, the fitted slopes will be large (>2) or close to 0 depending on whether the "verification set" reaction is used as independent or dependent variable, respectively.

In addition to identifying the oxygen−oxygen bond as dominant source of functional dependence and establishing that identical functional dependence is observed for all reactions in the Gas Phase Set and Adsorbate Set, the


DOI: 10.1021/acs.jpcc.6b09141
J. Phys. Chem. C 2016, 120, 24910−24916

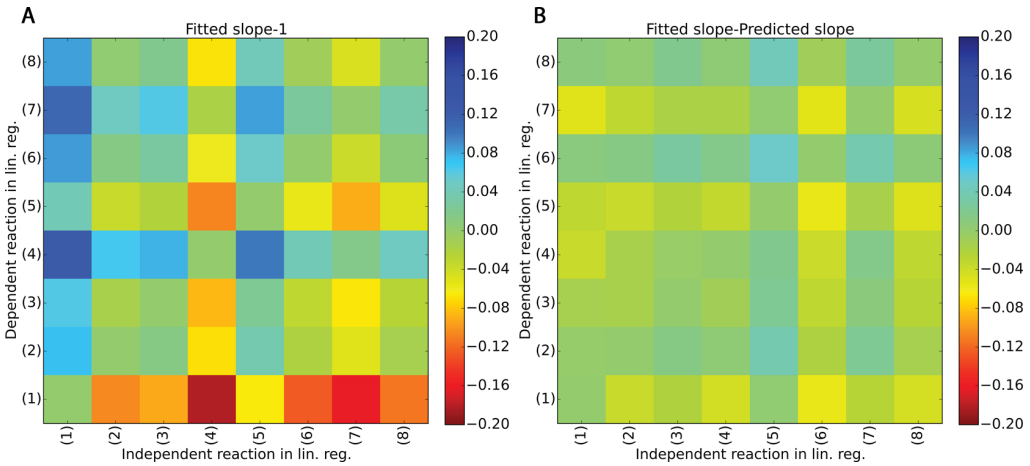


**Figure 3.** (a) Difference between the slope found through linear regression and a slope of 1. (b) Difference between the slope found through linear regression and a slope predicted with a $H_2O$ molecule impacting the slope with 8% relative to the impact of the peroxide bond.

correlation heat map in Figure 2 can also be used to identify an additional minor contribution to functional dependence. As mentioned above, the trend in errors obtained with the self-consistent functionals (Table 2) suggest that $H_2O$ can cause a minor error. The same trend with reactions 1, 4, and 7 differing from the rest is observed for the uncorrected standard deviations in Table 3. We examine whether the trend is also reflected in the slopes obtained from linear regression for correlations in the "gas phase set" as seen in Figure 3. In Figure 3a, the difference between the slope obtained through linear regression and a slope of 1 is depicted. The most significant differences are observed in cases where reactions 1, 4, or 7 are involved. The pattern fits well with the cause being two reactant $H_2O$ molecules in reaction 1, none in reactions 4 and 7, and one in the other reactions. To test this hypothesis, the slopes are predicted, $a_{\text{predicted}}$, taking the possibility of $H_2O$ contributing to functional dependence into account.

$$a_{\text{predicted}} = \frac{1 - \alpha n_{H_2O,x}}{1 - \alpha n_{H_2O,y}} \quad (3)$$

$n_{H_2O,x}$ and $n_{H_2O,y}$ are the number of $H_2O$ molecules in the independent and dependent reactions, respectively. $\alpha$ is a parameter which relates the influence of $H_2O$ on the slope with that of the peroxide bond. In case $H_2O$ contributes to the functional dependence in a manner which correlates with the functional dependence of the peroxide bond, the optimal value of $\alpha$ is different from 0. Using $\alpha = -0.08$, the predicted and fitted slopes are very similar for all reactions as observed in Figure 3b. Each reactant $H_2O$ molecule thus influences the slope with an impact of approximately 8% of that of the peroxide bond. The negative value of $\alpha$ is caused by $H_2O$ being a reactant molecule and the peroxide bond being present in the product molecule.

The difference between correcting for errors due to the oxygen−oxygen bond and $H_2O$ independently, as opposed to correcting for a combined total error is insignificant for the purpose of correcting the OH*/OOH* scaling relation. This is due to both the common presence of both species in most reactions and the apparent error caused by $H_2O$ being 1 order of magnitude smaller than the error caused by the oxygen−oxygen bond.

With correlation in functional dependence between reactions in the "gas phase set" and "adsorbate set" established, the systematic error of 0.22 eV found for the "gas phase set" reactions with the RPBE functional can be applied to update the scaling relation between OH* and OOH*. The lack of van der Waals interaction in the RPBE functional is in principle included in the 0.22 eV systematic error for gaseous molecules. However, using the TS method for adding vdW interactions, we found the stabilizing effect to be significant only for adsorbates. This must be considered when transferring the systematic error observed in gas phase to adsorbates. The difference in the missing vdW stabilization for OH* and OOH*, ∼0.1 eV, will to some degree counteract the systematic error on the oxygen−oxygen bond. Based on this, the scaling relation offset can be corrected by 0.1 eV such that it is now largely functional independent.

The more robust scaling relation is $\Delta G_{OOH*} = \Delta G_{OH*} + 3.3$ eV ± 0.2 eV. The ±0.2 eV still denotes the uncertainty induced by modeling scattered data with a straight line and not the calculational uncertainty for a given surface. The latter is now quantified and as seen in Table 3 to be reduced from 0.19 to 0.05 eV after correction of the systematic error.

Using the functionally independent scaling relation, more robust predictions of minimum overpotentials and optimal adsorption free energies can be performed for a given surface. In general, the minimum thermodynamic overpotential of ∼0.4 eV will increase by 0.05 eV. Predictions of optimal catalyst reactivities are also modified. For ORR catalysts, the optimal adsorption free energy of OH* (∼0.8 eV) predicted from the improved scaling relation requires a slightly more reactive catalyst, which adsorbs OH* 0.05 eV stronger, than previously predicted. For OER, the predicted optimum adsorption free energy difference between O* and OH* (∼1.7 eV) has increased by 0.05 eV. This requires a slightly less reactive catalyst than previously predicted.

The relatively small changes in optimal adsorption energies and theoretical minimum overpotential will arguably have little impact on the search for new catalysts, especially considering that the scaling relation has only been shown universally valid with 0.2 eV accuracy across different catalytic surfaces. More important is the realization that in spite of being a relatively simple functional approach suffering from a here documented systematic error and lacking description of van der Waals


DOI: 10.1021/acs.jpcc.6b09141
J. Phys. Chem. C 2016, 120, 24910−24916

interactions, previous determination of the scaling relation offset based on RPBE calculations has come remarkably close to the functional independent scaling relation offset obtained here. This, in combination with the now quantified and reduced calculational uncertainty, strengthens the applicability of the scaling relation in both prior and future predictions and modeling of catalyst activity.

## CONCLUSIONS

We have identified systematic errors on the order of 0.2 eV in the description of peroxide gas phase species using GGA level density functionals. The systematic error was shown to also be present for adsorbed OOH*. It thus impacts the constant free energy difference in the scaling relation previously discovered between adsorption free energies of OH* and OOH*, which are intermediate adsorbates in both ORR and OER. By identifying and correcting for the systematic error, which for adsorbates was partially canceled by inclusion of van der Waals interaction not previously considered, the calculational uncertainty can be significantly reduced from 0.19 to 0.05 eV and a functional independent scaling relation determined. The scaling relation offset is changed from 3.2 to 3.3 eV. This directly alters predictions of optimal adsorption energies and theoretical minimum potential by 0.05 eV. The relative small change from the earlier version of the scaling relation confirms that, although derived using a method suffering from systematic errors, the earlier version of the scaling relation is sufficiently accurate to be applicable in catalysis research.

## ASSOCIATED CONTENT

### Supporting Information

The Supporting Information is available free of charge on the ACS Publications website at DOI: 10.1021/acs.jpcc.6b09141.

Computational details, conversion of scaling relation to free energies and specific treatment of error on $H_2O$ (PDF)

## AUTHOR INFORMATION


### Corresponding Author

*E-mail: teve@dtu.dk. Phone: (+45) 51 64 17 87.


### Notes

The authors declare no competing financial interest.

## ACKNOWLEDGMENTS

The authors thank The Niflheim Linux cluster supercomputer installed at the Department of Physics at the Technical University of Denmark for computational resources. This work was supported by a research grant (9455) from VILLUM FONDEN (V-SUSTAIN).

## REFERENCES


(1) Nie, Y.; Li, L.; Wei, Z. Recent Advancements in Pt and Pt-Free Catalysts for Oxygen Reduction Reaction. *Chem. Soc. Rev.* **2015**, *44*, 2168−2201.

(2) Trotochaud, L.; Boettcher, S. W. Precise Oxygen Evolution Catalysts: Status and Opportunities. *Scr. Mater.* **2014**, *74*, 25−32.

(3) Fabbri, E.; Habereder, A.; Waltar, K.; Kotz, R.; Schmidt, T. J. Developments and Perspectives of Oxide-Based Catalysts for the Oxygen Evolution Reaction. *Catal. Sci. Technol.* **2014**, *4*, 3800−3821.

(4) Cheng, Y.; Jiang, S. P. Advances in Electrocatalysts for Oxygen Evolution Reaction of Water Electrolysis - From Metal Oxides to Carbon Nanotubes. *Prog. Nat. Sci.* **2015**, *25*, 545−553.

(5) Debe, M. K. Electrocatalyst Approaches and Challenges for Automotive Fuel Cells. *Nature* **2012**, *486*, 43−51.

(6) Keith, J. A.; Jacob, T. In Theory and Experiment in Electrocatalysis. Balbuena, B. P., Subramanian, R. V., Eds.; *Modern Aspects of Electrochemistry*; Springer: New York, 2010; Vol. *50*, pp 89−132.

(7) Greeley, J.; Stephens, I. E. L.; Bondarenko, A. S.; Johansson, T. P.; Hansen, H. A.; Jaramillo, T. F.; Rossmeisl, J.; Chorkendorff, I.; Nørskov, J. K. Alloys of Platinum and Early Transition Metals as Oxygen Reduction Electrocatalysts. *Nat. Chem.* **2009**, *1*, 552−556.

(8) Nørskov, J. K.; Rossmeisl, J.; Logadottir, A.; Lindqvist, L.; Kitchin, J. R.; Bligaard, T.; Jónsson, H. Origin of the Overpotential for Oxygen Reduction at a Fuel-Cell Cathode. *J. Phys. Chem. B* **2004**, *108*, 17886−17892.

(9) Koper, M. T. M. Thermodynamic Theory of Multi-Electron Transfer Reactions: Implications for Electrocatalysis. *J. Electroanal. Chem.* **2011**, *660*, 254−260.

(10) Rossmeisl, J.; Logadottir, A.; Nørskov, J. K. Electrolysis of Water on (Oxidized) Metal Surfaces. *Chem. Phys.* **2005**, *319*, 178−184.

(11) Man, I. C.; Su, H.-Y.; Calle-Vallejo, F.; Hansen, H. A.; Martínez, J. I.; Inoglu, N. G.; Kitchin, J.; Jaramillo, T. F.; Nørskov, J. K.; Rossmeisl, J. Universality in Oxygen Evolution Electrocatalysis on Oxide Surfaces. *ChemCatChem* **2011**, *3*, 1159−1165.

(12) Viswanathan, V.; Hansen, H. A.; Rossmeisl, J.; Nørskov, J. K. Universality in Oxygen Reduction Electrocatalysis on Metal Surfaces. *ACS Catal.* **2012**, *2*, 1654−1660.

(13) Halck, N. B.; Petrykin, V.; Krtil, P.; Rossmeisl, J. Beyond the Volcano Limitations in Electrocatalysis - Oxygen Evolution Reaction. *Phys. Chem. Chem. Phys.* **2014**, *16*, 13682−13688.

(14) Rossmeisl, J.; Qu, Z.-W.; Zhu, H.; Kroes, G.-J.; Nørskov, J. Electrolysis of Water on Oxide Surfaces. *J. Electroanal. Chem.* **2007**, *607*, 83−89.

(15) Zhao, Z.; Zhang, L.; Xia, Z. Electron Transfer and Catalytic Mechanism of Organic Molecule-Adsorbed Graphene Nanoribbons as Efficient Catalysts for Oxygen Reduction and Evolution Reactions. *J. Phys. Chem. C* **2016**, *120*, 2166−2175.

(16) Calle-Vallejo, F.; Loffreda, D.; Koper, M. T. M.; Sautet, P. Introducing Structural Sensitivity into Adsorption-Energy Scaling Relations by means of Coordination Numbers. *Nat. Chem.* **2015**, *7*, 403−410.

(17) Greeley, J. Theoretical Heterogeneous Catalysis: Scaling Relationships and Computational Catalyst Design. *Annu. Rev. Chem. Biomol. Eng.* **2016**, *7*, 605−635.

(18) Deshpande, S.; Kitchin, J. R.; Viswanathan, V. Quantifying Uncertainty in Activity Volcano Relationships for Oxygen Reduction Reaction. *ACS Catal.* **2016**, *6*, 5251−5259.

(19) Hammer, B.; Hansen, L. B.; Nørskov, J. K. Improved Adsorption Energetics within Density-Functional Theory Using Revised Perdew-Burke-Ernzerhof Functionals. *Phys. Rev. B: Condens. Matter Mater. Phys.* **1999**, *59*, 7413−7421.

(20) Koper, M. T. M. Theory of Multiple Proton-Electron Transfer Reactions and Its Implications for Electrocatalysis. *Chem. Sci.* **2013**, *4*, 2710−2723.

(21) Viswanathan, V.; Hansen, H. A. Unifying Solution and Surface Electrochemistry: Limitations and Opportunities in Surface Electrocatalysis. *Top. Catal.* **2014**, *57*, 215−221.

(22) Stephens, I. E. L.; Bondarenko, A. S.; Grønbjerg, U.; Rossmeisl, J.; Chorkendorff, I. Understanding the Electrocatalysis of Oxygen Reduction on Platinum and Its Alloys. *Energy Environ. Sci.* **2012**, *5*, 6744−6762.

(23) Lejaeghere, K.; Bihlmayer, G.; Björkman, T.; Blaha, P.; Blügel, S.; Blum, V.; Caliste, D.; Castelli, I. E.; Clark, S. J.; Dal Corso, A. Reproducibility in Density Functional Theory Calculations of Solids. *Science* **2016**, *351*, aad3000.

(24) Wellendorff, J.; Lundgaard, K. T.; Møgelhøj, A.; Petzold, V.; Landis, D. D.; Nørskov, J. K.; Bligaard, T.; Jacobsen, K. W. Density Functionals for Surface Science: Exchange-Correlation Model Development with Bayesian Error Estimation. *Phys. Rev. B: Condens. Matter Mater. Phys.* **2012**, *85*, 235149.




DOI: 10.1021/acs.jpcc.6b09141
J. Phys. Chem. C 2016, 120, 24910−24916

(25) Christensen, R.; Hansen, H. A.; Vegge, T. Identifying Systematic DFT Errors in Catalytic Reactions. *Catal. Sci. Technol.* **2015**, *5*, 4946−4949.
(26) Yoo, J. S.; Christensen, R.; Vegge, T.; Nørskov, J. K.; Studt, F. Theoretical Insight into the Trends that Guide the Electrochemical Reduction of Carbon Dioxide to Formic Acid. *ChemSusChem* **2016**, *9*, 358−363.
(27) Jones, R. O.; Gunnarsson, O. The Density Functional Formalism, Its Applications and Prospects. *Rev. Mod. Phys.* **1989**, *61*, 689−746.
(28) Christensen, R.; Hummelshøj, J. S.; Hansen, H. A.; Vegge, T. Reducing Systematic Errors in Oxide Species with Density Functional Theory Calculations. *J. Phys. Chem. C* **2015**, *119*, 17596−17601.
(29) Hummelshøj, J. S.; Luntz, A. C.; Nørskov, J. K. Theoretical Evidence for Low Kinetic Overpotentials in Li-$O_2$ Electrochemistry. *J. Chem. Phys.* **2013**, *138*, 034703.
(30) Kang, S.; Mo, Y.; Ong, S. P.; Ceder, G. Nanoscale Stabilization of Sodium Oxides: Implications for Na-$O_2$ Batteries. *Nano Lett.* **2014**, *14*, 1016−1020.
(31) Yan, J.; Hummelshøj, J. S.; Nørskov, J. K. Formation Energies of Group I and II Metal Oxides using Random Phase Approximation. *Phys. Rev. B: Condens. Matter Mater. Phys.* **2013**, *87*, 075207.
(32) *NIST Chemistry WebBook, NIST Standard Reference Database Number 69*; Linstrom, P. J., Mallard, W. G., Eds.; National Institute of Standards and Technology: Gaithersburg, MD, 2005.
(33) Simmie, J. M.; Black, G.; Curran, H. J.; Hinde, J. P. Enthalpies of Formation and Bond Dissociation Energies of Lower Alkyl Hydroperoxides and Related Hydroperoxy and Alkoxy Radicals. *J. Phys. Chem. A* **2008**, *112*, 5010−5016.
(34) Sabbe, M. K.; Reyniers, M.-F.; Reuter, K. First-Principles Kinetic Modeling in Heterogeneous Catalysis: An Industrial Perspective on Best-Practice, Gaps and Needs. *Catal. Sci. Technol.* **2012**, *2*, 2010−2024.
(35) Perdew, J. P.; Burke, K.; Ernzerhof, M. Generalized Gradient Approximation Made Simple. *Phys. Rev. Lett.* **1996**, *77*, 3865−3868.
(36) Becke, A. D. Density-Functional Exchange-Energy Approximation with Correct Asymptotic Behavior. *Phys. Rev. A: At., Mol., Opt. Phys.* **1988**, *38*, 3098−3100.
(37) Lee, C.; Yang, W.; Parr, R. G. Development of the Colle-Salvetti Correlation-Energy Formula into a Functional of the Electron Density. *Phys. Rev. B: Condens. Matter Mater. Phys.* **1988**, *37*, 785−789.
(38) Dion, M.; Rydberg, H.; Schröder, E.; Langreth, D. C.; Lundqvist, B. I. Van der Waals Density Functional for General Geometries. *Phys. Rev. Lett.* **2004**, *92*, 246401.
(39) Lee, K.; Murray, E. D.; Kong, L.; Lundqvist, B. I.; Langreth, D. C. Higher-Accuracy van der Waals Density Functional. *Phys. Rev. B: Condens. Matter Mater. Phys.* **2010**, *82*, 081101.
(40) Wellendorff, J.; Silbaugh, T. L.; Pintos, D. G.; Nørskov, J. K.; Bligaard, T.; Studt, F.; Campbell, C. T. A Benchmark Database for Adsorption Bond Energies to Transition Metal Surfaces and Comparison to Selected DFT Functionals. *Surf. Sci.* **2015**, *640*, 36−44.
(41) Kresse, G.; Furthmüller, J. Efficient Iterative Schemes for *Ab Initio* Total-Energy Calculations Using a Plane-Wave Basis Set. *Phys. Rev. B: Condens. Matter Mater. Phys.* **1996**, *54*, 11169−11186.
(42) Blöchl, P. E. Projector Augmented-Wave Method. *Phys. Rev. B: Condens. Matter Mater. Phys.* **1994**, *50*, 17953−17979.
(43) Kresse, G.; Joubert, D. From Ultrasoft Pseudopotentials to the Projector Augmented-Wave Method. *Phys. Rev. B: Condens. Matter Mater. Phys.* **1999**, *59*, 1758−1775.
(44) Klimeš, J.; Bowler, D. R.; Michaelides, A. Van der Waals Density Functionals Applied to Solids. *Phys. Rev. B: Condens. Matter Mater. Phys.* **2011**, *83*, 195131.
(45) Studt, F.; Abild-Pedersen, F.; Varley, J. B.; Nørskov, J. K. CO and $CO_2$ Hydrogenation to Methanol Calculated Using the BEEF-vdW Functional. *Catal. Lett.* **2013**, *143*, 71−73.
(46) Studt, F.; Behrens, M.; Kunkes, E. L.; Thomas, N.; Zander, S.; Tarasov, A.; Schumann, J.; Frei, E.; Varley, J. B.; Abild-Pedersen, F.; et al. The Mechanism of CO and $CO_2$ Hydrogenation to Methanol over Cu-Based Catalysts. *ChemCatChem* **2015**, *7*, 1105−1111.
(47) Ramalho, J. P. P.; Gomes, J. R. B.; Illas, F. Accounting for van der Waals Interactions Between Adsorbates and Surfaces in Density Functional Theory Based Calculations: Selected Examples. *RSC Adv.* **2013**, *3*, 13085−13100.
(48) Tkatchenko, A.; Scheffler, M. Accurate Molecular Van Der Waals Interactions from Ground-State Electron Density and Free-Atom Reference Data. *Phys. Rev. Lett.* **2009**, *102*, 073005.


DOI: 10.1021/acs.jpcc.6b09141
*J. Phys. Chem. C* 2016, 120, 24910−24916

# Extract of Paper VI

---

The Atomic Simulation Environment — A Python library for working with atoms
Ask Hjorth Larsen, Jens Jørgen Mortensen, Jakob Blomqvist, Ivano E. Castelli, Rune Christensen, Marcin Dułak, Jesper Friis, Michael N. Groves, Bjørk Hammer, Cory Hargus, Eric D. Hermes, Paul C. Jennings, Peter Bjerre Jensen, James Kermode, John R. Kitchin, Esben Leonhard Kolsbjerg, Joseph Kubal, Steen Lysgaard, Jón Bergmann Maronsson, Tristan Maxson, Thomas Olsen, Lars Pastewka, Andrew Peterson, Carsten Rostgaard, Jakob Schiøtz, Ole Schütt, Mikkel Strange, Kristian Thygesen, Tejs Vegge, Lasse Vilhelmsen, Michael Walter, Zhenhua Zeng, and Karsten Wedel Jacobsen
*Submitted*

The extract includes the following parts of the full manuscript: Title page with authors and affiliations, Abstract, Introduction, Estimation of exchange-correlation errors (Main contributor: Rune Christensen), Acknowledgments, and references cited in this extract.

# The Atomic Simulation Environment — A Python library for working with atoms

Ask Hjorth Larsen[1,2], Jens Jørgen Mortensen[3], Jakob Blomqvist[4], Ivano E. Castelli[5], Rune Christensen[6], Marcin Dułak[3], Jesper Friis[7], Michael N. Groves[8], Bjørk Hammer[8], Cory Hargus[9], Eric D. Hermes[10], Paul C. Jennings[6], Peter Bjerre Jensen[6], James Kermode[11], John R. Kitchin[12], Esben Leonhard Kolsbjerg[8], Joseph Kubal[13], Steen Lysgaard[6], Jón Bergmann Maronsson[14], Tristan Maxson[13], Thomas Olsen[3], Lars Pastewka[15], Andrew Peterson[9], Carsten Rostgaard[3,16], Jakob Schiøtz[3], Ole Schütt[17], Mikkel Strange[3], Kristian Thygesen[3], Tejs Vegge[6], Lasse Vilhelmsen[8], Michael Walter[18], Zhenhua Zeng[13], and Karsten Wedel Jacobsen[3]

[1]Nano-bio Spectroscopy Group and ETSF Scientific Development Centre, Universidad del País Vasco UPV/EHU, San Sebastián, Spain

[2]Dept. de Ciència de Materials i Química Física & IQTCUB, Universitat de Barcelona, c/ Martí i Franquès 1, 08028 Barcelona, Spain

[3]Department of Physics, Technical University of Denmark

[4]Faculty of Technology and Society, Malmö University, Sweden

[5]Department of Chemistry, University of Copenhagen, Denmark

[6]Department of Energy Conversion and Storage, Technical University of Denmark

[7]SINTEF Materials and Chemistry, Norway

[8]Interdisciplinary Nanoscience Center (iNANO), Department of Physics and Astronomy, Aarhus University, Denmark

[9]School of Engineering, Brown University, Providence, Rhode Island, USA

[10]Theoretical Chemistry Institute and Department of Chemistry, University of Wisconsin–Madison, USA

[11]Warwick Centre for Predictive Modelling, School of Engineering, University of Warwick, UK

[12]Department of Chemical Engineering, Carnegie Mellon University, Pittsburgh, USA

[13]School of Chemical Engineering, Purdue University, West Lafayette, Indiana, USA

[14]Síminn, Reykjavík, Iceland

[15]Institute for Applied Materials - Computational Materials Science, Karlsruhe Institute of Technology, Germany

[16]Netcompany IT and business consulting A/S, Copenhagen, Denmark

[17]Nanoscale Simulations, ETH Zürich, 8093 Zürich, Switzerland

[18]Freiburg Centre for Interactive Materials and Bioinspired Technologies, University of Freiburg, Germany

November 1, 2016

**Abstract**

The Atomic Simulation Environment (ASE) is a software package written in the Python programming language with the aim of setting up, steering, and analyzing atomistic simulations. In ASE, tasks are fully scripted in Python. The powerful syntax of Python combined with the NumPy array library make it possible to perform very complex simulation tasks. For example, a sequence of calculations may be performed with the use of a simple "for-loop" construction. Calculations of energy, forces, stresses and other quantities are performed through interfaces to many external electronic structure codes or force fields using a uniform interface. On top of this calculator interface, ASE provides modules for performing many standard simulation tasks such as structure optimization, molecular dynamics, handling of constraints and performing nudged elastic band calculations.

# 1 Introduction

The understanding of behaviour and properties of materials at the nanoscale has developed immensely in the last decades. Experimental techniques like scanning probe microscopy and electron microscopy have been refined to provide information at the sub-nanometer scale. At the same time, theoretical and computational methods for describing materials at the electronic level have advanced and these methods now constitute valuable tools to obtain reliable atomic-scale information [1].

The Atomic Simulation Environment (ASE) is a collection of Python modules intended to set up, control, visualise, and analyse simulations at the atomic and electronic scales. ASE provides Python classes like "Atoms" which store information about the properties and positions of individual atoms. In this way, ASE works as a *front-end* for atomistic simulations where atomic structures and parameters controlling simulations can be easily defined. At the same time, the full power of the Python language is available so that the user can control several interrelated simulations interactively and in detail.

The execution of many atomic-scale simulations requires information about energies and forces of atoms, and these can be calculated by several methods. One of the most popular approaches is density functional theory (DFT) which is implemented in different ways in dozens of freely available codes [2]. DFT codes calculate atomic energies and forces by solving a set of eigenvalue equations describing the system of electrons. A simpler but also more approximate approach is to use interatomic potentials (or so-called force fields) to calculate the forces directly from the atomic positions [3]. ASE can use DFT and interatomic potential codes as *backends* called "Calculators" within ASE. By writing a simple Python interface between ASE and, for example, a DFT code, the code is made available as an ASE calculator to the users of ASE. At the same time, researchers working with this particular code can benefit from the powerful setup and simulation facilities available in ASE. Furthermore, the uniform interface to different calculators in ASE makes it easy to compare or combine calculations with different codes. At the moment, ASE has interfaces to about 30 different atomic-scale codes as described in more detail later.

A few historical remarks: In the 1990s, object-oriented programming was widespread in many fields but not used much in computational physics. Most physics codes had a monolithic character written in compiled languages like Fortran or C using static input/output files to control

the execution. However, the idea that physics codes should be "wrapped" in object-oriented scripting languages was put forward [4]. The idea was that the object-oriented approach would allow the user of the program to operate with more understandable "physics" objects instead of technical details, and that the scripting would encourage more interactive development and testing of the program to quickly investigate new ideas. One of the tasks was therefore also to split up the Fortran or C code to make relevant parts of the code available individually to the scripting language. Also in the mid-nineties, the book on Design Patterns [5] was published discussing how to program efficiently using specific object-oriented patterns for different programming challenges. These patterns encourage better structuring of the code, for example by keeping different sub-modules of the code as independent as possible, which improves readability and simplifies further development.

Inspired by these ideas, the first version of ASE [6] was developed around the turn of the century to wrap the DACAPO DFT code [7] at the Center of Atomic-scale Materials Physics at the Technical University of Denmark. DACAPO is written in Fortran and controlled by a text input file. It was decided to use Python both because of the general gain in popularity at the time – although mostly in the computer science community – and because the development of numerical tools like Numeric and NumArray, the predecessors of NumPy [8], were under way. Gradually, more and more features, like atomic dynamics, were moved from DACAPO into ASE to provide more control at the flexible object-oriented level.

A major rewrite of ASE took place with the release of both versions 2 and 3. In the first version of the code, the "objectification" was enthusiastically applied, so that for example the position of an atom was an object. This meant that the user applying the "get position" method to an Atom object would receive such a Position object. One could then query this object to get the coordinates in different frames of reference. Over time, it turned out that too much "objectification" made ASE more difficult to use, in particular for new users who experienced a fairly steep learning curve to become familiar with the different objects. It was therefore decided to lower the degree of abstraction so that for example positions would be described by simply the three coordinates in a default frame of reference. However, the general idea of creating code consisting of independent modules by applying appropriate design patterns has remained. One example is the application of the "observer-pattern" [5], which allows for development of a small module of code (the "Observer") to be called regularly during a simulation. By just attaching the Observer to the "Dynamics" object, which is in control of the simulation, the Observer calculations will automatically be performed as requested.

ASE has now developed into a full-fledged international open-source project with developers in several countries. Many modules have been added to ASE to perform different tasks, for example the identification of transition states using the nudged elastic band method [9, 10]. Recently, a database module which allows for convenient storage and retrieval of calculations including a web-interface has also been developed. More calculators are added regularly as backends, and new open-source projects like Amp (Atomistic Machine-learning Package) [11] build on ASE as a flexible interface to the atomic calculators. The refinement of libraries like NumPy allows for more and more tasks to be efficiently performed at the Python level without the need for compiled languages. This also opens up new possibilities for both inclusion of more modules in ASE and for efficient use of ASE in other projects.

### 9.1 Estimation of exchange–correlation errors

The major approximation within DFT is the exchange–correlation functional. The `BEEFEnsemble` class in ASE provides tools for estimating errors due to the choice of exchange-correlation functional. The most efficient method is tightly linked with the BEEF functionals [122, 123, 124]. The BEEF-vdW functional [123], which we will use to explain and exemplify the method, has the functional form

$$E_{xc} = \sum_{m=0}^{29} a_m E_m^{\mathrm{GGA-x}} + \alpha_c E^{\mathrm{LDA-c}} + (1-\alpha_c) E^{\mathrm{PBE-c}} + E^{\mathrm{nl-c}}, \tag{21}$$

where $E_m^{\mathrm{GGA-x}}$ is GGA exchange with the Legendre polynomial of order $m$ used as enhancement factor. $E^{\mathrm{LDA-c}}$, $E^{\mathrm{PBE-c}}$, and $E^{\mathrm{nl-c}}$ are LDA, PBE, and non-local van der Waals correlation, respectively. The exchange sum expansion coefficients $a_m$ and the correlation weighting parameter $\alpha_c$ are fitted to databases such that the functional performs well for a range of different properties [123, 125]. In addition to the best set of coefficients, which constitutes the main BEEF-vdW functional, an ensemble of functionals with perturbed coefficients are constructed in a procedure inspired by Bayesian statistics, such that the computed ensemble standard deviation for a given calculation is a good estimate of the uncertainty and thus also the potential errors for a range of different properties like reaction enthalpies [123]. The energy of the individual terms in (21) can be parsed from any interfacing calculator to ASE, which contains the ensemble coefficient matrices and generates an energy ensemble using simple multiplication operations without any calls back to the calculator. It is currently implemented for the GPAW and VASP calculators.

As an example, consider two possible reactions in the industrial Fischer–Tropsch process.

$$\mathrm{CO} + 3\,\mathrm{H_2} \rightarrow \mathrm{CH_4} + \mathrm{H_2O} \qquad \text{(Reaction 1)}$$

$$\mathrm{CO} + \tfrac{5}{2}\,\mathrm{H_2} \rightarrow \tfrac{1}{2}\,\mathrm{C_2H_6} + \mathrm{H_2O} \qquad \text{(Reaction 2)}$$

The enthalpies of the reactions are calculated and the errors estimated using the ensemble. In addition, the net reaction difference between the two is simultaneously considered as an independent reaction.

$$\mathrm{CH_4} \rightarrow \tfrac{1}{2}\,\mathrm{C_2H_6} + \tfrac{1}{2}\,\mathrm{H_2} \qquad \text{(Reaction 3)}$$

Upon comparison with experimental data, see Table 2 and Figure 12, it is found that the errors

Table 2: Enthalpies of reaction

| | Calc. [eV] | Est. error [eV] | Exp.[†] [eV] | Error [eV] |
|---|---|---|---|---|
| Reaction 1 | -1.86 | ±0.25 | -2.14 | -0.28 |
| Reaction 2 | -1.53 | ±0.25 | -1.80 | -0.27 |
| Reaction 3 | 0.33 | ±0.02 | 0.34 | 0.02 |

[†]Reference [126]

versus experimental data and the calculated error estimates are of similar size. Errors and uncertainties within DFT are often systematic, making relative errors much smaller. Considering Reaction 3, both the error and the error estimate are one order of magnitude smaller than for

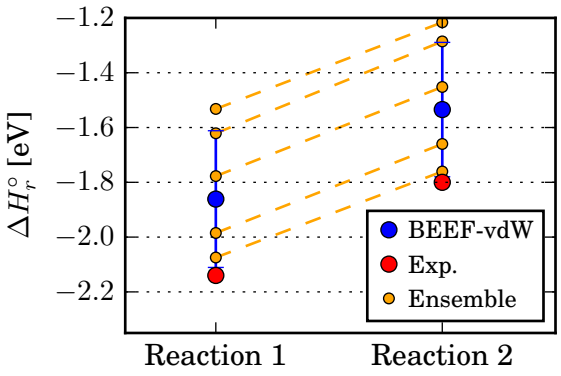


Figure 12: Experimental and calculated enthalpies. The error is well estimated using the ensemble standard deviation. The enthalpy difference between the two reactions is nearly functional independent as illustrated by 5 selected functionals from the ensemble.

the other reactions, since the errors obtained with any given functional are similar in Reaction 1 and Reaction 2 as illustrated on Figure 12.

Another method for testing possible favorable error cancellation to reduce uncertainty without relying on reference data is by establishing correlations in functional dependence for a set of reactions as demonstrated by Christensen *et al.* [127]. In addition to error cancellation such analysis can also be used to reveal causes of systematic errors.

## 12 Acknowledgements

The authors acknowledge funding from: The European Union's Horizon 2020 research and innovation program under grant agreement no. 676580 with The Novel Materials Discovery (NOMAD) Laboratory, a European Center of Excellence; research grant 9455 from VILLUM FONDEN; Deutsche Forschungsgemeinschaft (grant PA2023/2); the UK Engineering and Physical Sciences Research Council (grants EP/L014742/1, EP/L027682/1 and EP/P002188/1).

## References

[1] R.O. Jones. Density functional theory: Its origins, rise to prominence, and future. *Reviews of Modern Physics*, 87(3):897–923, August 2015.

[2] Quantum chemistry and solid-state physics software. `https://en.wikipedia.org/wiki/List_of_quantum_chemistry_and_solid-state_physics_software`.

[3] Knowledgebase of interatomic models. `https://openkim.org`.

[4] Paul F. Dubois. Making Applications Programmable. *Computers in Physics*, 8(1):70–73, January 1994.

[5] Erich Gamma, Richard Helm, Ralph Johnson, and John Vlissides. *Design Patterns*. Elements of Reusable Object-Oriented Software. Addison-Wesley, 1995.

[6] Sune R. Bahn and Karsten W. Jacobsen. An object-oriented scripting interface to a legacy electronic structure code. *Computing in Science & Engineering*, 4(3):56–66, 2002.

[7] DACAPO code. `https://wiki.fysik.dtu.dk/dacapo`.

[8] NumPy. `http://www.numpy.org`.

[9] Greg Mills and Hannes Jónsson. Quantum and thermal effects in $H_2$ dissociative adsorption: Evaluation of free energy barriers in multidimensional quantum systems. *Physical Review Letters*, 72(7):1124–1127, February 1994.

[10] Hannes Jónsson, Greg Mills, and Karsten Wedel Jacobsen. Nudged elastic band method for finding minimum energy paths of transitions. In Bruce J. Berne, Giovanni Ciccotti, and David F. Coker, editors, *Classical and Quantum Dynamics in Condensed Phased Simulations, Proceedings of the International School of Physics "Computer Simulation of Rare Events and Dynamics of Classical and Quantum Condensed-Phased Systems" : Lerici, Villa Marigola, 7 July-18 July 1997*, pages 385–404. World Scientific Publishing Company Incorporated, January 1998.

[11] Alireza Khorshidi and Andrew A. Peterson. Amp: A modular approach to machine learning in atomistic simulations. *Comput. Phys. Commun.*, 207:310–324, 2016.

[12] Travis E. Oliphant. Python for scientific computing. *Computing in Science & Engineering*, 9(3):10–20, 2007.

[117] Ivano E. Castelli, Kristian S. Thygesen, and Karsten W. Jacobsen. Calculated pourbaix diagrams of cubic perovskites for water splitting: Stability against corrosion. *Topics in Catalysis*, 57(1):265–272, 2013.

[118] Ivano E. Castelli, Falco Hüser, Mohnish Pandey, Hong Li, Kristian S. Thygesen, Brian Seger, Anubhav Jain, Kristin A. Persson, Gerbrand Ceder, and Karsten W. Jacobsen. New light-harvesting materials using accurate and efficient bandgap calculations. *Advanced Energy Materials*, 5(2):1400915, 2015.

[119] J. Tersoff and D. R. Hamann. Theory of the scanning tunneling microscope. *Phys. Rev. B*, 31:805–813, Jan 1985.

[120] Hendrik J. Monkhorst and James D. Pack. Special points for Brillouin-zone integrations. *Phys. Rev. B*, 13(12):5188–5192, 1976.

[121] Wahyu Setyawan and Stefano Curtarolo. High-throughput electronic band structure calculations: challenges and tools. *Computational Materials Science*, 49:299–312, 2010.

[122] J. J. Mortensen, K. Kaasbjerg, S. L. Frederiksen, J. K. Nørskov, J. P. Sethna, and K. W. Jacobsen. Bayesian error estimation in density-functional theory. *Phys. Rev. Lett.*, 95:216401, Nov 2005.

[123] Jess Wellendorff, Keld T. Lundgaard, Andreas Møgelhøj, Vivien Petzold, David D. Landis, Jens K. Nørskov, Thomas Bligaard, and Karsten W. Jacobsen. Density functionals for surface science: Exchange–correlation model development with Bayesian error estimation. *Phys. Rev. B*, 85:235149, Jun 2012.

[124] Jess Wellendorff, Keld T. Lundgaard, Karsten W. Jacobsen, and Thomas Bligaard. mBEEF: An accurate semi-local Bayesian error estimation density functional. *The Journal of Chemical Physics*, 140(14), 2014.

[125] Jess Wellendorff, Trent L. Silbaugh, Delfina Garcia-Pintos, Jens K. Nørskov, Thomas Bligaard, Felix Studt, and Charles T. Campbell. A benchmark database for adsorption bond energies to transition metal surfaces and comparison to selected DFT functionals. *Surface Science*, 640:36 – 44, 2015. Reactivity Concepts at Surfaces: Coupling Theory with Experiment.

[126] P. J. Linstrom and W. G. Mallard, editors. *NIST Chemistry WebBook, NIST Standard Reference Database Number 69*. National Institute of Standards and Technology, June 2005.

[127] Rune Christensen, Heine A. Hansen, and Tejs Vegge. Identifying systematic DFT errors in catalytic reactions. *Catal. Sci. Technol.*, 5:4946–4949, 2015.

[128] R. Landauer. Spatial variation of currents and fields due to localized scatterers in metallic conduction. *IBM Journal of Research and Development*, 1(3):223–231, July 1957.

[129] Rolf Landauer. Electrical resistance of disordered one-dimensional lattices. *Philosophical Magazine*, 21(172):863–867, 1970.